TECHNISCHE
UNIVERSITÄT
WIEN
Vienna | Austria

Dissertation

The Physics of Non–Equilibrium Reliability Phenomena

zur Erlangung des akademischen Grades

Doktor der technischen Wissenschaften

eingereicht an der Technischen Universität Wien
Fakultät für Elektrotechnik und Informationstechnik
von

Markus Jech

Matrikelnummer 0625384

Flugfeldstraße 61/3/27

1220 Wien, Österreich

Betreuer: Univ.Prof. Dr. Tibor Grasser
Gutachter: Assoc.Prof. Dr. Mathieu Luisier
Gutachter: Dr. Alain Bravaix

Wien, im Oktober 2020

Abstract

The Physics of Non–equilibrium Reliability Phenomena

Continuous downscaling of silicon based technology enabled by Moore's law is still the main focus of the international roadmap for devices and systems (IRDS). The currently implemented 7 nm nodes inside modern smartphones and processors will be soon replaced by 5 nm nodes which are in production now. While these nodes do no longer correspond to physical dimensions, as for instance the 5 nm node has a gate length of 18 nm, this dramatic reduction in size from the original micrometer–sized regime is indeed impressive. Even more astonishing, the 1 nm node, based on gate–all–around devices and 3D integration, is expected to be ready at the end of the decade to satisfy the emerging trend for ultra–low–power devices with "always on" features used in upcoming applications such as cloud–based and mobile computing, sensing and, of course, Internet–of–Things.

However, this ongoing trend drives the involved materials – channel materials (Si, Ge) and amorphous oxides (SiO_2, HfO_2) alike – closer towards their physical limitations. Considering that 1 nm is *scarcely the width of five silicon layers* implies that novel device architectures with gate lengths within the nanometer regime contain a countable number of atoms in the active region. As a consequence, *device reliability* and *variability* is strongly influenced by quantum mechanical effects caused by the atomistic nature of modern transistor architectures. For example, *individual defects* at or near the Si/SiO_2 interface, which are known to be responsible for reliability issues such as **bias temperature instability** (**BTI**) and **hot–carrier degradation** (**HCD**), increasingly affect the behavior of the device. In order to understand these effects, the focus therefore has to be shifted towards atomistic simulations and approaches, such as *ab initio* methods, to investigate and reveal the physics behind these adverse phenomena.

In this sense, this thesis focuses on the **interaction of non–equilibrium charge carriers** with **hydrogen–related defects and precursors** in semiconductor devices. A major part of this work focuses on the **investigation of the Si/SiO_2 interface** and the **microscopic nature of Si–H bond breakage**. Various available *ab initio* methods, including the methods of *well–tempered metadynamics*, *nudged–elastic–band calculations* and *the modern theory of polarization* based on density functional theory (DFT) have been used to study the Si–H bond within its realistic 3D environment. In addition, to capture the **excitation and breaking dynamics** of the Si–H bond due to the *coupling with*

its surrounding, particularly the **interaction with energetic charge carriers**, a quantum kinetic framework has been developed. In addition, the **influence of non–equilibrium carrier distributions onto the charging and discharging kinetics of defects in the oxide** has been investigated. The state–of–the–art modeling framework based on **nonradiative multiphonon theory** (**NMP**) has been extended to replace the previously used equilibrium carrier distribution by a realistic non–equilibrium distribution obtained from a solution of the Boltzmann transport equation which goes *far beyond* existing approaches.

Ultimately, the *individual* modeling approaches have been benchmarked and validated against dedicated measurement sets, *revealing interesting new phenomena and insights* into the degradation dynamics. Furthermore, a comprehensive study on the *degradation and recovery dynamics in full bias space* is a special challenge and highlight. The *full simulation framework*, covering the charge transition kinetics of oxide defects as well as the creation of interface states, provides a physical understanding of the underlying mechanisms. The supporting analysis definitely *challenges* the conceptual limits of independent degradation regimes as previously assumed.

The presented results and developed methods clearly reveal new degradation physics and can be seen as a *next step* towards unraveling device reliability issues. Particularly the focus on the microscopic picture of the Si/SiO_2 interface can aid future investigations concerning the elusive role of hydrogen in degradation phenomena. Furthermore, the derived approaches are free of empirical parameters and can easily be generalized to describe emerging material combinations such as Ge/GeO_2 based devices.

Kurzfassung

Die Physik von Zuverlässigkeitsphänomenen im Nichtgleichgewicht

Die kontinuierliche Miniaturisierung von Silizium–basierter Technologie, ermöglicht und getrieben durch das Mooresche Gesetz, ist weiterhin ein wichtiger Bestandteil der International Roadmap for Devices and Systems (IRDS). Die aktuell in modernen Smartphones und leistungsstarken Prozessoren verbaute 7 nm Technologie wird bald durch noch kleinere und leistungsstärkere 5 nm Transistoren ersetzt werden. Obwohl die aktuellen Technologiebezeichnungen nicht mehr mit den eigentlichen physikalischen Dimensionen übereinstimmen, 5 nm Transistoren haben eine Gatelänge von 18 nm, so ist die deutliche Skalierung der Abmessungen in den letzten Jahre dennoch eindrucksvoll. Noch erstaunlicher ist, dass die zukünftige 1 nm Technologie, basierend auf Gate–all–Around Bauteilen und 3D Integration, für das Ende dieses Jahrzehnts erwartet wird um die steigende Nachfrage an Ultra–Low–Power Elektronik für "Always–On" Anwendungen zu befriedigen welche für aufstrebende Bereiche wie Cloud– und Mobile Computing, Sensorsysteme und natürlich Internet–of–Things benötigt wird.

Dieser anhaltende Trend bringt die dabei verwendeten Materialien – kristalline Kanal– (Si, Ge) und amorphe Oxidmaterialien (SiO_2, HfO_2) gleichermaßen – an ihre physikalischen Grenzen. Angesichts der Tatsache, dass 1 nm *annähernd der Dicke von fünf atomaren Siliziumschichten entspricht*, bedeutet dies für neuartige Bauteilarchitekturen, dass die aktive Kanalregion aus einer abzählbaren Anzahl von Atomen besteht. Daraus resultierend wird die *Zuverlässigkeit und Variabilität* von Bauelementen immer stärker von quantenmechanischen Effekten geprägt aufgrund der atomaren Natur von modernen Technologien. Daher werden Zuverlässigkeitsphänomene, wie z.B. die **Spannungs–Temperaturinstabilität** (*engl. bias temperature instability*, **BTI**) und die **Degradation durch heiße Ladungsträger** (*engl. hot–carrier degradation*, **HCD**), immer stärker von *einzelnen Defekten*, welche sich direkt *an* oder *nahe* der Si/SiO_2 Grenzschicht befinden, beeinflusst. Um die beteiligten Prozesse untersuchen zu können, rücken daher heutzutage atomistische Simulationen immer mehr in den Mittelpunkt, wie z.B. *ab initio* Methoden, um die Physik und die Mechanismen hinter diesen nachteiligen Phänomenen zu beschreiben.

In diesem Sinne konzentriert sich die vorliegende Dissertation auf die **Interaktion von Ladungsträgern im Nichtgleichgewicht mit Defekten und**

chemischen Bindungen im Zusammenhang mit Wasserstoff in Halbleiterbauteilen. Ein Großteil dieser Arbeit verfolgt das Ziel die **Si/SiO$_2$ Grenzschicht**, und in diesem Zusammenhang, die **mikroskopische Natur des Aufbrechens der Si–H Bindung** zu untersuchen. Um die Eigenschaften von Si–H Bindungen innerhalb einer möglichst realistischen dreidimensionalen Umgebung zu simulieren und zu charakterisieren wurden verschiedene *ab initio* Methoden verwendet, wie z.B. *well–tempered metadynamics*, *nudged elastic band Berechnungen* und *modern theory of polarization* basierend auf Dichtefunktionatheorie (DFT). Parallel dazu wurde ein quantenmechanisches Modell zur **Beschreibung der Anregungsdynamik und des Aufbrechens des Si–H Bindung** entwickelt welches versucht alle relevanten *Wechselwirkung mit der Umgebung* berücksichtigt, speziell die **Interaktion mit energetischen Ladungsträgern** im Kanal des Transistors. Darüber hinaus wurde der **Einfluss von Ladungsträgern im Nichtgleichgewicht auf das Verhalten von Oxiddefekten und deren Einfang– und Emissionsprozesse von Ladungsträgern** untersucht. Dazu wurde das derzeitige Modell, welches auf der Theorie der Übergange mittels **nichtstrahlenden Multiphononen** (*engl. nonradiative multiphonon*, **NMP**) basiert, entsprechend erweitert, sodass eine vollständige Lösung der Boltzmann Transportgleichung berücksichtigt wird. Diese Beschreibung geht *weit über die aktuellen Ansätze*, welche hauptsächlich auf elektrostatischen Überlegungen aufbauen, hinaus.

Die Ergebnisse und Vorhersagen der entwickelten *individuellen* Modelle wurden schlussendlich mit einer Vielzahl von verschiedenen Messdaten verglichen und erlauben einen *Einblick in bisher unentdeckte Phänomene und Verhalten* der Degradationsmechanismen. Eine besondere Herausforderung und den Höhepunkt dieser Arbeit stellte die *umfassende Modellierung der Degradation und anschließenden Ausheilung* (*engl. recovery*) **eines Transistors im gesamtem Spannungsraum** dar. Das *vollständige Modellsystem*, welches sowohl die Dynamik von Oxiddefekten wie auch Erzeugung von Defekten an der Si/SiO$_2$ Grenzschicht umfasst, erlaubt hierbei eine detaillierte physikalische Beschreibung der zugrunde liegenden Mechanismen. Die Simulationsergebnisse sowie umfassende Auswertungen der Ergebnisse zeigen hier klar die konzeptionellen Schwachstellen in der vorherrschenden Annahme von unabhängigen Degradationsregimen.

Die hier entwickelten Methoden und Ansätze erlauben neue Erkenntnisse in die Physik von Degradationsprozessen in elektronischen Bauteilen und können als *weiterer Puzzlestein* zu einem vollständigen Verständnis dieser gesehen werden. Im besonderen der vorliegende Schwerpunkt und die neuen Einblicke in die mikroskopische Struktur der Si/SiO$_2$ Grenzschicht kann als Grundbaustein für weitere Studien bezüglich der noch immer ungeklärten Rolle von Wasserstoff gesehen werden. Abschließend sei noch zu erwähnen, dass die abgeleiteten Formalismen frei von empirischen Parametern sind und somit ebenso auf neue und aufstrebenden Materialkombinationen, wie z.B. Ge/GeO$_2$ basierte Bauteile, anwendbar sind.

Contents

List of Acronyms

BTI	bias temperature instability
NBTI	negative bias temperature instability
PBTI	positive bias temperature instability
HCD	hot–carrier degradation
TDDB	time dependent dielectric breakdown
CMOS	complementary metal–oxide–semiconductor
VLSI	very large–scale integrated
NMP	nonradiative multiphonon
PES	potential energy surface
PEC	potential energy curve
RC	reaction coordinate
MEP	minimum energy path
MECP	minimum energy crossing point
NEB	nudged elastic band
CI–NEB	climbing–image nudged elastic band
BOA	Born–Oppenheimer approximation
TST	transition state theory
TS	transitions state
FGR	Fermi's Golden Rule
FCP	Franck–Condon principle
LSF	lineshape function
WKB	Wentzel–Kramers–Brillouin

TCAD	technology computer–aided design
MOSFET	metal–oxide–semiconductor field–effect transistor
VB	valence band
CB	conduction band
EDF	energy distribution function
TDDS	time–dependent defect spectroscopy
OV	oxygen vacancy
HB	hydrogen bridge
HE′	hydroxyl–E′ center
FPT	first passage time
FD	Fermi–Dirac
BTE	Boltzmann transport equation
II	impact ionization
DD	drift–diffusion
eMSM	extended Measure–Stress–Measure
DFT	density functional theory
CDFT	constrained density functional theory
SP	single particle
MP	multiple particle
STM	scanning tunneling microscope
DB	dangling bond
ESR	electron spin resonance
DOS	density of states
MD	molecular dynamics
BC	bond–center
AB	antibonding
WTMD	well–tempered metadynamics
CV	collective variable

FES	free energy landscape
MO	molecular orbital
DOF	degrees of freedom
LUMO	lowest unoccupied molecular orbital
HOMO	highest occupied molecular orbital

CHAPTER 1

Introduction & Motivation

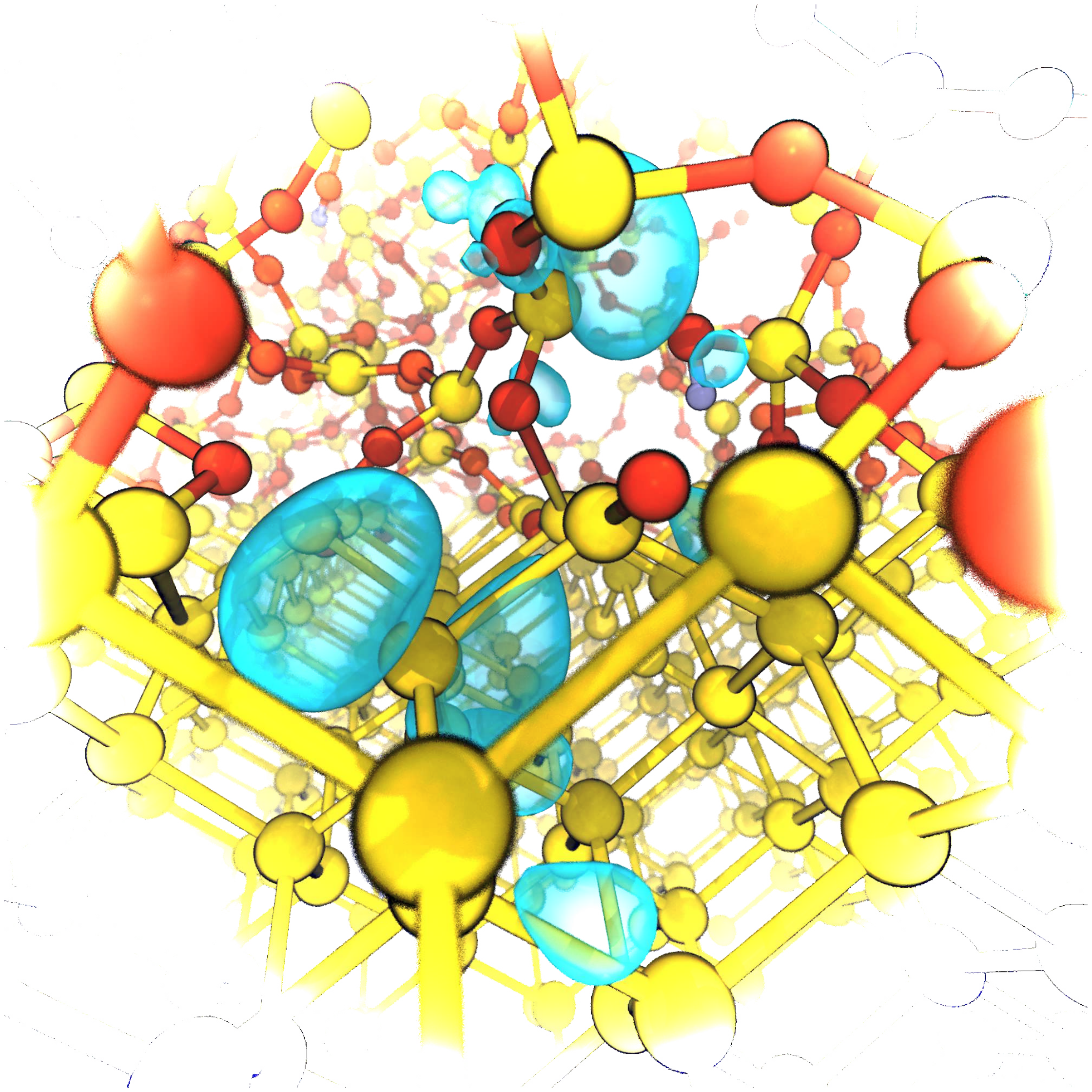

In modern very large–scale integrated (VLSI) technologies complementary metal–oxide–semiconductor (CMOS) transistors face a broad range of operating, and hence, potential degradation regimes. For example, n– and p–channel FETs in a logic gate experience various V_G and V_D bias combinations during switching between logic levels. Assessing the reliability, on the other hand, typically focuses on idealized degradation modes, such as bias temperature instability (BTI), hot–carrier degradation (HCD) and time dependent dielectric breakdown (TDDB). Each of these reliability issues is usually evaluated in a certain bias space regime, see Fig. 1.1, and is experimentally and theoretically characterized around their respective worst–case stress condition. The individual degradation modes are, therefore, reasonably well understood and rather intricate models have been developed to capture the nature and characteristics of each phenomenon.

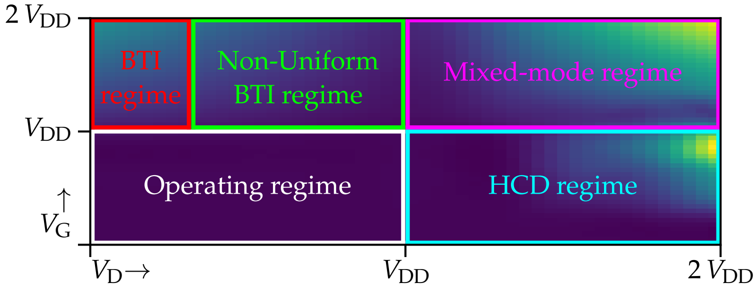

FIGURE 1.1: Schematic representation of the full $\{V_\mathrm{G}, V_\mathrm{D}\}$ bias space together with the various degradation regimes discussed in this thesis.

On the one hand, **bias temperature instability** and specifically the theoretical concepts behind this detrimental phenomenon, has gained much attention over the last decades [1]. Due to the aggressive downscaling of modern CMOS technologies together with the introduction of nitrogen into the oxide, the main research focus has been on the *negative* bias temperature instability (NBTI) in pMOSFETs. However, with the adoption of high–κ materials for the gate stack its counterpart, the *positive* bias temperature instability (PBTI), in nMOSFET transistors plays an equally important role nowadays. Despite the numerous research efforts BTI remains an active and controversial topic which is also reflected in the diversity of modeling approaches and their fundamentally diverging microscopic description.

In its early stages modeling approaches of BTI were based upon phenomenological observations which led to the model of JEPPSON and SVENSSON in 1977 [2]. They assumed two different mechanisms within the low– and high–field regime to be responsible for the macroscopic shift of the threshold voltage: Breaking of interfacial Si–H bonds and the formation of mobile hydrogen or hydroxyl species and tunneling injection and trapping of holes activating surface states. This work provides the original formulation of the so–called *Reaction–Diffusion* model [1], which was able to explain the known power law dependence of the degradation, and served as a basis for further modifications until today. However, the introduction of new technology nodes using thin oxides together with advanced measurement setups such as time–dependent defect spectroscopy (TDDS) [3] revealed severe inconsistencies between the theoretical and experimental data [4]. Subsequently the research focus shifted towards the second mechanism which involves charge trapping into the oxide. The underlying physical process, however, has only been vaguely understood until KIRTON and UREN in the 1990s described noise within the context of nonradiative multiphonon (NMP) theory of charge transitions [5]. Their pioneering work paved the way for further development by a broader community and was adopted by GRASSER *et al.* to model the characteristics of BTI [6–11]. Within the recently published 4–state NMP model [6, 7, MJJ7] BTI, in particular its *recoverable* component, is attributed to charge trapping at pre–existing oxide defects in the gate stack. Thereby, it provides an accurate physical framework capturing even peculiar features such as defect metastability and has been successfully applied across various technologies [12–14, MJC11, MJC12, 15]. Despite the increasing acknowledgement of the NMP theory in the reliability community, soon after its development criticism was raised related to the role of the *quasi permanent*[1] component of degradation and also the assumption that the 4–state formulation solely relies on pre–existing defects in the oxide. In response to these comments pursuing research efforts culminated in an evolution of the 4–state NMP framework in which the dynamic redistribution of hydrogen provides a link between the *recoverable* and *quasi permanent* component of degradation and further implements a possible defect creation mechanism [17–19]. Nevertheless, the heavily disputed field of bias temperature instability exhibits a continuously growing number of publications containing partially contradictory conclusions which renders it almost impossible for single a model to capture its various features and peculiarities.

On the other hand, **hot–carrier degradation** is attributed to a *more permanent*[2] damage and is related to a different type of defect. It is widely accepted that Si–H bond rupture at or near the Si/SiO$_2$ interface results in electrically active amphoteric traps. Over the past decades the phenomenon of HCD has evolved towards being the dominant and most troublesome reliability concern in modern technology nodes [20, 21]. Moreover, due to the continuous downscaling new challenges have emerged such as device–to–device variability and its implications on the reliability behavior has become a major issue. Random dopant variability and the generation of discrete random traps [22–25, MJJ5, 26, MJC7, MJC6] need to be taken into consideration as well as the effect of self–heating [27–30], which exacerbates the phenomenon of hot–carrier induced degradation in three–dimensional structures. All this serves to demonstrate the increasing complexity of modeling HCD to cover its broad physical spectrum. In that respect, modeling approaches have also advanced from phenomenological descriptions [31, 32] to more complex (semi–empirical) formulations [33–35, MJJ12] to capture the manifold phenomena contributing to HCD. However, while it is commonly accepted that hot–carrier

---

[1] Note that the term *quasi permanent* components refers to the extremely slowly recovering contribution which sometimes is assumed to be *permanent* [16].

[2] Although, also the damage created due to HCD can be annealed again.

damage is due to breaking of interfacial Si–H bonds resulting in electrically active P_b centers, its underlying fundamental physical mechanisms have not been fully clarified yet.

Hot–carrier degradation started to gain attention in the early 1970s with the first reports of this phenomenon [36]. Thereby, the term *hot* describes carriers in the channel which have been accelerated by the (high) electric field, particularly in the drain region of the metal–oxide–semiconductor field–effect transistor (MOSFET), and thus have gained a considerable amount of kinetic energy. Writing the energy as kT shows that the *effective* carrier temperature is many orders of magnitude higher than the surrounding lattice temperature. The first successful, although phenomenological, description of HCD characteristics was proposed by Hu *et al.* [31, 37]. The so–called *Lucky Electron* model originates from the work of SHOCKLEY [38] modeling the substrate and gate current and assumes that an energetic, *lucky*, electron impinges and surmounts the potential barrier at the interface thereby triggering the creation of a defect. Due to its simplicity it is still firmly entrenched in the community and several (semi–) empirical extensions have been suggested providing the foundations for the *field–driven* formulation of HCD [39–42]. Downscaling of transistor geometries below the micrometer regime together with the reduction of the operating voltages was expected to remedy hot–carrier related reliability issues. Yet, exactly the opposite has happened and HCD is highly relevant in scaled device architectures. In a series of experimental studies the IBM group investigated various stress regimes[3] and concluded that the rate of interface state generation exclusively depends on the deposited energy by the carriers, independent of the stress mode [43–45]. These findings strongly inspired the development of the *energy–driven* paradigm of HCD by RAUCH and LAROSA in which the driving force is the available carrier energy to trigger the creation of interface defects [33, 46]. The continued downscaling of CMOS technology further supported the idea that the carrier energy distribution function (EDF) becomes increasingly important and strongly depends on the bias conditions, which is also reflected in the change of the worst–case stress conditions from $V_\mathrm{G} \sim 0.5V_\mathrm{D}$ to $V_\mathrm{G} = V_\mathrm{D}$ for devices scaled into the nanometer regime. However, once again a next step in the evolution of HCD modeling was required for an advanced characterization and description of this phenomenon. The ground–breaking work by the group of HESS on the defect creation kinetics provides the cornerstone of modern modeling approaches and still defines the current understanding [47–52]. Acknowledging the crucial role of the EDFs, two individual degradation modes, known as the *single carrier* and *multiple carrier* mechanism, have been introduced accounting for the sparsely populated high energy tail as well as the part of the carrier ensemble having moderate energies. Unfortunately, the proposed formalism has never been applied to model the effect of HCD in an actual device. Nevertheless, the main concepts have been used by two groups, namely the group of

---

[3] Often stress regimes such as channel–, drain avalanche–, secondary generated and substrate hot–carrier stress can be found in the literature. In modern devices only *channel* hot–carrier stress is the relevant stress modes, which, however, includes the effects of drain avalanche and secondary generation of carriers.

Bravaix [34, 53–56] and Tyaginov [35, MJJ12, 57, MJC13, MJJ11, MJC18], and strongly influenced further developments[4]. Both modeling frameworks have successfully proven to capture the various trends of HCD across different technologies. However, technological innovations such as the introduction of FinFETs and nanowires in conjunction with new promising materials such as germanium constantly challenge the prevailing assumptions and demand a continuously improved and in–depth description of hot–carrier degradation [MJC13, MJC8, MJC9].

Motivation & Scope

Reading the Introduction might suggest that the current modeling approaches already cover the full spectrum related to bias temperature instability and hot–carrier degradation, which would be a very abrupt end for this thesis. (Un–) Fortunately, a closer inspection reveals several open questions and missing links which initially triggered the research within this work and will hopefully be answered by the end.

Non–equilibrium carrier dynamics related reliability issues play *the* central role in this thesis. Charge carriers in the channel of a MOSFET are accelerated by the electric field and undergo various scattering mechanisms, thereby exchanging energy. This evolution results in a complex carrier energy distribution function (EDF), severely shifted from the equilibrium.

Carriers which have gained sufficient energy can trigger the creation of interface defects, known as HCD. Although the most recent stage of model developments relies on the concepts of a single and multiple carrier mechanism, their origin remains dubious and the fundamental excitation processes are not fully established yet. Furthermore, there is still no consensus on the actual microscopic Si–H bond–breaking kinetics and the associated potential barrier to form an electrically active interface trap. A major part of this thesis is devoted to the development of a general quantum kinetic formulation describing the dynamics of bond excitation and breaking mechanisms. All relevant system–bath interactions, such as vibrational relaxation and dipole scattering as well as resonance–induced excitations have been extracted using the close analogy to H terminated Si surfaces and the wealth of available experimental and theoretical studies. *Ab initio* methods performed on a realistic Si/SiO$_2$ model have been applied to characterize the contribution of each individual mechanism and, furthermore, have been used to systematically address the question on how the H eventually dissociates away from the Si.

On the other hand, energetic carriers can penetrate into the oxide and get trapped at pre–existing oxide defects. However, the effect of charge trapping is usually evaluated within the BTI regime and hardly any studies have investigated the effect of non–equilibrium processes onto the (de–) trapping dynamics of oxide defects. Interestingly, also the 4–state NMP model is based on the equilibrium EDFs in order to evaluate the transition rates associated with charge capture and emission events. Therefore, an appealing and natural extension of the current BTI

---

[4] These formulations are sometimes referred to as *current–driven* formulations

modeling framework towards full bias space explicitly includes non–equilibrium EDFs calculated as a solution of the Boltzmann transport equation (BTE). Additionally, a model variant with reduced complexity will be introduced which is particularly suited for modern technology computer–aided design (TCAD) applications.

This work not only aims at developing a better understanding of each individual degradation mode and the interaction of carriers with interface and oxide defects, but also gives new insights into the processes in full bias space. Overall, the presented results constitute a further step towards a *Grand Unified Theory*[5] in the field of reliability, in which the two standard models for BTI and HCD are merged into a single framework.

Outline

Chapter 2 reviews the state–of–the–art modeling frameworks for the creation of interface defects (HCD) and charge trapping at pre–existing oxide defects (BTI). Open questions and shortcomings of the current approaches are identified and the main ideas and concepts to address these open issues are introduced. Special attention is paid to the interaction of energetic charge carriers with individual chemical bonds. Several excitation mechanisms well known in the field of *surface chemistry* are highlighted and compared to the characteristics of HCD, which allows to derive the most important contributions given the conditions in a MOSFET: vibrational relaxation, dipole–induced as well as excitations due to a resonant scattering mechanism. Oxide defects, on the other hand, and the influence of non–equilibrium conditions onto the charging and discharging behaviour are considered as well. Possible extensions and approximations of the 4–state NMP model to calculate the phonon assisted transition rates are discussed: an extended model variant as well as a full non–equilibrium model using the calculated EDFs.

Chapter 3 presents a detailed atomistic characterization of the Si–H bond and its properties using *ab initio* methods. First, the Si–H bond breaking trajectory will be revealed by means of different simulation methods using a classical force–field in conjunction with density functional theory (DFT). Furthermore, various properties of the Si–H complex and its environment are analyzed which are the key ingredients required by the theoretical concepts introduced before. Among them is the response to an applied electric field, the calculation of excited states and the vibrational coupling to its surrounding. In order to establish a complete picture of hydrogen related phenomena at the Si/SiO_2 interface, H migration pathways along and across the interface as well as potential passivation reactions are examined at the end.

---

[5] This might sound familiar to a physicist.

Chapter 4 focuses on the theoretical formulations of the individual excitation and transitions rates. The dynamics of interface defects triggered by energetic charge carriers are described using open–system density–matrix theory. All relevant system–bath interactions are considered within this approach and the individual formulas are based on well established formulations in the literature. However, in contrast to existing theories, the modeling framework described here is coupled to a BTE solver to take the formation of non–equilibrium EDFs into account. Possible approximations to reduce the model complexity are discussed as well. Additionally, the theoretical foundations to describe the kinetics of oxide defects in full bias space will be established. Two variants of the 4–state NMP model with increasing levels of complexity will be presented. First, an extended model variant considering the electrostatics and the effect of impact ionization which, however, does not require information on the EDFs. Second, a full non–equilibrium 4–state model variant which explicitly relies on the coupled EDFs for electrons and holes.

Chapter 5 summarizes the simulation results and compares them to experimental data. At the beginning both simulation approaches are individually tested in order to verify their capabilities. Comparing hot–carrier induced damage for an nMOSFET and a pMOSFET having different channel lengths at two temperatures reveals interesting degradation characteristics. The behaviour of oxide defects under non–equilibrium conditions, on the other hand, is examined using the measurements of single traps. Both developed modeling approaches are thoroughly tested and an in–depth analysis of the results further supports the corresponding findings. Subsequently, the presented work culminates in the modeling of a full $\{V_\mathrm{G}, V_\mathrm{D}\}$ bias map and a dedicated experiment with alternating stress conditions. Both results ultimately stress the conceptual limits of independent degradation modes.

Chapter 6 briefly summarizes the key achievements of this thesis and highlights the most important findings. Furthermore, some suggestions and ideas for future improvements are listed.

CHAPTER 2

State of the Art & Shortcomings

The following Chapter provides an overview of the most advanced modern modeling approaches developed to capture the nature of bias temperature instability (BTI) and hot–carrier degradation (HCD). Shortcomings and open questions will be discussed and the key ideas to surmount the current limitations will be introduced.

Due to the in–depth description of both phenomena, the models are already based on the microscopic concept of **potential energy surfaces** (PESs). A PES describes the relation between the energy of a system and its geometry and is usually parametrized with respect to the position of the atoms. The Born–Oppenheimer approximation (BOA) is the cornerstone of modern computational chemistry and simplifies the full Schrödinger equation by separating it into an electronic and ionic part due to the mass disparity [58, 59]. This allows one to focus on the solution of the electronic wavefunction $V(\mathbf{R})$ which acts as a potential for the ionic cores and includes Coulomb interactions as well as the contribution of the kinetic energy terms. For a system containing N atoms a PES is therefore a $3N$–dimensional object defining the energy as a function of the atomic coordinates. Modern *ab initio* codes offer a variety of functional forms with increasing complexity to evaluate the *adiabatic* potential. However, the large configuration space often prohibits the consideration of all degrees of freedom, particularly for transitions between different PESs involved in charge transfer reactions. Reducing a multi–dimensional PES $V(\mathbf{R})$ to a one–dimensional potential energy curve (PEC) $V(q)$ by selecting a reaction trajectory $\mathbf{R}(q)$ and mapping the collective motion of atoms onto an effective reaction coordinate (RC) q is, therefore, desired for all practical applications. The reaction path ideally properly reflects the actual minimum energy path (MEP) connecting two minimum configurations with the lowest energy barrier. While for transitions *within* a single PEC this criterion is sufficiently fulfilled using a variant of the nudged elastic band (NEB) method, transitions *across* different PECs are determined by their crossing point and strongly depend on the chosen RC q and/or possible approximations schemes of the PEC, such as the harmonic approximation [8, MJJ7, 60–64]. Finding the minimum energy crossing point (MECP) of PECs for non–adiabatic charge transfer reactions is still a non–trivial optimization issue and an active research topic [65, 66]. Note that, regardless of the type of transition – within or across PEC(s) – the utilized MEP, hence the transition barrier, obeys *classical* mechanics.

2.1 Hot–Carrier Degradation

The major breakthrough in modeling and understanding HCD in electronic devices is due to the work by the group of Hess [47–52]. This work serves as a basis for subsequent developments by two groups, namely the group of Bravaix [54, 56] and Tyaginov [35, MJJ12, MJC13, MJC19]. The main concept proposed by HESS is to link a thorough carrier transport treatment with two different but interacting regimes for defect creation.

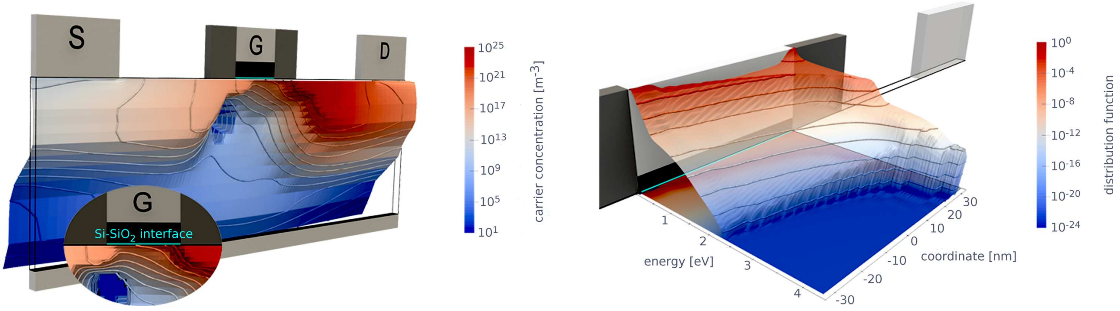

FIGURE 2.1: A solution of the BTE for a 65 nm nMOSFET employing SiON as the gate dielectric calculated with the deterministic solver VIENNASHE [67]. **Left:** The distribution of electrons with energies larger than 1 eV. Clearly visible is the accumulation of *hot* carriers at the drain end of the channel. **Right:** The full EDF along the Si/SiO$_2$ interface. One can see the characteristic increase of the carrier energy towards the drain end of the channel.

While carriers move through the channel of a MOSFET, they can undergo various scattering events. Scattering at ionized impurities, surface scattering as well as particle–particle, particle–phonon scattering and impact ionization facilitates energy exchange while particles are accelerated from source to drain by the electric field. This results in a broad and intricate distribution of energies including a high energy tail, i.e. *heated* carriers. The important quantity which, therefore, needs to be addressed is the carrier **energy distribution function** (**EDF**) [33–35, MJJ12, 48, 56, MJC17, MJJ10, 68], see Fig. 2.1, which provides information on how carriers are distributed over energy. Consequently, a solution of an appropriate (classical) transport equation, e.g. the Boltzmann transport equation (BTE), establishes the cornerstone of any microscopic HCD model.

Furthermore, according to HESS, the actual defect creation mechanism is governed by two modes, namely a **single particle** (**SP**) and a **multiple particle** (**MP**) mechanism. The SP process accounts for the high energy fraction of the carrier ensemble in the channel. Only one *heated* solitary carrier, with an energy greater than the threshold of this process, triggers direct desorption of hydrogen at the Si/SiO$_2$ interface. Within its original formulation this interacting regime is based on the physical context of an *electronic excitation* of one of the bonding electrons. On the other hand, the MP mechanism describes a subsequent interaction of a multitude of carriers provoking a *vibrational excitation* of the Si–H bond. The authors of the original *multi–carrier model of interface state generation* [51] speculated about a resonance based process [52] as the underlying physical mechanism. Electrons potentially scatter into an accessible resonance state and thereby excite phonon modes of the Si–H system. However, this idea has never been implemented in an actual model. Modern approaches did not further pursue this concept and instead rely on empirical descriptions using a Keldysh like cross section of the MP mechanism [34, 35, 54], despite its importance in recent studies.

The most advanced model formulation developed by TYAGINOV *et al.* assumes a harmonic potential energy profile for the Si–H bond with a dissociation energy of $E_\mathrm{D} = 2.56\,\mathrm{eV}$ and an energy spacing of the eigenlevels of $0.25\,\mathrm{eV}$, which mimics the Si–H bonds stretching motion [MJJ12, MJC13]. However, no rigorous calculation of the Si–H bond breaking PES has been conducted so far, rendering the harmonic oscillator and its parameters an empirical approximation. The individual excitation rates between the eigenstates (MP) and direct dissociation (SP) are calculated using a formulation introduced by McMahon, the so–called *acceleration integral* [50, 51]. Initially derived from Fermi's Golden Rule (FGR) to capture the interaction and scattering of an incident electron at the Si–H bond in order to explain the nonlinear dependence of HCD on the source–drain current using a *multi–carrier* process, it was later generalized towards the *single carrier* mode[1]. The acceleration integral represents the rate of excitation as the energy dependent carrier flux impinging the bond times a cross section

$$\Gamma_\mathrm{AB/SP} = \int f(E)g(E)v(E)\sigma(E - E_{\mathrm{th},i})^p \mathrm{d}E, \tag{2.1}$$

with f and g being the EDF and the density of states (DOS), v is carrier velocity and σ the cross section. Note that the term $E_{\mathrm{th},i}$ in the cross section considers already excited phonon modes of the potential which reduces the effective barrier height and thus the threshold energy to trigger dissociation. Nevertheless, the energy dependence of the cross section, reflected by the exponent p, is at best an empirically found relation. Despite its success, the model fails to fully and accurately describe the fundamental processes responsible for bond excitation.

The following Sections provide an overview of well known excitation mechanisms triggered by energetic carriers in the field of surface– and photochemistry. The close analogy to hot–carrier related reliability issues in electronic devices allows to establish the key concepts explaining the mechanisms leading to Si–H bond breakage at the Si/SiO$_2$ interface. While dedicated experimental data sets are, however, only available within limited energy ranges, e.g. for scanning tunneling microscope (STM) induced Si–H bond breakage, it can be assumed that the same fundamental physical mechanisms are responsible for hot–carrier induced damage at the Si/SiO$_2$ interface. The clear advantage of using deuterium over hydrogen to passivate a silicon dangling bond (DB), known as the giant isotope effect, has been found to be qualitatively the same for all studied systems, i.e. electronic devices [47, 69–73] and passivated surfaces [74–82]. Furthermore, the corresponding defect configurations, known as silicon dangling bonds (DBs), investigated on passivated Si surfaces are the same kind of defects also present in electronic devices, referred to as P_b centers. The technologically relevant (100) Si/SiO$_2$ interface exhibits two dominant types, the so–called P_b0 and P_b1 center. Both defects have been clearly identified using electron spin resonance (ESR) spectroscopy as a single sp^3 hybrid facing a silicon atom vacancy with the (111) directions being a symmetry axes for P_b0, while the P_b1 defect possesses a lower

---

[1] Strictly speaking, the single particle (SP) process is physically prohibited due to the selection rules of a harmonic oscillator allowing only transitions of $\Delta n \pm 1$. However, an excited state as an intermediate step is assumed which effectively enables overtone transitions such as the SP mechanism.

symmetry [83–96]. This led to the conclusion that the P_{b0} center is clearly associated with a trivalent interfacial Si back bonded to three Si atoms in the bulk. The properties of the P_{b1} center, on the other hand, are quite controversial and different groups have suggested contradictory atomistic structures, ranging from a slightly distorted P_{b0} center due to the amorphous Si/SiO$_2$ interface to a silicon being bonded to two other silicons and an oxygen atom from the SiO$_2$ [83, 84, 89, 91, 92, 97–99]. However, the overall characteristics of the P_{b0} and P_{b1} defect types at the Si/SiO$_2$ interface render them compatible to DBs observed at passivated Si surfaces. This strongly indicates the similarities of the underlying processes, such as excitation and dissociation mechanisms.

Experimentally Induced Excitations

Silicon and its properties are already well examined due to its extensive use as a semiconductor in solid–states devices and microelectronic applications. Controlling single adsorbates on surfaces has been proven to be a useful tool towards the understanding of individual reactions involving silicon [100]. Popular methods to modify surface patterns on the atomic scale, i.e. exciting and/or desorbing a single surface–adsorbate complex, include the scanning tunneling microscope (STM) and lasers, using either infrared or ultraviolet photons. While STM experiments use electrons to induce excitations, lasers can trigger adsorbate dynamics either directly or indirectly: In the direct case photons couple to the complex's transition dipole moment, whereas the indirect route has been found to be substrate mediated [101]. Short pulses of light are able to excite a large number of electrons in the substrate which rapidly thermalize (due to the short electron–electron scattering length). The resulting *hot* electrons can interact with adsorbate resonances which eventually leads to dissociation [102, 103].

Reviewing the wealth of information available for Si–H bond breakage on passivated Si surfaces facilitates the separation of various excitation mechanisms and allows to extract the most important contributions. By comparing the requirements of individual processes to the conditions in a MOSFET, it is possible to link the well known DIET (desorption induced by electronic transitions) and DIMET (desorption induced by *multiple* electronic transitions) regimes to potential excitations in electronic devices. Note that, while the energetic situation in a MOSFET is certainly different compared to dedicated experiments using passivated surfaces, it can still be assumed that the physical principles of carrier interactions with solids, to be more specific, Si–H bonds, remain the same in both situations, see Fig. 2.2.

Electronic Excitation

A significant contribution towards the understanding of STM induced Si–H bond breaking was made by the group of Avouris [78, 104, 105]. A major part of these studies is devoted to H dissociation triggered by electronic excitations. An excited electronic state of an adsorbate complex can be formed, for example, when one of the bonding electrons is excited to an (unoccupied) antibonding orbital. In

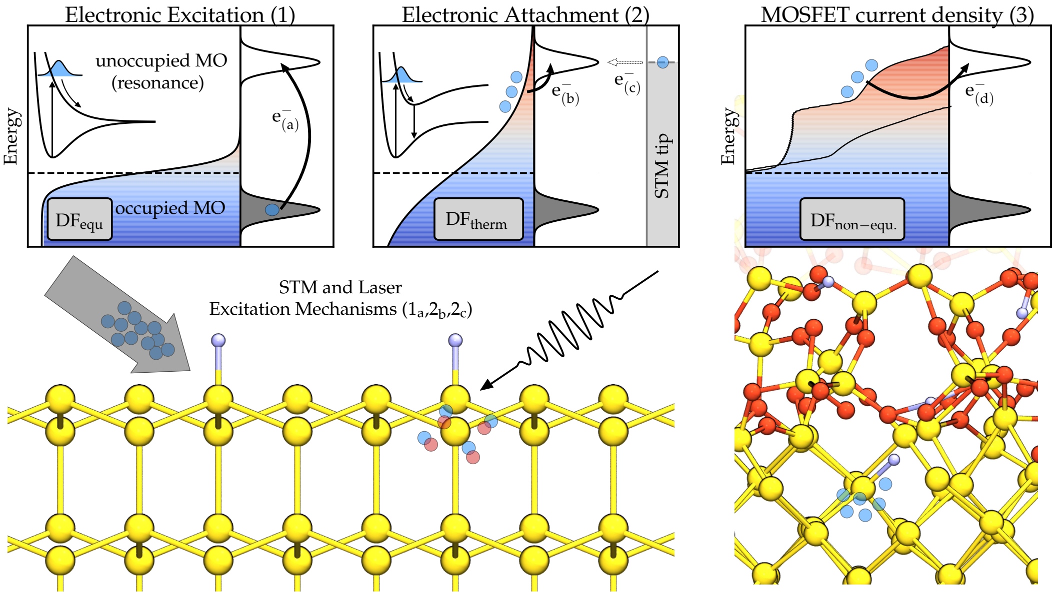

FIGURE 2.2: Schematics of possible electronic excitation processes (lower panels) together with their respective energetics (upper panels). (1a) Electronic excitation of one of the bonding electrons to an antibonding orbital of the Si–H bond on a silicon surface. Provided that the nascent excited state exhibits a repulsive potential, bond breaking can be induced. Such a process can be triggered by either electrons emitted by an STM tip or photons from a laser light with sufficient energy. (2b) Substrate–mediated photochemistry on a surface. The incident photon creates a thermalized carrier distribution ($T_{\text{carrier}} > T_{\text{lattice}}$, described by a Fermi–Dirac (FD) distribution) and sufficiently *hot* carriers are able to scatter into an unoccupied state. (2c) STM–induced excitation of a Si–H bond via electron attachment. Carriers can tunnel into an available adsorbate induced resonance and upon inelastic relaxation produce (multiple) vibrational excitations. (3d) Charge carriers with distributed energies supplied by a current flowing through a MOSFET. The carriers are accelerated by the electric field and undergo various scattering events which results in a complex distribution function (note that contrary to (1) and (2) the superimposed EDF is shown on a logarithmic scale), severely distorted from equilibrium. If carriers gain enough energy they can as well localize in a resonance, similar to (2b) and (2c).

order to cause such an electronic transition, the energy of the tunneling electrons emitted by the STM needs to exceed the threshold for this process, see Fig. 2.2 (1a). Provided that the newly created state is sufficiently repulsive, breaking of adsorbate–surface bonds can be induced. In the case of Si–H bonds this excitation channel is associated with a $\sigma \Rightarrow \sigma^*$ transition[2], leading to a repulsive potential energy profile. Such a mechanism for Si–H bond breaking has been suggested in a series of papers [80–82, 106–113] with a threshold of $\sim 6.5\,\text{eV}$ and a peak at $8\,\text{eV}$. Note that on a H terminated Si surface the release of a single atomic hydrogen

---

[2] σ: occupied bonding orbital, σ^*: unoccupied antibonding orbital

is assumed to proceed via the Si–H stretching mode with a dissociation energy (into vacuum) of $\sim 3.6\,\mathrm{eV}$ [114, 115], see Fig. 2.2. Experimentally it was found that further increasing the energy of the STM electrons beyond 8.5 eV did not impact the hydrogen desorption yield. Comparable results have been reported using laser light (157 nm, 7.9 eV) to provoke direct photodesorption of H from silicon surfaces with various orientations [116–118]. Both methods show an almost linear dependence of the dissociation yield Y with respect to the tunneling current I (or laser fluence F), $Y \sim I$, which corresponds to the classic DIET regime. However, theoretical studies showed that an important competing effect of motion on the excited energy profile is the so–called electronic quenching [74, 104], which will relax the system back to its ground state. Due to the very short lifetime of the excited state (in the order of femtoseconds), this efficient mechanism results in hydrogen desorption originating from a rather *hot* ground state instead of the excited potential.

Multiple–Vibrational Excitations

Reducing the sample bias of the STM below the threshold of the electronic excitation, results in a lower, but non–zero H desorption yield [106, 114, 119]. Within the energy range of the incident electrons between 2 and 6 eV the yield Y strongly depends on the applied voltage and the tunneling current [114, 115, 119–121]. This corresponds to the characteristics of the DIMET regime, where $Y \sim I^n$, $(n > 1)$ with n being approximately the number of electrons needed to trigger dissociation. The underlying mechanism is due to tunneling electrons resonantly scattering at an adsorbate state, see Fig. 2.2 (2c), thereby exciting vibrational modes of the ground state potential [104, 114, 119]. Such a *resonance state* and the corresponding *scattering process* on solid state systems and surfaces is defined in close analogy to its gas phase counterpart [112, 122]. Essentially, it is an *electron–impact* phenomenon where the impinging carrier triggers the formation of a transient *atomic* or *molecular ion*. Thereby, the incident electron (or hole) is temporarily captured in the vicinity of the molecule in a (quasi–) bound molecular orbital, typically an antibonding orbital, forming a short–lived negative (positive) ion resonance state. The trapped electron (hole) will be re–emitted again after 10^{-10} to $10^{-15}\,\mathrm{s}$, which is the typical lifetime of a resonance. Such a process is manifest as a characteristic peak or *resonance* in the incoming carrier energy as well as the scattering cross section, hence it is commonly referred to as *resonance carrier scattering* or *resonance excitation*.

In the case of the Si–H bond it is assumed that the anionic resonance (a scattering state for an electron) is associated with the unoccupied σ^* orbital, whereas the cation resonance state for energetic holes is formed by the occupied σ orbital [114, 115, 119]. Qualitatively similar results, albeit on different adsorbate–substrate combinations, have been obtained using optically excited *hot* substrate electrons scattering into an available resonance [101–103, 123, 124]. This, however, shows the universal applicability and validity of resonance mediated excitations.

Although the measurement data reported by various groups [104, 106, 114, 119] could be explained quite well by different vibrational heating models, using either a coherent or an incoherent formulation, the details of the mechanism are not fully understood yet. Both models assume that an electron attaches to an unoccupied orbital, thus forming a *negative ion resonance*. Upon inelastic electronic relaxation, it transfers a part of its energy to the bond's vibrations. While in the incoherent formulation only one quantum of energy can be transferred, the coherent model allows the electron to excite a larger number of vibrational quanta within the bonding potential. However, in more recent publications [119, 125] it was shown that fewer electrons are needed to dissociate hydrogen than assumed in the incoherent model[3]. The conclusions drawn by the authors render the coherent formulation to be more compatible to the observed behaviour.

Dipole–Induced Excitations

Another important excitation mechanism is related to the interaction of the vibrational transition dipole of an adsorbate with an electric field. The electric field caused by the electrons which tunnel from the STM tip to the surface is able to couple to the bond's dipole moment and induce transitions between vibrational states. However, his mechanism usually requires a rather high current density between the tip and the sample. On the other hand, for a large current of energetic, *hot*, carriers, the resonance scattering process described above typically dominates the excitation dynamics and, thus, renders dipole induced excitations of only minor importance.

Key Concepts

Based on the detailed picture of the various excitation processes together with the understanding of how charge carriers can interact with an adsorbate complex, the fundamental framework to describe hot–carrier related degradation phenomena in MOSFETs can be derived. There is an unambiguous connection between experimentally observed Si–H bond breaking processes induced by dedicated measurement techniques, Fig. 2.2 (1) and (2), and HCD in electronic devices, see Fig. 2.2 (3). One possibility is clearly associated with an **electronic excitation**, namely the $\sigma \Rightarrow \sigma^*$ transition. However, rather high energetic carriers of about $6 - 8\,\mathrm{eV}$ are needed to trigger such a mechanism, which renders it incompatible to carrier energies typically observed in MOSFETs. On the other hand, a combination of **resonance scattering** and **vibrational heating** seems more likely to be the driving force for the creation of defect states at the Si/SiO$_2$ interface. The moderate carrier energies required for this excitation channel together with its strong current dependence agree well with the characteristic features of hot–carrier effects in MOSFETs. Dipole–induced vibrational excitations are more complicated to quantify. Contrary to STM experiments, where tunneling currents are injected

---

[3] In which the number of electrons equals the number of bound states in the potential.

from the tip and the Si–H bond is assumed to be perpendicular to the surface[4], the conditions at the Si/SiO$_2$ interface are not that well defined. Charge carriers move parallel to the interface in the inversion layer of the MOSFET with additional spatial varying electric fields being present during operation. Furthermore, the Si–H bond direction is not necessarily perpendicular to the Si/SiO$_2$ interface and its dipole moment is not aligned with the field direction.

2.2 Non–Equilibrium Bias Temperature Instability

The central foundations of the following Section is the current state–of–the–art understanding of charge trapping at pre–existing defect sites, accurately described within the framework of the 4–state NMP model by GRASSER *et. al* [6, 7, MJJ7]. Its development is heavily based on the pioneering work of KIRTON and UREN [5], who investigated noise due to single defects in the context of NMP theory and the subsequent application of TEWKSBURY to model the threshold voltage drift in MOSFETs [126]. Furthermore, the original formulation was inspired by *irradiation damage* in SiO$_2$, which has been explained by taking the neutral oxygen vacancy and its two (meta–) stable charged configurations into account, known as E'_γ and E'_δ [127, 128].

Nonradiative Multiphonon Framework

The dynamics of charge exchange between a defect in the gate stack and the carrier reservoir of a MOSFET is determined by a combination of field – via an applied **bias** – accelerated nonradiative multiphonon transitions together with **temperature** activated structural reconfigurations. Its universal formulation is independent of the actual defect structure and relies on the description using one–dimensional **potential energy curves** (PECs). Their knowledge reveals the respective barriers which determine the transition rates and hence the dynamics of charge trapping. As already outline in the Introduction of this Chapter, transitions can be split into thermally activated structural relaxations *within* a PEC and charge transfer reactions *across* different PECs, see Fig. 2.3.

Thermal transitions can be accounted for using classical transition state theory (TST) [64, 129–131] which assumes the initial state to be in thermal equilibrium with a distribution given by the Boltzmann form. The transitions state (TS) between the initial and final state represents a bottleneck for the reaction to occur with a barrier high enough that the time between escape events into the final configuration is longer than the (vibrational) relaxation time. Furthermore, an essential factor in TST is a negligible back flow once the TS has been crossed which implies that the system spends an extended time in the final state compared to

---

[4] This is true for a H:Si(111) surface and partly fulfilled for a H:Si(100)-(2×1) surface where the top layer is dimerized due to the surface reconstruction.

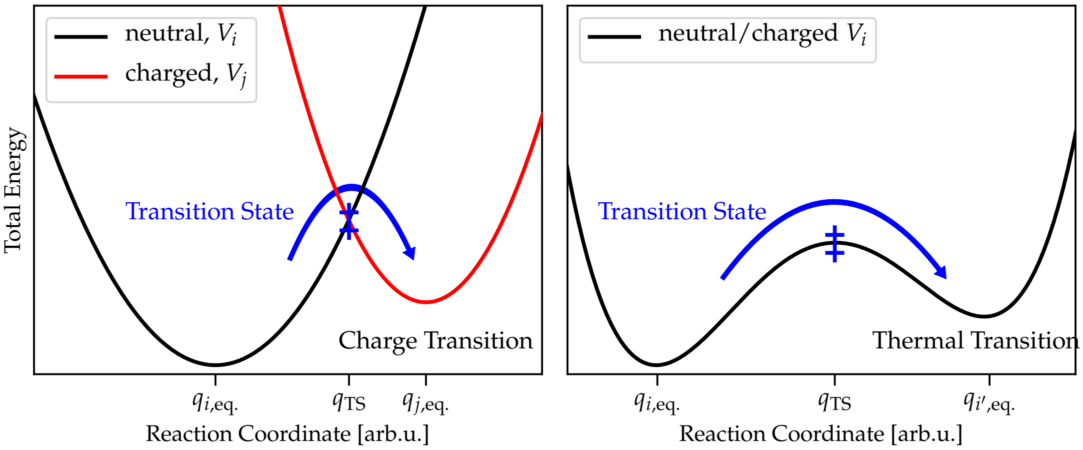

FIGURE 2.3: Schematic representations of the potential energy curves (PECs) involved for charge transitions (**Left**) and thermal transitions (**Right**). Thermally activated structural relaxation proceed within a PEC, while (nonradiative) charge transfer provokes a change of the PEC from the neutral to the charged state.

being in the vicinity of the transition point. According to TST the rate is given by the probability that the system reaches the TS multiplied with the flux through the TS, i.e. the rate crossing from the initial state I to the final state F

$$k^{\text{TST}} = \frac{\int_{\text{TS}} \mathrm{e}^{-V(\mathbf{q})/k_{\text{B}}T} \mathrm{d}\mathbf{q}}{\int_{\text{I}} \mathrm{e}^{-V(\mathbf{q})/k_{\text{B}}T} \mathrm{d}\mathbf{q}} v_{\perp}. \tag{2.2}$$

The average velocity $v_{\perp}$ in the direction perpendicular to the TS surface can be calculated from the Maxwell distribution

$$v_{\perp} = \sqrt{\frac{k_{\text{B}}T}{2\pi\mu_{\perp}}}, \tag{2.3}$$

where $\mu_{\perp}$ is the effective mass for the motion across the TS due to the movement of the involved atoms. The general rate for a multidimensional TST is given as

$$k^{\text{TST}} = \sqrt{\frac{k_{\text{B}}T}{2\pi\mu_{\perp}}} \frac{\mathcal{Z}_{\text{TS}}}{\mathcal{Z}_{\text{I}}}, \tag{2.4}$$

with $\mathcal{Z}$ being the integrals of the Boltzmann factors over the specified regions TS and I in configuration space, often referred to as partition functions or configuration integrals, respectively. Due to the exponential dependence on the barrier height E_{B}, the escape rates are determined by the path with the lowest possible barrier, also known as the minimum energy path (MEP). Choosing the MEP for the reaction coordinate (RC) where the transition state as a first order saddle point on the energy surface allows one to use harmonic transition state theory [64, 129]. The total energy of the system can be expanded up to second order around the initial minimum $\mathbf{q}_{\text{I}}$ and the saddle point $\mathbf{q}_{\text{TS}}$ which allows for an analytic evaluation of $\mathcal{Z}_\mathrm{I}$ and $\mathcal{Z}_\mathrm{TS}$. The harmonic TST yields [132, 133]

$$k^\mathrm{TST} = \frac{1}{2\pi\sqrt{\mu_\perp}} \sqrt{\frac{\prod_{i=1}^{3N} k_{\mathrm{I},i}}{\prod_{i=1}^{3N-1} k_{\mathrm{TS},i}}} \mathrm{e}^{-E_\mathrm{B}/k_\mathrm{B}T}, \tag{2.5}$$

with $k_{\mathrm{I},i}$ and $k_{\mathrm{TS},i}$ are the eigenvalues of the Hessian matrix. Since only vibrational contributions to the partition functions $\mathcal{Z}$ are to be considered, (2.5) can be written in terms of the angular frequencies $\omega = \sqrt{k/\mu}$

$$k^\mathrm{TST} = \frac{1}{2\pi} \frac{\prod_{i=1}^{3N} \omega_{\mathrm{I},i}}{\prod_{i=1}^{3N-1} \omega_{\mathrm{TS},i}} \mathrm{e}^{-E_\mathrm{B}/k_\mathrm{B}T}. \tag{2.6}$$

In the denominator the imaginary frequency corresponding to the unstable vibrational mode at the saddle point is left out from the product. Finally, (2.6) can be interpreted as a prefactor, the so–called *attempt frequency*, which is related to the number of attempts per unit time to overcome the barrier, and an activation term associated with the barrier height. The multi–dimensional transition rate can be simplified by assuming a single reaction coordinate q and a one–dimensional PEC $V(q)$. In this case (2.6) reduces to the well known empirical Arrhenius law

$$k^\mathrm{TST} = \frac{\omega_0}{2\pi} \mathrm{e}^{-E_\mathrm{B}/k_\mathrm{B}T}. \tag{2.7}$$

In the context of charge trapping at oxide defects (2.7) is used to describe thermally activated structural reconfigurations within a single PEC.

Contrary to thermal transitions, **nonradiative multiphonon transitions** involve the capture or emission event of a charge which is characterized by a change of the adiabatic potential energy curve (assuming again a one–dimensional reaction coordinate) [MJJ7, 134–138]. Such phonon assisted reactions are associated with a deformation and subsequent relaxation of the defect site [63]. The charge exchange process can be assumed as instantaneous and preferably occurs *at* or *near* the intersection point of the involved PECs [10, 11, MJJ7, 63].

Using a first order perturbation theory approach the rate $k_{i\alpha,j\beta}$ for a NMP transition from the inital state $|\Phi_i \otimes \eta_{i\alpha}\rangle$ to the final state $|\Phi_j \otimes \eta_{j\beta}\rangle$ is given by FGR [139]

$$\begin{aligned} k_{i\alpha,j\beta} &= \frac{2\pi}{\hbar} \left|M_{i\alpha,j\beta}\right|^2 \delta(E_{i\alpha} - E_{j\beta}), \\ M_{i\alpha,j\beta} &= \langle \eta_{i\alpha} | \langle \Phi_i | \hat{H}' | \Phi_j \rangle | \eta_{j\beta} \rangle \,. \end{aligned} \tag{2.8}$$

Here, $\hat{H}'$ is the perturbation operator, i and j denote the electronic states and α and β are the vibrational states. The delta function ensures the conservation of energy for the transition, where $E_{i\alpha}$ and $E_{j\beta}$ include the phonon as well as electronic energies. Invoking the Born Oppenheimer (more precisely the Born Huang) or adiabatic approximation [58, 59] together with the Franck–Condon principle (FCP) [140–142] the perturbation Hamiltonian can be split into an electronic $\hat{H}'_\mathrm{el}$ and a phonon $\hat{H}'_\mathrm{phon}$ part which allows to rewrite the matrix element $M_{i\alpha,j\beta}$ as

$$M_{i\alpha,j\beta} = \langle \Phi_i | \hat{H}'_\mathrm{el} | \Phi_j \rangle \langle \eta_{i\alpha} | \eta_{j\beta} \rangle \,. \tag{2.9}$$

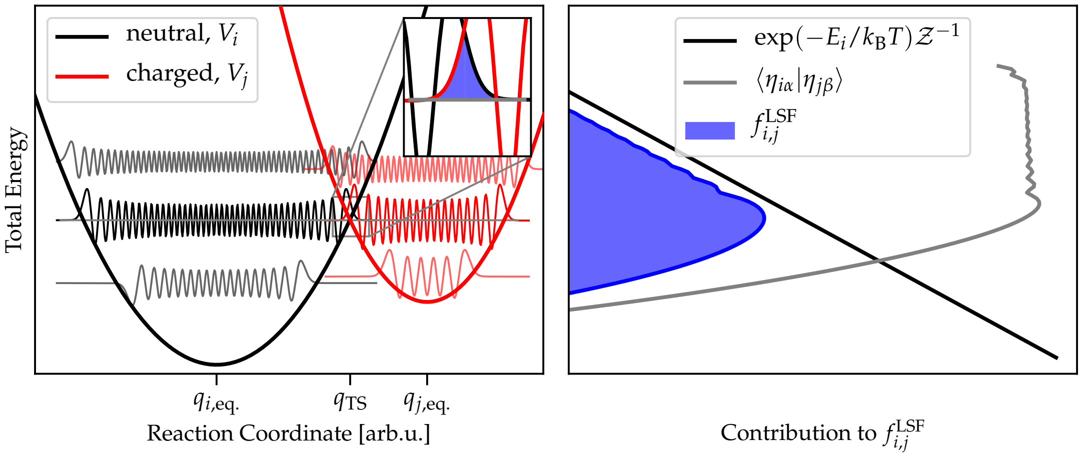

FIGURE 2.4: The lineshape function (LSF) of NMP transitions. **Left:** Potential energy profiles with the corresponding vibrational eigenmodes of two differently charged defect configurations schematically representing a typical NMP process. According to (2.11), the LSF is proportional to the overlap integral of the wavefunctions $|\eta_{i\alpha}\rangle$ and $|\eta_{j\beta}\rangle$ within the two PECs. The delta function guarantees the conservation of energy, thus only pairs of energy where $E_{i\alpha} = E_{j\beta}$ is fulfilled contribute to $f_{i,j}^{\mathrm{LSF}}$. For all practical applications the delta peaks are broadened depending on the temperature. **Right:** Individual contributions to the total LSF. While the overlap of the vibrational wavefunctions rapidly increases towards the classical crossing point and approximately stays constant above, the (temperature dependent) occupation probability of the eigenmodes decays. The interplay of both terms yields the lineshape function (LSF) indicated as the blue area.

The BOA decouples the electronic and nuclear wave functions, while the Franck–Condon principle (FCP) splits vibronic transitions, the simultaneous occurrence of electronic and vibrational transitions, into individual products due to their different timescales. Therefore, (2.9) can be interpreted as the product $A_{i,j} f_{i\alpha,j\beta}^{\mathrm{LSF}}$, where $A_{i,j}$ describes the instantaneous electronic excitation and is the electronic matrix element and $f_{i\alpha,j\beta}^{\mathrm{LSF}}$, the so–called *lineshape function* (LSF), considers the vibrational interactions occurring during the lattice reconfigurations. In order to capture the effect of charge trapping at oxide defects under elevated temperatures with NMP theory, all vibrational modes of a potential representing one electronic state have to be taken into account [11, MJJ7, 143]. The total transition rate $k_{i,j}$ is the thermal average of all individual rates $k_{i\alpha,j\beta}$ across the canonical ensemble. The partial rates must be averaged over all initial states α weighted with a Boltzmann factor and all final states have to be summed over

$$k_{i,j} = \underset{\alpha}{\mathrm{average}}\Big(\sum_{\beta} k_{i\alpha,j\beta}\Big). \tag{2.10}$$

Finally, the total NMP transition rate which describes a charge transfer process can be written as:

$$\begin{aligned} f_{i,j}^{\mathrm{LSF}} &\mathrel{\widehat{=}} \underset{\alpha}{\mathrm{ave}}\Big(\sum_{\beta} \left| \langle \eta_{i\alpha} | \eta_{j\beta} \rangle \right|^2 \delta(E_{i\alpha} - E_{j\beta})\Big), \\ k_{i,j} &= A_{i,j} f_{i,j}^{\mathrm{LSF}}, \\ A_{i,j} &\mathrel{\widehat{=}} \frac{2\pi}{\hbar} \left| \langle \Phi_i | \hat{H}'_{\mathrm{el}} | \Phi_j \rangle \right|^2. \end{aligned} \tag{2.11}$$

Regarding physical aspects, the electronic matrix element $A_{i,j}$ defines the coupling strength between the involved electronic wavefunctions and the LSF is the overlap integral of the initial and final vibrational eigenmodes, see Fig. 2.4. In the context of charge trapping in MOSFETs, $A_{i,j}$ determines the interaction of a band state in the silicon conduction/valence band and the defect wavefunction in the gate stack. Due to the strong localization of the defect wavefunction, $A_{i,j}$ can be reasonably well approximated using the Wentzel–Kramers–Brillouin (WKB) approximation [11, MJJ7]. Calculating the LSF requires the quantum mechanical vibrational eigenstates of the PECs. Analytical solutions are only available for simple potentials, such as the harmonic approximation, and even then their overlaps need to be calculated using recurrence schemes to obtain the necessary accuracy [144, 145]. For more generic energy profiles $f_{i,j}^{\mathrm{LSF}}$ solely relies on numerical results which is unfeasible for TCAD simulations. Therefore, a harmonic PEC together with the classical limit of the LSF is mostly used in such applications. In the classical limit the LSF is a Dirac peak at the intersection point of the two PECs. However, also in the quantum mechanical picture using the overlap integrals of the vibrational wavefunctions, mainly contributions in the direct vicinity of the classical crossing point determine the total LSF, compare with Fig. 2.4, which justifies this seemingly crude approximation.

Oxide defects in MOSFETs and the associated charge trapping involves more than just two isolated states. Charge capture and emission events can occur from (to) a **whole band of states**, namely the valence and conduction bands of the silicon substrate (as well as of the gate material) [8, MJJ7, 146]. The present work investigates hole traps in a pMOSFET, i.e. a defect which can be in its neutral or positively charged (meta–) state with the transitions 0 ⇔ +. Such defects mainly interact with carriers in the valence band (VB), assuming pMOSFETs and negative bias conditions, and thus the invoked transitions are governed by trapping a hole from the VB (or emitting an electron, which is equivalent). Therefore, in the following the energy minimum of the positively charged state is chosen as the reference energy, $V_{+,\mathrm{min}} \mathrel{\widehat{=}} 0\,\mathrm{eV}$. It is convenient to introduce the electrostatic trap level E_{T} of the neutral configuration with respect to the VB edge in the absence of an electric field as $E_{\mathrm{T}} \mathrel{\widehat{=}} V_{0,\mathrm{min}} - E_{\mathrm{V}}$[5]. Interacting with a continuous spectrum of carriers in the valence or conduction band, the energy E of the charge in the initial state is not uniquely defined, which is represented by a shifted charged (positive) PEC, see Fig. 2.5. This is also reflected in the NMP transition rate, which now

---

[5] Conversely, the conduction band (CB) edge is used for electron traps $E_{\mathrm{T}} \mathrel{\widehat{=}} E_{\mathrm{C}} - V_{0,\mathrm{min}}$.

depends on the reservoir energy E and the trap level E_T

$$k_{i,j} = A_{i,j}(E, E_\mathrm{T}) f_{i,j}^\mathrm{LSF}(E, E_\mathrm{T}). \tag{2.12}$$

Integration of all band states yields the final set of transition rates:

$$\begin{aligned} k_{0,+}^\mathrm{VB} &= \int_{-\infty}^{E_\mathrm{V}} g_p(E) f_p(E) A_{0,+}(E, E_\mathrm{T}) f_{0,+}^\mathrm{LSF}(E, E_\mathrm{T}) \mathrm{d}E \\ k_{+,0}^\mathrm{VB} &= \int_{-\infty}^{E_\mathrm{V}} g_p(E)(1 - f_p(E)) A_{+,0}(E, E_\mathrm{T}) f_{+,0}^\mathrm{LSF}(E, E_\mathrm{T}) \mathrm{d}E \\ k_{0,+}^\mathrm{CB} &= \int_{E_\mathrm{C}}^{\infty} g_n(E)(1 - f_n(E)) A_{0,+}(E, E_\mathrm{T}) f_{0,+}^\mathrm{LSF}(E, E_\mathrm{T}) \mathrm{d}E \\ k_{+,0}^\mathrm{CB} &= \int_{E_\mathrm{C}}^{\infty} g_n(E) f_n(E) A_{+,0}(E, E_\mathrm{T}) f_{+,0}^\mathrm{LSF}(E, E_\mathrm{T}) \mathrm{d}E \end{aligned} \tag{2.13}$$

Here, g_p (g_n) is the density of states of the valence band (VB) and conduction band (CB), respectively, and f_p (f_n) denotes the EDF, how carriers are distributed over energy. For the reaction $0 \Rightarrow +$ a filled (hole) state in the VB, or an empty (electron) state in the CB, must be taken into account. The opposite applies for the reverse transition $+ \Rightarrow 0$.

The last component is the **interaction of a defect with the electric field** present in the oxide. Applying a gate bias imposes an electric potential inside the oxide which changes the defect's energy and hence its trap level E_T [61, 144]. A simple model, neglecting all trapped charges inside the oxide, predicts a linear relation between the oxide field F_ox and the defect's depth

$$\Delta_\mathrm{S} = q x_\mathrm{T} F_\mathrm{ox}. \tag{2.14}$$

This additional energy shifts the trap level accordingly

$$E_\mathrm{T,eff} = E_\mathrm{T} + \Delta_\mathrm{S}, \tag{2.15}$$

and its effect can be seen in Fig. 2.5.

For the sake of completeness, it is worth noting that the discussed framework exhibits a few **shortcomings** due to the approximations used owing to the broad distribution of defect parameters associated with the amorphous nature of SiO_2. The subsequently discussed advances are performed (mainly) in the context of crystalline materials where defect structures and their characteristics are well defined. Each of the discussed effects and its extension of the NMP model described above would make the corresponding DFT calculations prohibitively expensive and even the TCAD simulations unfeasible.

First, the theory derived above relies on the calculated (and approximated) PECs and their crossing points. Therefore, the rate of a charge transfer process is determined by the classical energy barriers and the probability to reach a certain value of the reaction coordinate characterized a vibrational mode. This classical approximation is usually referred to as *Marcus theory* [147]. However, recent

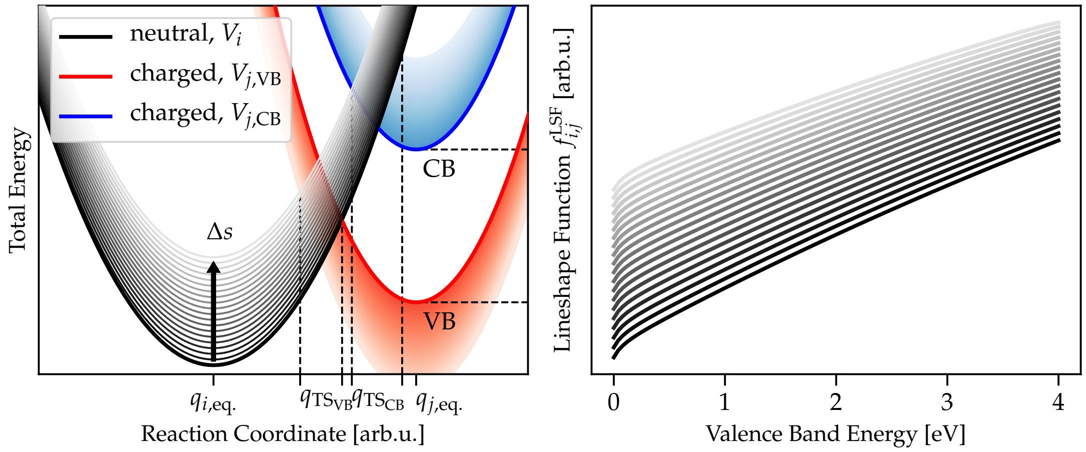

FIGURE 2.5: Interactions with an oxide field as well as a whole band of states. **Left**: Applying an electric field shifts the defects' trap level accordingly (gray parabolas). Additionally, due to the interaction with the carrier reservoir in the channel, the charged PEC is shifted with respect to the carrier energy E. The defect can interact with holes in the valence band (red parabolas) and electrons in the conduction band (blue parabolas). The combination of these two effects leads to a distribution of configurations and hence crossing points which is reflected in the LSF $f_{i,j}^{\mathrm{LSF}}(E, E_{\mathrm{T}})$. **Right:** The valence band lineshape function for the neutral ⇒ charged transition. With increasing carrier energy E the transition barrier is reduced, thus the LSF increases. Furthermore, also the shift Δs induced by the electric field F_{ox} alters the energetic alignment of the two parabolas and modifies the LSF.

progress of computational methods for atomistic calculations allows one to calculate the *electron–phonon coupling* which is beyond the BOA [148–152], see (2.8) and (2.9). Usually the additional terms are referred to as nonadiabatic terms and contain derivatives of the electronic wavefunction with respect to the nuclear coordinates. They describe the coupling of electronic states with respect to the dynamics of the lattice atoms and are called electron–phonon coupling.

Second, quite recently it has been demonstrated that the electronic matrix element, the first term in (2.9) and $A_{i,j}$ in (2.11), respectively, can be calculated explicitly. Using an atomistic Si/SiO$_2$ model, however, it is not possible to directly calculate a positively charged defect below the Fermi level (or a negatively charged defect above E_{F}), and hence the involved wavefunctions. Nevertheless, the authors in [153, 154] showed that by applying an external perturbation, e.g. an electric field, the respective band and *neutral* defect wavefunctions can be shifted with respect to each other until an avoided crossing is observed. The minimum energy gap between both states is directly proportional to the electronic coupling strength. However, this approach relies upon the assumption that the defect wavefunction does *not* substantially change upon the charge capture process[6]. A more

---

[6] The methodology would break down e.g. for intrinsic electron traps (self–trapped polarons) in SiO$_2$ [155] which dramatically change its wavefunction upon charge capture.

rigorous approach is provided by the method of constrained density functional theory (CDFT) which allows one to directly construct the Hamiltonian in a charge localized *diabatic* basis, as was shown in [156–158]. However, the studies attempted to model the coupling of degenerated defects within a bulk material and not across an interface system.

Furthermore, the effect of an applied electric field is accounted for only via a linear response upon the electric potential inside the oxide thereby shifting the energy position of the defect, see (2.15). On the other hand, the interaction with the defects' dipole moment, which potentially alters the PECs and, hence, the energy barriers [159, 160], is neglected. Contrary to recent investigations on symmetric systems where the migration or dissociation pathway follows a certain direction, the situation is much more complicated for amorphous systems like SiO_2 and which results in enormous computational efforts.

Last but not least, the utilized methods to calculate the MEP, within a PEC or across different PECs, obey classical mechanics for the nuclei. Over the past decade, however, methods have been developed which allowed one to take nuclear quantum effects into account which opened new insights into chemical processes, particularly for light atoms such as hydrogen [161]. Practical applications, such as quantum transition state theories and ring polymer molecular dynamics methods have shown that they yield accurate rates at low temperatures where the effects of tunneling dominate [162–165]. Even though defects in SiO_2 are associated with hydrogen where tunneling effects are potentially important, the aforementioned methods rely on an extensive sampling of the free energy surface which is beyond computational possibilities due to the variety of defect structures encountered in amorphous SiO_2.

Note that each of these advances and dedicated studies is a very challenging research field on its own and virtually impossible to be applied within the description of amorphous structures exhibiting a broad distribution of defect parameters using currently available computational resources.

Equilibrium 4–State Model

Striking evidence for the 4–state NMP formulation has been found using TDDS [3] and the characteristics of single defects. Based on the defect's emission behaviour, two different types of oxide traps can be identified: *fixed positive charge traps*, which feature a rather constant emission time τ_e over V_G, and *switching traps*, which show a rapid decrease of τ_e towards low gate voltages [4, 7]. A consistent and unified approach to explain both defect types is given by the 4–state NMP model [4, 7, 166], see Fig. 2.6. It accounts for two *stable* states representing the neutral and charged defect (1 and 2) as well as two *metastable* configurations for both charge states ($1'$ and $2'$). While charging is assumed to always proceed via the metastable (positive) state $2'$ ($1 \Rightarrow 2' \Rightarrow 2$), the discharging dynamics are governed by two different pathways. Defect configurations with an unfavourable energy barrier via state $1'$ will possess a constant emission time determined by the (bias independent) thermal barrier $\varepsilon_{2,2'}$. On the other hand, if the lowest energy path to emit a charge is given by $2 \Rightarrow 1' \Rightarrow 1$, discharging is governed by the bias dependent barrier $\varepsilon_{2,1'}$. Since the energetic alignment of the PECs, hence their crossing point, depends on the electric field F_{ox} and the VB (CB) state energy E, the favourable emission pathway potentially changes from $2 \Rightarrow 2' \Rightarrow 1$ to $2 \Rightarrow 1' \Rightarrow 1$ and vice versa with applied recovery conditions.

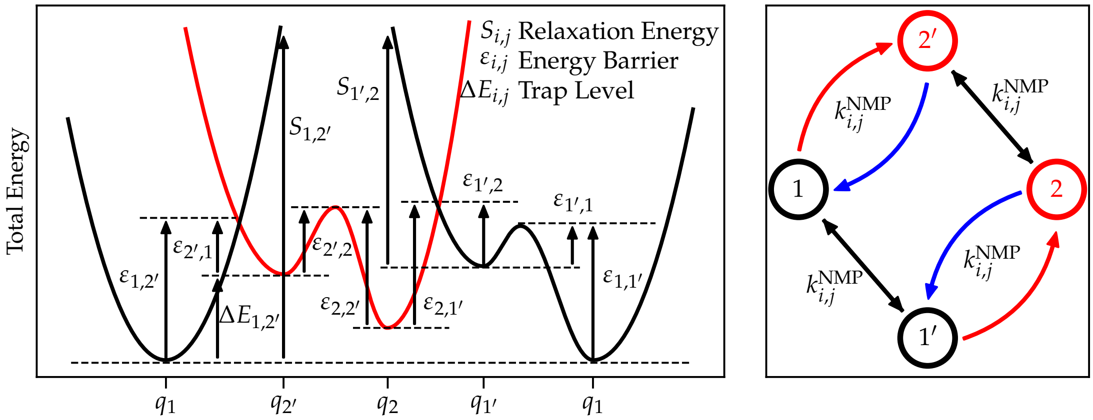

FIGURE 2.6: Schematic reaction coordinate (RC) diagram together with a simple state diagram. **Left:** An example of a 4–state NMP defect which is uniquely defined given the defect energies $\Delta E_{i,j}$, the relaxation energies $S_{i,j}$ and the energy barriers $\varepsilon_{i,j}$. **Right:** A state diagram visualizing the NMP transitions between the state $1 \Leftrightarrow 2'$ and $1' \Leftrightarrow 2$ as well as the thermally activated relaxations $1 \Leftrightarrow 1'$ and $2 \Leftrightarrow 2'$.

The proposed four states also impose very stringent limits on the atomistic defect configuration. In order to be compatible with the 4–state model, the microscopic defect candidate needs to exhibit a stable and a metastable configuration in each charge state which are connected via structural relaxations. The oxygen vacancy (OV) has been suggested to be the main cause of BTI for the last decades [167–170]; however, recent publications have shown that its charge transition levels are too far below the silicon VB which rules the OV out as a BTI active trapping site [62]. On the other hand, an inevitable connection between hydrogen and BTI has been demonstrated [17, 18, 171, 172], suggesting hydrogen based defects such as the hydrogen bridge (HB) and (or) the hydroxyl–E′ center (HE′) as potential defect structures. Recent studies employing *ab initio* calculations have indicated that the respective energy levels of the HB and the HE′ are much closer to the Si VB which renders them compatible with experimental BTI investigations [62, 173–175]. Nevertheless, searching for a suitable atomistic defect structure in SiO_2 (SiON) as well as in high–κ materials such as HfO_2 is still an active research field.

The four states proposed above can be translated into a one dimensional reaction coordinate (RC) using the parabolic approximation for the PECs which is shown in Fig. 2.6. The shape of the respective quantum harmonic oscillators together with their intersection points is uniquely defined by the following relations

$$\begin{aligned} \Delta E_{i,j} &= E_{j,\mathrm{min}} - E_{i,\mathrm{min}}, \\ S_{i,j} &= \mathcal{S}_{i,j}\hbar\omega = c_i(q_j - q_i)^2, \\ R_{i,j}^2 &= \frac{c_i}{c_j}, \end{aligned} \tag{2.16}$$

where $S_{i,j}$ is the relaxation energy, $R_{i,j}$ describes the ratio of the curvatures and $\Delta E_{i,j}$ is the energy difference. The crossing points of the parabolas determine the classical energy barriers $\varepsilon_{i,j}$ which can be calculated as

$$\begin{aligned} \varepsilon_{i,j} &= \frac{S_{i,j}}{R_{i,j}^2 - 1}\Big(1 - R_{i,j}\sqrt{\frac{S_{i,j} + \Delta E_{j,i}(R_{i,j}^2 - 1)}{S_{i,j}}}\Big) && \text{for} \quad R_{i,j} \neq 1, \\ \varepsilon_{i,j} &= \frac{(S_{i,j} + \Delta E_{j,i})^2}{4S_{i,j}} && \text{for} \quad R_{i,j} = 1. \end{aligned} \tag{2.17}$$

Both sets of equations, (2.16) and (2.17), in conjunction with the parameters highlighted in Fig. 2.6, unambiguously define the 4–state model with all its barriers $\varepsilon_{i,j}$. The NMP transition rates $1 \Leftrightarrow 2'$ and $1' \Leftrightarrow 2$ as well as the thermal transitions $2' \Leftrightarrow 2$ and $1 \Leftrightarrow 1'$ can be calculated using (2.13) (NMP) and (2.7) (thermal). The resulting rates $k_{i,j}$ determine the occupation probability P_i of the system to be in state i which is given by the master equation

$$\frac{\mathrm{d}P_i(t)}{\mathrm{d}t} = k_{j,i}P_j(t) + k_{k,i}P_k(t) - (k_{i,j} + k_{i,k})P_i(t), \tag{2.18}$$

with the initial condition $P_{i=1}(0) = 1$ and $P_{i\neq 1}(0) = 0$. The time to reach the stable configuration 2, describing a hole capture process, for the first time is called *first passage time* (FPT). The transitions between the states 1 and 2, however, proceed via the metastable states $1'$ or $2'$. The FPTs in such an effective 3–state system which describes the transitions $1 \Leftrightarrow 2$ via the states $1'$ or $2'$ is given by the following approximation[7]

$$\tau_{\mathrm{c,FPT}}^i = \frac{k_{1,i} + k_{i,1} + k_{i,2}}{k_{1,i} + k_{i,2}} \qquad \tau_{\mathrm{e,FPT}}^i = \frac{k_{i,1} + k_{i,2} + k_{2,i}}{k_{i,1} + k_{2,i}}, \tag{2.19}$$

with i being the intermediate state. The final capture and emission times τ_{c} and τ_{e} within the 4–state model which can be compared to experimental results are

$$\tau_{\mathrm{c}} = \Big(\sum_i \frac{1}{\tau_{\mathrm{c,FPT}}^i}\Big)^{-1} \qquad \tau_{\mathrm{e}} = \Big(\sum_i \frac{1}{\tau_{\mathrm{e,FPT}}^i}\Big)^{-1}. \tag{2.20}$$

---

[7] This approximation assumes that there is only one *active* capture or emission path for a given bias condition, which is typically fulfilled.

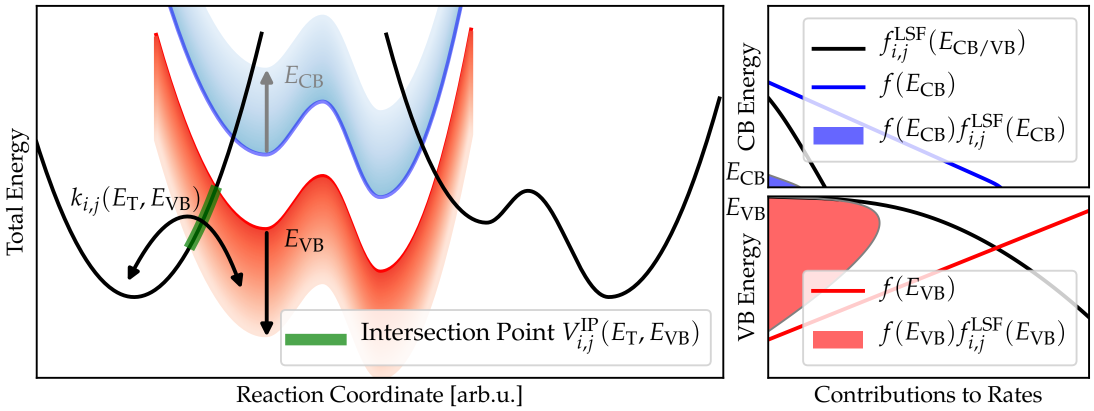

FIGURE 2.7: The PECs as the cornerstone of the $\mathrm{NMP}_{\mathrm{eq.}}$ model. Due to the negligible carrier concentration in the conduction band, assuming normal operating conditions of a pMOSFET, the transition rates $k_{i,j}$ are determined by the interaction with holes in the valence band (**Left**). The biggest contribution to the total rate using the LSF together with the Fermi–Dirac statistics for the carriers is close to the VB edge and, therefore, validates the so–called *band edge approximation* (**Right**).

The 4–state NMP model is designed to accurately describe the degradation due to BTI as well as (anomalous) random telegraph noise. It takes the interaction of the defect with charge carriers in the substrate's valence and conduction band into account and assumes their occupation probability to be given by the FD distribution. During the worst–case conditions for BTI, namely $V_{\mathrm{G}} \gg V_{\mathrm{DD}}$ and $V_{\mathrm{D}} = 0\,\mathrm{V}$, charge carriers are indeed in thermal equilibrium, which validates this assumption. Within this approach, the total transition rates are mainly dominated by the interaction with the valence band due to the negligible (intrinsic) concentration of electrons in the CB[8], see Fig. 2.7. This model variant will be termed **equilibrium 4–state model**, **$\mathrm{NMP}_{\mathrm{eq.}}$**, in the following. Further simplifications can be made by considering the set of equations given in (2.13). The integrals are dominated by the product $f_{\mathrm{p}}(E) f_{i,j}^{\mathrm{LSF}}(E, E_{\mathrm{T}})$ which features the biggest contribution close the band edges as shown in Fig. 2.7. It can, therefore, be inferred that the rates $k_{i,j}$ and the individual terms only depend on the respective band edges which can be factored out from the integral. Using the classical limit of the LSF together with the fact that the integral over the product $g_p(E) f_p(E)$ equals the carrier concentration p, finally yields an analytical expression for the rate $k_{i,j}$ which exponentially depends on the barrier. This simplification is termed the *band edge approximation*. However, the quality of this approximation strongly depends on the curvature and the corresponding intersection points of the involved parabolas. For example, if the neutral state does *not* intersect the parabola which represent the valence band *edge* at a certain bias condition, the band edge approximation breaks down and

---

[8] This, of course, is only true for hole traps in pMOSFETs, where a negative gate voltage is applied. For positive bias temperature instability (PBTI) in nMOSFETs electron traps mainly interact with the Si CB.

fails to describe the corresponding time constants. Although excited carriers in the valence band can still interact with the defect, this effect is not included in the original formulation of the band edge approximation. However, a recently presented extension overcomes this limitations, see [146, MJJ8, MJC14].

Key Concepts

The NMP$_{\mathrm{eq.}}$ model described above is not intended or conceived to simulate the behaviour of oxide defects in full $\{V_{\mathrm{G}}, V_{\mathrm{D}}\}$ bias space. Only an inhomogeneous oxide field $F_{\mathrm{ox}}(x)$ along the Si/SiO$_2$ interface which, according to (2.15), determines the *effective* trap level is taken into account. Important non–equilibrium effects related to the carrier ensemble and the energy distribution functions are not considered in the aforementioned approach. However, due to its physically sound description, the interaction of oxide defects with a whole band of charge carriers is already included via the term $f_{n/p}(E) f_{i,j}^{\mathrm{LSF}}(E, E_{\mathrm{T}})$, where f is the EDF and f^{LSF} is the lineshape function, see (2.13). Therefore, the NMP$_{\mathrm{eq.}}$ model can naturally be extended towards additional non–equilibrium effects, such as the formation of a heated, non–equilibrium carrier ensemble and the generation of secondary carriers, by using a full solution of the Boltzmann transport equation. This model variant will be referred to as full non–equilibrium NMP$_{\mathrm{neq.}}$ model. On the other hand, this procedure is computationally very costly and not practical for modern TCAD applications. Instead, semi–empirical approximations will be introduced to consider the interactions with secondary generated carriers. Within this approach, which will be referred to as extended–equilibrium NMP$_{\mathrm{eq.+II}}$ model, the EDFs will be still assumed to obey a Fermi–Dirac distribution.

CHAPTER 3

Atomistic Characterization of the Si–H Bond

In order to calculate the contributions of each mechanism to HCD described Chapter 1, the Si–H bond and its characteristics need to be explored and analyzed by means of *ab initio* methods. The **bond breakage trajectory** of how H would eventually dissociate away from Si at the Si/SiO_2 environment is largely unknown and no consensus has been reached on a microscopic level. Furthermore, the theoretical treatment of resonance induced excitations requires the knowledge of the associated **excited states**. An electron scattering into a resonance forms a temporary anionic system[1], which evolves within its lifetime on the excited potential energy profile. Therefore, a major ingredient in the above proposed descriptions are the **energetic positions of the resonances**, their **lifetimes** and the **excited potential energy surfaces** (PESs). Additionally, the Si-H bonds' response upon an applied electric field, i.e. its **dipole moment**, needs to be investigated. All of the aforementioned interactions trigger *vibrational* excitations and eventually dissociation of the Si–H bond. Therefore, the vibrational coupling with its environment, described as a phonon *bath* of oscillator, also needs to be accounted for. The coupling strength determines the **vibrational relaxation**, and thus the lifetime of vibrationally excited states, which influences the dynamics of the bond.

3.1 Calculation Setup & Preliminaries

The following part of this thesis focuses on the theoretical description of Si–H bonds and Si dangling bonds (DBs) at the Si/SiO_2 interface. In order to be confident that the results are truly representative of the properties of Si/SiO_2 structures and the corresponding defects, the initial atomistic models must be consistent with experimental perceptions of the atomic configurations and characteristics. This Section discusses the techniques used to create realistic Si/SiO_2 models and the methods applied to subsequently model the behavior and properties of interfacial Si–H bonds.

Models of Si/SiO_2/Si interfaces were created using classical potentials by adapting the well known *melt–quench* technique applied to construct amorphous bulk models, similar to recent approaches reported in the literature [176–181]. The obtained models were further optimized using the DFT setup described below. The electronic structure as well as geometric properties have been extracted and validated against experimental data from various results reported in the literature. Additionally, the Si dangling bond defects, which natively formed during the melt and quench procedure, have been carefully investigated and compared against the stringent limitations of P_b center characteristics found experimentally. Their structural properties as well as their behavior upon charge capture agree well with the measured specifications.

---

[1] Conversely, a hole temporarily forms an excited cationic system.

DFT Setup

All simulations were carried out using the Cp2k package, a DFT code which uses a mixed Gaussian and plane waves approach to represent the electrons in the system. 3D periodic boundary conditions were used for the Si/SiO$_2$ system throughout this work. A double–ζ Gaussian basis set optimized for condensed phase systems for Si, O and H was employed in conjunction with the Goedecker–Teter–Hutter (GTH) pseudopotentials. The plane wave cutoff used in these calculations was set to 650 Ry[2]. In order to minimize errors related to energies, i.e. band gaps and barrier calculations, the non–local, hybrid functional Pbe0_Tc_LRC was used for most of the work. It contains a 20% contribution of Hartree–Fock exchange and correlation in addition to a truncated Coulomb operator with a cutoff radius set to 2 Å. To mitigate the computational cost of calculating the Hartree–Fock integrals within the non–local functional, the auxiliary density matrix method (ADMM) was employed. In addition to the main basis set, a more sparse auxiliary basis set (pFIT basis set for Si, O and H) was used to calculate the exchange terms, which allows to further reduce the computational expenses. All geometry and cell optimizations were performed using the BFGS algorithm to minimize forces on atoms and the cell to within 1.5×10^{-2} eV/Å (5×10^{-3} GPa). Energy barriers between different atomistic configurations were calculated using the climbing–image nudged elastic band (CI–NEB) method. The algorithm linearly interpolates between the initial and final configuration to generate a trajectory which is connected by springs. Subsequently, the whole band is then simultaneously relaxed with the spring's force constant set to 19.5 eV/Å^2.

Si/SiO$_2$ Interface Creation

Constructing credible interface structures between amorphous oxides and a crystalline substrate has proven to be an extremely challenging problem [176–181], mainly due to the lack of detailed information regarding the microscopic interfacial region which, however, also depends on the exact process conditions. It is known from measurements performed in thin SiO$_2$ films that thermal oxidation of silicon results in an intrinsic compressive stress within the oxide [182–186]. Depending on the oxide thickness and the processing temperature, the reported values vary between 0.5 and 2.0 GPa[3]. X–ray reflectivity experiments [187] confirm this trend and, furthermore, found an increased SiO$_2$ density in an Si/SiO$_2$ system compared to bulk amorphous silica together with a compresed Si–O–Si angle distribution [188, 189]. Moreover, transmission electron microscopy (TEM) images [190, 191] and atomic–scale electron–energy–loss spectroscopy (EELS) [192, 193] indicate a transition region of approximately $5 - 7$ Å between crystalline silicon and the amorphous oxide structure. Within this interfacial region the band

---

[2] The cutoff was increased to 1200 Ry for calculations including an electric field.

[3] A recent study which investigates low–temperature processing of SiO$_2$ yields comparable results. A lower processing temperature effectively increases the interfacial strain and hence the defect density [MJC1].

gap as well as the dielectric constant continuously change between Si and SiO_2, as was also proposed in recent DFT studies [194, 195]. Together with photoemission measurements [190, 196], which investigated the chemical structure of ultrathin interfaces, the data suggest three transition layers with increasing concentration of partially oxidized silicon. In summary, all experimental investigations provide a number of constraints an interface model must satisfy to reliably reflect realistic conditions.

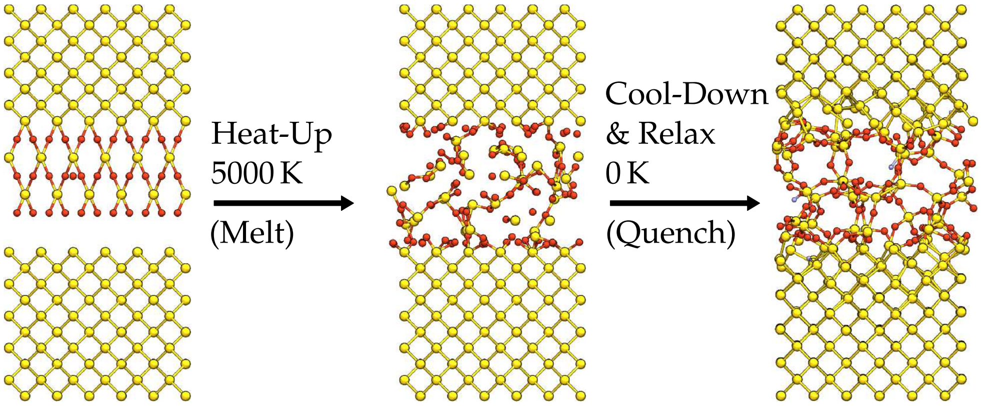

FIGURE 3.1: Schematic illustration of the adapted melt and quench procedure applied to construct Si/SiO_2 interface models. In the first phase β–cristobalite gets randomized by melting it at 5000 K while the crystalline Si lattice is kept fixed. Subsequently the system is slowly cooled down and all atoms are allowed to equilibrate at 300 K to account for the interfacial regions. In a final step possible defect configuration in the oxide and the interface are passivated by H and the structure is further optimized using DFT.

The utilized methodology to create a 3D periodic $Si/SiO_2/Si$ model with two interface regions adapts the melt and quench procedure previously used to create a–SiO_2 cells [62, 174] and is schematically shown in Fig. 3.1. Due to the excessive number of calculation steps required within the molecular dynamics (MD) simulations, the REAXFF force field [197] implemented in the LAMMPS code [198] was used. REAXFF is a sophisticated potential, describing covalent interactions in terms of a bond order which allows for the dynamic formation and annihilation of bonds. In a recent study the applicability of REAXFF to model glassy silica has been investigated [199]. The authors concluded that REAXFF is a promising potential for creating and modeling amorphous systems which would even allow to study the surface reactivity thanks to its dynamical ability. Starting from a 3×3×3 β–cristobalite cell, whose lateral cell dimensions were fixed to that of silicon, the energy has been minimized by allowing the cell to relax in the c direction. It was found that this procedure gives an oxide density of $\sim 2.3\,\mathrm{g/cm^3}$, in agreement with measured values [190][4]. Subsequently, the cell dimensions were fixed during the

---

[4] The density of β–cristobalite is closer to the one of a–SiO_2 compared to crystalline α–quartz.

melt and quench procedure. Crystalline silicon was added at the top and bottom and the respective atoms on either side were frozen while the remaining atoms were given random velocities from a Gaussian distribution. Furthermore, reflective walls have been introduced along both interfaces which prevent the oxygen atoms to penetrate into the *c*–Si lattice. In a first step the system was equilibrated at 300 K for 10 ps using a Berendsen thermostat. Afterwards the temperature was linearly increased to 5000 K over 60 ps to melt SiO_2 and the system was further equilibrated for an additional 100 ps[5]. Finally, the system was quenched to 0 K at a rate of 1.6 K/ps and the whole structure, including all atoms, was allowed to relax at 300 K. Selected snapshots of the different phases are shown in Fig. 3.1. In total over 100 Si/SiO_2 models were created, which resulted in various defect configurations at the interface as well as in the oxide. The three most promising models, in terms of their geometrical properties such as coordination number, bond angles and lengths, were chosen and further examined as well as optimized using the DFT setup. Note that all undercoordinated atoms, at the interface as well as within the oxide, have been passivated with H for subsequent calculations.

Model Properties & Defects

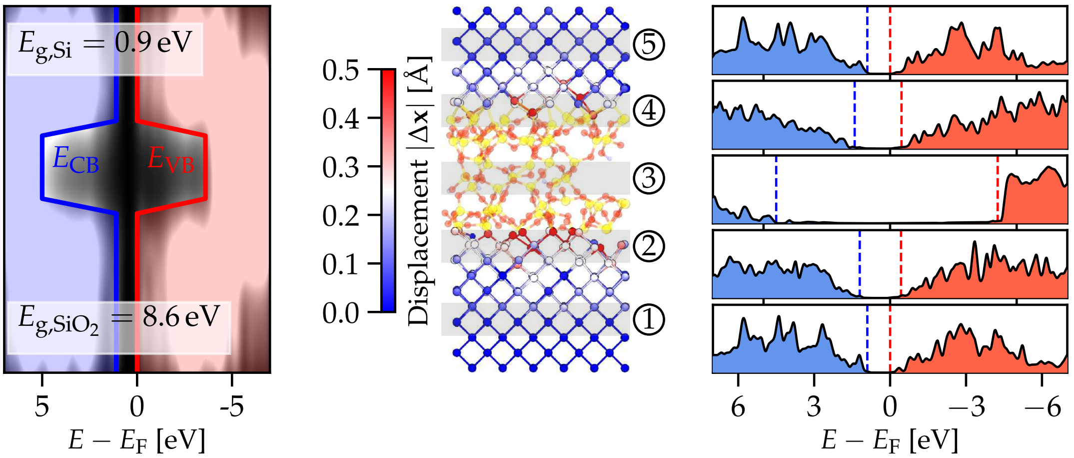

FIGURE 3.2: A density functional theory (DFT) simulation of one of the Si/*a*-SiO_2/Si interface structures containing 475 atoms. **Left:** The local density of states (DOS) across the slab. The obtained results are in good agreement with well established results. The band gap of Si as well as of SiO_2 is underestimated by ∼10% (compared to $E_{g,Si} = 1.12\,eV$ and $E_{g,SiO_2} = 9.1\,eV$). **Middle:** The interface model together with the displacements of the Si atoms from their respective equilibrium position in *c*–Si. Blue means a displacement of less than 0.2 Å, while the highlighted red atoms directly at the interface are strongly distorted. **Right:** The DOS at different positions across the slab. One can see a continuous change of the bandgap, particularly at the interfacial regions ② and ④.

---

[5] Within the simulations the melting point is at ∼ 4500 K and by 5000 K the system is in its liquid phase.

Simulations of the nonoptimized interfaces, i.e. structures obtained from ReaxFF, indeed gave rise to a rather high intrinsic compressive stress of $\sim$ 3.5 GPa. Thus, in order to obtain a more realistic model structure which is compatible with experimental values mentioned above for the subsequent simulations and investigations, full cell optimizations including the ionic positions of the models have been performed with an external pressure of 1 GPa parallel to the interface. Since the initial simulations did not show large off diagonal elements of the stress tensor, i.e. a shear stress, the original tetragonal cell symmetry was kept fixed during the optimizations. All three structures converged to a very similar cell size, $a = b = 16.203$ Å, $c = 32.965$ Å, with a variance of 0.007 Å in the lateral dimensions and 0.014 Å in the c direction.

The extracted geometrical properties of the final interface models are in good agreement with experimental data. The Si–O bond length ranges from 1.46 to 1.84 Å and peaks at around 1.64 Å, which is consistent with infrared absorption measurements [190]. The Si–O–Si angle averages at 133.5°, which agrees well with the conclusions reached in [189], that the angle is reduced to 135° compared to 148° in amorphous bulk structures. On the other hand, the O–Si–O angles remain almost unchanged compared to bulk SiO_2, around 109°. In order to further quantify the interface quality, the deformation of the c–Si lattice was calculated. This deformation is defined as the deviation of the atomic positions from their respective positions in crystalline silicon, see Fig. 3.2 (middle panel). Already three layers away from the Si/SiO_2 interfacial region the crystalline structure is almost completely restored, with displacements less than 0.2 Å. However, directly at the transition region, distortions are stronger due to the formation of Si–O bonds, giving rise to a higher strain directly at the interface between Si and SiO_2. A detailed discussion on the geometrical properties as well as the influence of the cell size and the oxide thickness is given in Appendix A.

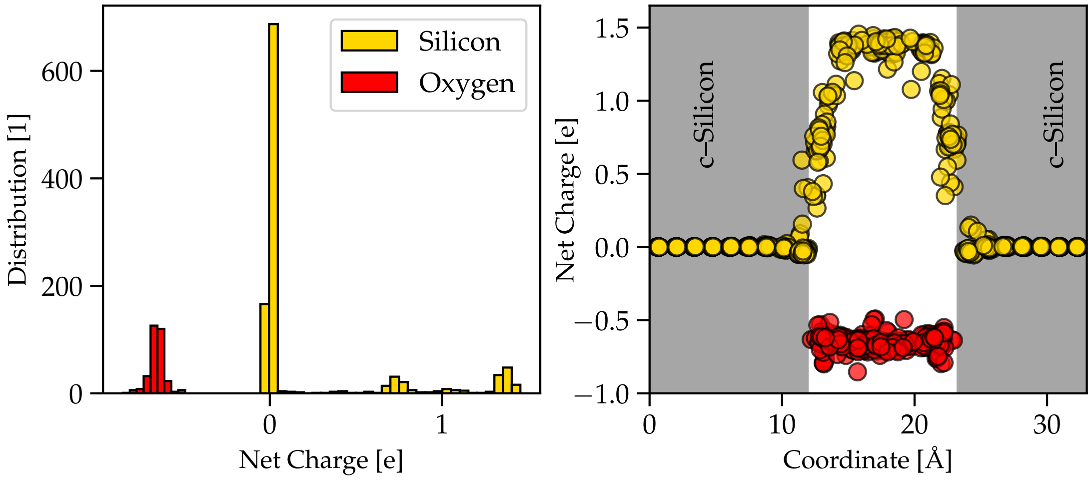

FIGURE 3.3: Mulliken charges associated with Si and O atoms within the utilized interface models. **Left:** Total distribution of charge states for the different atom species. **Right:** Charge states of silicon and oxygen across the interface model.

In addition to the structural quality, the electronic structure of the interface systems have also been investigated. Mulliken population analysis was used to determine the oxidation state of silicon across the Si/SiO$_2$ model, see Fig. 3.3. The profile clearly shows a gradual change from Si^0 in the crystalline Si part to its fully oxidized form Si^{+4} (which corresponds to a net charge of $\sim 1.4e$ in our DFT setup) in the SiO$_2$ region over a $\sim 5\,\text{Å}$ transition region. Such a characteristic is qualitatively very similar to the measurement results in [196]. Furthermore, this transition region is also reflected in the calculated DOS across the model. While in the bulk regions the corresponding band gaps compare well to the known values, one can see a continuous change within the interfacial regions, see Fig. 3.2 (left and right panels). However, additional electronic states within the band gap for the interface as well as in bulk SiO$_2$ are visible. These induced states can be identified as silicon band wave functions extending into the near oxide region, see Fig. 3.4. Such features have been also reported in recent experimental studies [192, 193], where the authors concluded that this actually limits the practical oxide thickness to 1.2 nm. It may be inferred that within the models used here, having an oxide thickness of 1.1 nm, even region ③ does not exhibit actual full bulk SiO$_2$ properties.

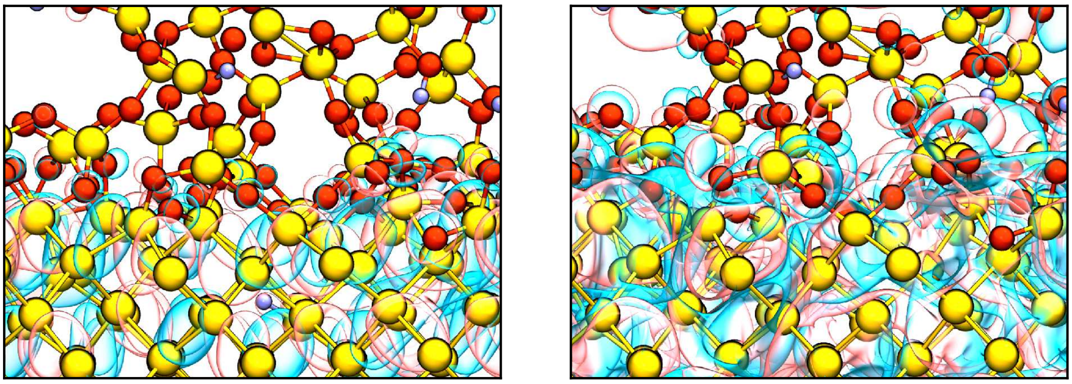

FIGURE 3.4: Visualization of the highest occupied molecular orbital (HOMO) for different isovalues, 0.05 (**left**) and 0.01 (**right**). One can clearly see that the wavefunction is a Si band states which, however, does penetrate into the oxide region.

The preselected (using REAXFF) and optimized (using DFT) interface models possess three different silicon dangling bond configurations (which have been passivated by H) at the interface as shown in Fig. 3.5: a) a Si–DB back–bonded to two Si's and one O atom, b) a Si–DB directly at the interface with an hydroxyl group 1.9 Å away and c) a subinterfacial (one layer away from the interface) Si trivalently back–bonded to three other Si atoms with no other O or H atoms in the direct vicinity. All defect structures possess an unpaired electron, as indicated by the spin density, with no other defect being present in the model. Compared to ESR studies [83, 88, 91–93], which suggest that a P_b center consists of a Si vacancy bonded to three Si atoms with an sp^3 hybridized dangling bond orbital, configuration (c) fully meets these requirements, and is therefore chosen as a *prototypical*

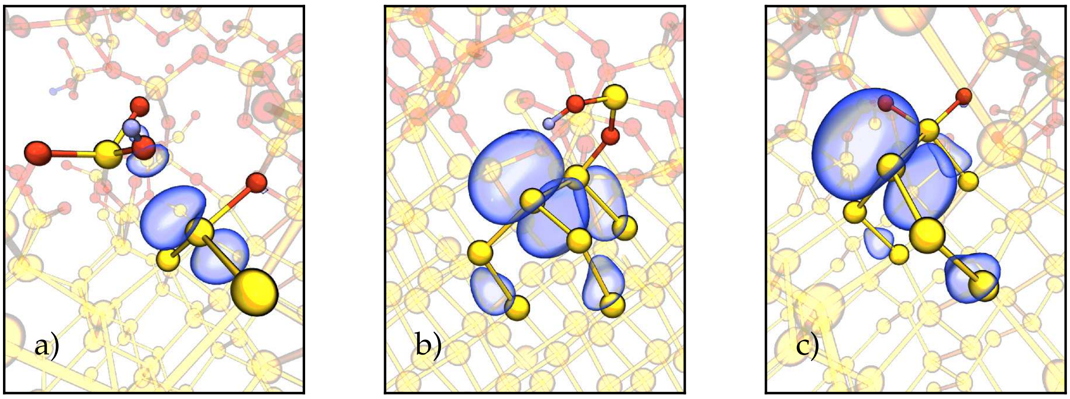

Figure 3.5: Three examples of silicon dangling bond (DB) interface defects created within the Si/SiO_2 interface models. Configuration a) at a first glance is consistent with a P_{b1} center (back bonded to two Si and one O atom). The spin density suggests that the defect state is mainly a nonbinding p orbital, which, however, contradicts experimental results [84–86, 90, 92, 94]. Configurations like b) have an extra H (or O–H group) next to the passivated defect which might distort the calculation results. Finally, configuration c), where the unpassivated Si is trivalently bonded to three other Si's with an sp^3 hybridized dangling bond orbital, closely resembling the well known P_{b0} center.

defect within this study. Subsequently, the different charge states, neutral, negative and positive, of different defect configurations have also been calculated. The structural reconfigurations with respect to their neutral configuration are shown in Fig 3.6. One can see that due to the rigid crystalline silicon structure the Si–DB does not undergo large atomic relaxations, neither in the negative (blue) nor positive (red) charge state. However, the flexibility of the a–SiO_2 network allows close–by oxygen atoms to reconfigure according to the Si–DB charge state, particularly when positively charged. This, however, is to be expected, since oxygen is slightly negatively charged in the SiO_2 system. In order to reliably extract the formation energies and the respective charge transition levels, the electrostatic correction methodology presented in [200] and implemented in SXDEFECTALIGNMENT2D has been applied to calculate the correction energy. All three defects exhibit two charge transition levels ($+/0$ and $0/-$) within the Si band gap, see Fig 3.6, as is also shown in [84–86, 88, 93, MJC3]. Even the defect structure (c) in Fig. 3.6, although potentially resembling a P_{b1} configuration, exhibits two transition levels within the Si band gap[6]. A detailed defect analysis can be found in Appendix B.

---

[6] The P_{b1} center properties are quite controversial and ongoing discussions about its electrical activity can be found in [91, 97].

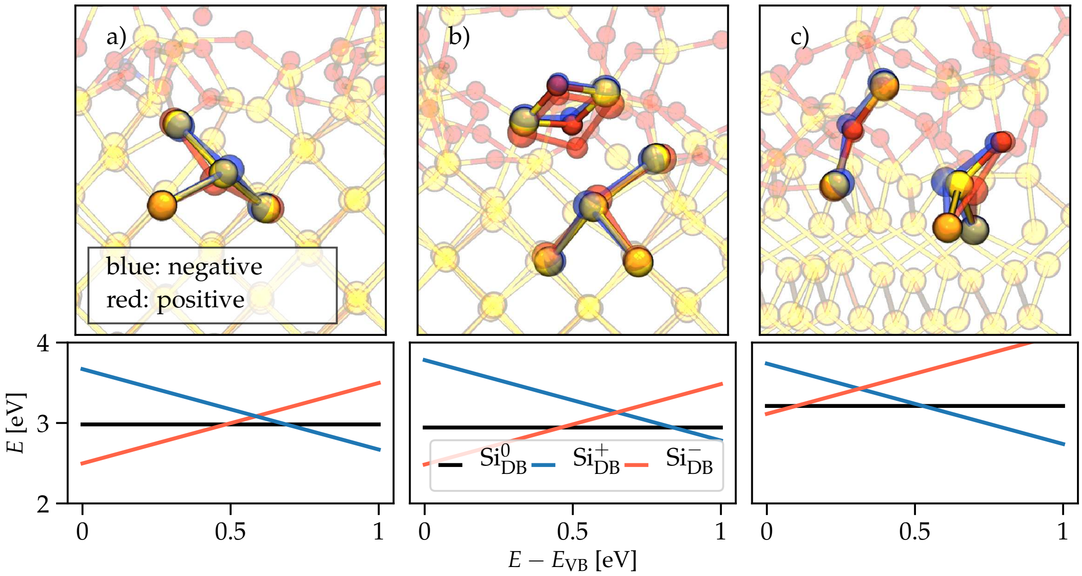

FIGURE 3.6: Investigation of the different charge states and the corresponding formation energies of interfacial Si–DBs. Two prototypical P_{b0} defects (a and b) and one candidate resembling a P_{b1} center (c) have been chosen for the study. **Top:** Structural reconfigurations associated with the negatively (blue) and positively (red) charged defect and its surrounding. **Bottom:** Plots of the defect formation energy versus the Fermi level with respect to the Si valence band.

3.2 Si–H Bond Rupture

The search for the detailed kinetics responsible for the creation of silicon dangling bonds at the Si/SiO$_2$ interface has proven to be a challenging task with no consensus being reached within the past decades. While experimental investigations for thermal dissociation in conjunction with ESR studies by BROWER [73] and STESMANS [201] converged to an activation energy between 2.5 and 2.8 eV, the theoretical picture behind this phenomenon is not well understood. Pioneering theoretical calculations have been conducted by TUTTLE *et al.* [202–206] and VAN DE WALLE *et al.* [207–209] investigating the structural and energetic properties of various configurations of hydrogen in periodic models of crystalline and amorphous Si. Both authors concluded that H dissociation along the Si–H bond direction (stretching mode) into SiO$_2$ is not the main dissociation path, due to its high reaction barrier of 3.6 eV , basically the Si–H binding energy[7]. The authors proposed that the Si–Si bond–center (BC) in bulk Si provides a stable configuration for the hydrogen atom, particularly in its neutral charge state [48, 210, 211], which is confirmed by experimental data [212–214]. By investigating different configurations it was shown that placing H between strained Si–Si bonds is between 1.7 eV and 2.5 eV higher in energy than the Si–H equilibrium configuration, depending on the actual position of the BC site. However, it was argued that the reaction

---

[7] Assuming a void above the Si–H bond which renders it compatible to dissociation into free space.

barrier would be essentially the same as the difference in energy, indicating that the H would spontaneously reform the Si–H bond as there is no reverse barrier. In [203] it was then speculated that by bending the H across the next BC site into the Si–H antibonding configuration (AB), which is a 180° flipped position of the H, emerging energy levels in the Si band gap may aid the dissociation process by allowing the Si–H complex to become charged. However, as we have shown recently [MJJ3], the AB site is actually only a metastable configuration without active trapping levels in bulk Si and as such a dead–end in the reaction dynamics. Instead, a new dissociation trajectory was proposed where in an initial step the hydrogen bends towards an adjacent silicon atom, and subsequently relaxes into the *next but one* Si–Si bond on the silicon side of the Si/SiO_2 interface. The details of these calculations and the derived conclusions will be discussed in the following.

Reaction Paths via Metadynamics

Finding the reaction dynamics and the corresponding pathway, i.e. locating a saddle point on a multidimensional PES $V(\mathbf{q})$, is a highly challenging issue in modern computational chemistry methods. Among the various methods, the NEB method [215, 216] is a popular way to find reaction pathways and minimum energy paths (MEPs) when *both*, the initial and final states, are *known*. However, for the problem at hand, the reaction kinetics for Si–H, only the equilibrium position, i.e. the initial state, is known, which renders the NEB method inappropriate. A complimentary method to NEB is the so–called dimer method [217], which only requires an initial state as input. Without any assumption regarding the unstable normal mode associated with the transition state, the initial dimer vector is randomly chosen. Test calculations, however, showed that this approach fails to converge to any reasonable results for finding the transition state for a single bond configuration in a solid–state system. A more rigorous approach would require a reasonable guess for the transition state together with the respective imaginary phonon mode, which, however, is the great unknown and a major subject of the current investigations.

A very recently developed enhanced–sampling method is WTMD [218, 219]. This method allows one to efficiently explore the free energy landscape (FES) by adding an *artificial* Gaussian potential to the *real* energy landscape which continuously expands the sampling of the FES and simultaneously discourages the system of returning to previously sampled configurations. Biasing certain collective variables (CVs), therefore, drives the Si–H complex out of its equilibrium and triggers possible reactions along the stretching and bending mode, while at the same time the environment can be kept at a constant temperature, e.g. $T = 300\,\mathrm{K}$. Thus, reaction barriers can be overcome which are not accessible in conventional molecular dynamics (MD) simulations. Having obtained the free energy surface, parametrized in terms of the CVs, the MEP connecting two configurations can be extracted.

The simulations conducted here are performed using the rather large Si/SiO_2 model system ($\sim$ 500 atoms) described above. Together with the con-

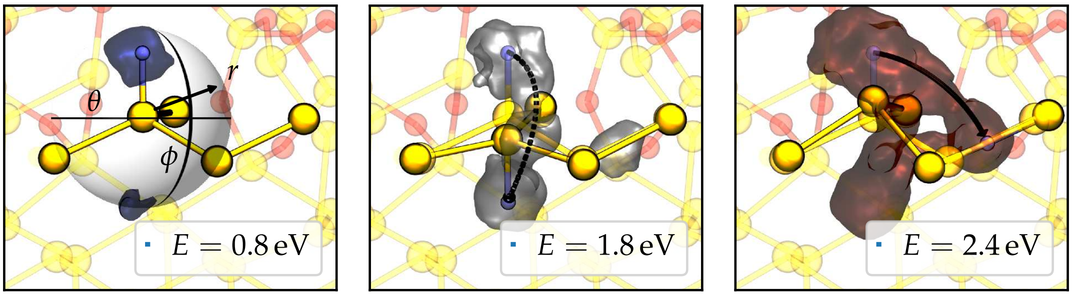

FIGURE 3.7: Representation of the free energy landscape $V(r, \phi, \theta)$ in 3D space obtained from the well–tempered metadynamics (WTMD) simulations parametrized with respect to the three collective variables. **Left:** Isosurface for $E = 0.8\,\mathrm{eV}$; one can see the vicinity of the Si–H equilibrium positions and the AB site. **Middle:** Isosurface for $E = 1.8\,\mathrm{eV}$; the trajectory between the initial and AB configuration is already explored. Furthermore, the newly found *next but one* BC site is visible. **Right:** Isosurface for $E = 2.4\,\mathrm{eV}$; an emerging transition path between the equilibrium and the next but one BC configuration.

siderable amount of simulation steps necessary to converge such simulations, only classical force–fields, such as ReaxFF [197], can be applied. All calculations again use the MD engine Lammps [198] in conjunction with the library Plumed [220]. The starting point is again an equilibration phase for 100 ps at $T = 300\,\mathrm{K}$ by assigning random, normally distributed velocities to the whole system. Subsequently, several WTMD simulations with different bias factors and bias heights have been conducted for a maximum of 50×10^6 timesteps with a stepsize of 0.5 fs. Detailed informations about the convergence is given in Appendix F. Within the simulations two CVs were biased and monitored to describe the system. The Si–H bond distance r as well as the polar angle ϕ with respect to its equilibrium position. The additional azimuthal angle, however, was only monitored and not explicitly biased during the WTMD simulations. The accessible region was limited to within 4 Å to ensure sampling of the free energy landscape only in the direct vicinity of the Si–H bond's equilibrium position.

The *raw data*, $V(r, \phi, \theta)$, are shown in 3D space as isosurfaces for selected values of the potential energy, see Fig 3.7. In order to give a more intuitive picture of the free energy landscape, the potential was mapped into 2D space by only considering the CV r and the polar angle ϕ. Three distinct minima can be identified: ① the intact Si–H bond in its equilibrium configuration, ③ corresponds to the H being in the AB site and ⑤ represents a newly identified minimum formed by the H being in the *next but one* BC configuration between Si_2 and Si_3. The respective atomistic configurations are schematically illustrated in Fig. 3.8 together with the extracted FES. The marked minimum energy paths connecting the three configurations have been verified in separate subsequent simulations using more efficient CVs, such as $r' = 1/\sqrt{2}(r_{\mathrm{Si}_3,\mathrm{H}} - r_{\mathrm{Si}_1,\mathrm{H}})$ and simply the angle ϕ.

The free energy map shows that inverting the H around Si_1 into the AB site ③, which is 0.8 eV higher in energy, proceeds via the dashed path. The transition

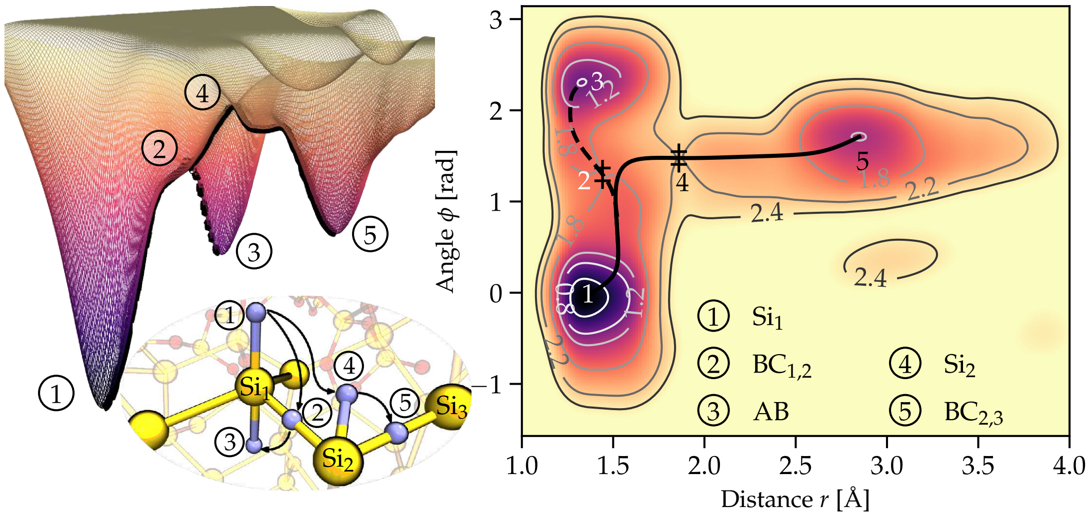

FIGURE 3.8: The free energy landscape together with a schematic of the different atomistic configurations in the vicinity of the interfacial Si–H bond obtained from WTMD with the REAXFF force field. Three distinct minima are visible: The equilibrium position ① at $r = 1.37\,\text{Å}$ and $\phi = 0°$, the hydrogen atom in the AB site labeled with ③, as well as the BC$_{2,3}$ configuration ⑤ where the H moved in between the next but one Si$_2$–Si$_3$ bond. The crosses ② and ④ mark the transition barriers for the extracted minimum energy paths (dashed and solid line) connecting the different minima.

barrier is 1.75 eV and its configuration corresponds to the H atom in the BC$_{1,2}$ site ②. Interestingly, although the H forms a bond–center configuration between Si$_1$ and Si$_2$, it is not a preferred metastable configuration for H along the given path, contrary to it being a stable site for H in bulk *c*–Si. In addition to the configuration ③ the hydrogen can also be moved into the BC$_{2,3}$ site ⑤, shown as the solid black line. The extracted MEP yields a transition state ④ where the H is stretched away from its initial silicon, Si$_1$, and attached to the adjacent Si$_2$. With a forward barrier of 2.25 eV and a reverse activation energy of 1.05 eV this trajectory could potentially explain the measurement data by STESMANS [201], reporting a barrier height of 2.83 eV for the Si–H depassivation process. The reverse passivation barrier $\mathrm{Si}^{\bullet} \Rightarrow \mathrm{Si{-}H}$, on the other hand, is assumed to be mainly driven by the cracking of molecular H$_2$, $\mathrm{Si}^{\bullet} + \mathrm{H_2} \Rightarrow \mathrm{Si{-}H} + \mathrm{H}^0$, where the additional (neutral) atomic H potentially is released into the SiO$_2$ side. Therefore, the backward barrier can not be directly compared to the measured values in [221, 222]. Nevertheless, a barrier of around 1 eV prevents the H from directly going back to the created Si–DB and potentially enables new insight into device degradation due to interface defects. A further discussion will be given in Section 3.6.

Detailed Dynamics via DFT

Building on top of the results derived above, the Si–H kinetics have been further investigated using density functional theory (DFT). The initial ① and final

⑤ configurations obtained from the classical force–field calculations were used to construct a trajectory with 13 frames in total by using linear interpolation[8]. Subsequently, CI–NEB simulations optimized the whole band, including its endpoints. Fig. 3.9 shows the resulting energy along the converged trajectory, i.e. the one–dimensional PEC for the introduced RC which represents a collective motion of atoms. The resulting path possesses very similar features as already predicted by ReaxFF observed in Fig. 3.8. First, the hydrogen moves towards Si_2, marking the transition state, and eventually moves in between the Si_2–Si_3 bond which was stretched from 2.34 Å to 3.13 Å, thereby forming a BC configuration. The total reaction barrier along the trajectory separating the intact Si–H configuration and the $BC_{2,3}$ site is 2.77 eV for the forward reaction and 1.30 eV for repassivating the Si dangling bond. Compared to the calculations with the classical force–field ReaxFF, the activation energy for creating a Si–DB is even closer to the experimentally extracted barrier of 2.83 eV [201]. Both, the transition state ④ as well as the final state ⑤, introduce two localized electronic levels in the Si band gap; a filled state close to the valence band edge and an empty level in the upper half of the band gap, see Fig. 3.9. Furthermore, the molecular orbitals (MOs) associated with these states, the highest (lowest) occupied (unoccupied) MO, are fully localized around the unpassivated Si, see Fig 3.10, indicating the creation of an electrically active interface defect [88, 93, MJC3]. In contrast the next lower (higher) MOs clearly show the delocalized characteristics expected for band states. Compared to the Si–DB characteristics shown above, the spin density, however, suggests a slightly distorted sp^3 hybridized DB orbital with a significant spread onto the back–bonded Si atoms.

Additionally, the charges associated with the atoms along the bond breakage path and the various atomic configurations have been analyzed using Mulliken and Bader charge analysis [223–225]. Both methods show that the hydrogen actually dissociates in its neutral charge states, leaving one remaining electron on the created Si–DB, in accordance with the occupation of the MOs. Details of the Bader charge analysis can be seen in Fig. 3.11, which shows the change of the electronic density at the transition and final state. Integrating over the associated Bader volumes of Si_1 shows that the respective charge changes by $0.78\,e$ as the H migrates to Si_2, and by $0.95\,e$ for the H being in its final position. This clearly indicates that one electron remains on the Si–DB. Analyzing the H along the trajectory shows that its charge changes by $-0.18\,e$, becoming slightly negatively charged in the final BC configuration. However, in summary one can conclude that the H would dissociate in its neutral charge state. Another important detail can be extracted using the Bader charge analysis. Along the path the H first attaches to Si_2 until it relaxes into the final position between Si_2 and Si_3. Note that such a configuration was already confirmed in the literature to be a stable position for H^0 [210–214]. A closer look reveals that the H would actually be bound to Si_3, as suggested by the electronic density as well as the distance between the H and the respective Si atoms. While at the transition point the H–Si_2 distance is 1.65 Å, it increases to

---

[8] Note that this corresponds to a direct connection between the minima in Fig. 3.8.

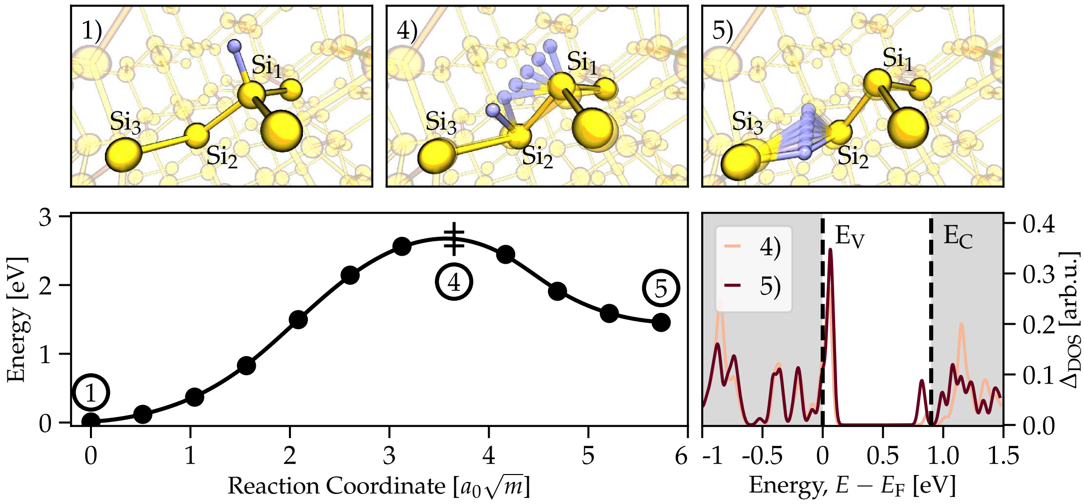

FIGURE 3.9: The results of a climbing–image nudged elastic band (CI–NEB) simulation investigating the direct MEP connecting the intact Si–H configuration ① and the next but one BC site between Si$_2$ and Si$_3$ ⑤ via the transition state ④ where the H is attached to the adjacent Si$_2$. **Top**: Simulation snapshots showing the atomistic configurations of the initial, final and transition state. **Left:** The total energy required for the forward reaction is 2.77 eV, whereas the backward barrier is 1.30 eV for moving the H back to its initial configuration. **Right:** Difference of the projected DOS onto the Si$_1$ atom along the path compared to the intact Si–H configuration. It is clearly visible that the transition and also the final state introduce localized electronic states in the Si band gap.

1.68 Å for the final position, compared to 1.55 Å between the H and Si$_3$. Thus, the Si$_2$ also possesses the character of a Si–DB with one unpaired electron. However, no additional states in the Si band gap are created due to the interaction with the nearby H atom which moves its energy levels inside the valence and conduction band.

Statistical Analysis

The inherent structural disorder at the Si/SiO$_2$ interface gives rise to a distribution of Si–Si and Si–O bond lengths and angles. Linking theoretical data and experimental results is, therefore, only possible at the statistical level. To expand the simulation results, three different Si/a–SiO$_2$ models have been used with a total number of 13 variations of pristine Si–H bond configurations, consistent with the perceptions of a P_b center. The different Si–H bonds were created by breaking and passivating selected Si–Si or Si–O bonds at the interface. Thus, the statistics include P_b0 (back–bonded to three Si's) and P_b1 (back–bonded to two Si's and one O)–like types as well as configurations with a nearby H atom and hydroxyl groups, respectively, see Fig. 3.5. In order to facilitate comparison with experimental results, all initial Si–H configurations were placed within 4 Å of the subinterfacial Si side. For all 13 starting configurations the three next but one BC

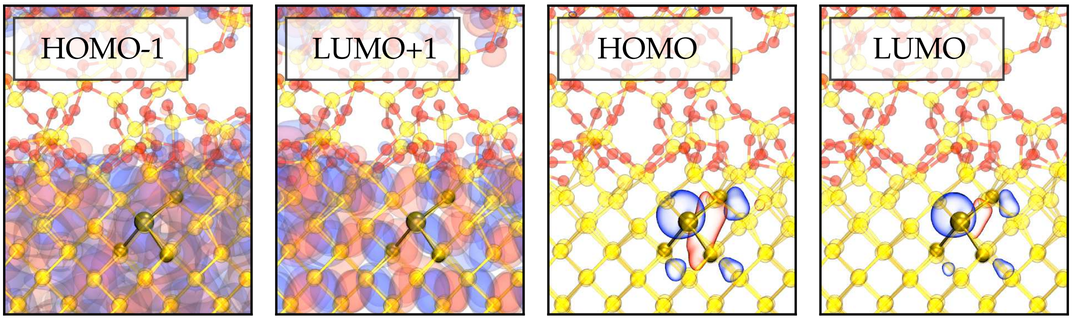

FIGURE 3.10: **Left:** The HOMO-1 and LUMO+1 are delocalized Si band states. However, they partially penetrate into the oxide region as was already discussed in Sec. 3.1. **Right:** The HOMO and the lowest unoccupied molecular orbital (LUMO) are clearly localized around the Si–DB. Comparing the wavefunctions to the prototypical defect configuration in Fig. 3.5 suggests the dangling bond orbital to be constituted by a slightly distorted unpaired Si sp^3 hybrid.

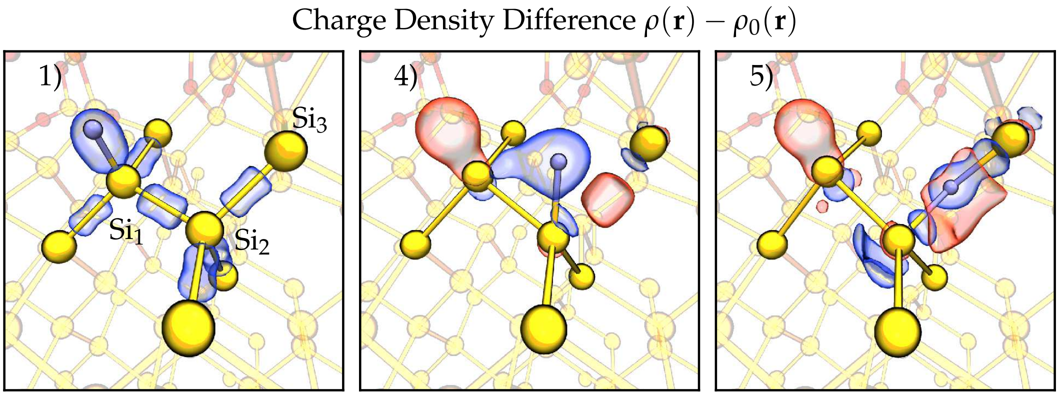

FIGURE 3.11: The charge density is represented by the blue and red translucent profiles along the dissociation trajectory (blue: increase of the electron density, red: decrease of the electron density w.r.t. the initial configuration). **Left:** The equilibrium Si–H configuration and the corresponding distribution of charge. **Middle:** In the initial step the H attaches to an adjacent Si atom (Si_2) with a distance of 1.57 Å. Thereby, one electron remains on the initial Si_1 as indicated by the Bader charge analysis. **Right:** In the final configuration the H forms a Si–H–Si complex between the next but one Si–Si bond. Being in this position, the H is slightly negatively charged and almost fully bonded to Si_3 as suggested by the charge density difference as well as the distances to Si_2 and Si_3.

sites were chosen and the direct trajectories were calculated using the CI–NEB method. Overall, this procedure gave 38 dissociation paths together with their respective energetics[9].

---

[9] One calculation did not converge to the defined criteria and was therefore discarded.

Owing to computational limitations, the CI–NEB simulations have been performed using the Pbe functional. Subsequently, single point calculations based on the hybrid Pbe0 functional were carried out on the optimized structures along the trajectory.

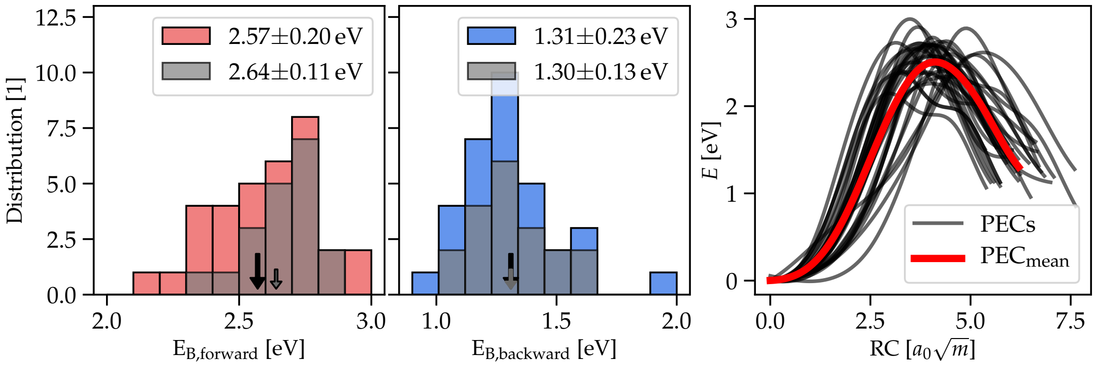

Figure 3.12: Statistical analysis of 38 calculated dissociation trajectories and barriers for various initial Si–H configurations using the CI–NEB method. **Left:** While the colored bars show the full results using all defect configurations, the gray bars present a limited statistics where the initial Si–H bonds have been selected to be at least one layer away from the interface. **Right:** The extracted potential energy curves together with the mean PEC. One can clearly see the variation of the reaction coordinate (RC) due to the amorphous interface region.

The simulation results show a broad distribution of forward (backward) barriers of the investigated reaction, see Fig. 3.12, ranging from 2.07 (0.95) to 2.95 eV (1.94 eV) with a standard deviation of 0.20 and 0.23 eV, respectively. The mean value for breaking the bond averages at 2.57 eV and nicely matches the experimental value of 2.83 eV; however, the extracted standard deviation σ is actually much larger than the value reported by Stesmans and Brower ($\sigma = 0.06$ eV). Two main factors possibly influence the results leading to the observed discrepancy. First, the created and utilized atomistic models possibly introduce an artificial local strain at the transition region due to their finite dimensions. This would result in artificially distorted bond angles and lengths, see Appendix A, which broadens the calculated statistics. However, further increasing the model sizes challenges the computational limits and prohibits accurate calculations using hybrid functionals. Secondly, the spatial placement of the initial Si–H bond could bias the resulting statistics. Within the presented statistics the pristine configurations are also placed directly at the Si/SiO$_2$ interface, where the atoms experience the maximum distortion due to the amorphous oxide, see Sec. 3.1 and Fig. 3.2. Limiting the statistics to initial configurations residing in a subinterfacial Si environment, at least one layer away from the interface, results in a much narrower distribution, see Fig 3.12. The concept of interface defects not being directly at the transition region, was already proposed in recent publications [92, 94], motivated by the small σ measured for the activation as well as the narrow ESR spectra, and thereby is consistent this assumption.

3.3 Impact of an Electric Field

The metal–oxide–semiconductor structure is routinely used in electronic devices and subjected to external electric fields during normal operation. Previous phenomenological studies [226–228] led to diverging results and ensuing discussions concerning the Si–H dipole moment and its response upon an applied electric field. A method particularly designed to account for the effect of an electric field within DFT calculations of 3D periodic systems is the *modern theory of polarization* [229–234]. It explicitly includes a self–consistent response of the electron density to electric fields, thereby rendering it an ideal approach to study processes in solid state systems. By minimizing the electric enthalpy functional introduced in [231, 233], the new field–polarized groundstate of the system is determined:

$$\mathcal{F}[\rho;\boldsymbol{F}] = E_{\mathrm{KS}}[\rho;\boldsymbol{F}] - \Omega \boldsymbol{P}_{\mathrm{mac}}[\rho;\boldsymbol{F}]\cdot\boldsymbol{F}, \tag{3.1}$$

with E_{KS} being the usual Kohn–Sham energy and Ω is the unit cell volume. The field coupling term is given by $-\boldsymbol{P}_{\mathrm{mac}}[\rho;\boldsymbol{F}]\cdot\boldsymbol{F}$, where $\boldsymbol{P}_{\mathrm{mac}} = \boldsymbol{P}_{\mathrm{ion}} + \boldsymbol{P}_{\mathrm{el}}$ is the macroscopic polarization as defined in [231, 233]. Within this approach the polarization is calculated from the Berry phase of the Bloch wavefunction, as described and implemented in [235]. However, an important feature of this formulation is that the polarization is actually a *multi–valued* quantity, due to its interpretation as a geometric quantum phase. Thus, it is formally defined within one modulo of a *quantum of polarization*, $2\pi\boldsymbol{R}$, where $\boldsymbol{R}$ is the lattice vector, see [232]. To ensure that the results and extracted dipole moments presented in this work can be compared to each other (i.e. they belong to the same polarization branch), they were analyzed and, if necessary, manually corrected by a polarization quantum.

To gain insight into individual processes within the Si/SiO$_2$ model when applying an electric field, the representation using Wannier centers has been utilized. Unlike Bloch functions, the localized nature of a Wannier center provides an intuitive *atomic-like* description of a charge density in a solid. This concept allows one to calculate the polarization by summing over the contributions of point charge ions, plus the corresponding electronic charges centered at the Wannier center of each occupied Wannier function [232]

$$\boldsymbol{P} = \frac{1}{\Omega}\Big(\sum_i (q_i\boldsymbol{r}_i)^{\mathrm{ions}} + \sum_n^{\mathrm{occ}} (q_n\boldsymbol{r}_n)^{\mathrm{WFs}}\Big). \tag{3.2}$$

A detailed comparison of the approach using Wannier centers and the Berry phase methods is given in Appendix C.

The defect creation process under an electric field is calculated by the following approach: Using the CI–NEB result at zero field, see Sec. 3.2, static, homogeneous electric fields up to 10 MV/cm with a 1 MV/cm step were applied across the interface structure in the z direction. The results of these calculations are summarized in Fig. 3.13. Each data point was obtained employing a single-point calculation, without including the effect of lattice relaxations. However, as can be seen in Fig. 3.13, the interaction of the neutral Si–H bond with an electric field

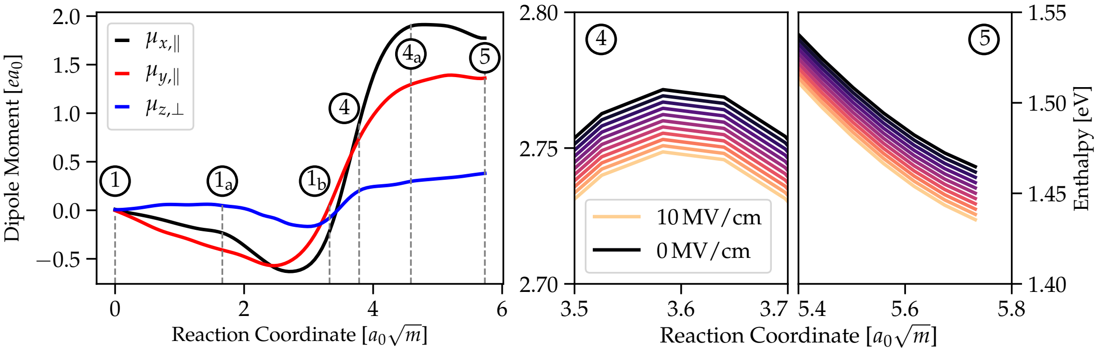

FIGURE 3.13: The effect of an electric field up to 10 MV/cm across the interface structure onto the proposed bond breakage trajectory. **Left:** The extracted change of the components of the dipole moment vector $\boldsymbol{\mu}$ along the given pathway for zero applied field. These quantities can be further used to obtain an estimate of the change by defining an effective dipole moment μ_{eff}. **Right:** The results of the self consistent calculation with an electric field suggest that the interaction is extremely weak. Applying a field of 10 MV/cm lowers the barrier by only 0.023 eV and leaves the Si–H bond breaking process virtually unaffected.

is extremely weak, rendering errors related to this approximation irrelevant. The electric enthalpy along the bond breaking pathway is virtually unaffected, even for fields as high as 10 MV/cm. Maximum changes of 0.023 eV for the forward barrier, defined as the enthalpy difference between the initial and the transition state, can be extracted, while the enthalpy of the final state changes by $\sim$ 0.03 eV.

Additionally, the components of the dipole moment vector and the respective changes have been extracted along the trajectory, see the left panel of Fig. 3.13, for zero applied field. The largest contribution within this approach results from the dissociating Si–H bond and also includes accompanying relaxation effects. Together with Fig. 3.14, which shows selected frames along the pathway including the Wannier centers, this provides some intuitive understanding of this process. Within the first steps, the trajectory is governed by bending the H in the direction of the adjacent Si_2 atom, see 1 and 1_a. Thereby, only the H atom and the associated Wannier center change their positions without further lattice relaxations, which does not significantly change the dipole moment. Moving the H further away from the initial Si atom (1_b) results in a structural and electronic reconfiguration and eventually breaks the Si–H bond, marking the top of the transition barrier, see 4. This is also reflected in the change of dipole moment in Fig. 3.13. Subsequently, the H and the surrounding Si atoms relax to their final bond–center positions, 4_a and 5, forming a Si–H–Si complex.

Following [160], one can define an *effective dipole moment* vector $\boldsymbol{\mu}_{\text{eff}} = \boldsymbol{\mu}_2 - \boldsymbol{\mu}_1$, where $\boldsymbol{\mu}_2$ is the dipole moment at the transition state and $\boldsymbol{\mu}_1$ is associated with the initial configuration. Both quantities can be extracted at zero field, see Fig. 3.13, and used within $\Delta E_\text{B} = -\boldsymbol{\mu}_{\text{eff}} \cdot \mathbf{F}$ to estimate the change of barrier due to an applied field. Extracting the z component of $\boldsymbol{\mu}_{\text{eff}}$ for the given trajectory yields a value of 1.15 D which leads to a reduction of the barrier of 0.024 eV. This is

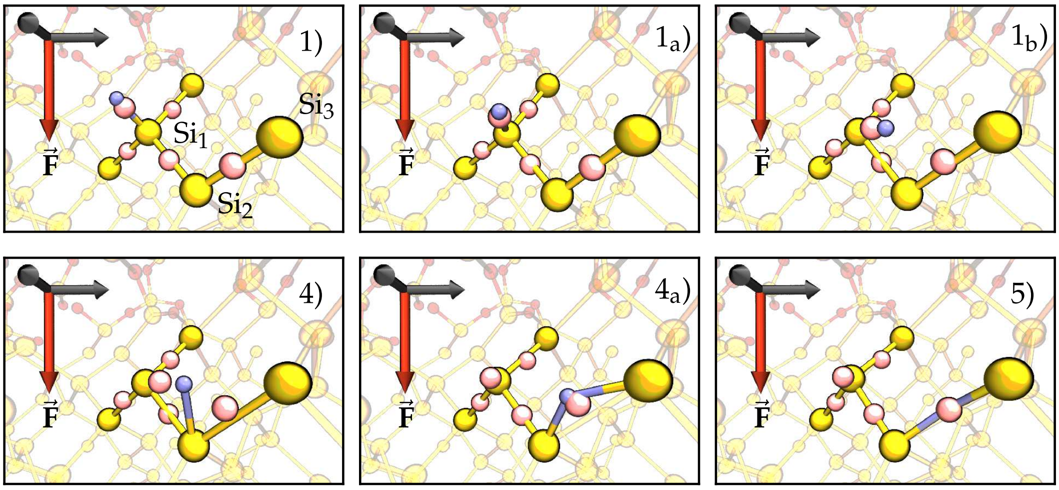

FIGURE 3.14: Selected simulation snapshots along the dissociation pathway including the atomistic configurations as well as the associated Wannier centers (pink spheres). The representation using Wannier functions allows to obtain an intuitive, albeit qualitative, understanding of the change of the dipole moment. During the first steps (1-1_b) the H bends towards the adjacent Si atom without significant lattice relaxations. Only the Wannier center associated with the Si–H bond changes its position, thereby leaving the dipole moment virtually unaffected. However, breaking of the initial Si–H bond (4) is accompanied with structural and electronic reconfigurations which leads to an increase of the dipole moment. Frames 4_a and 5 show the subsequent relaxation into the final position, which possesses a higher dipole moment due to the resulting distorted Si–H–Si complex.

in excellent agreement with the self–consistently calculated DFT results using the Berry phase method.

3.4 Resonances & Energies

The proposed *multiple vibrational mechanism*, see Section 2.1, where an incident carrier scatters into an available resonance state and upon inelastic electronic relaxation triggers the transition between vibrational states in the ground state potential, requires knowledge about the associated excited states. Unfortunately, excited state properties and dynamics are rather difficult to calculate and hardly accessible within standard DFT. A popular method of approximating the anionic or cationic PECs is to apply *Koopmans theorem*. Within this approach the negative of the energies of the highest occupied and lowest unoccupied molecular orbitals (HOMOs and LUMOs) is related to the ionization potentials and electron affinities. The respective orbital energies can, therefore, be used to approximate the excited PECs. The utilized cluster model here consists of 10 Si atoms and 23 H atoms, where 22 are needed to passivate the Si atoms and one represents the Si–H bond of interest. Assuming the same reaction coordinate (RC) as for the bond breakage trajectory in the neutral ground state, 150 single point calculations along the path have been carried out. The resulting 10 highest occupied and lowest unoccupied α and β–spin states were used to construct adiabatic resonance PECs. The constructed PECs for the negatively and positively charged complex show a similar behaviour, see Fig. 3.15. The approximated resonance energy (at $q = 0\,\mathrm{a_0}\sqrt{\mathrm{m}}$) of the anionic state is between 2.7 eV and 4.2 eV, whereas the cationic state is about 0.5 eV higher, which is in good agreement with previous findings [106, 114, 115, 236, 237]. Furthermore, all excited energy profiles share that their minimum is shifted with respect to the ground state potential $V(q)$ as well as a lower transition barrier. While for the anionic PECs the barriers are lowered by $\sim 0.9 - 1.2\,\mathrm{eV}$, the cationic charged states possess activation energies of around 2.0 eV. On the other hand, the left well minima of the constructed $V^-(q)$ are shifted by $\Delta q = 0.74 - 0.96\,\mathrm{a_0}\sqrt{\mathrm{m}}$ towards the barrier, whereas the positive PECs are only shifted by $\sim 0.45\,\mathrm{a_0}\sqrt{\mathrm{m}}$. However, also the transition state along the trajectory seems to change for $V^+(q)$. Nevertheless, these calculations only provide a qualitative understanding of the excited potential curves. A more rigorous approach is given by the method of CDFT [238, 239] which allows one to directly construct diabatic potential energy curves. CDFT as implemented in the CP2K package [240, 241] has been used where an *additional* charge (negative and positive) has been restricted to be localized on the Si–H bond. Single point calculations along the *neutral* trajectory with fixed ionic positions have been performed. The effect of lattice relaxations was explicitly neglected due to the short resonance lifetime, which is on the order of a few femtoseconds [114, 115, 236].

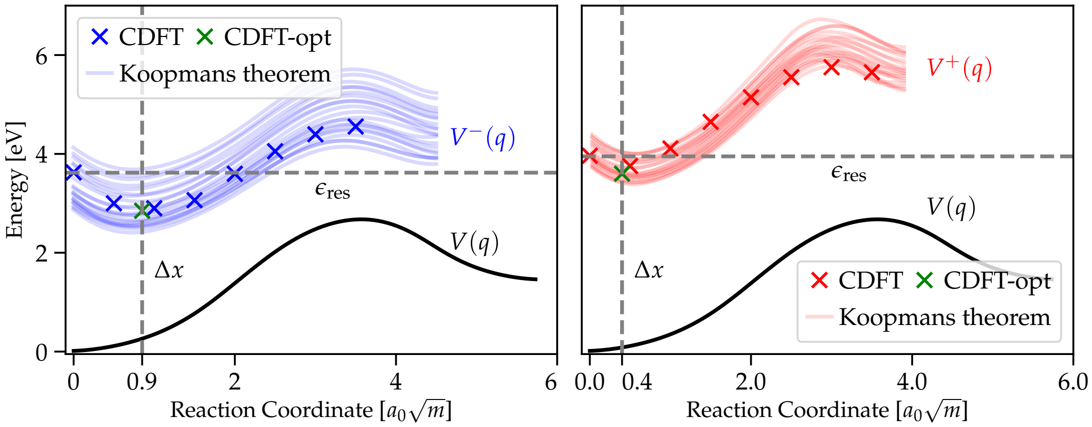

FIGURE 3.15: Potential energy curves along the reaction coordinate for the neutral bond breakage pathway, see Sec. 3.2 and [MJJ3]. Two approximations were employed to construct the potential profile for the excited complexes: Koopmans theorem using the 10 lowest (un–) occupied α and β–spin orbitals, and the method of constrained density functional theory (CDFT) to directly assess the diabatic states. **Left:** The results for the excited anionic complex $V^-(q)$ together with the ground state potential $V(q)$. **Right:** The constructed adiabatic PECs as well as the diabatic PEC for the positively charged Si–H bond.

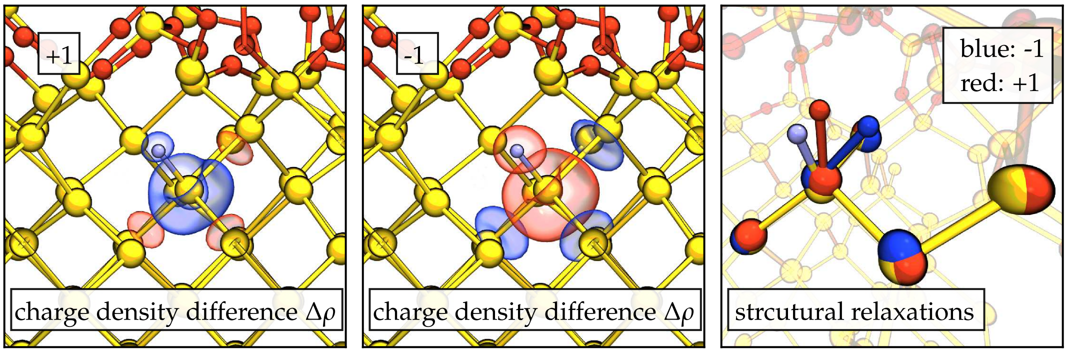

FIGURE 3.16: Details of the CDFT calculations. **Left and Middle:** The difference of charge density $\Delta\rho = \rho_{\mathrm{DFT}} - \rho_{\mathrm{CDFT}}$ for the negatively (left) and positively (middle) charged Si–H complex. Blue (red) indicates a higher (lower) electron density. One can see that for both states the additional charge is mainly localized on the Si atom. **Right:** The effect of structural relaxations for the charged Si–H bond. For the negative charge state the Si–H distance as well as the Si–Si–H angle increase, forcing the H in the direction of the bond breaking trajectory. The positive charge state does not show such a pronounced reconfiguration where only the central Si atom slightly moves out of its plane.

Furthermore, the calculations were restricted up to the transition state to ensure that the charge can indeed be localized on the Si–H complex. Investigations using the method of Bader charge analysis show that the Si–H bond is indeed negatively (positively) charged ($\Delta(q_{\mathrm{SiH}} - q_{\mathrm{SiH^-}}) = -0.93\,e$, $\Delta(q_{\mathrm{SiH}} - q_{\mathrm{SiH^+}}) = 0.86\,e$) and the additional charge is mainly localized around the Si atom, see Fig. 3.16.

The CDFT results for both charge states are shown in Fig. 3.15 (symbols). The diabatic PECs are in good agreement with the results obtained from Koopmans theorem and again yield shifted minima configurations as well as altered transition state. Furthermore, at the equilibrium position of the neutral state $V(q_{\mathrm{eq}})$ the charge–localized states are 3.64 eV (negative) and 3.96 eV (positive), respectively, higher in energy. In order to qualitatively understand the new charged equilibrium configurations, full geometry optimizations within the CDFT simulations have been performed, see Fig. 3.16. Interestingly, for the negatively charged Si–H complex the bonding distance changes from 1.48 Å ($V(q_{\mathrm{equ}})$) to 1.75 Å ($V^-(q_{\mathrm{equ}})$) and the Si–Si–H angle opens from 109° to 141°. Such a structural reconfiguration forces the H atom in the direction of the dissociation path, which explains the shifted minimum of $V^-(q)$[10]. The positive charge state does not undergo such pronounced relaxations. The reconfigurations are mainly determined by the Si atom slightly moving out of its plane and thereby stretching the Si–Si bonds in the vicinity. This, however, suggests a potentially different bond breakage trajectory in the positive charge state.

---

[10] Qualitatively, this result can be compared to intrinsic electron traps in SiO_2 where wide O–Si–O bond angles serve as efficient electron trapping sites [242].

3.5 Vibrational Spectrum

The interplay of the Si–H bond with its environment is one of the fundamental interactions which strongly influences the bond dynamics by governing its vibrational lifetime. The coupling strength between a *phonon bath* and the motion of a bond, i.e. a particular vibrational mode, can be quantified using the phonon spectrum.

The system studied here is the Si/SiO_2 model described in Sec. 3.1 which contains 472 atoms. A normal–mode analysis based on DFT, which uses a finite–difference scheme to calculate the dynamical matrix, yields the spectrum shown in Fig. 3.17. The resulting density of states (DOS) can be divided into collective vibrations from the Si/SiO_2 system (low and intermediate frequencies) and sharp peaks at higher frequencies related to particular movements of individual atoms, e.g. Si–H and O–H stretching modes. Furthermore, by projecting the phonons onto particular atom types and regions one can split the collective modes into contributions form the *c*–Si lattice (yellow), the amorphous oxide (red) and the interfacial regions (blue). One can see that the silicon spectrum nicely resembles the phonon DOS of its bulk counterpart, while the phonon mode spectrum of SiO_2 is slightly distorted due to the interface.

Additionally, the applicability of the classical force–field REAXFF has been tested for further calculations, see Chapter 4.

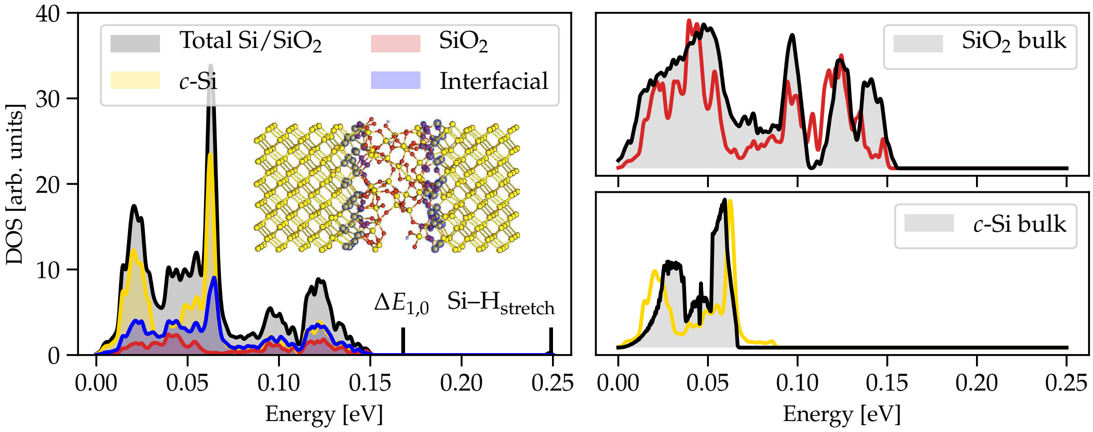

FIGURE 3.17: **Left:** Phonon density of states (DOS) of a Si/SiO_2 interface model together with the fundamental frequency of the Si–H bond breaking potential, see Sec. 3.2. **Right:** The projected phonon spectra for the Si and the SiO_2 part compared to their calculated bulk counterparts.

3.6 Hydrogen Migration & Passivation Dynamics

Building on top of the results of Sec. 3.2, that the Si–H bond breakage dynamics are determined by hydrogen moving into the next but one BC configuration, further migration pathways as well as the passivation kinetics can be investigated. In this context two important questions arise: What happens with the hydrogen after being released into the BC site and how exactly can Si–DBs be passivated again? As was shown in Sec. 3.2, the backward barrier for the H being in the $BC_{2,3}$ position to re–passivate the Si–DB is around 1.30 eV. Assuming a thermally activated reaction following an Arrhenius law[11] would, however, be incompatible with the conclusions by Brower [222] and Stesmans [221, 243–245]. Rather, these studies suggest that the passivation of P_b centers is inevitably linked to the presence and cracking of molecular H_2. Although dedicated experiments investigated the effects of atomic H onto the passivation and depassivation kinetics of P_b centers [246, 247], experimental studies conducted on a device level confirmed the prevailing opinion of H_2 passivation [95, 248–250].

Migration Trajectories

First, the **hydrogen in a Si–Si BC configuration at the interface and possible migration trajectories** will be discussed. Well–tempered metadynamics (WTMD) in conjunction with ReaxFF has again been utilized to sample the free energy surface of interfacial H atoms. Five H atoms have been randomly inserted between Si–Si bonds at the interface layer. Subsequently, the simulations were run in parallel with a total number of 1×10^9 timesteps, corresponding to a simulation time of 0.5 μs. During these simulations only the x and y coordinates of the respective hydrogen atoms were biased with no additional restrictions regarding their spatial position, i.e. the H atoms were allowed to move freely within the structure. The final result is summarized in Fig. 3.18.

Although the motion of the hydrogens was not limited in any way, they remained within the interfacial Si region and did not cross into the SiO_2 side, see Fig. 3.18. Rather, the analysis suggests that once the H was released into a BC site, it can further *diffuse* along the interface by *hopping* to the next BC. The positions of the potential minima together with extracted minimum energy paths (MEPs) (right panel of Fig. 3.18) strongly indicate that the released hydrogen is mobile within the subinterfacial Si side (see upper left panel of Fig. 3.18), possessing a *hopping* barrier smaller than 1 eV. Furthermore, such an observation implies that the potential barrier into the oxide region is larger than the lateral *hopping* barrier for hydrogen along the interface. In order to be able to also quantify the barrier across the interface, additional simulations using Lammps and ReaxFF have been performed. An xz slice with 5 Å thickness has been chosen to sample the energy landscape, see Fig. 3.19. Placing the hydrogen at 20000 positions within this slice yields the potential map shown in the right panel of Fig. 3.19. One can clearly see the highlighted red isoline for $E = 1.8$ eV at the Si/SiO_2 interfaces, representing a barrier almost twice as large compared to the BC site hopping along the transition region.

---

[11] assuming an attempt frequency of $\nu_0 \sim 1 \times 10^{12} - 1 \times 10^{13}\,\mathrm{s}^{-1}$

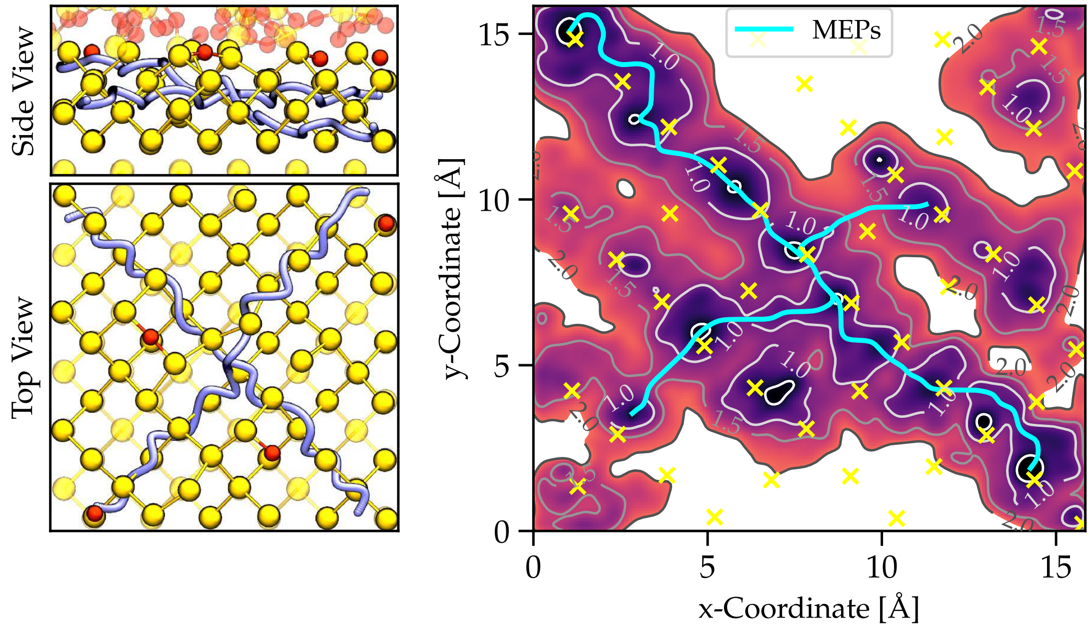

FIGURE 3.18: Simulation results for hydrogen migration *along* the Si/SiO$_2$ interface using the classical force field REAXFF and the methods of metadynamics. **Left:** Top and side view of the (fully equilibrated) interfacial region in which the hydrogen remained during the simulations. Additionally, two individual migration pathways for a hydrogen atom extracted from dedicated simulations using the methods of steered MD are also shown. **Right:** The free energy surface extracted from the WTMD simulations. The yellow crosses mark the equilibrium positions of the interfacial Si atoms (see the left panels) and indicate that the various minima are Si BC sites. The highlighted MEPs are directly extracted from the potential landscape. Note that regions of higher energy are not properly sampled and explored within the simulations and therefore left white within the map.

However, due to the large configuration space for the above simulations even an excessive amount of spatial points or simulations steps does not guarantee a converged sampling which potentially leads to an overestimation of the involved transition barriers[12]. To further access the distribution of barriers, subsequently individual migration paths have been simulated. A technique particularly suited for the problem at hand is the so–called *moving restraint bias*, or *steered* MD method, implemented in PLUMED [220]. It allows one to drag the system from an initial to a final state by adding a time–dependent, harmonic restraint on the CV(s). The simulations start from the equilibrated initial configuration and can be divided into three phases. First, the force constant for the restraint is slowly increased over 50000 timesteps to lock the system in its initial state without stressing it. Afterwards, the system is smoothly moved towards the final configuration using 1×10^6 timesteps to allow the system to equilibrate and follow a relaxed trajectory. Finally, the force constant is released again to end up in a equilibrated

---

[12] as well as shifted MEPs

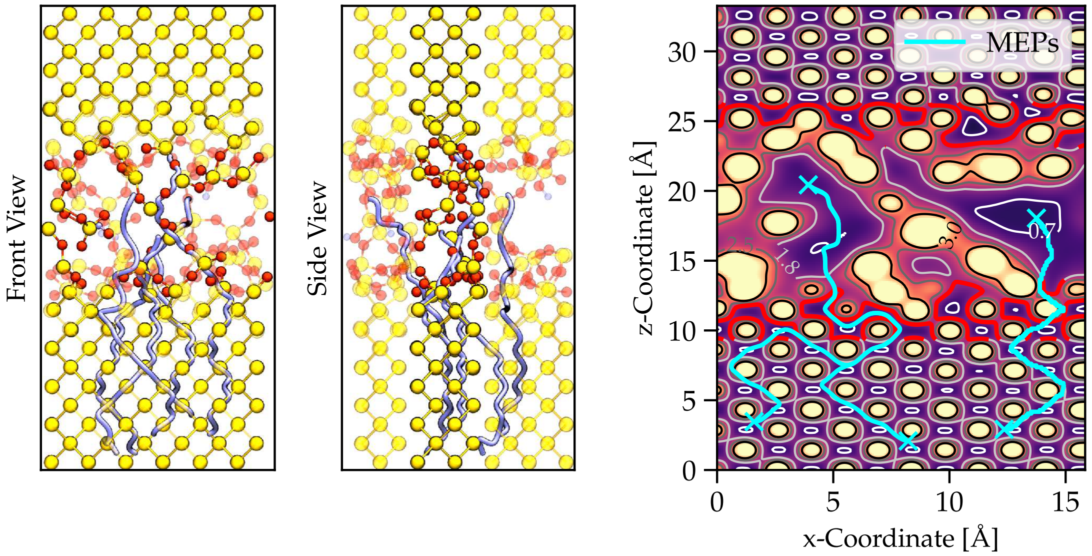

FIGURE 3.19: Simulation results for hydrogen motion *across* the Si/SiO$_2$ interface structure using the classical force field REAXFF. **Left:** Front and side view of the (fully equilibrated) xz slices used for the sampling of the energy landscape. Furthermore, several individual hydrogen migration trajectories are shown which have been simulated using the method of steered MD within the full atomistic model. **Right:** The energy landscape extracted from sampling the reduced configuration space, i.e. the xz slice. One can clearly recognize the atomistic structure (see left panels) as well as potentially advantageous migration paths possessing low energy barriers. Furthermore, note the highlighted red isoline for $E = 1.8\,\text{eV}$ at the interfacial transition regions for crossing into the SiO$_2$ side.

and unconstrained final configuration. Various migration trajectories *along* and *across* the Si/SiO$_2$ interface with different, and specifically chosen, initial and final configurations have been simulated, see the left panels of Fig. 3.18 and 3.19. All results and potential profiles are summarized in Fig. 3.20. Note that within these simulations the change of the systems' free energy is connected to the work performed over time. However, the large noise and error bar associated with this quantity would require large statistics for a quantitative analysis. Nevertheless, the results shown in Fig. 3.20 allow for a qualitative understanding of the underlying mechanisms, particularly due to the large differences of the involved barriers.

The resulting *hopping* barriers *along* the interface connecting the different BC configurations are between $0.3-1.3\,\text{eV}$, see Fig. 3.20 (left panels). The rather large variation of the barriers can be explained by taking into account the deformation of the silicon lattice due to the residual strain at the Si/SiO$_2$ interface. The MEPs across the structure, starting in the Si bulk and ending in the SiO$_2$ see Fig. 3.19, yield a very narrow and consistent distribution of barriers in the bulk silicon side of around $E_{\text{B,hop}} = 0.4\,\text{eV}$. The diffusion trajectory of hydrogen in bulk crystalline silicon also tends to *hop* from one to the next BC site, which is indeed a well known stable position reported in the literature [212–214]. On the other

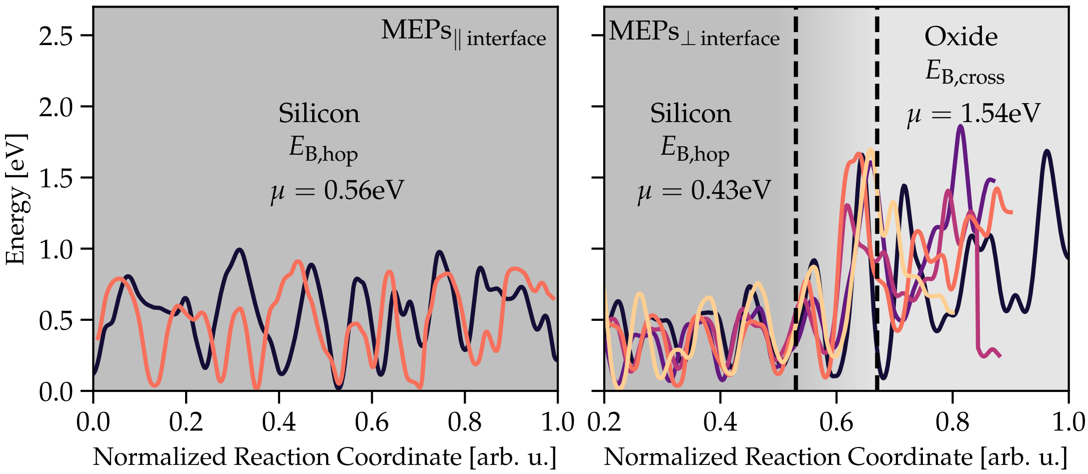

FIGURE 3.20: Extracted migration paths and energy profiles using the method of steered MD. **Left:** Two trajectories, see Fig. 3.18, for H *hopping* between BC sites *along* the interface. **Right:** Five simulated migration pathways for H *across* the Si/SiO_2 interface, see Fig. 3.19. The dashed lines indicate the Si/SiO_2 transition region.

hand, approaching the transition region and crossing into the bulk oxide shows an increase of the barriers on the Si side and ultimately a large potential barrier between $E_{\text{B,cross}} = 1.2 - 1.9\,\text{eV}$ for the H moving into the SiO_2 side.

To establish a more accurate picture for the *hopping* barriers along the interface which is comparable to the results presented in Sec. 3.2, subsequent DFT simulations have been conducted. Five initial positions, relaxed BC configurations, of the hydrogen atom have been chosen and the respective barriers to the three closest BC sites were calculated using the CI–NEB method.

The individual hopping barriers are summarized in Fig. 3.21. The calculated values range from 0.16 eV to 1.04 eV with two outliers possessing barriers of $\sim 1.35\,\text{eV}$. The average barrier height is 0.53 eV and, therefore, in very good agreement with the predicted values using the MEPs in the left panel of Fig. 3.18 and the respective energy paths shown in Fig. 3.20. Additionally, comparing the lateral H *hopping* barriers E_{hop} to the reverse barrier E_{backward} for H in the $BC_{2,3}$ site re–passivating the Si–DB defect, see Fig. 3.12, shows that the *hopping* barriers are considerably lower ($E_{\text{hop}} \ll E_{\text{backward}}$).

Furthermore, the stability of H in various configurations within the interfacial region has been calculated. A hydrogen atom has been placed at different positions, i.e. a BC site in the Si side of the interface, interstitial within a void in the SiO_2 network as well as close to O and Si atoms in the interfacial oxide region. The energy of the respective configurations has been determined using geometry optimizations within DFT. All results are summarized in the right panel of Fig. 3.21. The mean value of H being in a Si BC configuration has been used as the reference energy. One can see that the energy of such configurations shows a distribution of around 1.5 eV, which is consistent with the barriers calculated in the left panel of

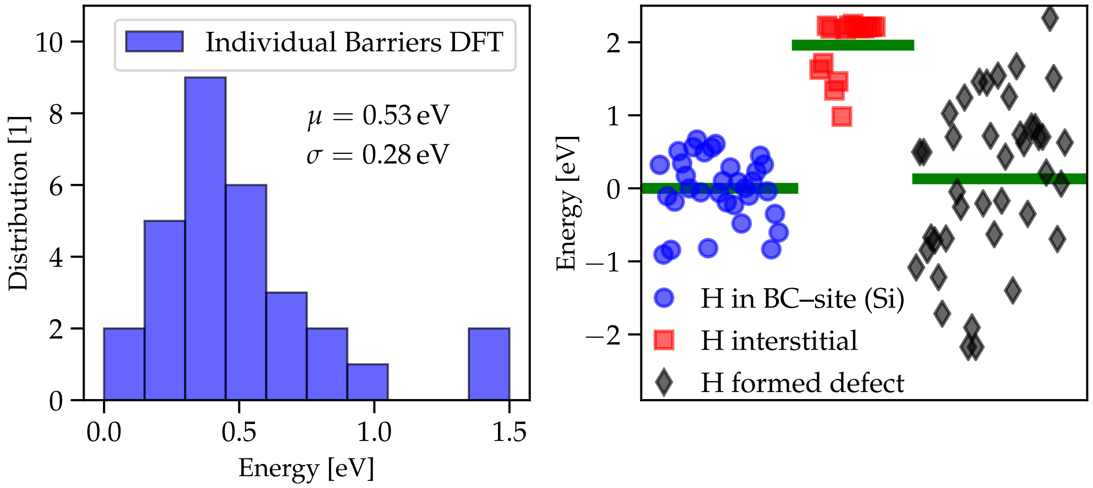

FIGURE 3.21: **Left:** Simulated distribution of barriers for hydrogen *hopping* between bond–center sites at the subinterfacial Si side of the Si/SiO$_2$ interface using the method of CI–NEB in conjunction with the PBE functional. Paths for connecting five initial BC configurations with the three next nearest BC sites have been calculated, yielding in total 30 barriers (forward and backward transition barriers). **Right:** Energy of various H configurations obtained from geometry optimizations. The mean value of hydrogen in a Si BC site serves as a reference for energy alignment.

Fig. 3.21. On the other hand, the H in an SiO$_2$ interstitial position possesses on average a 1.8 eV higher energy, as indicated by the green bar. Additionally, it is worth noting that only around 30% of the hydrogens placed within a void actually stayed in an interstitial position. The remaining calculations showed that it is more likely for a neutral H to move back into the Si side (if the H was directly placed within an interfacial SiO$_2$ void) or to form some defect by breaking Si–O bonds in the oxide. The third group shows the total energy of defect configurations formed by the hydrogen atom. Such defects can be either hydroxyl–E′ centers (HE′) or [SiO$_4$/H]^0 configurations [173–175][13]. While the average energy for forming a SiO$_2$ defect is only 0.2 eV higher in energy than the BC configuration, its distribution is rather broad with 4 eV. A thorough statistical analysis including the calculation of barriers using the CI–NEB method, is, however, beyond the scope of this work. Nevertheless, the results clearly suggest that in the majority of investigated cases the Si BC site provides an energetically favorable position for the H atom, although – in the most extreme variant – forming a defect in SiO$_2$ can be up to 3 eV lower in energy.

To summarize, one can conclude that once the Si–H bond is broken and the H is released into the next but one BC site, the hydrogen atom faces a rather small *hopping* barrier to a neighbouring BC configuration and is effectively mobile along

---

[13] In around 10% of the simulations the H formed a Si–H bond by breaking an Si–O bond with a remaining oxygen dangling bond. However, these configurations have been discarded. This, however, could possibly be an artefact due to limited cell size as discussed in Appendix A

the interface. Similar results have been obtained by the group of PANTELIDES *et. al* and others [251–257]; however, they mainly focused on the migration of charged hydrogen species. They report a rather small migration barrier for H moving laterally within the subinterfacial Si region ($0.3 - 0.5\,\mathrm{eV}$), while the potential barrier to cross over into the SiO_2 side is at least twice as much. Due to the *negative-U* character of H [213, 214, 258, 259], it is indeed likely that the released hydrogen becomes charged (the BC provides a stable position for H^0 and H^+, whereas the negatively charged species prefers the AB configuration).

Additionally, the presented results potentially shed light on peculiarities of reliability issues. Once the initial Si–H bond is broken and the hydrogen released into a BC configuration, it potentially becomes charged. However, the H would be mobile along the interface and thereby possibly be able to trigger further reactions. Such a picture nicely fits into recent observations regarding reliability phenomena in MOSFETs. Occasional reports observe a peculiar feature of microelectronic devices: After removing the stress from a device, it tends to continue degrading, referred to as *post–stress degradation build–up*. Recent theoretical modeling approaches [17, 18] link this behaviour to the release of H during stress which is subsequently stored near the interface, assumed to be in a charged configuration. Such a theoretical description would be fully consistent with the conclusions drawn here.

Passivation Reactions

The actual passivation mechanism of a P_b center, however, can not be properly described by only taking into account atomic hydrogen at the interface. Instead BROWER and later also STESMANS converged to the same conclusion by performing dedicated experiments: The **passivation reaction is dominated by the cracking of molecular $\mathbf{H_2}$** [221, 222, 244]. The proposed mechanism reforms a Si–H bond by breaking a H_2 molecule, $\equiv\mathrm{Si}^\bullet + \mathrm{H}_2 \longrightarrow \equiv\mathrm{Si{-}H} + \mathrm{H}^0$, having an activation barrier of $E_\mathrm{B} = 1.51\,\mathrm{eV}$ with a Gaussian spread of $\sigma_\mathrm{B} = 0.06\,\mathrm{eV}$. Recent experimental studies conducted on a device level, where MOSFETs were stressed under various HCD bias points and subsequently annealed at elevated temperatures, confirm the proposed mechanism and activation energy [248–250]. The detailed atomistic dynamics, on the other hand, remain unclear with only a few *ab initio* based studies assessing the theoretical description [204, 206, 260]. The initial breaking of the extremely stable H_2 molecule ($E_\mathrm{bind} \sim 4.5\,\mathrm{eV}$) together with the remaining atomic hydrogen and its final configuration play a decisive role whether the passivation reaction would occur or not. Within this context interstitial H in Si and SiO_2 has been investigated [204] as well as the interaction of H_2 with defect free and defective SiO_2 to identify possible H_2 cracking sites [173, 174, 206, 260]. However, due to the multitude of different possible reactions, depending on the local environment of the amorphous oxide, no rigorous picture could be deduced so far.

In order to explore possible reactions DFT in conjunction with the NEB method has again been applied. Two different Si/SiO_2 models have been used, with in total six different interface defect configurations. A H_2 molecule has been placed in the direct vicinity and several final configurations for the remaining H including the respective barriers were calculated, see Fig. 3.22.

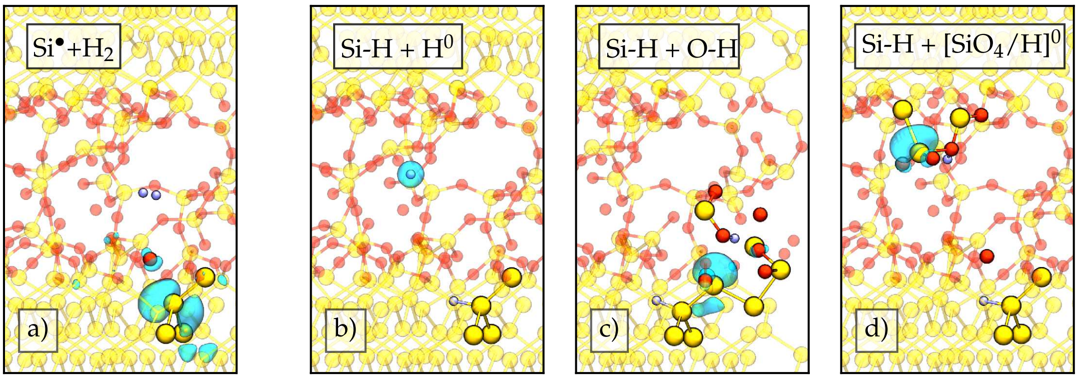

FIGURE 3.22: Passivation of an interface defect by H_2. The cyan translucent profiles show the spin density of the respective snapshots. As an initial configuration the H_2 molecule is placed in the direct vicinity of the SI–DB. Within the investigated reactions the remaining H can trigger different mechanisms leading to different final configurations. First, the neutral hydrogen becomes interstitial within the SiO_2 network. Second, the remaining H breaks a Si–O–Si complex and forms a hydroxyl E' defect. Furthermore, the last reaction shows that the H in its neutral state can also bind to a bridging oxygen and form a variant of the $[SiO_4/H]^0$ configuration.

For the first reaction the remaining hydrogen moves into a void above the formed Si–H bond and becomes interstitial neutral H. The CI–NEB calculations for all different defect configurations properly converged and yield a broad distribution of forward reaction barriers between 0.89 and 2.24 eV. The results show an apparent strong dependence on the local environment of the Si–DB defect and/or the final interstitial position. The backward barriers, on the other hand, for de–passivation reactions is much lower, suggesting that a P_b center can be effectively recreated in the excess of H atoms. Nevertheless, interstitial hydrogen can undergo further reaction dynamics in the SiO_2 network. Due to its *negative U character* [209, 261], H potentially becomes charged and binds within the oxide, e.g. a proton can attach to a bridging oxygen atom [61, 62, 174, 261, 262]. Furthermore, H^+ can effectively move through SiO_2 by hopping between bound states, as was shown in [62, 252, 263–265]. Such a hopping mechanism was recently further extended and investigated for neutral hydrogen as well [61]. Despite H's *negative U character*, in the same work it was found that H^0 indeed exhibits possible metastable neutral configurations. Furthermore, theoretical studies demonstrate the possibility of H^0 migration between voids [205, 266, 267] as well as interactions with the defect–free and defective SiO_2 matrix [173, 174]. Overall, this suggests an extremely broad spectrum of possible reactions for the remaining hydrogen moving into the SiO_2 region.

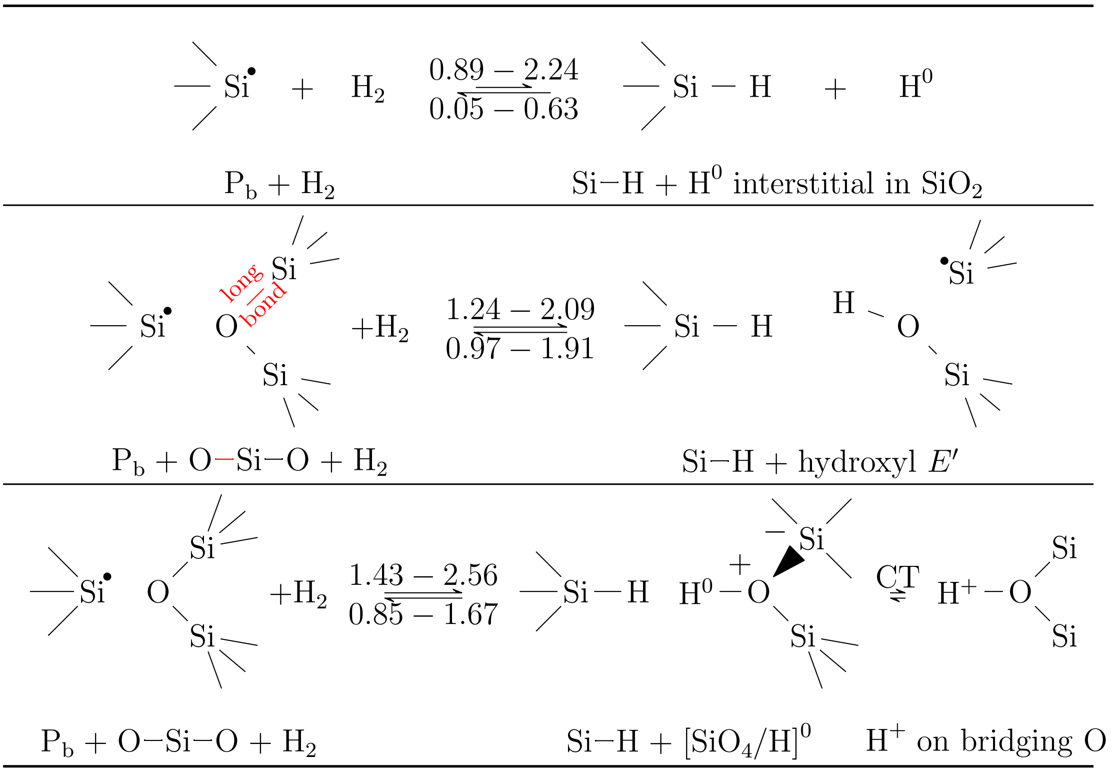

TABLE 3.1: Possible P_b center passivation reactions with H_2. For the first reaction the remaining neutral hydrogen becomes interstitial in the SiO_2 matrix, whereas reactions 2) and 3) represent defect transformations associated with the H. All energies are in eV.

In order to further investigate possible reactions of the remaining H atom, two test cases have been chosen to examine the interaction with the defect–free oxide. The first one accounts for the transformation of the remaining interstitial H^0 into a hydroxyl–E' center, see Fig. 3.22 and Reaction 2 in Table. 3.1. Out of the 15 configurations introduced into the Si/SiO_2 structure only six converged to a realistic hydroxyl–E' center configuration within a geometry optimization and have been used in subsequent NEB calculations. A common feature of the converged precursor sites is an elongated Si−O bond within the Si−O−Si unity, as indicated in Table. 3.1. The total transition barriers to break H_2, passivate a P_b center and create a hydroxyl–E' center are between 1.24 and 2.09 eV. Due to the relatively strong Si–H and O–H bonds, the backward transition barriers are of similar height, indicating that the induced final configuration would be indeed stable once the H_2 is broken.

The second possibility is schematically illustrated as Reaction 3 in Table 3.1 and shown in Fig. 3.22. Thereby, the hydrogen binds to a bridging oxygen forming a so–called $[SiO_4/H]^0$ center[14]. The structural relaxations are mainly associated with the opening of the O−Si−O angle resulting in an electron trapping site at an

---

[14] Note that in [174, 175] it was shown that the hydroxyl–E' center is thermodynamically more stable than the $[SiO_4/H]^0$ defect configuration and the transformation barrier is only around 0.1 eV.

adjacent Si atom [174]. Therefore, the defect actually resembles a proton bound to the oxygen atom where the additional electron is trapped at an adjacent Si site, see Table 3.1 and Fig. 3.22. For the simulations twelve initial defect configurations have been constructed with the H atom placed 0.8 Å away from a bridging O. Unfortunately, only three of the structures converged to a $[SiO_4/H]^0$ defect within the geometry optimizations, the remaining ones transformed into either interstitial H, hydroxyl–E' center like configurations or other odd defective formations, e.g. breaking of Si−O bonds, which have been discarded, as mentioned above. The total energy of the optimized system suggests that the stability of $[SiO_4/H]^0$ is comparable to interstitial H, whereas a hydroxyl–E' defect is usually more stable being around 0.8 eV lower in energy. The final activation energies for the full reaction starting with H_2 are given in Table 3.1. The forward reaction is slightly shifted towards higher values compared to the hydroxyl–E' center calculations, indicating a higher barrier to create the defect site, whereas the backward barrier to reform H_2 seems to be lower with values ranging from 0.85 to 1.67 eV. However, due to the rather small sample size the results can only provide a qualitative understanding. Additionally, the bound hydrogen, i.e. the $[SiO_4/H]^0$, potentially becomes positively charged via a charge transfer reaction with a reservoir which could enhance its stability resulting in a proton sticking to an oxygen [17, 62, 173].

The presented results provide a qualitative understanding and insight of the P_b center passivation kinetics. The complex and manifold reaction dynamics involving mechanisms related to charged hydrogen species allow a quantitative analysis and conclusions only at a much broader statistical level, which is beyond the scope of this work. However, already the transition barriers derived here clearly suggest that the efficiency of the H_2 passivation process heavily depends on the remaining H and its final configuration. Interstitial hydrogen for example, would most probably immediately reform H_2, particularly at elevated temperatures, due to the small backward barrier according to Reaction 1 in Table 3.1. On the other hand, due to the small migration barrier between voids in SiO_2 it could effectively diffuse away or form H related defects in the oxide which provide a sufficiently large backward barriers. Thus, the interaction of H with defect–free or defective sites in the amorphous SiO_2 system inevitably plays an important facet in understanding and describing the passivation mechanism of interface defects.

CHAPTER 4

Theoretical Approaches & Models

Electrochemical reactions triggered by a non–equilibrium carrier ensemble fundamentally define the degradation mechanisms discussed in this work. In particular *heated* carriers can provoke Si–H bond excitation at the Si/SiO_2 interface or influence the dynamics of defects in the SiO_2 via charge trapping. This Chapter addresses the key concepts introduced in Chapter 2 and establishes the theoretical descriptions relevant for the model applications in the last Chapter 5. The methods presented here are not limited to the Si/SiO_2 material system and have been used in a much broader field to understand the interactions within emerging material combinations and related phenomena.

4.1 Hot–Carriers & Interface Defects

This part of the thesis focuses on the theoretical formulation of transition rates $\Gamma_{i,f}$ between individual vibrational eigenstates of the Si–H ground state potential $V(q)$ ultimately leading to bond breakage and the creation of interface defects. The cornerstone is a consistent description of the interaction between a Si–H bond and its environment, including energetic, *hot* charge carriers. It will be shown that two major components determine the kinetics: Dynamics related to vibrational relaxation and inelastic scattering. The latter one can be split into dipole–induced transitions and excitations due to a transient population of a resonance electronic state.

System–Bath Interactions

Ideally, all dissipative and inelastic couplings leading to changes of the states in both *subsystems*[1] are taken into account. However, due to the macroscopic nature of the *bath* (the Si/SiO_2 environment), an explicit treatment of the *system's* (the Si–H bond) dynamics is desired, while the *bath* entity is implicitly described. Therefore, focussing solely on the dynamics and properties of the *system*, it is convenient to separate the total system into a *system* and *bath* entity

$$\hat{H} = \hat{H}_{\mathrm{S}} + \hat{H}_{\mathrm{B}} + \hat{V}_{\mathrm{SB}} = \hat{H}_0 + \hat{V}_{\mathrm{SB}}, \tag{4.1}$$

where $\hat{V}_{\mathrm{SB}}$ is the *system-bath* coupling operator. *Open–system–density–matrix theory* is a well suited approach for the problem at hand where the evolution of the system is described by the reduced density operator $\hat{\rho}_{\mathrm{S}}$, satisfying the open-system Liouville-von Neumann (LvN) equation [268]

$$i\hbar\frac{\partial}{\partial t}\hat{\rho}_{\mathrm{S}} = i\hbar\mathcal{L}\hat{\rho}_{\mathrm{S}}(t) = \left[\hat{H}_0, \hat{\rho}_{\mathrm{S}}(t)\right] + \int_0^t d\tau\mathcal{L}_{\mathrm{D}}(t,\tau)\hat{\rho}_{\mathrm{S}}(\tau). \tag{4.2}$$

Within this formulation the *system–bath* interaction is included in the dissipative Liouvillian (superoperator) $\mathcal{L}_{\mathrm{D}}$. However, for all practical applications the dissipative part of (4.2) needs to be approximated. Thereby, the Lindblad semigroup

---

[1] The Si–H complex and its environment

functional formulation [269] provides the most general type of a Markovian and time–homogeneous master equation preserving the laws of quantum mechanics[2]. Within this approach the *bath* modes have been already traced out resulting in equations of motion solely for the *system* part of the problem. The reduced density operator $\hat{\rho}_\mathrm{S}$ can be written as

$$\frac{\partial}{\partial t}\hat{\rho}_\mathrm{S}(t) = \mathcal{L}_\mathrm{S}\hat{\rho}_\mathrm{S} + \mathcal{L}_\mathrm{D}\hat{\rho}_\mathrm{S} = -\frac{i}{\hbar}\left[\hat{H}_\mathrm{S}, \hat{\rho}_\mathrm{S}\right] + \mathcal{L}_\mathrm{D}\hat{\rho}_\mathrm{S}, \tag{4.3}$$

where $\mathcal{L}_\mathrm{S}$ and $\mathcal{L}_\mathrm{D}$ denote the *system* Hamiltonian and the dissipative superoperator. Furthermore, utilizing the eigenstate representation of $\hat{\rho}_\mathrm{S}$, such as the eigenfunctions $|\phi_n\rangle$ of the *system* Hamiltonian, $\rho_{nm} = \langle\phi_n|\hat{\rho}|\phi_m\rangle$, allows the interpretation of the diagonal elements ρ_{nn} as the level populations P_n and the off–diagonal represents the coherences between two states.

The superoperator $\mathcal{L}_\mathrm{D}$ within the Lindbladian is given by

$$\mathcal{L}_\mathrm{D}\hat{\rho}_\mathrm{S} = \sum_k \left(\hat{C}_k\hat{\rho}_\mathrm{S}\hat{C}_k^\dagger - \frac{1}{2}\left[\hat{C}_k^\dagger\hat{C}_k, \hat{\rho}_\mathrm{S}\right]_+\right), \tag{4.4}$$

with $\hat{C}_k$ being the *Lindblad operators*, defining the nature of k dissipative channels. They account for population transfer between eigenstates of the ground state PEC $V(q)$ of the *system* due to vibrational relaxation and inelastic scattering. The Lindblad operators can be expressed as

$$\hat{C}_k = \sqrt{\Gamma_{i,f}}\,|\phi_f\rangle\,\langle\phi_i|\,, \tag{4.5}$$

which is the projection of an initial state onto a final state weighted with a rate $\Gamma_{i,f}$. The individual transition rate depends on the type of perturbation as well as on the bond complex and its properties. A general formulation is given by FGR

$$\Gamma_{i,f} = \frac{2\pi}{\hbar}\sum_{I,F} f_I(T)\left[1 - f_F(T)\right]\cdot|\langle\phi_f\Phi_F|\hat{V}|\phi_i\Phi_F\rangle|^2\delta(E_{i,I} - E_{f,F}). \tag{4.6}$$

The summations run over all collective initial I and final states F, weighted with the energy distribution function f of carriers. Furthermore, the coupling operator $\hat{V}$ specifies the nature of the perturbation, and thus the interaction strength of $|\phi_i\rangle$ and $|\phi_f\rangle$.

In the following (4.6) is used to calculate transfer rates of localized Si–H eigenstates due to various mechanisms. Contributions originating from bond vibration-phonon coupling as well as from inelastic electron tunneling are included. The latter can either arise due to dipole scattering or resonance scattering. Eventually, the total rate $\Gamma_{i,f}$ is the sum of all individual contributions:

$$\Gamma_{i,f}^\mathrm{tot} = \Gamma_{i,f}^\mathrm{vib} + \Gamma_{i,f}^\mathrm{dip,inel} + \Gamma_{i,f}^\mathrm{res,inel} \tag{4.7}$$

---

[2] i.e. it is trace preserving and completely positive by mathematical construction

Model Potential

As was shown in Section 3.2 and in [MJJ3], Si–H bond breakage at the Si/SiO$_2$ interface follows a trajectory which is a combination of the bond's bending and stretching mode. The one–dimensional PEC, where the collective ionic motion has been mapped onto a single reaction coordinate, can be assessed directly from the DFT results. For all practical applications[3], however, an analytic fit of the following form has been used:

$$V_{\mathrm{g}}(q) = v_0 q^4 - v_2 q^2 + \sigma \sqrt{\frac{v_0}{2 v_2}} q, \tag{4.8}$$

which represents an asymmetric double–well potential, see Fig. 4.1. The parameters v_0, v_2 and σ are given in Table 4.1a. Overall the (reference) potential supports two minima at $q = -3.2\,\mathrm{a}_0\sqrt{\mathrm{m}}$ and $q = 3.0\,\mathrm{a}_0\sqrt{\mathrm{m}}$ with a barrier of 2.7 eV at $q = 0$ and exhibits 32 bound states (below the barrier), localized either in the left or right well. Selected eigenstates of the ground state potential $V(q)$ are summarized in Table 4.1b. Furthermore, also the characteristics of the excited PECs are captured by the same functional form as the ground state potential, see Sec. 3.4. The negatively (positively) charged profile possesses a substantially lowered transition barrier of $\sim 1.7\,\mathrm{eV}$ ($\sim 2.1\,\mathrm{eV}$) and a shifted equilibrium position by $\sim 0.9\,\mathrm{a}_0\sqrt{\mathrm{m}}$ ($\sim 0.4\,\mathrm{a}_0\sqrt{\mathrm{m}}$), see Fig. 4.1 and Tab. 4.1a. Note that the positive potential $V^+(q)$ additionally exhibits a shifted transition point.

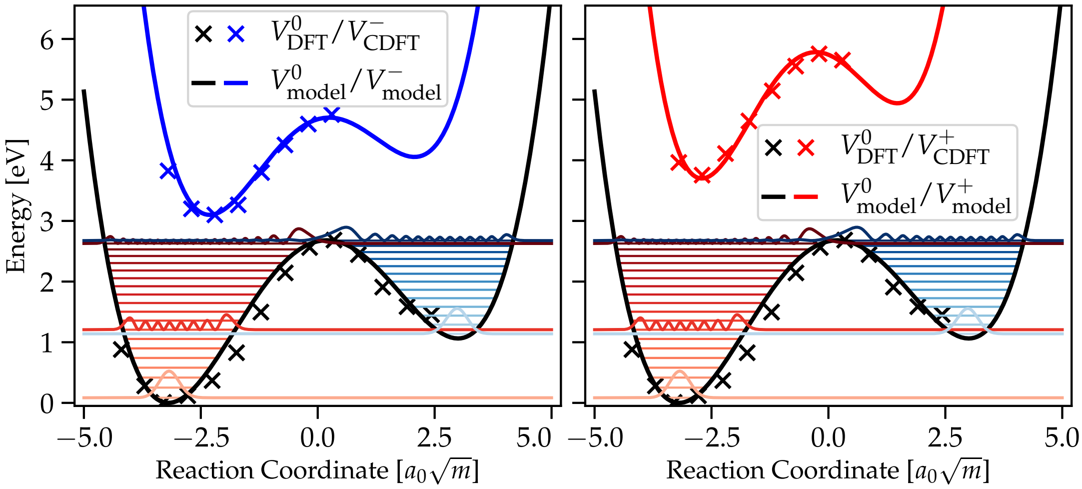

FIGURE 4.1: Model potentials for the ground and excited state potential energy curves (PECs). The left well of $V(q)$ corresponds to the initial equilibrium position of the Si–H bond, whereas the right well describes the final position of the H in the next but one bond–center site. **Left:** The ground state PEC together with the negatively charged energy profile $V^-(q)$. **Right:** The ground state potential and the corresponding PEC $V^+(q)$ when the Si–H is temporarily positively charged.

---

[3] In order to account for a distribution of paramaters, see Sec. 3.2.

	v_0	v_2	σ
$V^0(q)$	0.023	0.442	1.062
$V^-(q)$	0.046	0.459	0.955
$V^+(q)$	0.072	0.640	1.241

(A) The corresponding parameters for the ground and excited potential energy curves, see (4.8). The mean DFT data, see Sec. 3.2 and Fig. 3.12 have been used as a reference for the ground state PEC.

n	E_n (meV)	$E_{n,\mathrm{min}}$ (meV)	$E_{n,\mathrm{max}}$ (meV)
$\phi_{0,\mathrm{L}}$	84.44	73.22	113.54
$\phi_{1,\mathrm{L}}$	251.98	219.34	309.56
$\phi_{2,\mathrm{L}}$	417.25	386.72	491.47
$\vdots$	$\vdots$	$\vdots$	$\vdots$
$\phi_{6,\mathrm{L}}$	1054.09	597.78 ($\phi_{4,\mathrm{L}}$)	1724.06 ($\phi_{10,\mathrm{L}}$)
$\phi_{7,\mathrm{R}}$	1138.60	693.31 ($\phi_{5,\mathrm{R}}$)	1788.93 ($\phi_{11,\mathrm{R}}$)
$\vdots$	$\vdots$	$\vdots$	$\vdots$
$\phi_{30,\mathrm{L}}$	2627.90	2131.35 ($\phi_{26,\mathrm{L}}$)	3154.57 ($\phi_{34,\mathrm{L}}$)
$\phi_{31,\mathrm{R}}$	2675.69	2127.86 ($\phi_{25,\mathrm{R}}$)	3266.36 ($\phi_{35,\mathrm{L}}$)

(B) Selected eigenstates for the ground state potential $V^0(q)$ together with the respective energies and their localization (L/R). The minimum and maximum values for the selected states indicate the intrinsic distribution of $V^0(q)$ due to the amorphous character of the interface, see Sec. 3.2.

TABLE 4.1: **Upper**: Model potential parameters. **Lower:** Calculated eigenstates and their localization.

The analytic fits presented here do *not* aim to provide the most accurate description of the DFT results, but to give a qualitatively correct description of the ground and excited state potential energy surfaces. Due to the amorphous nature of the Si/SiO$_2$ system and the interface itself, an intrinsic distribution of the parameters such as the transition barrier and the minimum position as well as the resonance energy is to be expected, see Table 4.1b.

Dissipative Relaxation

The basic interaction between the Si–H bond and its environment can be described by the coupling of the bond potential to a *bath* of oscillators. The resulting **vibrational relaxation** rates $\Gamma_{i,f}^{\mathrm{vib}}$, and thus the lifetimes τ_i, strongly influence the bond dynamics. As already mentioned above, the reaction coordinate of Si–H breakage at a Si/SiO$_2$ interface is a combination of the Si–H bending and Si–H stretching modes. Experimental and theoretical studies, however, have focused on the vibrational relaxation of various Si–H modes on a *silicon surface*. These studies revealed lifetimes on the order of ns and ps for the stretching and bending mode [270–273], respectively. However, for the problem at hand – a mixture of various Si–H modes and a substantially different phonon spectrum – these values can only be used to derive an *educated guess* for the vibrational relaxation.

Investigating the detailed coupling between the fundamental frequency of the ground state PEC $V(q)$ and the substrate is, therefore, an essential component in the presented framework[4]. Following a perturbation theory approach allows to calculate the *system–bath* coupling elements and ultimately the transition rates using Fermi's Golden Rule, see [271, 272, 274]. By introducing a new set of coordinates one can separate the $3N$–dimensional coordinates $\mathbf{r}$ of the total system into *system* and *bath* degrees of freedom (DOF). The new DOF $\mathbf{q}$ and $\mathbf{Q}$ can be constructed using an orthogonal transformation

$$R_i = \sum_{j=1}^{3N} O_{i,j} r_j, \quad \text{with} \quad \sum_{i=1}^{3N} O_{i,k} O_{i,l} = \delta_{k,l}, \tag{4.9}$$

where $q_i = R_i (i = 1 \ldots M)$ describes the *system* coordinates and $Q_i = R_{i+M}(i = 1 \ldots 3N - M)$ corresponds to the *bath* modes. The total Hamiltonian can be decomposed in the usual *system–bath* form:

$$\hat{H} = \hat{H}_S + \hat{H}_{SB} + \hat{H}_B, \tag{4.10}$$

with the individual contributions of the *system*, *bath* and the *system–bath* coupling given by:

$$\begin{aligned}
\hat{H}_S &= -\frac{\hbar^2}{2} \sum_{i=1}^{M} \frac{\partial^2}{\partial q_i^2} + V(\mathbf{q}, \mathbf{Q} = 0), \\
\hat{H}_{SB} &= \sum_{i=1}^{3N-M} \lambda_i(\mathbf{q}) Q_i + \frac{1}{2} \sum_{i,j=1}^{3N-M} \Lambda_{i,j}(\mathbf{q}) Q_i Q_j, \\
\hat{H}_B &= \sum_{i=1}^{3N-M} \big(-\frac{\hbar^2}{2} \frac{\partial^2}{\partial Q_i^2} + \frac{1}{2} \omega_i^2 Q_i^2 \big).
\end{aligned} \tag{4.11}$$

The one– and two–phonon coupling functions $\lambda_i(\mathbf{q})$ and $\Lambda_{i,j}(\mathbf{q})$ (corresponding to one– and two–phonon relaxations) can be obtained by calculating the derivative of $V(\mathbf{q}, \mathbf{Q})$ as

$$\begin{aligned}
\lambda_i(\mathbf{q}) &= \frac{\partial V}{\partial Q_i}\Big|_{\mathbf{q},\mathbf{Q}=0} = \sum_{k=1}^{3N} O_{M+i,k} \frac{\partial V}{\partial r_k}\Big|_{\mathbf{q},\mathbf{Q}=0}, \\
\Lambda_{i,j}(\mathbf{q}) &= \frac{\partial^2 V}{\partial Q_i \partial Q_j}\Big|_{\mathbf{q},\mathbf{Q}=0} = \sum_{k,l}^{3N} O_{M+i,k} O_{M+j,l} \frac{\partial^2 V}{\partial r_k \partial r_l}\Big|_{\mathbf{q},\mathbf{Q}=0}.
\end{aligned} \tag{4.12}$$

---

[4] Note that in a fully rigorous approach the 2D potential energy surface (PES $V(\boldsymbol{q})$) of the Si–H bond would be considered, which effectively enables coupling between the low–energy bending and the high–energy stretching modes, see [270]. However, this requires a well–parametrized 2D PES which is outside of the scope of this work.

These couplings are used within Fermi's Golden Rule (FGR) to compute the phonon–induced transition rates between *system* eigenstates ϕ_i and ϕ_f as

$$\Gamma_{i,f} = \frac{2\pi}{\hbar} |\langle \Phi_f | \hat{H}_{\mathrm{SB}} | \Phi_i \rangle|^2 \delta(E_i - E_f), \tag{4.13}$$

where one can choose the initial and final states Φ_i and Φ_f as product states of *system* and *bath* states which can be integrated out. Thermal averaging over the initial states and summing over the final *bath* states allows to account for the thermal population of bath oscillator at finite temperature ($T \neq 0\,\mathrm{K}$) and the respective upward rates.

Following [270, 272, 273, 275], and in particular the derivation in [274], the **one–phonon** coupling term in (4.11) and (4.12) yields the following rate expressions

$$\begin{aligned} \Gamma_{i,f}^{(1),\downarrow} &= \pi \sum_k |\langle \phi_i | \lambda_k(\mathbf{q}) | \phi_f \rangle|^2 \frac{\langle n_k \rangle + 1}{\omega_k} \delta(\varepsilon_i - \varepsilon_f - \hbar\omega_k) \\ \Gamma_{i,f}^{(1),\uparrow} &= \pi \sum_k |\langle \phi_i | \lambda_k(\mathbf{q}) | \phi_f \rangle|^2 \frac{\langle n_k \rangle}{\omega_k} \delta(\varepsilon_i - \varepsilon_f + \hbar\omega_k), \end{aligned} \tag{4.14}$$

where $\langle n_k \rangle = \sum_n n p_{n,k}(T)$ is the thermally averaged quantum number of the kth bath mode with $p_{n,k}(T)$ being the thermal population of its nth level. However, if the energy of the system mode is above $\omega_{\max}$, the highest phonon frequency, **two–phonon** terms become important. The corresponding rates for the simultaneous (de–) excitation of two different bath modes are given by

$$\begin{aligned} \Gamma_{i,f}^{(2a),\downarrow} &= \frac{\pi\hbar}{8} \sum_{k \neq l} |\langle \phi_i | \Lambda_{k,l}(\mathbf{q}) | \phi_f \rangle|^2 \frac{\langle n_k \rangle + 1}{\omega_k} \frac{\langle n_l \rangle + 1}{\omega_l} \delta(\varepsilon_i - \varepsilon_f - \hbar\omega_k - \hbar\omega_l), \\ \Gamma_{i,f}^{(2a),\uparrow} &= \frac{\pi\hbar}{8} \sum_{k \neq l} |\langle \phi_i | \Lambda_{k,l}(\mathbf{q}) | \phi_f \rangle|^2 \frac{\langle n_k \rangle}{\omega_k} \frac{\langle n_l \rangle}{\omega_l} \delta(\varepsilon_i - \varepsilon_f + \hbar\omega_k + \hbar\omega_l) \end{aligned} \tag{4.15}$$

whereas the expression for two identical bath modes is

$$\begin{aligned} \Gamma_{i,f}^{(2b),\downarrow} &= \frac{\pi\hbar}{8} \sum_k |\langle \phi_i | \Lambda_{k,k}(\mathbf{q}) | \phi_f \rangle|^2 \frac{\langle n_k^2 \rangle + 3\,\langle n_k^2 \rangle + 2}{\omega_k^2} \delta(\varepsilon_i - \varepsilon_f - 2\hbar\omega_k) \\ \Gamma_{i,f}^{(2b),\uparrow} &= \frac{\pi\hbar}{8} \sum_k |\langle \phi_i | \Lambda_{k,k}(\mathbf{q}) | \phi_f \rangle|^2 \frac{\langle n_k^2 \rangle - \langle n_k^2 \rangle}{\omega_k^2} \delta(\varepsilon_i - \varepsilon_f + 2\hbar\omega_k) \end{aligned} \tag{4.16}$$

For the sake of completeness two–phonon processes also give rise to the simultaneous creation and annihilation of phonons, however, this contribution can be neglected [274]. For all practical applications at finite temperatures, the delta–functions in (4.14), (4.15) and (4.16) need to be replaced by functions with a finite broadening, e.g. Lorentzians

$$\delta(E) \rightarrow \frac{1}{\pi} \frac{\gamma}{\gamma^2 + E^2}, \tag{4.17}$$

with the broadening parameter γ.

The studied system is again the Si(100)/a–SiO$_2$ interface system containing 472 atoms for which the Si–H system mode has been identified in Chap. 3 and in [MJJ3] using DFT. However, using DFT to calculate the coupling terms (4.12) would have made the calculations prohibitively expensive since these couplings need to be calculated at various *system* coordinates $\boldsymbol{q}$. Thus, all linear and quadratic coupling terms (4.14), (4.15) and (4.16) have been calculated using the classical ReaxFF force–field [197] implemented in the LAMMPS code [198]. A comparison of the phonon spectrum calculated with DFT and the classical force–field for the Si/SiO$_2$ interface system, as well as for bulk crystalline Si and bulk SiO$_2$ is given in Fig. 4.2. One can see that ReaxFF is able to qualitatively reproduce the spectra calculated with DFT, albeit the individual spectra seem to extend towards higher energies. Surprisingly, the agreement between both methods is best for the most complex Si/SiO$_2$ model.

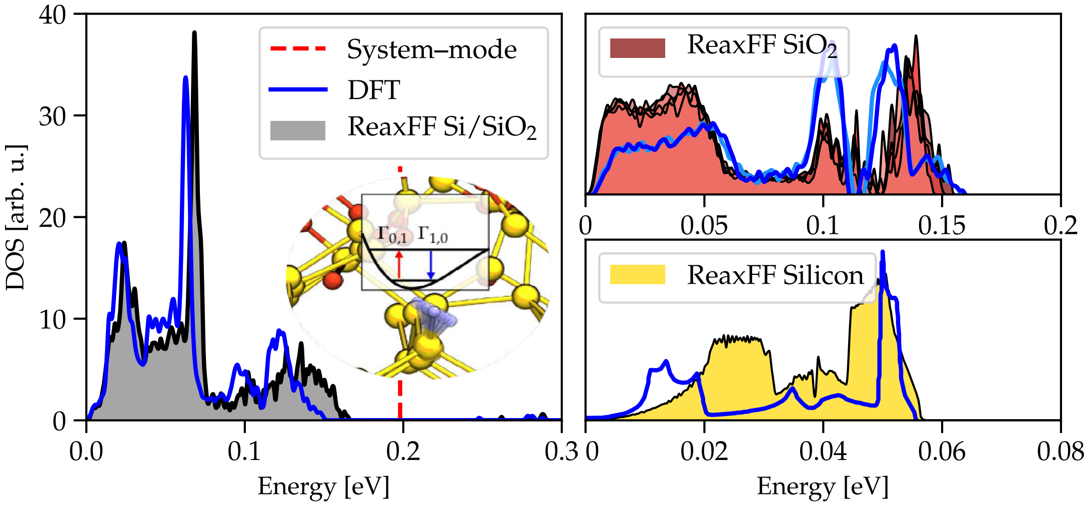

FIGURE 4.2: Phonon density of states for various systems calculated with DFT and the classical ReaxFF force–field to validate its applicability. **Left:** The vibrational spectrum of a Si/SiO$_2$ model together with the initial Si–H system motion and the respective eigenmode. **Right:** Further benchmarks against bulk models of silicon and SiO$_2$. Note that five different a–SiO$_2$ realizations have been calculated using ReaxFF and two models with DFT to also capture possible distributions of the spectra. While the DFT results yield a rather unique result, the classical potential shows a slightly broader distribution of phonon spectra.

The vector $\mathbf{e}_q$, which serves as the degree of freedom for the system mode q and defines its fundamental frequency, see Fig. 4.2, has been identified using the results presented in Sec. 3.2. Furthermore, for all subsequent calculations its $3N$ components representing the system motion have been restricted to atoms with displacements of at least 5% of the maximum displacement, all the other entries were set to zero. This was done to avoid an artificially large coupling due to the finite cluster size. In order to ensure orthogonality between the system mode vector $\mathbf{e}_q$ and the environment modes $\mathbf{e}_Q$, $3N$-1 random $3N$ dimensional vectors $\mathbf{u}_i$ have been selected. Subsequently, the system $(\mathbf{e}_q, \mathbf{u}_i)$ was orthogonalized and a

$(3N-1)\times 3N$ transformation matrix $\mathbf{U}$ was constructed using the orthogonalized vectors $\mathbf{u}_i$. The matrix $\mathbf{U}$ has been further used to transform the $3N\times 3N$ Hessian $\mathbf{H}=(\partial^2 V/\partial\mathbf{x}\partial\mathbf{x})|_0$ into a constrained (a subspace orthogonal to the system mode) $(3N-1)\times(3N-1)$ Hessian given by

$$\mathbf{H}'=\mathbf{U}\mathbf{H}\mathbf{U}^T, \tag{4.18}$$

which upon diagonalization yields $3N-1$ constrained bath normal modes $\mathbf{e}'_Q$, each of length $3N-1$. Using the inverse transformation

$$\mathbf{e}_Q=\mathbf{U}^T\mathbf{e}'_Q, \tag{4.19}$$

finally gives $3N-1$ bath mode vectors with a length of $3N$. This approach guarantees one anharmonic system mode, represented by $\mathbf{e}_q$, and $3N-1$ harmonic bath modes, $\mathbf{e}_Q$, all being orthogonal to each other, $\mathbf{e}_{Q_i}\mathbf{e}_{Q_j}=\delta_{i,j}$ and $\mathbf{e}_{Q_i}\mathbf{e}_q=0$, see [274].

The calculations for all individual one– ($\Gamma^{(1)}$) and two–phonon transition ($\Gamma^{(2)}$) rates have been conducted along the anharmonic system DOF $\mathbf{e}_q$ at 31 displacements $\mathbf{q}=q\mathbf{e}_q$ within the interval $[-0.75,+0.75]a_0\sqrt{m}$. Such a variation of $\mathbf{e}_q$ is sufficient to cover at least the lowest eigenstates. Ultimately, the described procedure yields the vibrational lifetime of the fundamental transition which is given by:

$$\tau_1^{-1}=\left(\Gamma_{1,0}^{(1),\downarrow}+\Gamma_{1,0}^{(2),\downarrow}\right)-\left(\Gamma_{0,1}^{(1),\uparrow}+\Gamma_{0,1}^{(2),\uparrow}\right). \tag{4.20}$$

The final result together with the individual contributions is summarized in Table 4.2. One can clearly see that the total lifetime τ_1^{total} is dominated by a two–phonon relaxation process. One–phonon transition rates are around one order of magnitude smaller, however, their origin is questionable. Such relaxations are actually energy–forbidden and only arise as a direct consequence of the finite broadening used to replace the delta–functions in (4.17). Therefore, these contributions should be completely discarded. Furthermore, the dependence of the rates on the broadening parameter γ has been investigated as well. While $\Gamma_{1,0}^{(1)}$ exhibits a strong dependence between $\gamma\in[1,10]\text{cm}^{-1}$ ($\tau_1^{(1)}=18.3\,\text{ns}-1.89\,\text{ns}$), $\Gamma_{1,0}^{(2)}$ is stable against changes in γ ($\tau_1^{(2)}=152.9\,\text{ps}-97.5\,\text{ps}$). Since the latter is the dominant contributor, the overall solution is not very sensitive to the precise choice of the *fitting* parameter γ, provided γ is chosen in a physically reasonable range.

Further insight into the dissipation mechanism can be gained by analyzing the two–phonon process in detail. Fig. 4.3 shows the individual contribution of phonon pairs $\{\omega_k,\omega_l\}$ within a 2D–histogram with a bin size of $5\,\text{cm}^{-1}\times 5\,\text{cm}^{-1}$. One can see a pronounced dissipation pathway via two similar phonons ($\omega_k\sim\omega_l$). However, as an alternative route, two phonons which in total fit $\Delta E_{1,0}$ can be seen as well in Fig. 4.3. Additionally, the lifetime τ_1 and its temperature dependence is shown in the right panel of Fig. 4.3. The decreasing lifetime with increasing temperature is a consequence of temperature–dependent weight factors in the rate expressions based on Fermi's Golden Rule and also temperature–dependent upwards rates $\Gamma_{0,1}^{\uparrow}$. For the sake of completeness, Fig. 4.3 also illustrates the influence of the

Mode	T [K]	τ_1^{total}	$\Gamma_{1,0}^{(1)}$	$\tau_1^{(1)}$	$\Gamma_{1,0}^{(2a)}$	$\Gamma_{1,0}^{(2b)}$	$\tau_1^{(2)}$
Si–$\text{H}_{\text{break}}^{1\to 0}$	0	0.1237	0.1930	5.1801	7.3745	0.5101	0.1268
	300 (↓)	0.1180	0.2116	4.9531	7.7452	0.5244	0.1209
	300 (↑)		0.0098		0.0009	0.0001	
Si–$\text{H}_{\text{break}}^{2\to 1}$	0	46.344	0.4238	2.359	19.9757	1.1779	47.273

TABLE 4.2: Calculated vibrational lifetimes (τ_1^{total}, $\tau_1^{(1)}$ and $\tau_1^{(2)}$) together with the corresponding rates ($\Gamma_{1,0}^{(1)}$, $\Gamma_{1,0}^{(2a)}$ and $\Gamma_{1,0}^{(2b)}$) for the first excited system–mode and two different temperatures. The units for the lifetimes and rates are ns and ns^{-1}, respectively. The last line shows the one– and two–phonon rates and lifetime calculated for the Si–H_{break} mode for the 2 → 1 transition.

only free parameter within the above framework, γ, (4.13), as described above. Based on the results $\gamma = 5\,\text{cm}^{-1}$ has been chosen as the reference here[5], which yields $\tau_{0\text{K}} = 0.126\,\text{ns}$ ($\tau_{300\text{K}} = 0.120\,\text{ns}$).

In practice, the model potential possesses overall 32 bound states for both wells, see Section 4.1, for which it would be necessary to calculate all individual relaxation rates $\Gamma_{i,f}$, ideally using the approach described here. However, for the problem at hand, the next vibrational state already yields an energy difference to the vibrational ground state $\Delta E_{2,0} > 2\hbar\omega_{\text{max}}$, which is beyond the two–phonon coupling included[6]. Therefore, for all practical applications an idealized harmonic model [101, 105, 270, 276] can be employed where the selection rule $\Delta n = \pm 1$ applies. Such a harmonic model possesses a linear scaling law $\Gamma_{i,i-1}^{\downarrow} = i\Gamma_{1,0}^{\downarrow}$ and has been demonstrated to show reasonable agreement with accurate calculations even for anharmonic system–modes [105, 270, 276]. In order to estimate the introduced error and further motivate this approximation, the one– and two–phonon rates as well as the lifetimes for the 2 → 1 transition have been calculated, see Table 4.2. Since the energy difference $\Delta E_{2,1}$ is still outside the Si/SiO$_2$ phonon band, $\Gamma_{2,1}^{(2)}$ again dominates the resulting lifetime. Furthermore, it is very likely that the direct transition 2 → 0 is less important, due to the fact that at least three bath modes are necessary to dissipate the energy[7]. Finally, one can see in Tab. 4.2 that the resulting lifetime of $\tau_2 = 46\,\text{ps}$ agrees well with the simple model prediction of $\tau_2 = \tau_1/2 = 61.5\,\text{ps}$.

Mapping the harmonic scaling law onto the double well model potential introduced above splits $V(q)$ into two harmonic oscillators where only *neighbouring transitions within* one well are allowed, whereas transitions between the oscillator

---

[5] The calculations show an approximated deviation of ±25% compared to $\gamma = 1\,\text{cm}^{-1}/10\,\text{cm}^{-1}$.

[6] Or by including excited vibrational states of the 2D potential surface, see 3.2.

[7] The inclusion of a three phonon term in the system–bath Hamiltonian is proportional to $Q_iQ_jQ_k$ which would render the calculation of the coupling element $\kappa_{i,j,k}$ computationally extremely challenging.

are prohibited. The corresponding single–phonon scaling law for the vibrational lifetime of an eigenstate $|\phi_n\rangle$ is then given by

$$\tau_n = \frac{\tau_1}{n}, \tag{4.21}$$

with τ_1 being the lifetime of the first eigenstate as calculated above.

A detailed comparison of the utilized methods including the ReaxFF potential to well established results associated with the Si–H bending mode is given in Appendix D.

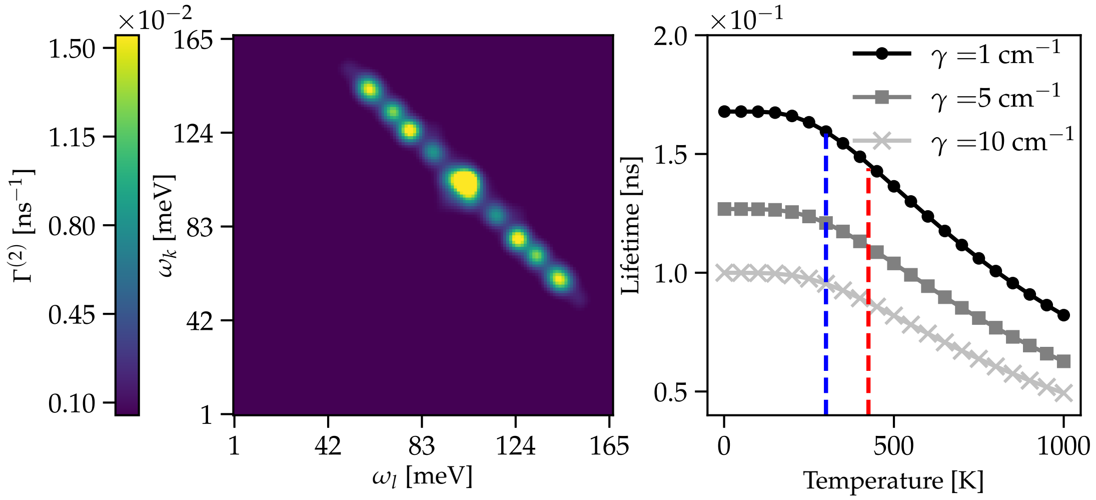

FIGURE 4.3: Detailed insight into the vibrational dissipation mechanisms. **Left:** The composition of the two–phonon transition rate $\Gamma^{(2),\downarrow}_{1,0}$ for pairs of phonons $\{\omega_k, \omega_l\}$ with a bin size of $5\,\mathrm{cm}^{-1} \times 5\,\mathrm{cm}^{-1}$. **Right:** The lifetime of the first vibrational eigenstate over a wide range of temperatures and for different broadening parameters γ.

Dipole Scattering

Next, one can consider the rate expressions for inelastic excitation channels which are usually induced due to *external* perturbations. As already mentioned in the experimental Section 2.1, one inelastic process is related to the electric field caused by moving electrons. The resulting field can interact with the dipole created by the vibration of the adsorbate complex and induce transitions between vibrational eigenstates. The **dipole scattering** rate can be described due to an electrostatic coupling to the transition dipole moment $\boldsymbol{\mu}$ and can be calculated by a formula derived by Persson *et al.* [277–279]

$$\Gamma^{\mathrm{dip}}_{i,f} = \frac{I}{e} \left| \frac{\langle \phi_f | \boldsymbol{\mu} | \phi_i \rangle}{e a_0} \right|^2, \tag{4.22}$$

where e is the elementary charge, a_0 the Bohr radius, $\hat{\mu}$ the dipole moment and I the current. Using the dipole moment vector extracted in Sec. 3.3, in particular the

x and y component due to the current density in the channel of a MOSFET being parallel to the (100) surface, one can estimate the importance of this component. The dipole–induced transition rates $\Gamma_{i,f}^{\mathrm{dip}}$ for $i \Rightarrow i+1$ and $i \Rightarrow i+2$ transitions have been calculated for different currents and compared to the vibrational upward rates $\Gamma_{i,f}^{\mathrm{vib}}$[8] at $T = 300\,\mathrm{K}$, see Fig. 4.4. Current densities in scaled MOSFETs already exceed $100\,\mathrm{nA/nm^2}$, which is of similar order as tunneling currents in Si–H related STM experiments ($1-10\,\mathrm{nA}$), assuming that the STM electron beam is of atomic dimensions. One can see that only at higher currents the respective upward rates for $\Delta n = +1$ are mainly determined by dipole induced scattering, whereas transitions to higher excited states ($\Delta n = +2$) are already orders of magnitude lower. Although Fig. 4.4 actually shows a non–negligible contribution of $\Gamma_{i,f}^{\mathrm{dip}}$, the importance of dipole–induced excitations is limited in hot–carrier related device reliability issues. Only at the source side, where carriers are still close to equilibrium, but a high current density is present, they potentially play a (minor) role. Nevertheless, starting from the channel region, carriers have already gained enough energy to (potentially) scatter into an available resonance which clearly dominates the upward transitions.

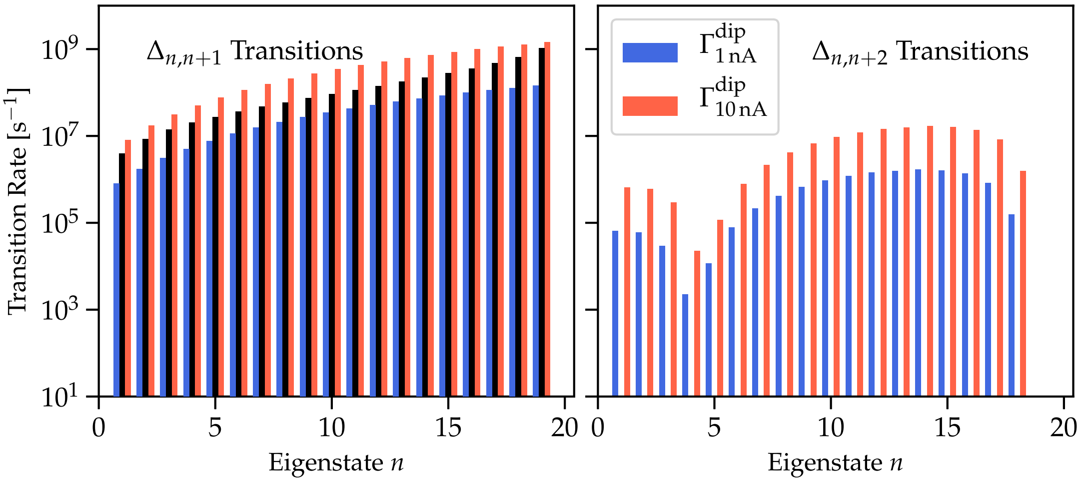

FIGURE 4.4: Comparison of dipole–induced upward rates $\Gamma_{i,f}^{\mathrm{dip}}$ (red and blue bars) and vibrational upward rates $\Gamma_{i,f}^{\mathrm{vib}}$ (black bars) at $T = 300\,\mathrm{K}$ for different currents. **Left:** Neighbouring transitions $\Delta_{n,n+1}$. **Right:** $\Delta_{n,n+2}$ transitions induced by dipole scattering are already lower by two orders of magnitude.

Resonance Scattering

As already mentioned in Section 2.1 another possible excitation channel is related to adsorbate resonances. A **resonance scattering** model accounts for carriers tunneling into available molecular orbitals (MOs) of the adsorbate. In the case of the Si–H bond the resonance states are associated with the LUMO (HOMO),

---

[8] $\Gamma_{i,f}^{\mathrm{vib}}$ are only available for $\Delta n \pm 1$ transitions, see Sec. 4.1.

forming a temporal negative (positive) ion resonance. The modified internuclear potential thereby induces a nuclear relaxation of the system. When the electron returns to the substrate an inelastic relaxation process transfers energy to the *system*, leaving the neutral ground state PEC $V(q)$ in a vibrationally excited state. Two formulations of a vibrational heating model for this mechanism have been developed: an *incoherent* multiple single-step process [280] and a theory of *coherent* multiple vibrational excitations [281]. Both variants are schematically illustrated in Fig. 4.5.

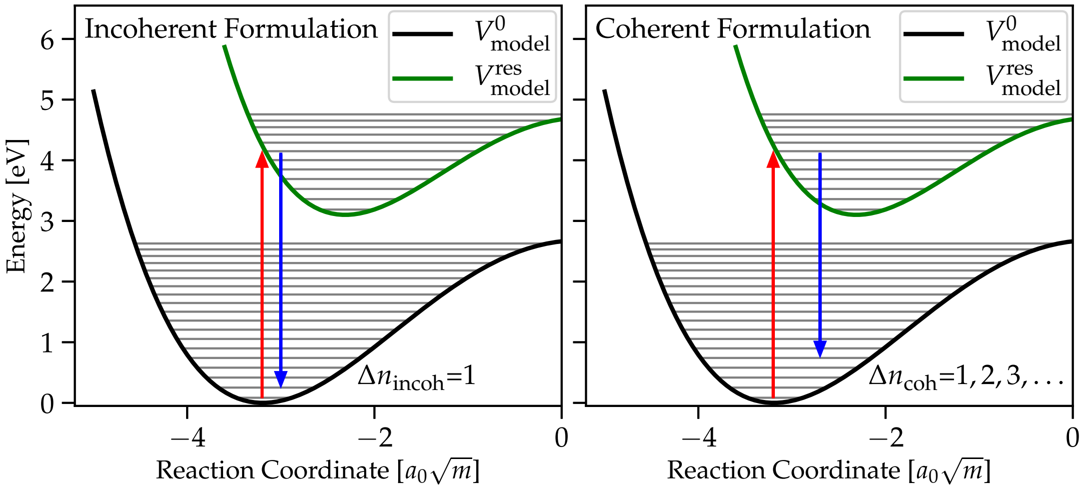

FIGURE 4.5: Schematics showing the two different vibrational heating models describing a resonant scattering interaction of tunneling carriers. In a first step an incident carrier creates a negatively or positively charged complex by temporarily occupying a resonance state. **Left:** Incoherent multiple single–step process. Each carrier is only able to transfer *one* quantum of energy during the inelastic relaxation process. Such a subsequent ladder–climbing mechanism requires n scattering carriers, where n is the number of eigenstates in the potential. **Right:** The coherent multiple vibrational excitation formulation allows for *overtone* transitions. Hence it facilitates a shorter excitation path and fewer interacting carriers.

Whereas the *incoherent* model requires a rather high current density (scattering electrons) compared to the vibrational lifetime, the *coherent* formulation accounts for overtone transitions which results in an excitation path with a smaller number of intermediate states [282, 283]. Recent results [119] have shown that indeed fewer electrons are needed to dissociate H than expected from the *incoherent* formulation and support the *coherent* formulation proposed by PERSSON *et al.* [284] and SALAM *et al.* [281]. The utilized expression within this work for the transition rates is therefore based on the above descriptions and was already applied to similar problems [285] as discussed here.

In this formulation it is assumed that an electron with incident energy ϵ can induce an excitation from state $|\phi_i\rangle$ to $|\phi_f\rangle$ via the vibrational eigenstate $|\psi_j\rangle$ of the resonance with

$$\Gamma_{i,f}^{\text{res}} = \frac{4\Delta_{\text{res}}^2}{\pi\hbar} \int d\epsilon f(\epsilon)\,[1 - f(\epsilon)] \cdot |\sum_j \frac{\langle\phi_f|\psi_j\rangle\,\langle\psi_j|\phi_i\rangle}{\epsilon_{\text{res}} - \epsilon + \epsilon_i - \epsilon_j + i\Delta_{\text{res}}}|^2. \tag{4.23}$$

This expression includes the energetic position of the resonance with respect to the Fermi level, ϵ_{res}, its width as the inverse of the resonance lifetime, $\Delta_{\text{res}} = \hbar/\tau_{\text{res}}$, as well as the energies of the eigenstates $|\phi_i\rangle$ and $|\psi_j\rangle$. Furthermore, it accounts for the energy distribution function $f(\epsilon)$ of charge carriers at the interface, which is a crucial ingredient as pointed out in the Outline, see the Chapters 1 and 2, of this thesis. All parameters entering the above formula can be extracted (or at least reasonably approximated) from DFT results, see Chap. 3.

Model Formulation

Based on the theoretical treatment introduced above, a model for describing hot-carrier induced damage at the Si/SiO$_2$ interface can be developed. The approach includes all the aforementioned processes, namely the vibrational relaxation mechanism, (4.13) and (4.21), as well as the inelastic channels, dipole, (4.22), and resonance scattering, (4.23). The total transition rate from the vibrational eigenstate $|\phi_i\rangle$ to $|\phi_f\rangle$ of the Si–H *system* is given by (4.7).

Experimental quantification of HCD is done on a macroscopic timescale. The device is stressed above operating conditions between seconds and hours to extract a gradual change of the device characteristic to ultimately evaluate its lifetime. On the other hand, the Si–H *system* interacting with the *environment* will tend towards a steady state on a much faster timescale, within femto– to nanoseconds. Thus, the time scales can be separated and only a quasi-equilibrium solution of (4.3) is required

$$\frac{\partial\rho_{\text{S}}}{\partial t} = \mathcal{L}_{\text{S}}\rho_{\text{S}} + \mathcal{L}_{\text{D}}\rho_{\text{S}} = 0, \tag{4.24}$$

to calculate the population P_i of each individual vibrational state of the *system*. Once the new equilibrium of the ground state potential $V(q)$ is known, one can calculate the bond breaking rate, defined as the transition from the left to the right well in the ground state potential, see Fig. 4.1, as tunneling rates through a potential barrier, employing the WKB–aproximation:

$$\Gamma^{\text{break}} = \sum_i \Gamma_{i,\text{WKB}}\, P_i = \sum_i \exp\big(-\frac{2}{\hbar}\int\limits_{x_{1,i}}^{x_{2,i}} \sqrt{2(V - E_i)}\text{d}x\big)\, P_i, \tag{4.25}$$

with P_i being the population of the eigenstate i and $\Gamma_{i,\text{WKB}}$ the tunneling rate which takes the classical turning points x_1 and x_2 for the respective energy levels E_i into account. Within this approach only eigenstates localized in the left well are considered by implicitly projecting out all $|\phi_{\text{R}}\rangle$ in the above calculation. A more detailed description of how to calculate the final rate Γ^{break} is given in Appendix E.

Knowing the bond–breaking rate Γ^{break} allows to formulate a reaction equation for the evolution of the concentration of broken and intact Si–H bonds with stress time. Two states for the forward reaction can be assumed, see Secs. 3.2 and [MJJ3], which is in analogy to previous observations [35, 201, 244], an intact Si–H bond (left well) and a broken state (right well) described as a P_b center and the released H atom. Once the hydrogen is in the next but one bond–center site, it is likely that it is mobile *along* the interface, see Sec. 3.6 and [251, 253, 254], facing a rather small barrier for *hopping* laterally within the subinterfacial Si region. Thus, once the H is released, it potentially triggers an additional reaction, e.g. the formation of defects or H_2. The backward reaction, on the other hand, passivating the defect with one hydrogen, is assumed to proceed via a different reaction pathway, namely by breaking an H_2 modelcule, see 3.6 and [201, 221, 248].

The reaction equation including the aforementioned chemical reactions is therefore

$$\frac{\mathrm{d}\,[\mathrm{SiH}]}{\mathrm{d}t} = -\Gamma^{\mathrm{break}}\,[\mathrm{SiH}] + \Gamma^{\mathrm{pass}}\,[\mathrm{H}_2]\,[P_\mathrm{b}]\,, \tag{4.26}$$

where Γ^{pass} describes cracking of H_2 and the subsequent passivation of P_b centers. According to [221, 222, 244, 248] this process is purely thermally activated and the rate constant is given by an Arrhenius equation $\Gamma^{\mathrm{pass}} = \Gamma_0^{\mathrm{pass}}\exp(-E_{\mathrm{pass}}/k_\mathrm{B}T)$ superimposed with a Gaussian distribution of the passivation energy E_{pass}[9]. The inferred parameters are $E_\mathrm{p} \sim 1.51\,\mathrm{eV}$, $\sigma_{E_\mathrm{p}} \sim 0.12\,\mathrm{eV}$ and $\Gamma_0^{\mathrm{pass}} \sim 5\times10^{-6}\,\mathrm{cm}^3/\mathrm{s}$[10], which were also used in a recent study to model the recovery of HCD induced damage in an actual MOSFET [248, 249]. In addition, one equation describing the maximum number of pristine Si–H bonds is introduced as

$$[\mathrm{SiH}] + [\mathrm{H}] = [\mathrm{H}]_{\mathrm{tot}}\,, \tag{4.27}$$

while the value for $[H_2]$ was set to a constant concentration of $5\times10^{17}\,\mathrm{cm}^{-3}$, given by the physical solubility of H_2 in vitreous silica [286]. Introducing the quantity $\mathrm{N}_0 \mathrel{\widehat{=}} [\mathrm{SiH}]_{\mathrm{max}}$ and solving for $f_{\mathrm{Pb}} \mathrel{\widehat{=}} [\mathrm{P_b}]/\mathrm{N}_0 = 1 - [\mathrm{SiH}]/\mathrm{N}_0$, the probability that a bond is broken is then given by

$$\frac{\partial f_{\mathrm{Pb}}}{\partial t} = (1 - f_{\mathrm{Pb}})\,\Gamma^{\mathrm{desorb}} - f_{\mathrm{Pb}}\Gamma^{\mathrm{pass}}[\mathrm{H}_2]. \tag{4.28}$$

In order to represent the density of bonds at the Si/SiO_2 interface, it is necessary to randomly sample the normally distributed quantities of the Si–H bond and scale them according to the technology dependent pristine density N_0, which is, virtually, the only *fitting* parameter in our model.

Relation & Connection to Previous Models

The framework introduced above is computationally challenging compared to previously used TCAD models describing degradation phenomena, in particular due

---

[9] Recent studies show that also an applied gate bias substantially influences the recovery dynamics [249, 250]. It is assumed that the Fermi level affects the defects charge state and hence the passivation barrier.

[10] Note that while the reported passivation barrier E_{pass} is consistent throughout the literature, the reaction rate constant Γ_0^{pass} varies between 10^{-4} and $10^{-9}\,\mathrm{cm}^3/\mathrm{s}$.

to the need to randomly sample the rather large parameter space together with the numerical solution for the energy profiles. In order to decrease its complexity and simultaneously increase the usability of the model within TCAD tools, further approximations can be applied. The ground and resonance potential profiles $V(q)$ and $V^-(q)/V^+(q)$ can be approximated using harmonic potentials, see the right panel of Fig. 4.6. Within this simplification the proposed resonance scattering formalism, see Sec. 4.1, is still valid. A charged carrier with an incident energy ϵ triggers a vibrational excitation from state $|\phi_i\rangle$ to $|\phi_f\rangle$ in the ground state $V(q)$ via the eigenstate $|\psi_j\rangle$ of the resonance. Comparing the resonance based description using harmonic potentials to previous modeling attempts by HESS [47, 49, 50, 52], BRAVAIX [34, 53, 56] and TYAGINOV [MJJ5, 35, MJJ12, MJC13, MJC16, MJC4] reveals an unambiguous connection. Obviously, the coherent formulation of the inelastic resonance scattering mechanism, see Sec. 4.1, naturally maps the single particle (SP) and multiple particle (MP) mechanisms discussed in Chapter 2 onto a single fundamental excitation channel. Furthermore, the analogy allows to reinterpret previous formulations in a physically meaningful context. For instance the model developed by TYAGINOV *et al.* uses the so–called *Acceleration Integral* to calculate the corresponding SP and MP transition rates

$$\Gamma_{\mathrm{MP/SP}} = \int_{\epsilon_{\mathrm{th}}} f(\epsilon)g(\epsilon)v(\epsilon)\sigma_{\mathrm{MP/SP}}(\epsilon)\mathrm{d}\epsilon, \tag{4.29}$$

where $f(\epsilon)$ is the EDF, $g(\epsilon)$ the DOS, $v(\epsilon)$ corresponds to the carrier velocity and $\sigma(\epsilon)$ is a phenomenologically derived capture cross section. The threshold energy, i.e. the minimum carrier energy needed to trigger the respective mechanism, is denoted as ϵ_{th}. The energy dependent cross section is assumed to follow an empirical Keldysh–like expression $\sigma(E) = \sigma_0(\epsilon - \epsilon_{\mathrm{th}})^p$ with $p_{\mathrm{MP}} = 1$ and $p_{\mathrm{SP}} = 11$. Various exponents have been extracted in the literature, depending on the actual implementation of the utilized model, and have been initially used to capture the multiple dependencies of HCD [33–35, MJJ12, 53, 57]. Using the quantum–chemistry formulation described within this work allows to reformulate (4.29) in terms of a single physical mechanisms

$$\Gamma_{i,f} = \frac{4\Delta_{\mathrm{res}}^2}{\pi} \int_{\epsilon} f(\epsilon)g(\epsilon)v(\epsilon)\sigma_{\mathrm{eff}}(\epsilon)\mathrm{d}\epsilon, \tag{4.30}$$

with the effective cross section

$$\sigma_{\mathrm{eff}}(\epsilon) = \sigma_0 \Big| \sum_j \frac{\langle\phi_f|\psi_j\rangle\langle\psi_j|\phi_i\rangle}{\epsilon_{\mathrm{res}} - \epsilon + \epsilon_i - \epsilon_j + i\Delta_{\mathrm{res}}} \Big|^2. \tag{4.31}$$

In analogy to (4.23) it is the probability of the vibrational transition from $|\phi_i\rangle$ to $|\phi_f\rangle$ in the ground state potential via the resonance eigenstate $|\psi_j\rangle$, given by the overlap of the wavefunctions, weighted by the resonance position represented by a Lorentzian. Thus, this formulation simultaneously accounts for neighbouring transitions $\Delta_{n,n+1}$ (ladder climbing, MP mechanism), overtone transitions $\Delta_{n,m}$ as well as transitions directly causing dissociation $\Delta_{n,f+1}$ where f denotes the last

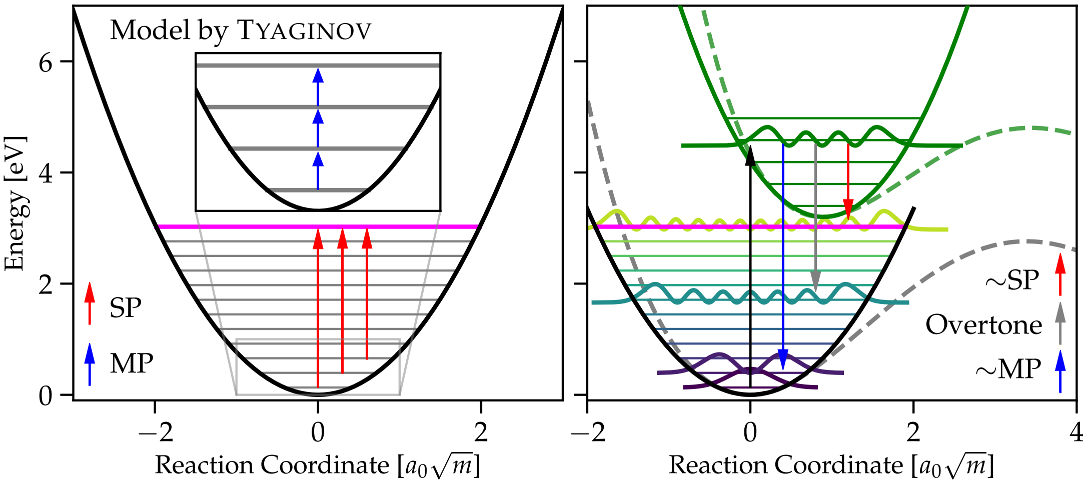

FIGURE 4.6: Relation to the model proposed by TYAGINOV *et al.* **Left:** The previously used approach considers a subsequent excitation of vibrational modes (multiple particle (MP)) as well as direct dissociation triggered by *hot* carriers (SP) based on an empirical description. **Right:** The presented resonance mediated mechanism naturally maps the MP and SP process onto a single meaningful physical interpretation. Additionally, the possibility of overtone transitions facilitates a bond breakage path with fewer number of intermediate excitations and eventually couples the full system of eigenstates in the ground state potential.

bound state in the potential (SP process). Note that such a resonance based description was already proposed by the group of HESS [52], albeit not rigorously included in their calculations. A detailed comparison of the cross section's energy dependence is given in Fig. 4.7. While the empirical Keldysh–like expression does not depend on the current eigenstate, i.e. the level of bond excitation, such subtleties are included in (4.31) via $\epsilon_{\text{res}} + \epsilon_i - \epsilon_j$. Note that within the proposed effective cross section overtone transitions can potentially have a higher excitation probability due to the wavefunction overlaps.

Additionally, due to the small effective dipole moment $\boldsymbol{\mu}_{\text{eff}}$ of the Si–H bond, see Sec. 3.3, and the the marginal relevance of dipole scattering rates, resulting therefrom Sec. 4.1, this component can be neglected. On the other hand, the harmonic scaling law for the vibrational lifetime (4.21), see Sec. 4.1, is now strictly fulfilled and can be applied. Therefore, a total transition rate can again be calculated, using the individual contributions of the resonance scattering mechanism (4.30) and (4.31) and the vibrational dissipation (4.21) and (4.13)

$$\Gamma^{\text{tot}}_{i,f} = \Gamma^{\text{res}}_{i,f} + \Gamma^{\text{vib}}_{i,f}. \tag{4.32}$$

Subsequently, again the new quasi–equilibrium solution of the Pauli Master equation, see (4.24), can be calculated which yields the individual state populations P_i of the ground state harmonic oscillator. Including the first *continuum* state (the first state above the Si–H bond breakage energy), the final bond breakage rate Γ^{break} can be *classically* defined as the vibrational eigenstate population P_i

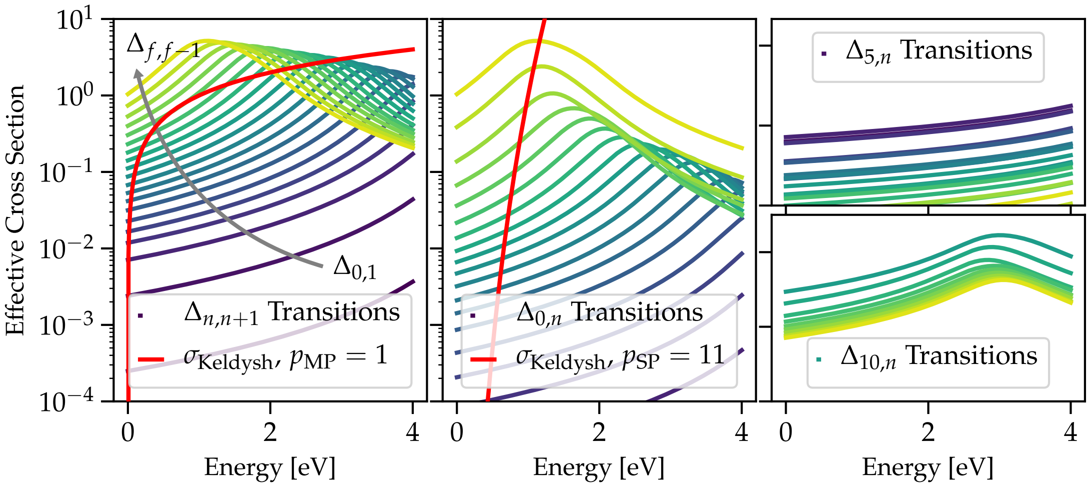

FIGURE 4.7: Comparison of the Keldysh–like cross section and the *effective* cross section, see (4.31). Regardless of the current vibrational mode of the Si–H bond, the Keldysh cross section is exclusively a function of the incident carrier energy. In contrast, the derived quantum–dynamical formulation depends on the initial state and its energy, the final state and the corresponding wavefunction overlap as well as the energetic position of the resonance. **Left and Middle:** Various MP and SP excitations mechanisms. Note that the formulation in (4.31) results in considerably different *effective* cross sections, while the empirical description does not distinguish between the different cases. **Right:** Possible overtone transitions within the presented description, see (4.31).

times the total transition rate from i to the continuum state $f+1$. The evolution of broken and intact Si–H bonds with stress time is again given by the reaction equation (4.26) and (4.28), respectively.

The major advantage of harmonic approximations is the availability of analytic solutions for the eigenvalues and eigenvectors. Furthermore, due to the simpler potential energy profile it effectively reduces the parameter set and allows to efficiently sample the distribution on a 3D grid.

4.2 Non-Equilibrium Processes & Oxide Defects

The fundamentals of bias temperature instability and charge trapping in the oxide based on nonradiative multiphonon theory is already explained in Chapter 2.2. However, capturing the charging and discharging kinetics of oxide defects under non–equilibrium conditions is beyond the applicability of the current 4–state framework. Nevertheless, the NMP$_{\mathrm{eq.}}$ model already provides a physically complete description as well as a native extension towards the integration of such processes. In the following the implications of a *heated* carrier ensemble in the valence and conduction band of a MOSFET will be discussed and two model extensions will be derived.

Extended 4–State Model

The described NMP$_{\text{eq.}}$ model does not account for non–equilibrium carrier dynamics in full $\{V_{\text{G}}, V_{\text{D}}\}$ bias space. Only an inhomogeneous shift of the *effective* trap level along the Si/SiO$_2$ interface is taken into account using the relation to the oxide field $F_{\text{ox}}(x)$ given in (2.15). However, this is a purely electrostatic effect. Emerging changes of the energy distribution functions (EDFs) due to the application of a drain bias V_{D}, such as the formation of a heated, non–equilibrium carrier ensemble and the generation of secondary carriers, are not included in the aforementioned approach. On the other hand, a thorough and consistent description requires a full solution of the coupled BTE for holes and electrons for each bias point which is computationally very costly. Moreover, using the EDFs in conjunction with the (classical) lineshape function (LSF) for a large ensemble of defects is again a very computation intensive task. In order to capture the charging dynamics of oxide traps also at higher V_{D} stress conditions in a more practical TCAD model, a simplified approach is highly desired.

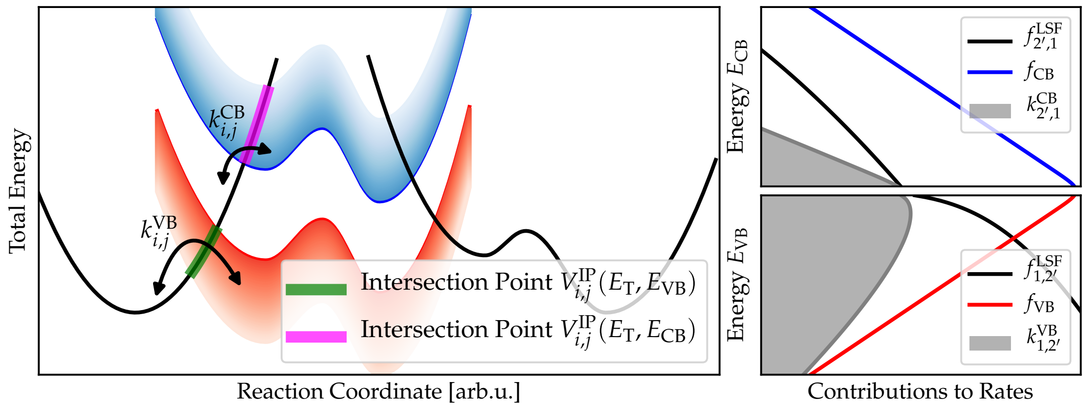

FIGURE 4.8: The extended 4–state model includes the effect of impact ionization (II) using semi–empirical approaches within the drift–diffusion (DD) simulations. Thus, interactions with electrons in the conduction band yield a non–vanishing contribution to the NMP transitions (**Left**). In particular, the hole emission processes (which are equivalent to capturing an electron), i.e. $2' \Rightarrow 1$ and $2 \Rightarrow 1'$, are expected to be affected by an increasing concentration of carriers in the conduction band. On the other hand, the reverse hole capture processes are still dominated by the interactions with the VB. The NMP$_{\text{eq.+II}}$ model assumes the carriers to be in thermal equilibrium (**Right**).

A possible approximation is given by including the effect of II within the DD simulations using semi–empirical II models. This simplified picture neglects the interplay of defects with a *heated* carrier ensemble, but includes the interaction with secondary created carriers in the conduction band (CB) of a pMOS, see Fig. 4.8. Particularly for the charge transitions $1 \Leftrightarrow 2'$ and $1' \Leftrightarrow 2$ this can have a large impact. While charging is associated with the capture event of a hole (or the emission of an electron), discharging is linked to the defect emitting a hole into the VB (or to capture an electron from the CB). Therefore, the emission processes $2' \Rightarrow 1$ and $2 \Rightarrow 1'$ are expected to be affected by an increasing carrier concentration n in the conduction band, see Fig. 4.8. This variant of the 4–state model is termed **extended equilibrium model**, **NMP$_{\mathbf{eq.+II.}}$**. Due to the (crude) approximation that carriers remain in thermal equilibrium, thus properly described by a FD distribution, the computationally effective band edge approximation is still applicable.

Non–Equilibrium 4–State Model

Despite the appealing model introduced above, it certainly lacks a detailed description of the interaction between oxide defects and energetic carriers described by a non–equilibrium energy distribution function (EDF). Their interaction, however, is given by the lineshape function (LSF), see (2.11) (or the classical limit) which is already a substantial part of the NMP$_{\mathrm{eq.}}$ model variant. The LSF is the sum of a multitude of contributions due to the various vibrational modes involved, see Fig. 2.4 in Chap. 2, for a specific configuration of the two parabolas. Furthermore, Fig. 2.5 and the set of equations, (2.13) in Sec. 2.2, show that the LSF additionally depends on the energy E of the reservoir state due to the interaction with a continuous band, which is represented by a shifted (charged) parabola. This shifted alignment translates into a changing intersection point of the parabolas and, thus, an energy dependent LSF. For a decreasing (increasing) barrier $\varepsilon_{i,j}$ with the reservoir energy E the LSF is therefore (usually) an increasing (decreasing) function over E. As already mentioned in Sec. 2.2, the rate $k_{i,j}$ is determined by the product $f_p(E) f_{i,j}^{\mathrm{LSF}}(E, E_{\mathrm{T}})$.

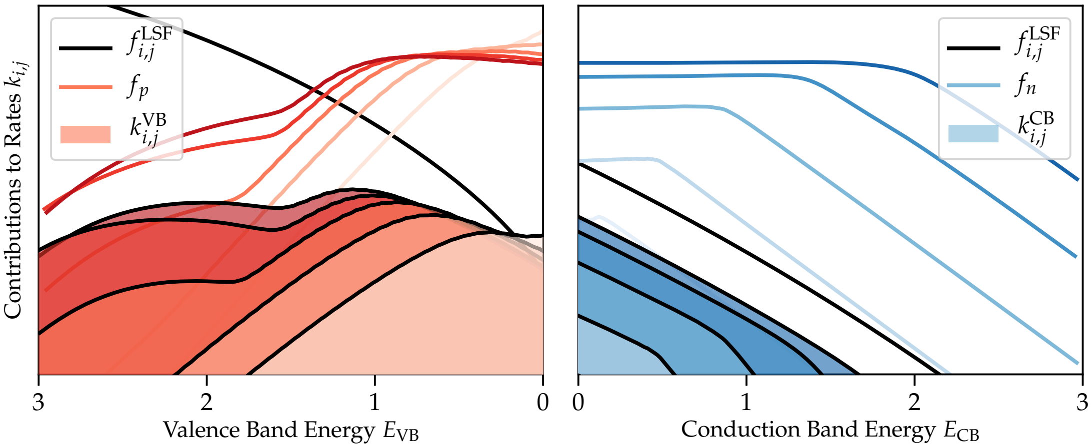

FIGURE 4.9: The impact of non–equilibrium energy distribution functions (EDFs) onto the NMP rates $k_{i,j}$. Heated carrier ensembles in the valence (**Left**) as well as conduction bands (**Right**) potentially increase the corresponding transition rates and therefore alter the defects' charging and discharging dynamics.

Fig. 4.9 shows that in the case of non–equilibrium EDFs, e.g. hole EDFs at the drain end of the channel or electron EDFs at the source end, the integral can be substantially different compared to a FD distribution. This not only implies considerably modified transition rates $k_{i,j}$ with increasing V_{D} conditions, but also that the (energetically) accessible defects change within $\{V_{\mathrm{G}}, V_{\mathrm{D}}\}$ bias space. The full consideration of this effect is termed **non–equilibrium 4–state model**, **NMP$_{\mathbf{neq.}}$**, and is based on a self consistent calculation of the coupled BTE for holes and electrons. Consequently, heated carrier ensembles for holes and electrons – which are created at the drain side and accelerated by the electric field towards the source – are taken into account. This variant of the 4–state model yields the most accurate description and reveals interesting phenomena as will be shown below.

CHAPTER 5

Modeling Results

In this Chapter the model approaches introduced in Chapter 4 will be applied to investigate the individual effects of HCD and non–equilibrium BTI. Together with an in–depth analysis the modeling frameworks and the respective results will be thoroughly tested and validated against a wide class of measurement sets. Subsequently, the first rigorous simulation study of a MOSFET in full $\{V_\mathrm{G}, V_\mathrm{G}\}$ bias space will be presented and analyzed. Furthermore, a particular experiment based on alternating stress sequences reveals the implications of different stress regimes onto the various types of defects. The presented studies will clearly reveal the conceptual limits of the assumption of independent descriptions of degradation regimes.

5.1 Hot–Carrier Regime

First, the modeling framework introduced in Sec. 4.1 will be challenged using two different types and technologies of devices, an nMOSFET and a pMOSFET with different gate lengths. This direct comparison was chosen due to occasional reports which show that the damage caused by HCD for nMOS devices is larger than for the pMOS counterparts [55, 56, 287, 288]. Note that the concept of resonance–induced excitations provides a physically meaningful explanation for this observation: If the accessible resonance state for holes is higher in energy than for electrons, $\epsilon_{\mathrm{res},n} = 3.64\,\mathrm{e}V$ and $\epsilon_{\mathrm{res},p} = 3.96\,\mathrm{e}V$ – as suggested by the *ab initio* results in Chapter 3 – it is less likely for holes to trigger bond excitation followed by the creation of interface defects.

Energy Distribution Functions

For the calculation of the carrier energy distribution functions (EDFs), which yield the information on how carriers are distributed over energy, the higher order spherical harmonics expansion simulator SPRING[1] has been used. The bipolar Boltzmann transport equation (BTE) was solved self–consistently on the calibrated 2D structures obtained from process simulations. The scattering mechanisms considered are acoustical and optical phonon scattering, impurity scattering as well as impact ionization with secondary carrier generation.

The results for two devices – a 65 nm nMOSFET and a 100 nm pMOSFET – and selected stress conditions are shown in Fig. 5.1. Clearly visible is the characteristic accumulation of highly energetic minority carriers at the drain end of the channel for both devices. As expected, increasing the stress conditions results in a more pronounced high energy fraction of the EDFs for holes (pMOS) and electrons (nMOS). However, while the EDFs of the secondary generated holes in the nMOS remain almost unchanged for the given stress conditions ($V_\mathrm{G} = V_\mathrm{D}$), the electron EDFs in the pMOS significantly change for higher stress bias. Thus, particularly for the highest drain bias conditions, $V_\mathrm{D} = -2.8\,\mathrm{V}$, electrons can be expected to

---

[1] developed by the group of Prof. Jungemann at RWTH Aachen

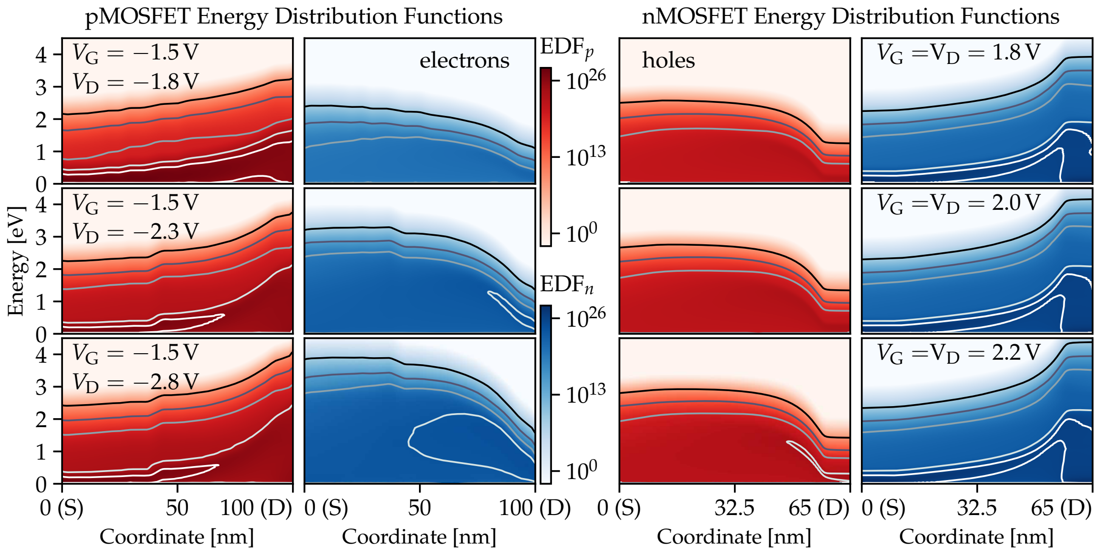

FIGURE 5.1: Energy distribution functions EDFs for the pMOSFET (**Left**) and the nMOSFET (**Right**) for various stress regimes obtained from a solution of the bipolar BTE coupled via II. While the pMOS shows a substantial contribution of secondary generated electrons for increasing stress bias, the hole EDFs for the nMOS remain almost unchanged with varying stress conditions.

contribute to the total degradation in pFETs, since their EDFs are populated for energies up to 3 eV along the channel region.

Influence of Temperature

In order to assess the reliability behaviour at elevated temperatures, the EDFs have been calculated at various temperatures, see Fig. 5.2, because the corresponding scattering rates are influenced by the lattice temperature, see [289]. Phonon and impurity scattering rates increase with T, via the occupation number for phonons given by the Bose–Einstein distribution and the screening length within the Debye formulation respectively, whereas the electron and hole II rates are assumed to be temperature independent and exclusively energy dependent. However, since phonon and impurity scattering at elevated T modify the EDF, the II rates are also, therefore, indirectly affected. Thus, low and medium energy carriers which are determined by phonon and impurity scattering are suppressed at increasing temperatures, while the high energy tail, represented by the tail of a thermalized Maxwell–Boltzmann distribution, is enhanced. These characteristic features are well represented by the EDFs for both devices and two different temperatures ($T = 298$ K and $T = 398$ K for the pMOSFET and $T = 348$ K for the nMOSFET, respectively) shown in Fig. 5.2.

pMOSFET versus nMOSFET

Measurements for the modeling benchmark have been performed on two different devices. A pMOSFET with a gate length of 100 nm and an nMOSFET with

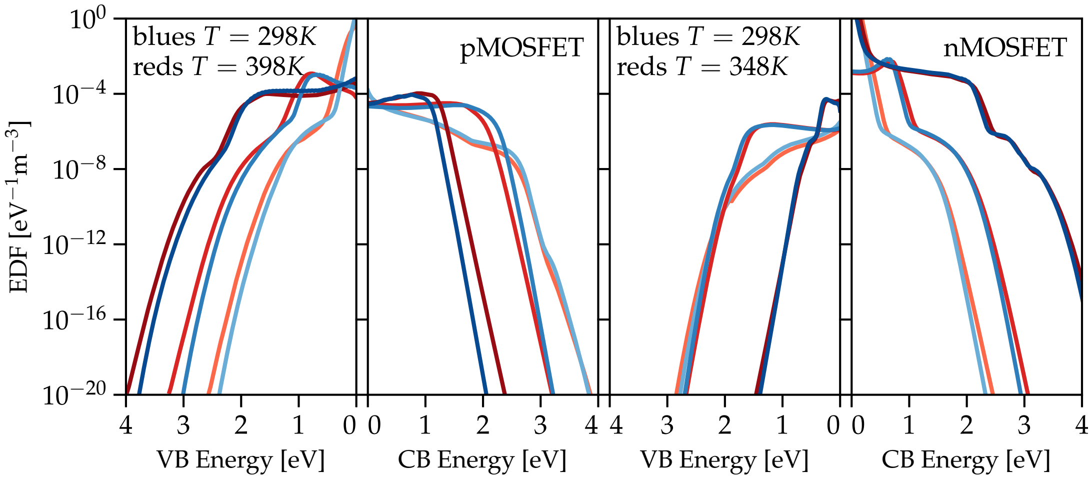

FIGURE 5.2: The effect of lattice temperature onto the EDFs for the pMOSFET (**Left**) and the nMOSFET (**Right**). The results show the EDFs for $V_{\mathrm{G}} = -1.5\,\mathrm{V}$, $V_{\mathrm{D}} = -2.8\,\mathrm{V}$ (pMOS) and $V_{\mathrm{G}} = V_{\mathrm{D}} = 2.2\,\mathrm{V}$ (nMOS) at the source and drain end as well as in the middle of the channel.

a gate length of 65 nm, both technologies employing a 2.2 nm SiON thick gate oxide and have an operating voltage of $|V_{\mathrm{DD}}| = 1.5\,\mathrm{V}$. The devices have been stressed at two temperatures, $T = 298\,\mathrm{K}$ as well as $T = 398\,\mathrm{K}$ for the pFET and $T = 348\,\mathrm{K}$ for the nFET, and were subjected to their respective nominal worst–case stress conditions, namely $V_{\mathrm{G}} = -1.5\,\mathrm{V}$ and $V_{\mathrm{D}} = -1.8, -2.3$ and $-2.8\,\mathrm{V}$ for the pMOS and $V_{\mathrm{G}} = V_{\mathrm{D}} = 1.8, 2.0$ and $2.2\,\mathrm{V}$ for the nMOS device. To monitor the degradation trend $\Delta I_{\mathrm{D,lin}}(t)$ traces up to 10 ks of stress were recorded.

The calculated energy distribution functions are shown in Fig. 5.1 and explained in detail in the corresponding Section 5.1. Interface state profiles $N_{\mathrm{it}}(x)$ along the Si/SiON interface have been calculated using the model introduced in Sec. 4.1, and subsequently the degradation characteristics has been calculated using TCAD tools. In order to give detailed insights into the calculations and shed light into the degradation processes, Fig. 5.3 shows the rate matrix of one Si–H bond potential with 20 eigenstates localized in the left well along the channel for both devices. At the source side minority carriers – holes in the pFET and electrons in the nFET – are close to equilibrium, compare with Fig. 5.1 and Fig. 5.4, and thus are not able to scatter into an available resonance. The upper triangle of the matrix is, therefore, mainly determined by dipole induced excitations and the detailed balance condition at the given temperature. However, along the interface carriers are accelerated by the electric field and exchange energy via various scattering mechanisms, resulting in a non–equilibrium EDF with a substantial *hot* energy tail at the drain side. This enables the formation and transient occupation of an ionic resonance, allowing for multiple excitations shown as large off diagonal elements in the rate matrix. Furthermore, as already discussed above, the effect of impact ionization potentially aids the excitation and dissociation mechanisms via energetic secondary generated carriers. Whereas for the nMOS this compo-

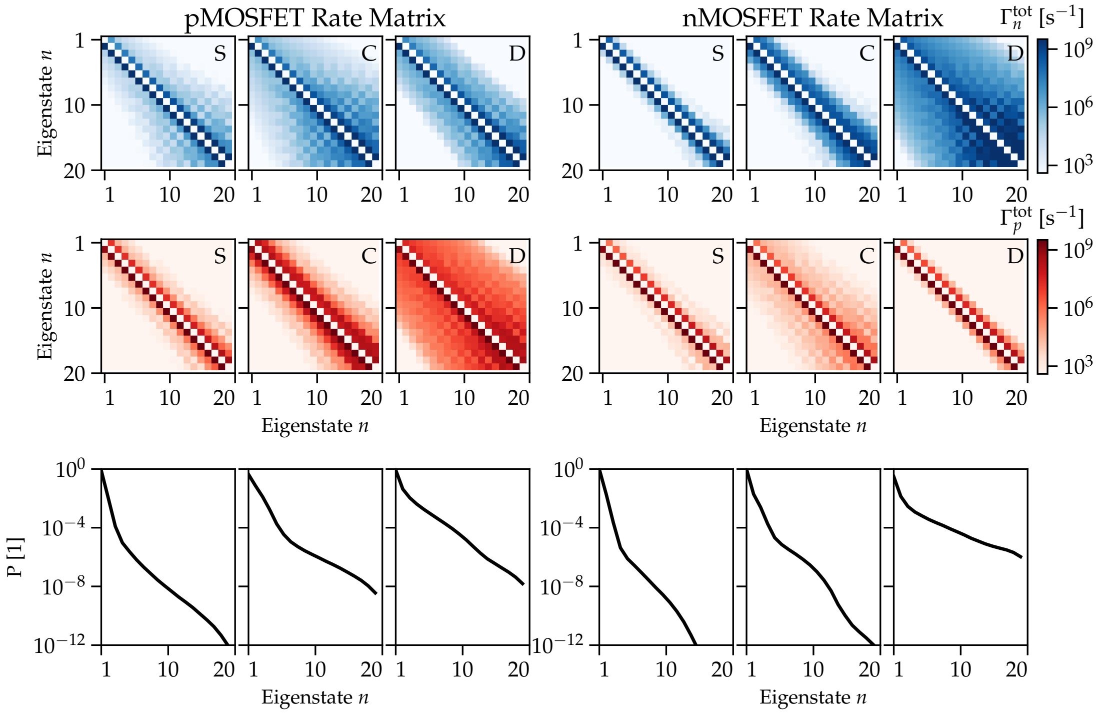

FIGURE 5.3: The density matrix projected onto the *left well* of a full model potential containing 20 eigenstates ϕ_L evaluated. The matrix is split into contributions from electrons and holes and evaluated at different positions along the Si/SiO$_2$ interface within the n– and pMOSFET. Clearly visible are the small upward rates due to the minority carriers at the source side and in the channel region. On the other hand, the accumulation of energetic (minority) carriers at the drain end results in the formation of a temporary excited state due to the resonance scattering process. Secondary generated carriers which have been accelerated towards the source seem to dominate the Si–H dynamics in the respective regions in the pMOS, whereas their contribution is negligible in the nMOS device. The lower panels show the populations of the Si–H bond eigenstates.

nent seems to be negligible, see the right panels of Fig. 5.3, secondary generated electrons in the pMOS seem to account for a major contribution to the overall excitations. Particularly in the channel region and towards the source side electrons up to 3 eV and more are present, see Fig. 5.4, which are able to scatter into the available anionic resonance state.

The calculated $N_{\mathrm{it}}(x)$ profiles reflect the analysis regarding the rate matrix and excitation processes, see Fig. 5.5. Clearly visible are the characteristic peaks at the drain end of the channel for both, the n– and pMOS device, for all stress conditions. This particular feature of HCD can evidently be explained quite well by the hot carrier ensemble at the drain end, see Figs. 5.5 and 5.4. However, while for the nMOSFET and the given stress conditions the damaged region continuously extends from the drain towards the channel region, the buildup of a second peak in the channel area is visible for increasing V_{D} bias in the pMOS device. Together with the individual bond breaking rates Γ_{break} for electrons and holes shown in

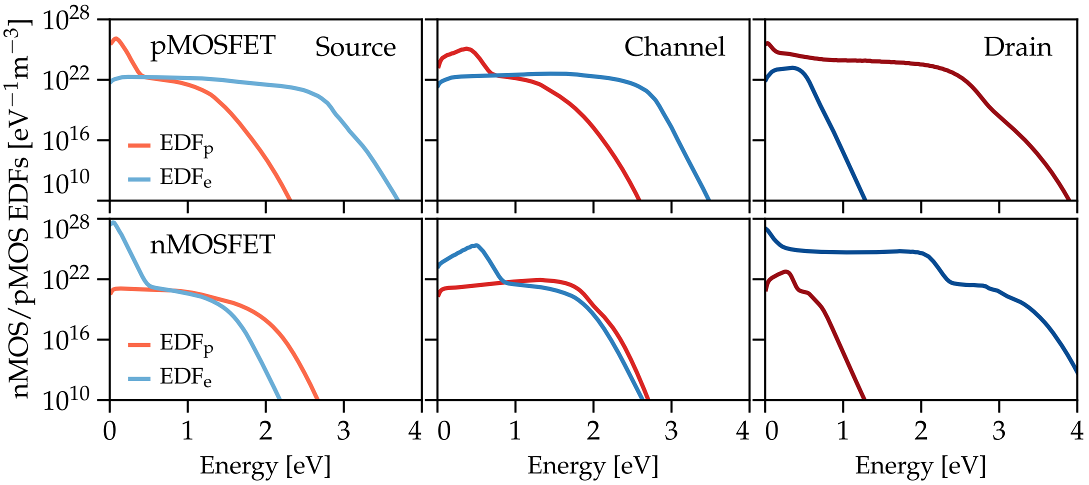

FIGURE 5.4: A comparison of the electron (EDF$_e$) and hole (EDF$_p$) energy distribution functions for both devices. One can see that the minority EDFs at the three evaluated positions are very similar. However, the effect of II and the amount of *heated* secondary carriers is much more pronounced in the pMOSFET.

the lower panels of Fig. 5.5, the EDFs in Fig. 5.4, and the rate matrix for the corresponding carriers in Fig. 5.3, a more detailed understanding of this behaviour can be established. Apparently, the degradation in the nMOS is exclusively determined by minority carriers, whereas in the pMOS a significant contribution is due to secondary generated electrons created by II.

There are two main reasons for this difference. First, the devices have been subjected to different stress conditions. The stress conditions $V_\mathrm{G} \sim 0.5V_\mathrm{D}$ for the pMOS have been chosen to represent the nominal worst–case conditions for long–channel devices which correspond to the maximum substrate current[2]. Contrary, the nMOS device has been subjected to $V_\mathrm{G} = V_\mathrm{D}$ stress conditions correlating to the well known worst–case stress for short–channel devices. Second, and more important due to being a key ingredient in the modeling framework introduced in Sec.4.1 is the impact of different resonance states accessible for electrons and holes. The available scattering state for electrons is about $\sim 0.4\,\mathrm{eV}$ lower in energy compared to the hole resonance. Moreover, the minimum of the potential energy curve for the excited anionic complex is shifted twice as much with respect to the ground state minimum compared to the cationic equilibrium position. Due to the overlap integral of the wavefunctions within the resonance mediated formulation, see (4.23), larger shifts enhance the probability of overtone transitions, see Fig. 5.3. Hence, electrons are more efficient in exciting and breaking the Si–H bond. This is particularly visible at the drain end of both devices. Although the energy distribution functions are comparable within this region, see Fig. 5.4 EDF$_e$ (nMOS) and EDF$_p$ (pMOS), the electron rates Γ_break are almost two orders of magnitude larger, see Fig. 5.5. Furthermore, secondary generated holes in the channel region of the nMOS do not contribute to the creation of damage at all, while electrons

---

[2] as well as the maximum impact ionization rate

generated by II rather dominate the degradation in the respective region within the pMOS. Resonance based excitations not only provide a fundamental understanding

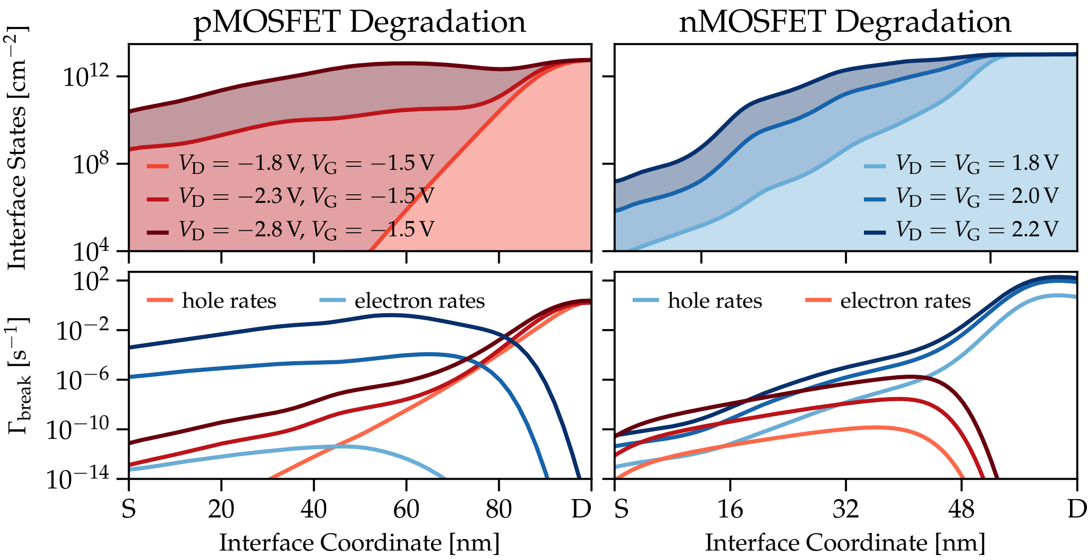

FIGURE 5.5: **Upper:** Interface state profiles, $N_{\mathrm{it}}(x)$, for the nMOS and the pMOS after 10 ks of stress. Note the increasing damage in the channel region due to electrons created via impact ionization, see Figs. 5.3 and 5.2, in the pMOSFET. The nMOS degradation characteristic on the other hand are solely determined by *heated* electrons. **Lower:** The individual bond breaking rates of electrons and holes along the interface provides a detailed picture of the excitation and bond breakage dynamics. Note that, although similar EDFs are obtained in the vicinity of the drain region, see Fig. 5.2, electrons posses higher bond breaking rates due to the lower resonance level compared to holes.

of how carriers interact and eventually break Si–H bonds, but also allow for an accurate microscopic description which properly captures the degradation trends, see Fig 5.6.

A unique, albeit slightly optimized, parameter set has been used to describe HCD in both devices, see Fig. 5.7 and Table 5.1. All parameters are within a reasonable range and close to reported values in the literature and the DFT results presented in Chap. 3. Only two parameters are associated with a higher degree of uncertainty where solely the results presented within this thesis are available or literature values. First, the resonance width $\Delta\epsilon_{\mathrm{res}}$, which was calculated by STOKBRO *et al.* to be 1 eV for the anionic and 0.6 eV for the cationic resonance state respectively [114, 115]. However, for a typical resonance lifetime of $\tau_{\mathrm{res}} = \hbar/\Delta\epsilon_{\mathrm{res}} \sim 1 - 2\,\mathrm{fs}$, the width is about $0.2 - 0.7\,\mathrm{eV}$ [236, 237, 276]. Second, the shift of the equilibrium position of the excited potential energy curves with respect to the ground state minimum. The calculations in Sec. 3.4 show a shift of $\sim 0.4\,\mathrm{a_0}\sqrt{\mathrm{m}}$ for the positively charged PEC and $\sim 0.9\,\mathrm{a_0}\sqrt{\mathrm{m}}$ for the negative PEC which served as an input for the model. Due to the amorphous interface an intrinsic variation of this quantity is, however, to be expected. Note that, in total

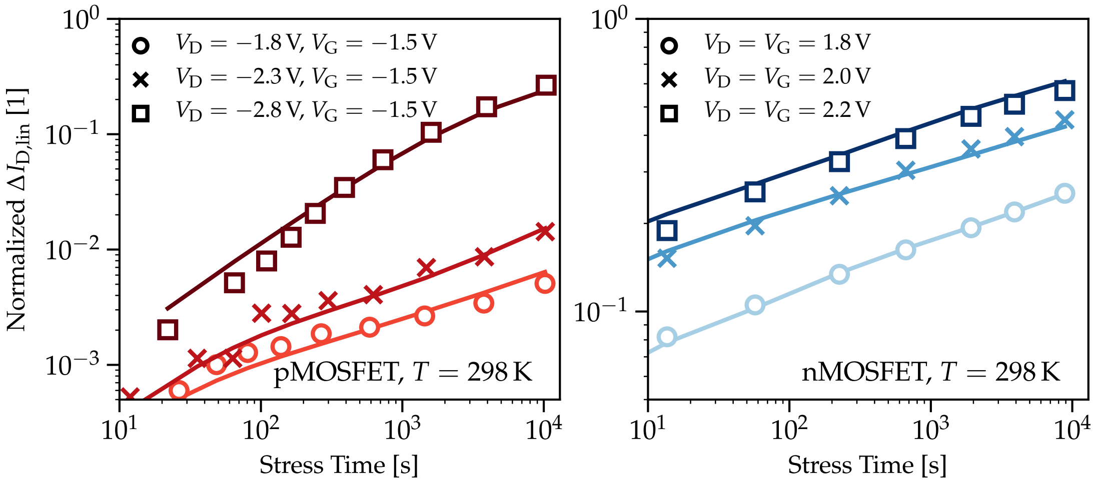

FIGURE 5.6: Measurements (symbols) and simulations (lines) for the model benchmark. The full simulation framework, see Sec. 4.1, was validated against experimental data of a 100 nm pMOSFET (**Left**) as well as a 65 nm nMOSFET (**Right**) subjected to each three different hot–carrier stress conditions. The model shows very good agreement with the measured characteristics.

750 unique configurations with individual PECs and resonances have been used by randomly selecting uniformly distributed parameters of the model potentials, see Sec. 4.1. The resulting important values for the modeling framework are shown in Fig. 5.7 and listed in Tab. 5.1, termed as *Full Model*.

Furthermore, Table 5.1 also shows the parameter used with the *Harmonic Model* introduced in Sec. 4.1. In order to reduce the complexity and the computational requirements of the calculations, the simplified model focuses on the decisive parameters which control the reaction dynamics, namely $E_{\mathrm{B,f}}$ together with the angular frequency of the oscillator as well as the shift of the respective PECs, $\Delta q_{\mathrm{e/p}}$. Such approximations allow to place the Si–H bond configurations on a grid spanned by the three distributed parameters and effectively enables deterministic simulations. Nevertheless, the harmonic model matches the experimental data very well while maintaining a physically reasonable parameter set. Further information is given in [MJC5].

Elevated Temperatures

The impact of temperature onto the degradation due to hot–carriers is still not fully understood. Traditionally, in long–channel devices with the worst–case stress conditions being $V_\mathrm{G} \sim 0.5 V_\mathrm{D}$, previous studies have shown that HCD is suppressed at elevated temperatures [290–292]. Quite to the contrary, an increasing temperature in short–channel devices, subjected to $V_\mathrm{G} = V_\mathrm{D}$ stress biases, typically results in an aggravation of HCD [55, 293, 294]. However, in a recent publication also the opposite trend has been reported [MJJ12].

Such, seemingly, ambiguous temperature trends stem from a complex inter-

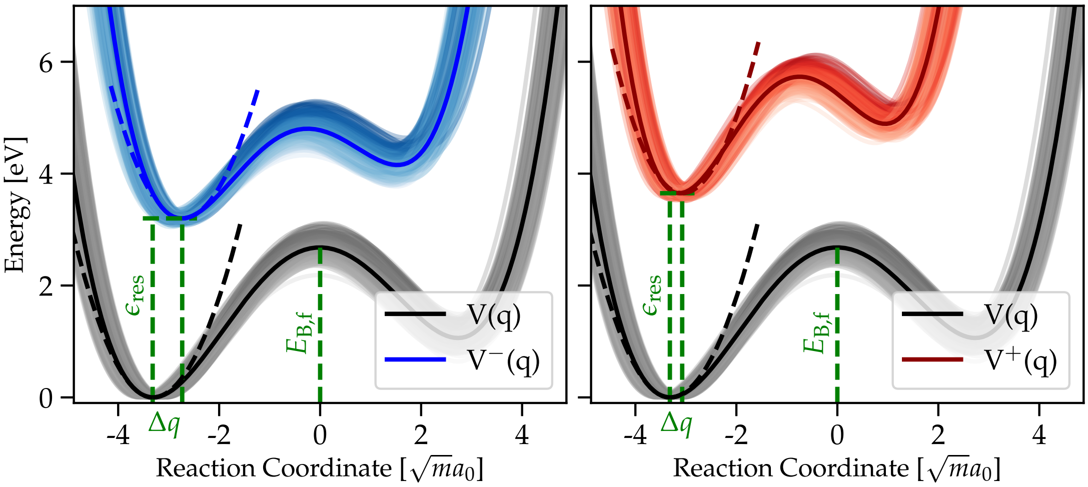

FIGURE 5.7: Model potentials used for $V(q)$, $V^-(q)$ (**Left**)and $V^+(q)$ (**Right**) to represent the measurement trends together with the respective parameters, see Sec. 4.1. Due to the amorphous nature of the Si/SiO$_2$ interface, quantities such as the barriers are assumed to be normally distributed.

play of various effects and processes together with a partly opposing influence of temperature. First, the implications on the transport properties itself. As shown above, see Fig. 5.2, the individual scattering rates are enhanced with temperature which decreases the population of low and medium energies. On the other hand, the high energy tail, which represents the thermalized carrier ensemble, is enhanced. Furthermore, the EDFs and the importance of low/medium and high energy carriers strongly depend on the device architecture and the applied bias conditions, which needs to be considered for the temperature behaviour of HCD. Second, the vibrational lifetime $\tau_{1,0}$ is a decreasing function with temperature, see Sec. 4.1, and therefore, represents a competing effect at elevated T. Third, a possible contribution of BTI and oxide defects, which is known to be strongly temperature accelerated. Due to the available defect bands this would particularly apply for negative bias temperature instability (NBTI) in SiO$_2$ based pMOSFETs and PBTI in scaled nMOS transistors employing high–κ gate stacks [MJJ7, MJJ8].

Both devices, the pMOSFET and the nMOSFET, have been stressed at elevated temperatures, $T = 398\,\mathrm{K}$ (pMOS) and $T = 348\,\mathrm{K}$ (nMOS), respectively. In order to exclude the third point, a concurrent contribution of BTI, the devices have been switched to recovery conditions after the stress sequence. Neither the n– nor the pMOS devices showed a noteable recovery of the measured parameters. The experimental data together with the simulation results are shown in Fig 5.8, where the data for $T = 298\,\mathrm{K}$ are marked as gray curves for comparison. One can clearly see an opposite temperature trend which is properly captured by the model. While for the pMOS an increasing T results in a more pronounced damage due to hot–carriers, the degradation in the nMOS is suppressed. However, note that for the highest stress condition the effect of temperature almost vanishes in both devices.

Parameter	Full Model	Harmonic Model	DFT Results	References
$E_{\mathrm{B,f}}$	$2.70\,\mathrm{eV}$	$2.75\,\mathrm{eV}$	$2.57\,\mathrm{eV}$	$2.83\,\mathrm{eV}^{\star}$
$\sigma_{E_{\mathrm{B,f}}}$	$0.12\,\mathrm{eV}$	$0.1\,\mathrm{eV}$	$0.22\,\mathrm{eV}$	$0.08\,\mathrm{eV}^{\star}$
$\epsilon_{\mathrm{res},n}$	$3.24\,\mathrm{eV}$	$3.46\,\mathrm{eV}$	$3.64\,\mathrm{eV}$	$4.10\,\mathrm{eV}^{\dagger}$
$\Delta_{\mathrm{res},n}$	$0.17\,\mathrm{eV}$	$1.12\,\mathrm{eV}$	-	$1.00\,\mathrm{eV}^{\dagger}$
Δq_n	$0.58\,\sqrt{\mathrm{m}}\mathrm{a}_0$	$0.72\,\sqrt{\mathrm{m}}\mathrm{a}_0$	$0.9\,\sqrt{\mathrm{m}}\mathrm{a}_0$	-
$\sigma_{\Delta q_n}$	$0.08\,\sqrt{\mathrm{m}}\mathrm{a}_0$	$0.10\,\sqrt{\mathrm{m}}\mathrm{a}_0$	-	-
$\epsilon_{\mathrm{res},p}$	$3.74\,\mathrm{eV}$	$4.45\,\mathrm{eV}$	$3.96\,\mathrm{eV}$	$4.8\,\mathrm{eV}^{\circ}$
$\Delta_{\mathrm{res},p}$	$0.12\,\mathrm{eV}$	$0.53\,\mathrm{eV}$	-	$0.60\,\mathrm{eV}^{\circ}$
Δq_p	$0.23\,\sqrt{\mathrm{m}}\mathrm{a}_0$	$0.43\,\sqrt{\mathrm{m}}\mathrm{a}_0$	$0.40\,\sqrt{\mathrm{m}}\mathrm{a}_0$	-
$\sigma_{\Delta q_p}$	$0.09\,\sqrt{\mathrm{m}}\mathrm{a}_0$	$0.10\,\sqrt{\mathrm{m}}\mathrm{a}_0$	-	-
$\tau_{1,0}$	$0.39\,\mathrm{ns}$	$0.78\,\mathrm{ns}$	$0.12\,\mathrm{ns}$	$1.0\,\mathrm{ps} - 1.5\,\mathrm{ns}^{\ddagger}$

TABLE 5.1: The model parameters utilized within the simulations. The results compare well to the values extracted from the DFT calculations, see Chapter 3, and also to literature results. For a detailed explanation of the parameters see Chap. 4. * [201, 222],† [115], ° [114], ‡ [270, 271, 274, 275]

The lower stress regimes chosen for the pMOSFET, $V_{\mathrm{G}} = -1.5\,\mathrm{V}, V_{\mathrm{D}} = -1.8\,\mathrm{V}$ and $V_{\mathrm{G}} = -1.5\,\mathrm{V}, V_{\mathrm{D}} = -2.3\,\mathrm{V}$, are actually dominated by the degradation due to holes within the drain region, see Fig. 5.5. At elevated temperatures the high energy ensemble is enhanced, aiding the overtone transitions and direct bond breaking process. Due to their small number of excitation steps, these processes depend only very weakly on the (decreasing) vibrational lifetime, resulting in an aggravation of HCD, particularly at short stress times. The most severe stress bias, $V_{\mathrm{G}} = -1.5\,\mathrm{V}, V_{\mathrm{D}} = -2.8\,\mathrm{V}$, on the other hand, is strongly affected by the presence of energetic electrons. The electron EDFs towards the drain end are slightly shifted towards higher energies at $T = 398\,\mathrm{K}$, see Fig. 5.2. However, this trend is compensates by the decreasing vibrational life $\tau_{1,0}$, resulting in virtually the same degradation behaviour as for $T = 298\,\mathrm{K}$.

The nMOSFET has been stressed at $T = 348\,\mathrm{K}$ which yields only minor differences in the calculated EDFs, see Fig. 5.2. Therefore, the overall degradation trend at the measured temperature is dominated by the reduction of the vibrational lifetime, resulting in a reduction of hot–carrier related degradation. Nevertheless, also for the nMOS a decreasing difference between the two temperatures is visible with increasing bias conditions. This is again due to the increasing importance and influence of the high energy tail at $V_{\mathrm{G}} = V_{\mathrm{D}} = 2.2\,\mathrm{V}$ where carriers are able to trigger, the almost lifetime independent, overtone excitations.

For all simulations the optimized parameter set presented in Table 5.1 has been used with a vibrational lifetime of $\tau_{1,0} = 0.35\,\mathrm{ns}$ at $T = 348\,\mathrm{K}$ and $\tau_{1,0} = 0.28\,\mathrm{ns}$ at $T = 398\,\mathrm{K}$, respectively.

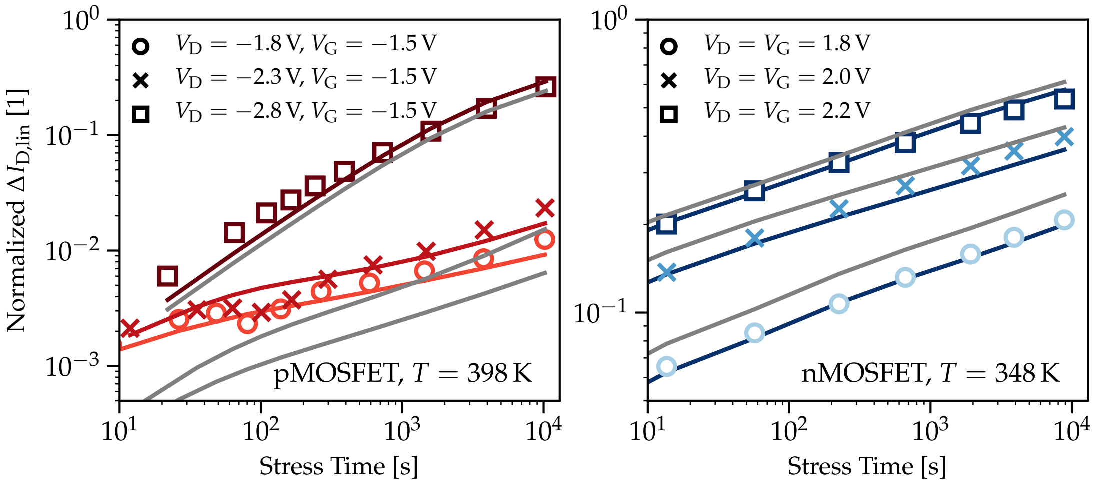

FIGURE 5.8: Measurements versus simulations at elevated temperatures for both devices. The pMOSFET was stressed at $T = 398\,\mathrm{K}$ (**Left**) and the nMOS at $T = 348\,\mathrm{K}$ (**Right**). The simulation results for $T = 298\,\mathrm{K}$ are superimposed in gray for a better comparison.

5.2 Non–Equilibrium Dynamics of Individual Oxide Defects

In a number of publications [295, MJC15, MJJ6] conducted on small–area SiON pMOSFETs, it has been shown that the charging and discharging characteristics of individual oxide defects can substantially change upon applying a drain bias. While in [MJC15, MJJ6] only defects with a decreasing occupancy, i.e. a reduced likelihood for the defect to trap a charge, have been found for increasing V_D, the authors in [295] concluded that oxide defects could actually be affected in both ways, i.e. an increasing occupancy with increasing drain voltage was also measured. Furthermore, in a recent study [296] the authors claim that the fingerprints of single defects in the oxide, such as their step height and emission time τ_e, change with intermediate hot–carrier stress cycles, but their initial characteristics can be restored after an extended rest period.

The following Section presents simulations applying different variants of the 4–state NMP model to explain the behaviour of single oxide defects. Individual defects have been explicitly chosen for this benchmark study due to the direct measurement of fundamental parameters such as their capture and emission time. These quantities are not accessible when measuring large–area devices and, hence, the influence of a heated carrier ensemble would be blurred by a collective response of a large number of traps. A detailed analysis provides insight into the charging and discharging dynamics to finally unravel the experimentally recorded characteristics. The non–equilibrium EDFs have been obtained using the higher order spherical harmonics expansion simulator SPRING [289, 297–299], see Sec. 5.1 for details.

The measurement results used to validate the model approaches described here are performed on 2.2 nm plasma nitrided SiON pMOSFETs of a 130 nm commercial technology with an operating voltage of $V_{\mathrm{DD}} = -1.5\,\mathrm{V}$ [MJJ6, 300, MJJ4], the same pMOSFET as has been used for the HCD study above. Individual oxide defects have been studied on nano–scale devices ($W = 160\,\mathrm{nm}$) applying the time–dependent defect spectroscopy (TDDS) technique [MJC15, MJJ6, MJJ4]. The devices have been subjected to a stress phase to induce the capture of holes by oxide traps. Subsequently V_{G} and V_{D} have been switched to recovery conditions to allow the trapped holes to be emitted again. This sequence has been repeated 100 times in order to collect statistics on active defects [MJC15, MJJ6].

Defect Characteristics

Two defects have been chosen for studying the behaviour of single oxide traps [MJJ6, MJJ4]. Both defects and their respective capture and emission times have been characterized over a broad range of stress and recovery conditions rendering them ideal candidates for a simulation study. Furthermore, both traps possess a rather unexpected and intriguing trend with increasing drain bias V_{D} which is beyond explanations solely based on electrostatic considerations.

The basis for subsequent simulations provides their behaviour for *pure* BTI ($V_{\mathrm{D}} \sim 0\,\mathrm{V}$) conditions. Applying the NMP$_{\mathrm{eq.}}$ model described in Sec. 2.2 is legitimate for such bias conditions and is able to represent the experimentally recorded characteristic capture and emission times for both defects, *B1* and *B2*, see Fig. 5.9 (left panels). Defect *B1* shows a *switching trap* behaviour: Its emission time below $V_{\mathrm{G}} \sim -0.5\,\mathrm{V}$ is strongly bias dependent and determined by the discharging path $2 \Rightarrow 1' \Rightarrow 1$ given by the first passage time (FPT) $\tau_{\mathrm{e,FPT}}^{1',1}$, see (2.19). Increasing V_{G} shifts the trap level accordingly and the preferred emission path changes to $2 \Rightarrow 2' \Rightarrow 1$ at high V_{G}. On the other hand, *B2* is a *fixed trap* with an (almost) constant emission time over V_{G} which is dominated by $2 \Rightarrow 2' \Rightarrow 1$.

Interestingly, the behaviour of both defects changes in a complex way when the device is stressed at $V_{\mathrm{G}} = -2.8\,\mathrm{V}$ and an increasing drain bias $V_{\mathrm{D}} = [0.0\,\mathrm{V}, -2.8\,\mathrm{V}]$ is applied, see Fig 5.9 (middle and right panels). Defect *B1*, which has been determined to be in the middle of the channel ($0.6L_{\mathrm{G}} - 0.7L_{\mathrm{G}}$) [MJC15, MJJ6], reveals a rather constants capture time. However, at the same time the defects' occupancy dramatically decreases. These observations have two implications. First, defects which are not located in the vicinity of the drain end of the channel can be affected by a drain bias. Second, a feasible explanation for the decreasing occupancy, despite the constant τ_{c}, would be an even faster reduction of the emission time τ_{e}. Thus, the defect would have already partially emitted its charge before the measurement switched to recovery conditions. Separate measurements at different

V_G conditions actually support this idea, see [MJJ6]. The lateral defect position of *B2*, on the other hand, was extracted to be in the drain region of the MOSFET ($0.8L_G - 0.9L_G$) [MJC15, MJJ6]. Although defects on the drain end of the channel should be heavily affected (due to the reduction of F_{ox}), its capture time is almost unperturbed and actually slightly decreasing. Even more remarkably, the occupancy of *B2* is still 0.4 at $V_G = V_D = -2.8\,\mathrm{V}$. This means that in 40% of the TDDS traces the defect was active and captured a charge during stress. Both observations clearly reveal the conceptual limits of simple electrostatic considerations to explain the charging dynamics of oxide defects for $|V_D| \gg 0.0\,\mathrm{V}$. Naturally, a unique parameter set for each defect, extracted by representing their characteristics for *pure* BTI conditions, has been used in all subsequent simulations.

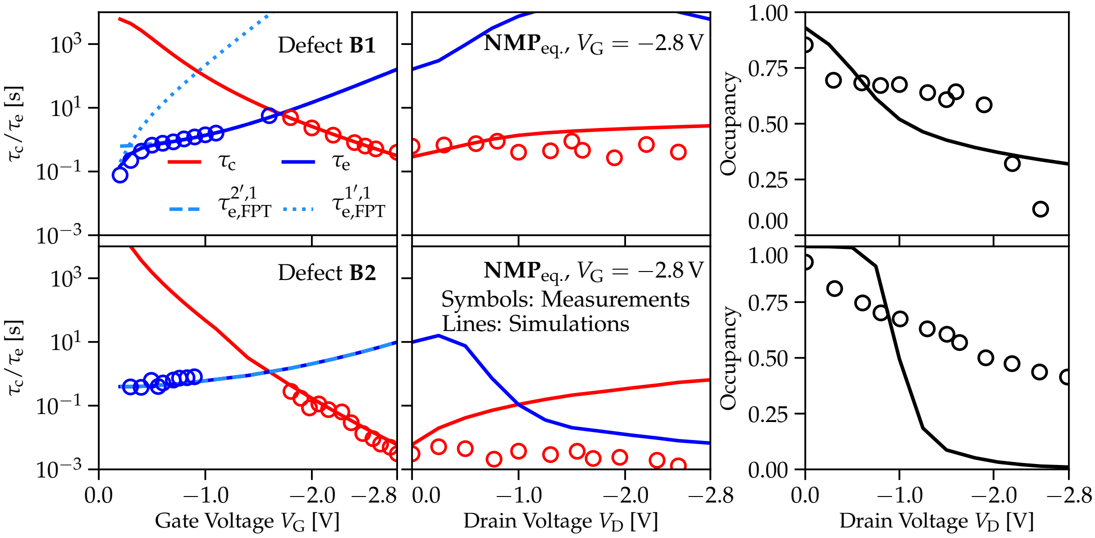

FIGURE 5.9: Experimental characterization of defects *B1* and *B2* versus simulations obtained with the NMP$_{eq.}$ model. **Left:** Trap behaviour for pure BTI conditions to extract their characteristic capture and emission times. **Middle:** τ_e and τ_c trends for increasing drain bias stress. The simulations fail to predict the measured data for the capture time. **Right:** The occupancy at $t_s = 2\,\mathrm{s}$ for various V_D conditions obtained from simulations compared to the experimental ones. The NMP$_{eq.}$ model reveals a different behaviour for both defects and is not able to represent the experimental data set. Symbols: Measurements, Lines: Simulations

Applying the **NMP$_{eq.}$** model yields the results shown in Fig. 5.9. While for *B1* both characteristic trap parameters, τ_c and τ_e, increase due to the changed electrostatics, the emission time of *B2* changes its trend at $V_D \sim -0.5\,\mathrm{V}$. This can be explained due to the formation of the pinch–off region and the associated reduction of the hole concentration. The extracted occupancies of the defects for a stress time of $t_s = 2\,\mathrm{s}$ show a decreasing trend for both traps, see Fig. 5.9 (right panels). However, the measurement data are not properly captured. While the experimental occupancy of *B1* shows a plateau up to $V_D \sim -2.0\,\mathrm{V}$ followed by a rapid decrease, the simulations predict a continuous reduction which saturates at ~ 0.4. In contrast, the simulations for *B2* yield a prompt reduction starting from $V_\mathrm{D} = -1.0\,\mathrm{V}$ and an inactive defect at high V_D, whereas the experimental data show an occupancy of 40%. Even worse, τ_c actually shows an opposite trend compared to the measurements. As expected, only taking electrostatic considerations into account in the NMP$_\mathrm{eq.}$ model is not enough to explain the measured observations.

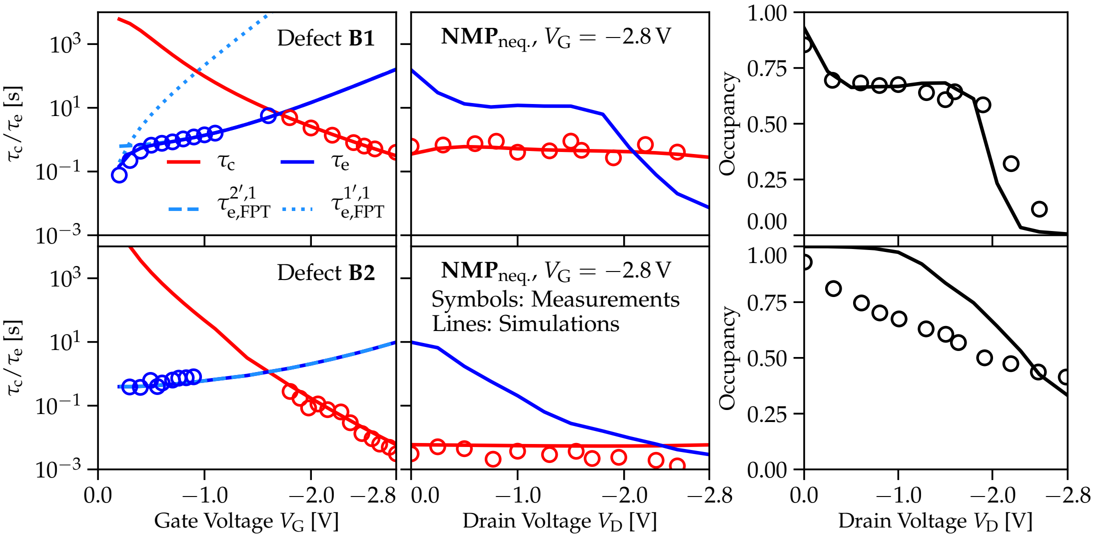

FIGURE 5.10: Experimental characterization of defects *B1* and *B2* versus simulations obtained with the NMP$_\mathrm{neq.}$ model. **Left:** Trap behaviour for pure BTI, the same as in Fig. 5.9. **Middle:** τ_e and τ_c trends for increasing drain bias stress. The simulations properly represent the rather constant capture time for increasing V_D. Furthermore, for *B1* the simulations result in a rapidly decreasing τ_e. **Right:** The occupancy at $t_\mathrm{s} = 2\,\mathrm{s}$ for various V_D conditions obtained from simulations compared to the experimental ones. The NMP$_\mathrm{neq.}$ model is able to capture the intricate and puzzling experimental trends and adequately describes all characteristic quantities of *B1* and *B2*. Symbols: Measurements, Lines: Simulations

In order to improve the quality of the simulations, non–equilibrium effects can explicitly be included within the simulation framework $\mathbf{NMP_{neq.}}$. A thorough description of the interaction with energetic carriers in the valence as well as the conduction band can dramatically increase the corresponding NMP transition rates $k_{i,j}$, see Sec. 4.2 and Fig. 4.9. As shown in Fig. 5.10, this refinement of the 4–state NMP framework yields an accurate description of the defect parameters. All relevant characteristics are well represented by the model. The capture times τ_c for both defects stay approximately constant while the emission times decrease with V_D. This translates into a very good agreement with the measured occupancies of *B1* and *B2*. Specific features, such as the constant occupancy for *B1* between $V_\mathrm{D} = -0.5\,\mathrm{V}$ and $-2.0\,\mathrm{V}$ as well as the remaining active defect *B2* at $V_\mathrm{D} = -2.8V$, are properly captured by the model approach.

A detailed analysis of the respective capture and emission pathways reveals the nature of these interesting phenomena, see Fig 5.11. While the path for charging the defect stays the same over the whole V_D bias range for both defects (1 ⇒

$2' \Rightarrow 2$), the discharging path changes for *B1*, similar to its switching behaviour for pure BTI conditions. At low V_D, *B1* emits its charge via $2 \Rightarrow 2' \Rightarrow 1$, while at elevated V_D the emission time τ_e is determined by the faster pathway $2 \Rightarrow 1' \Rightarrow 1$. In order to understand the interactions with the valence and conduction band as well as the resulting characteristic times, all relevant NMP rates $k_{i,j}$ are given in Fig. 5.11. The relationship between the rates $k_{i,j}$ and the first passage times are given in (2.19). Two important implications can be seen in Fig. 5.11. First, the valence band rates are rather constant (or even slightly increasing) for all stress conditions. This is quite surprising, since the electric field F_ox, and thus the effective trap level, typically determines the transition rates. An increasing drain bias, therefore, results in an inhomogeneous field which decreases towards the drain end of the channel. However, the non–equilibrium EDFs exhibit a pronounced high energy fraction of particles in the VB which compensate this effect, see Fig. 5.1. This phenomenon is particularly important for defects located in the vicinity of the drain end, e.g. *B2*. Second, it is clear that interactions with the conduction band potentially play a major role, specifically for *B1*. Starting from $V_\mathrm{D} < -1.5\,\mathrm{V}$ impact ionization (II) leads to an increasing concentration of (energetic) carriers in the CB. The interaction of the defect with electrons in the CB dominates the respective transition rate $k_{2,1'}$ and thus determines the new and faster emission pathway via $1' \Rightarrow 1$.

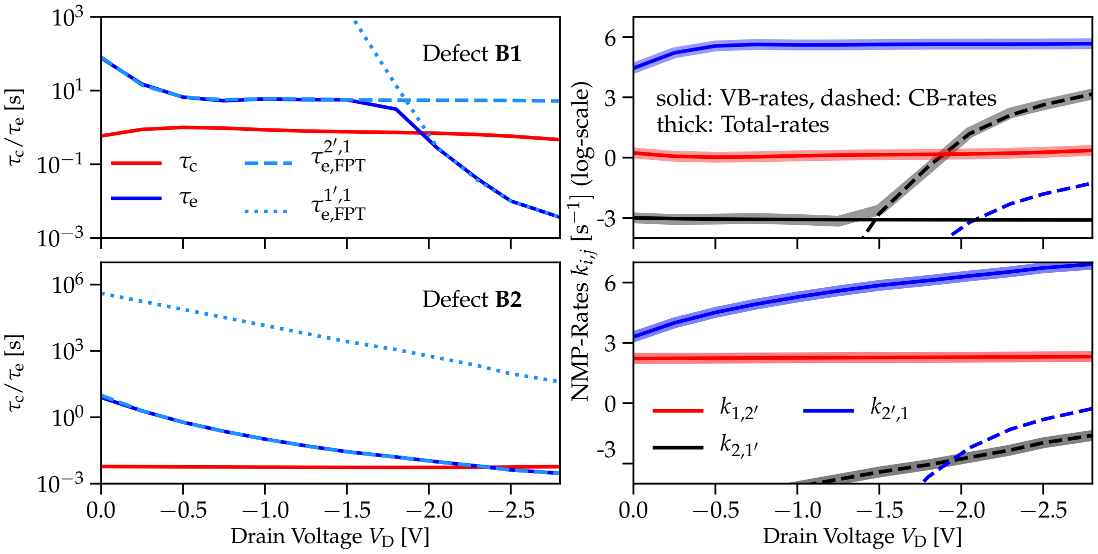

FIGURE 5.11: A detailed analysis of the various stress regimes for increasing V_D bias. **Left:** The simulated capture and emission time together with the first passage times (FPTs) for the two emission pathways using the $\mathrm{NMP_{neq.}}$ model variant. At around $V_\mathrm{D} =\sim -2.0\,\mathrm{V}$ the emission pathway of *B1* switches to the faster one via $1'$. **Right:** The corresponding NMP transition rates $k_{i,j}$ which determine the FPTs split into their VB and CB contributions. While the capture process for both defects is dominated by the interaction with (energetic) carriers in the VB, *B1* exhibits a pronounced interaction with carriers in the CB at higher V_D stress conditions which leads to a change of its emission pathway.

Although the measurement data have been rather puzzling, the non–equilibrium 4–state model NMP$_{\text{neq.}}$, which takes the full spectrum of effects into account, is able to fully explain the peculiar measurement trends. The presented analysis helps to understand how (energetic) holes in the VB and secondary generated (energetic) electrons in the CB interact with defects in the gate stack and thereby validates the modeling approach.

However, accessing the EDFs and including them within the NMP model is typically computationally very demanding and, therefore, not practical for TCAD simulations. The extended variant NMP$_{\text{eq.+II}}$ provides a considerably simplified implementation which does not require an additional solution of the Boltzmann transport equation (BTE) and where further approximations are applicable, such as the band edge approximations. To establish a full picture of the various model variants, Fig. 5.12 shows the simulation results using the NMP$_{\text{eq.+II}}$ model for the two individual defects *B1* and *B2*. For defect *B1* the simplified extended model approach is still able to capture the qualitative features of the full non–equilibrium model NMP$_{\text{neq.}}$, in particular the rapidly decreasing emission time with increasing drain bias V_{D}. This is a direct consequence of the interaction with carriers in the CB, as described in detail in Sec. 4.2. On the other hand, for the second defect, *B2*, the results are almost the same as for the NMP$_{\text{eq.}}$ model variant. However, this was to be expected due to the driving force of the defects' behaviour at increasing V_{D} bias being the interaction with *hot* holes in the VB. Such a peculiar feature can not be properly described by the NMP$_{\text{eq.+II}}$ model.

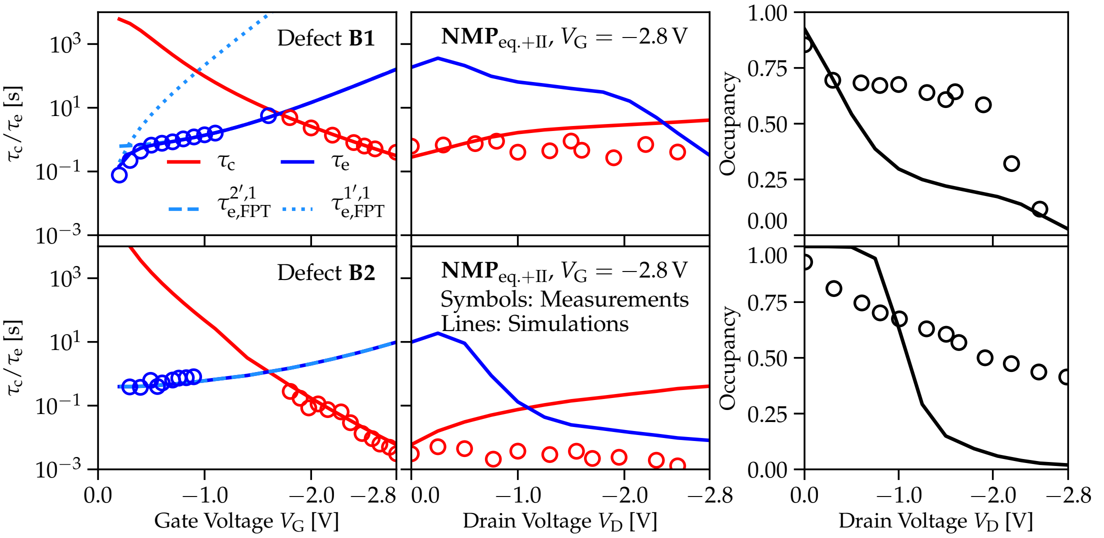

FIGURE 5.12: Simulation results obtained with the NMP$_{\text{eq.+II}}$ model variant for the two defects, *B1* and *B2*, investigated in Section 5.2. While the overall characteristics of *B1* are well captured by the NMP$_{\text{eq.+II}}$ model variant by including the effect of II, it fails to properly reflect the trend of *B2*, which is due to the interaction with energetic carriers in the VB.

Nevertheless, the accelerated decrease of the recoverable component R of degradation with increasing V_{D} bias [MJJ6, 300–303] is assumed to be well captured by the $\mathrm{NMP}_\mathrm{eq.+II}$ model. On the contrary, a potential increase of the defects' occupancy, see [295], due to the interaction with energetic carriers, in contrast, can not be reproduced with this approach. Due to the rather large physical parameter set of a 4–state defect as well as their broad distribution, a general behaviour can hardly be deduced from two single oxide defects. Furthermore, note that the two defects, *B1* and *B2*, have been particularly chosen for this study due to their *abnormal* behaviour. Nevertheless, out of the nine single traps characterized in [MJC15], six defects exhibited *expected* trends with respect to their lateral position.

5.3 Full $\{V_\mathrm{G}, V_\mathrm{D}\}$ Bias Maps

So far, only a very limited number of mainly experimentally driven studies have focused on several aspects of the manifold mutual influences and reactions of the various defect types in full $\{V_\mathrm{G}, V_\mathrm{D}\}$ bias space. In addition to the above mentioned investigations using single oxde traps, studies conducted on large–area devices [MJJ6, 300, MJJ4, 301–306, MJJ2, 307] further support the derived conclusions. They highlight two distinct features in the degradation and recovery characteristics for mixed–mode stress conditions. First, a drift minimum for increasing V_D and fixed V_G is observed, which depends on the applied gate voltage [MJJ6, 300, 302, MJJ2, 307]. Such a minimum was found to be at $V_\mathrm{D} \ll V_\mathrm{DD}$, which is often referred to as inhomogeneous BTI in the literature, and attributed to an inhomogeneous, decreasing, oxide field F_ox across the interface [301]. Second, it was shown that the recoverable component R of degradation reduces disproportionately with increasing V_D [MJJ6, 300–303, MJJ2], where R is almost completely absent for severe drain bias ($V_\mathrm{D} \gg V_\mathrm{DD}$, HCD regime), and that the recovery rate after pure BTI stress ($V_\mathrm{D} = 0\,\mathrm{V}$) is greater compared to mixed–mode conditions ($V_\mathrm{D} \neq 0\,\mathrm{V}$), i.e. the defects' emission times are shifted to longer times [300–302]. However, such rather intricate details can not be captured with simple electrostatic reasoning, where only the lateral dependence of F_ox is taken into account. On the other hand, the aforementioned results suggest that the source side of the channel is also affected by severe mixed–mode/HCD stress conditions. Furthermore, the distribution of accessible defects in the oxide, which actively participate in the degradation and recovery characteristics of the device, also changes with an applied drain bias. A series of recent publication reported by *imec* [308, 309, MJJ9, 310, 311] complements the above findings. Extended studies on n– and p–FETs employing high–κ gate stacks in full $\{V_\mathrm{G}, V_\mathrm{D}\}$ bias space show that non–equilibrium dynamics such as II are a crucial component for the understanding of the damage caused in certain bias space regions, particularly in the off–state stress regime where opposite polarity trapping dominates the degradation due to the available defect bands in SiO_2 and HfO_2. In addition, the degradation and recovery maps in full bias space clearly show that the two main degradation modes – charging of oxide defects due to BTI and the activation of interface traps caused by HCD – concurrently occur and indicate a possible interplay between the different defect types.

The incredible variety of experimental results showing peculiarities of mixed–mode BTI/HCD effects and the implications on the different types of defects facilitate a broad spectrum of explanations which range from macroscopic to microscopic considerations. A *unified* modeling approach which takes into account the multitude of effects associated with the various stress conditions in full $\{V_\mathrm{G}, V_\mathrm{D}\}$ bias space – from electrostatic changes in the device to an appropriate description of carrier transport to atomistic reactions – is therefore beyond the scope of this work.

The present Section aims at a physical description of the phenomena in full $\{V_\mathrm{G}, V_\mathrm{D}\}$ bias space as was shown in [MJJ2]. This ultimately involves the superposition of two reliability models due to the simultaneous occurrence of two phenomena: Charging of oxide defects due to BTI and the creation of interface defects triggered by energetic carriers, known as HCD. The developed methodologies are applied to capture the degradation and recovery characteristics of large–area pMOSFETs over a wide range $\{V_\mathrm{G}, V_\mathrm{D}\}$ stress conditions.

Preliminaries & Calibration

Large–area variants ($W = 10\,\mu\mathrm{m}$) of the pMOSFET devices already used above, see Sec. 5.2, have been investigated to elucidate the behaviour of a collective ensemble of defects in the oxide. To obtain complete degradation maps, the devices were characterized over a broad range of $\{V_\mathrm{G}, V_\mathrm{D}\}$ bias space, larger than the operating condition V_DD. The experiments are based on an extended Measure–Stress–Measure (eMSM) [312] technique where the threshold voltage has been extracted using an ultra–fast setup with a delay after stress of 10^{-6}s. Additionally, after 10 ks of stress time, an individual bias point corresponding to $I_\mathrm{D,lin}$ has been evaluated to quantify its degradation. All measurements have been performed at a temperature of $T = 398\,\mathrm{K}$, unless explicitly stated otherwise. Further experimental details can be found in [MJC15, MJJ6, 300].

A first and essential step towards understanding and modeling the processes responsible for the created damage in each region of the bias map, the models involved need to be calibrated. In order to ensure well calibrated model parameters possessing predictive quality, the respective worst–case conditions for each degradation mode have been chosen, namely $|V_\mathrm{G}| > V_\mathrm{DD}$, $V_\mathrm{D} = 0\,\mathrm{V}$ for BTI and $V_\mathrm{G} \sim 0.5 V_\mathrm{D}$ for HCD.

The effect of **BTI** and the mechanisms responsible for charge (de–) trapping in **oxide defects** has been modeled using the **equilibrium** 4–state NMP model described in Sec. 2.2. As shown in Fig. 5.13 (left panels) the model is able to accurately describe the experimental data sets for a broad range of gate stress conditions V_G and stress times t_s. The extracted NMP parameter set, see Sec. 2.2, is in full agreement with previous reports, particularly the frequently reported defect band in SiON of about 0.8 eV below the silicon valence band (VB), and summarized in Table 5.2.

On the other hand, describing **HCD** and the creation of **interface defects** due to the interaction of energetic carriers with interfacial Si–H bonds is based

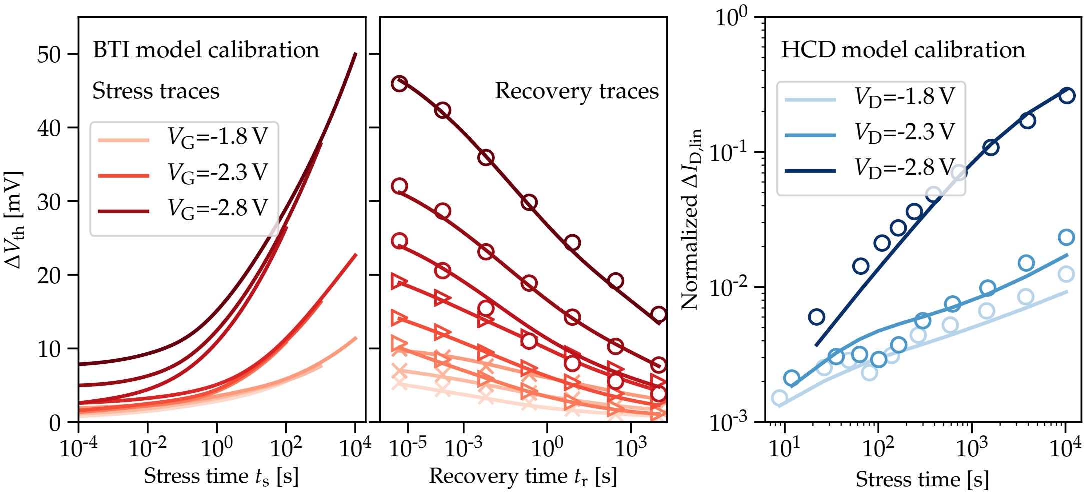

FIGURE 5.13: Calibration of the models used to describe BTI and HCD. **Left:** The $\text{NMP}_{\text{eq.}}$ model has been used to represent various pure BTI stress conditions in order to extract the NMP parameter set which describes the large ensemble of defects. **Right:** The framework introduced in Chapter 4 to model hot–carrier induced degradation has been applied to understand the characteristics of the HCD regime.

	Parameter	μ	σ
E_1	trap level in (stable) state 1	$-0.83\,\text{eV}$	$0.33\,\text{eV}$
$E_{1'}$	trap level in (metastable) state $1'$	$-0.52\,\text{eV}$	$0.42\,\text{eV}$
$E_{2'}$	trap level in (metastable) state $2'$	$0.43\,\text{eV}$	$0.37\,\text{eV}$
$R_{12'}$	squared curvature ratio of 1 and $2'$	1.1	0.48
$R_{1'2}$	squared curvature ratio of $1'$ and 2	0.84	0.48
$S_{12'}$	relaxation energy from $2' \rightarrow 1$	$2.74\,\text{eV}$	$0.81\,\text{eV}$
$S_{1'2}$	relaxation energy from $2 \rightarrow 1'$	$1.68\,\text{eV}$	$0.79\,\text{eV}$
$\epsilon_{11'}$	activation energy from $1 \rightarrow 1'$	$0.43\,\text{eV}$	$0.32\,\text{eV}$
$\epsilon_{22'}$	activation energy from $2 \rightarrow 2'$	$1.16\,\text{eV}$	$0.36\,\text{eV}$

TABLE 5.2: Parameters of the 4–state NMP model used within this work. The positively charged stable configuration 2 is aligned with the valence band and used as a reference.

on the physical framework of **resonance scattering** developed in Chapter 4.1. Due to the large number of bias points included within the following study, the *harmonic model* for HCD, see 4.1, has been used here. The calibrated parameter set is already given in Sec. 5.1. 5.13 (right panel) shows good agreement between simulation and experimental degradation traces which demonstrates the quality of the model. Note that calculated interface defect density has been considered in the simulations using a *donor state* 0.21 eV above the silicon valence band with a Gaussian distribution of 0.18 eV[3].

---

[3] Although interface defects possess an amphoteric character, their acceptor state in the upper half of the band gap can be neglected within the simulations.

Characterization in Complete Bias Space

The experimentally obtained degradation and recovery maps in full $\{V_\mathrm{G}, V_\mathrm{D}\}$ bias space are shown in Fig. 5.14. The maximum threshold voltage drift $V_\mathrm{th,max}^\mathrm{deg}$ is extracted as the first measurement point in the recovery traces with respect to the pristine threshold voltage of the device, whereas the amount of recovery $V_\mathrm{th,max}^\mathrm{rec}$ is defined as the change of the drift after a subsequent 10 ks recovery phase. The degradation map shows a strong degradation in the mixed–mode as well as in the HCD regime with $V_\mathrm{th,max}^\mathrm{deg}$ values ($\sim 150\,\mathrm{mV}$) that are three times larger than for the BTI mode ($\sim 50\,\mathrm{mV}$). Additionally, the data reveal that the transition region, from the HCD mode to the mixed–mode regime, is very sensitive to the applied gate bias V_G, which is particularly pronounced for $V_\mathrm{D} = -2.8\,\mathrm{V}$, see Fig. 5.14. The recovery behaviour on the other hand, shows that almost 70% of the degradation within the BTI stress regime recovers within 10 ks. Towards mixed–mode stress conditions one can observe a strong decreasing trend with finally less than 10% of the created damage being recovered. In the case of pure HCD, which is attributed to a more permanent degradation showing annealing effects only at elevated temperatures, see [221, 248], the recoverable component is almost completely absent. Only 2% of the ΔV_th drift recovers within 10 ks which can be considered negligible.

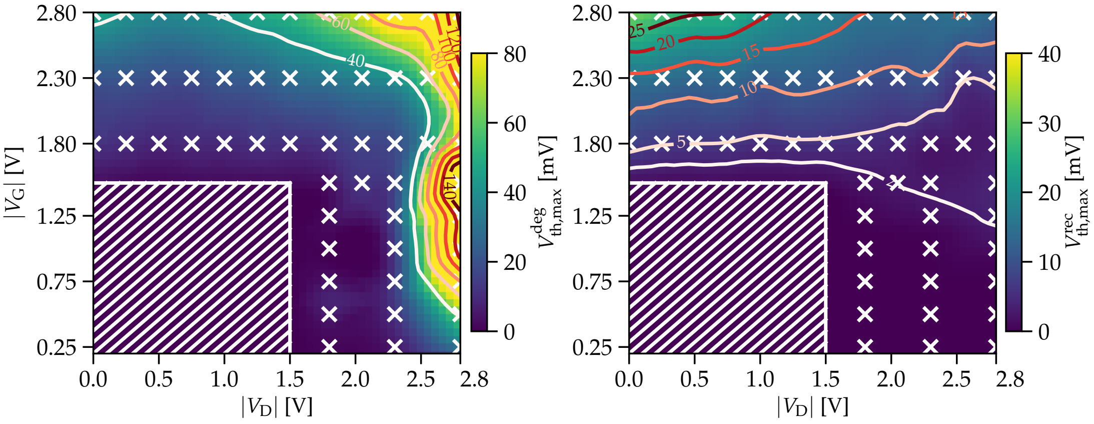

FIGURE 5.14: Experimentally extracted degradation (**Left**) and recovery (**Right**) maps in full bias space above the operating regime V_DD after 10 ks of stress and recovery time, respectively. In total 55 bias combinations have been measured as indicated by the crosses. The maximum degradation is strongly localized in the vicinity of the HCD regime, whereas the damage in the mixed–mode region is much broader and extends towards the non–uniform BTI area. The recovery map only shows a noteworthy contribution in the BTI regime with a decreasing trend towards the mixed–mode and HCD mode. The isolines of $\Delta V_\mathrm{th}^\mathrm{deg/rec}$ provide a better comparability with the simulation results.

In total 63 simulations have been performed in order to assess the behaviour of BTI, HCD and its interplay in full bias space, see Fig 5.15. As was shown in [MJJ4, MJJ2], carrier energy distribution functions (EDFs) not only play an important role for modeling HCD, see Chapters 2 and 4, but also to adequately capture the intricate non–equilibrium dynamics of oxide defects, see Sec. 5.2. Due to the computational effort of the NMP$_\mathrm{neq.}$ model, here the more practical implementation of the full bias space TCAD model for BTI, **NMP$_\mathrm{eq.+II}$** (see Sec. 4.2) is used. Its reduced complexity is more suited for the simulations of a large number of defects typically comprised in large–area devices, since the non–equilibrium EDFs are not considered within this model variant. Instead, the utilized impact ionization (II) model [313] within the DD setup ensures that hole and electron II rates are reasonably well represented and thus provides a suitably accurate description of the defects' interaction with the VB and CB. A detailed motivation and validation of this approach is given below, see Sec. 5.3.

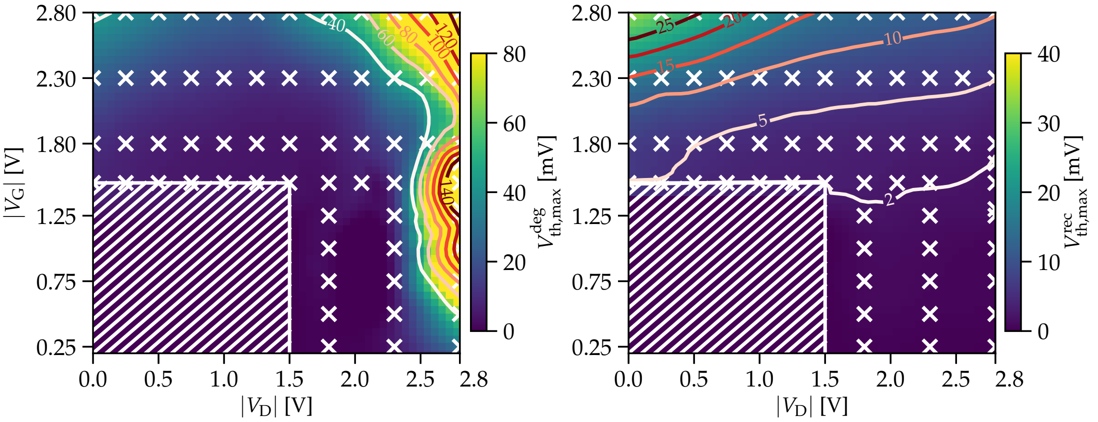

FIGURE 5.15: Simulation results for the bias conditions shown in Fig. 5.14 obtained by using the NMP$_\mathrm{eq.+II}$ model together with the HCD model to describe the effects of charge trapping in the gate oxide as well as the creation of interface states. Overall, the trends for degradation (**Left**) as well as recovery (**Right**) are well reproduced by the simulation approach.

Simulation results for all $\{V_\mathrm{G}, V_\mathrm{D}\}$ bias conditions are summarized in Fig. 5.15. The degradation map is in very good agreement with the experimental data, matching the measured trends well in the (non–uniform) BTI regime and also towards the transitions to HCD and mixed–mode conditions. Moreover, also the recovery behaviour is properly represented using the NMP$_\mathrm{eq.+II}$ model, particularly the strong decrease along increasing drain bias conditions.

Increasing V_D stress enhances the effect of II and the creation of secondary generated carriers along the channel. Defects in the oxide (potentially) interact with the electrons in the CB which typically accelerates their discharging dynamics, see Sec. 5.2. This effect also perturbs trap characteristics in the source and channel region of the device, see Fig. 5.16, which shows a comparison of the NMP$_\mathrm{eq.}$ and NMP$_\mathrm{eq.+II}$ model for a large ensemble of spatially distributed defects across the oxide. One can clearly see that for $V_\mathrm{G} = V_\mathrm{D} = -2.8\,\mathrm{V}$ the reduction of charged defects is enhanced using the NMP$_\mathrm{eq.+II}$ model variant: Less defects are charged within the channel region of the device which leads to a decreasing contribution of BTI as well as a reduction of the recoverable component. Such considerations are beyond electrostatic approximations which would overestimate the contribution of BTI during stress and recovery. Furthermore, note that this decreasing trend seems to be universally valid across the $\{V_\mathrm{G}, V_\mathrm{D}\}$ recovery map, see Figs. 5.14 and 5.15, and in detail in Fig. 5.17 which shows one–dimensional cuts along increasing V_G and V_D bias conditions.

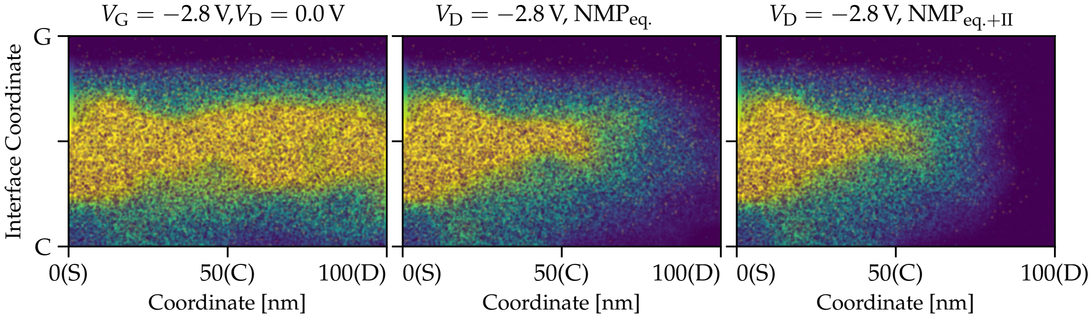

FIGURE 5.16: Simulation snapshots directly after stress comparing the distribution of charged defects across the oxide for pure BTI conditions (**Left**) and severe mixed–mode stress using the NMP$_\mathrm{eq.}$ model (**Middle**) and the extended variant NMP$_\mathrm{eq.+II}$ (**Right**). One can see that, in addition to electrostatic considerations, the NMP$_\mathrm{eq.+II}$ model takes the effect of II into account which results in a decreasing charge density in the middle of the channel.

On the other hand, the degradation characteristics across full bias space follows a more complicated behaviour, see Figs. 5.17 and 5.18. Horizontal cuts (at a fixed V_G) are intuitive to understand: The total degradation in the non–uniform BTI regime initially reduces, mainly due to the decreasing oxide field F_ox along the interface and thus the amount of charged traps. However, this trend is subsequently reversed for higher drain biases towards mixed–mode conditions due to the onset of HCD and the additional damage caused by the creation of interface defects. Fig. 5.18 shows the full $I_\mathrm{D} - V_\mathrm{G}$ curves along the cut. Note that, while oxide defects tend to only *shift* the curves, interface traps additionally severely affect the mobility, therefore, also degrade the sub–threshold slope.

While the overall agreement between measurement and simulations characteristics is very good, one feature is not properly captured: The degradation minima visible in the non–uniform BTI regime are shifted towards higher V_D conditions within the simulations compared to the experimentally extracted values. This leads to an underestimated degradation around $V_\mathrm{D} = V_\mathrm{DD}$, which is particularly pronounced for $V_\mathrm{G} = -2.8\,\mathrm{V}$. At the same time, however, the recoverable component, which is only attributed to discharging of oxide defects, is well represented by the model approach, see Fig. 5.17.

Vertical cuts along constant V_D conditions reveal a more complex behaviour, particularly for $V_\mathrm{D} = -2.8\,\mathrm{V}$. Initially, the total degradation increases towards the worst–case HCD stress bias ($V_\mathrm{G} = -1.5\,\mathrm{V}$, $V_\mathrm{D} = -2.8\,\mathrm{V}$), then, however, significantly drops and subsequently the collective degradation increases again towards $V_\mathrm{G} = V_\mathrm{D} = -2.8\,\mathrm{V}$, eventually causing a threshold voltage shift close to the

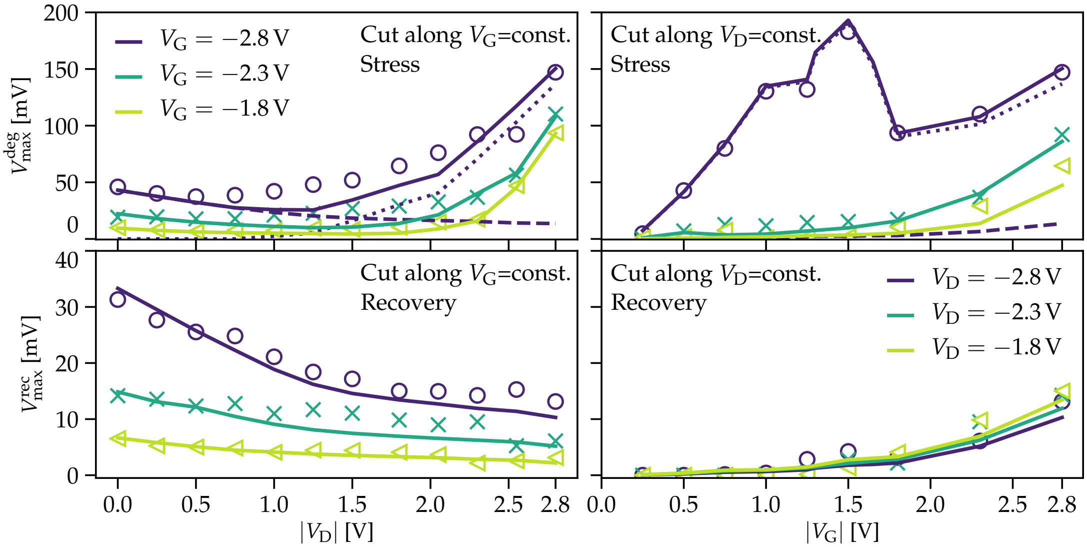

FIGURE 5.17: Cuts along horizontal lines (V_G–cut, **Left**) and vertical lines (V_D–cuts, **Right**) of the experimental and simulation degradation (**Top**) and recovery (**Bottom**) maps. Degradation and recovery traces for all $\{V_G, V_D\}$ combinations agree well with the measurement data (symbols). For the most severe stress condition within the cuts the individual contribution of oxide defects (dashed lines) and interface defects (dotted lines) is shown. The effect of recovery is assumed to be only attributed to oxide defects.

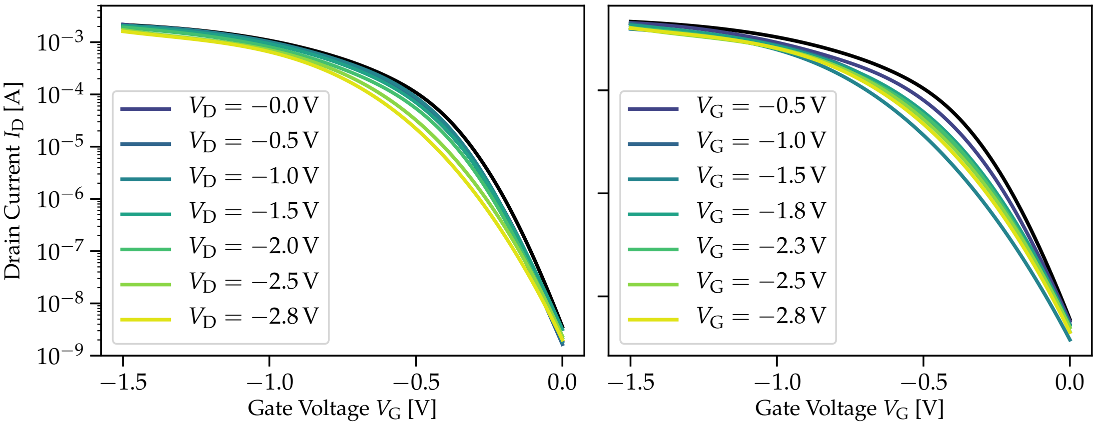

FIGURE 5.18: $I_D - V_G$ curves considering the effects of oxide and interface defects onto the device characteristics. **Left:** Cut along $V_G = -2.8$ V and increasing drain bias stress. **right:** Cut along $V_D = -2.8$ V and increasing gate bias stress.

$\Delta V_{th,max}$ at the overall worst–case conditions of the HCD regime. Note that such a feature is not clearly visible for reduced V_G bias conditions. Not surprisingly, the simulations show that the damage along these cuts is mainly governed by HCD and the creation of interface defects, while charged oxide traps only play a minor role at severe mixed–mode stress. Assuming that recovery is only due to oxide defects, this is also visible in the recovery traces, see Fig. 5.17. This trend, however, can be fully understood by considering the corresponding EDFs, though a self–consistent solution of the bipolar BTE is mandatory for a proper understanding. Fig. 5.19 shows isolines of the corresponding hole ($\mathrm{EDF_p}$) and electron ($\mathrm{EDF_e}$) EDFs along the Si/SiO$_2$ interface at 1 eV and 2 eV, respectively for the cuts with $V_\mathrm{G} = -2.8\,\mathrm{V}$ (left) and $V_\mathrm{D} = -2.8\,\mathrm{V}$ (right). Quite as expected, for fixed V_G and increasing V_D a higher concentration of *hot* holes is visible at the drain side which eventually trigger the effect of impact ionization (II) and cause a substantial accumulation of (energetic) electrons at the source end of the channel.

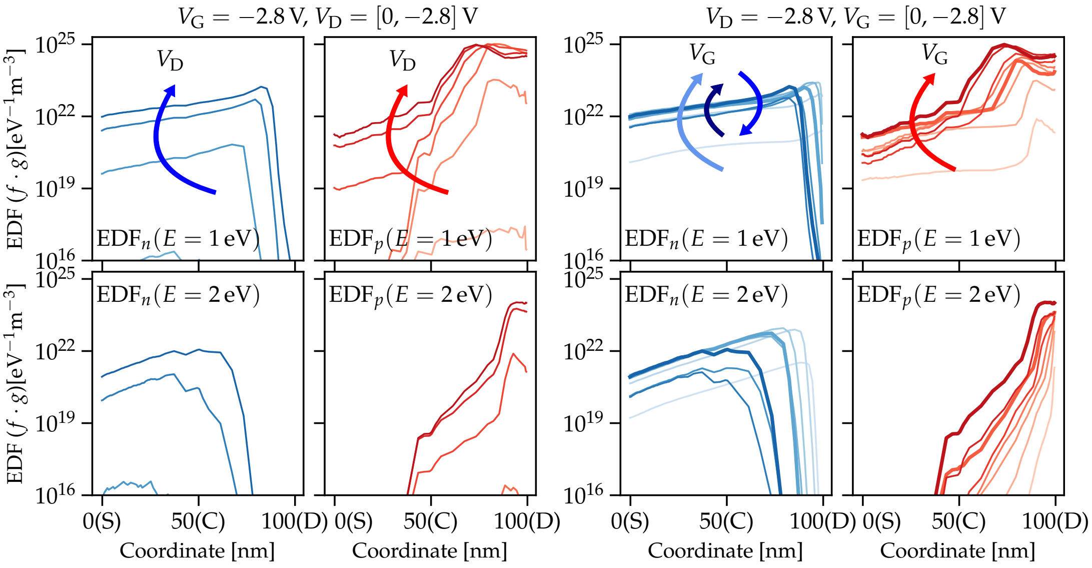

FIGURE 5.19: Energy isolines of the corresponding hole and electron EDFs along the channel/oxide interface at 1 eV (**Top**) and 2 eV (**Bottom**), respectively. **Left:** EDFs at a constant gate bias $V_\mathrm{G} = -2.8\,\mathrm{V}$ and increasing drain bias. **Right:** EDFs at a constant drain bias $V_\mathrm{D} = -2.8\,\mathrm{V}$ and increasing gate bias.

This effect has two implications. First, an acceleration and propagation of hot–carrier induced damage along the channel due to secondary generated *hot* electrons. Second, possibly modified discharging dynamics of oxide defects due to the interaction with electrons in the CB, which is covered within the $\mathrm{NMP_{eq.+II}}$ model. The cut along fixed $V_\mathrm{D} = -2.8\,\mathrm{V}$, on the other hand, discloses a more intricate V_G dependence. For increasing V_G up to $-1.5\,\mathrm{V}$ the impact ionization rate monotonously increases which is reflected in an increasing concentration of electrons with a substantial energy along the channel. Therefore, the damage in the HCD regime, particularly at the worst–case stress conditions ($V_\mathrm{G} = -1.5\,\mathrm{V}$, $V_\mathrm{D} = -2.8\,\mathrm{V}$, corresponds to $I_\mathrm{sub,max}$), is equally caused by energetic holes and electrons and distributed along the whole channel. Increasing V_G further indeed enhances the energy of holes at the drain side; however, it actually reduces the electronic energies along the channel towards the source side, see Fig. 5.19. This leads to a reduction of the interface state density in the respective regions. Since the density of interface states in the drain region is already saturated, the overall degradation reduces, starting from $V_\mathrm{G} = -1.5\,\mathrm{V}$. Only at severe mixed–mode stress bias this trend is reversed and electrons again gained more energy. Likewise, the threshold voltage drift ΔV_th again increased to a value similar to the worst–case conditions, see Fig. 5.17.

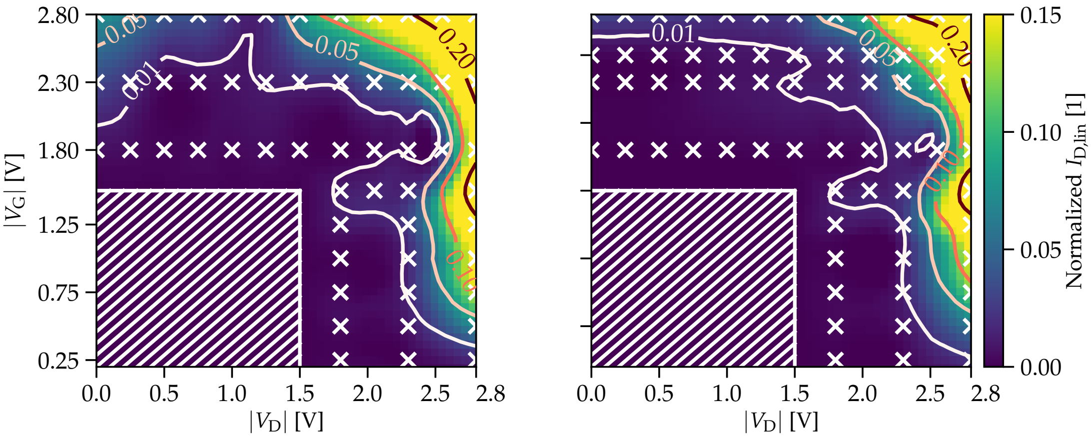

FIGURE 5.20: Experimental (**Left**) versus simulationed (**Right**) degradation map after 10 ks of stress using $I_\mathrm{D,lin}$ as a measure to quantify the generated damage. The results are qualitatively very similar to the ΔV_th drifts shown in Figs. 5.14 and 5.15.

Traditionally, studies related to hot–carrier induced damage analyze the degradation of the linear or saturation drain current, $\Delta I_\mathrm{D,lin}$ or $\Delta I_\mathrm{D,sat}$. However, the corresponding bias conditions would impose an additional stress during the recovery sequence and adversely affect the measurement results. Nevertheless, a single bias point associated with $I_\mathrm{D,lin}$ has been measured after 10 ks of stress. The measurement versus simulation results are shown in Fig. 5.20. Qualitatively, the behaviour is similar to the ΔV_th shifts shown above. While the simulations again agree very well with the experimental data in the highly damaged regions, the agreement deteriorates in the (non–uniform) BTI regime. The measurement data show a notable degradation of the linear drain current also in the BTI region as well as a degradation minimum around $V_\mathrm{D} = -1.2\,\mathrm{V}$, which is shifted towards higher $|V_\mathrm{D}|$ values compared to the drift minimum position of ΔV_th, see Fig. 5.14. On the contrary, the simulations predict a rather constant $I_\mathrm{D,lin}$ degradation in this regime(s) with no clear minimum visible. A possible explanation for this discrepancy could be the widely accepted assumption that BTI indeed creates defects at the Si/SiO$_2$ interface [1, 12, 16]. However, due to the empirical modeling approach used to account for this effect it has not been considered here. The creation of interface defects has been exclusively modeled using the (harmonic) HCD model which, however, predicts a vanishing contribution due to the equilibrium carrier EDFs within the BTI regime.

The presented results, see [MJJ2], and analysis clearly show that device degradation in full $\{V_\mathrm{G}, V_\mathrm{D}\}$ bias space can only be modeled and understood by performing thorough transport simulations and using proper modeling frameworks which take the fundamental physics into account.

Benchmark: NMP$_{\text{eq.+II.}}$ versus NMP$_{\text{neq.}}$

In order to be confident that the results presented above truly represents the dynamics of oxide defects under an applied drain bias, the assumptions of the NMP$_{\text{eq.+II}}$ need to be verified against the computationally most expensive full model variant NMP$_{\text{neq.}}$. Fig. 5.21 shows the results for a large ensemble of defects contained in the large area pMOSFETs simulated with all three different model variants and two stress conditions, namely $V_\text{G} = -2.8\,\text{V}$ and $V_\text{D} = -1.5\,\text{V}$ (upper pannels) and $V_\text{D} = -2.8\,\text{V}$ (lower panels). One can clearly see that the NMP$_{\text{eq.}}$ model overestimates the degradation, and hence, the recovery due to oxide defects. The other two approaches, NMP$_{\text{eq.+II}}$ and NMP$_{\text{neq.}}$, yield similar and consistent results with only minor differences visible in the stress and recovery characteristics. These subtle differences arise due to non–equilibrium EDFs and the heated carrier ensemble which is considered in the NMP$_{\text{neq.}}$ model.

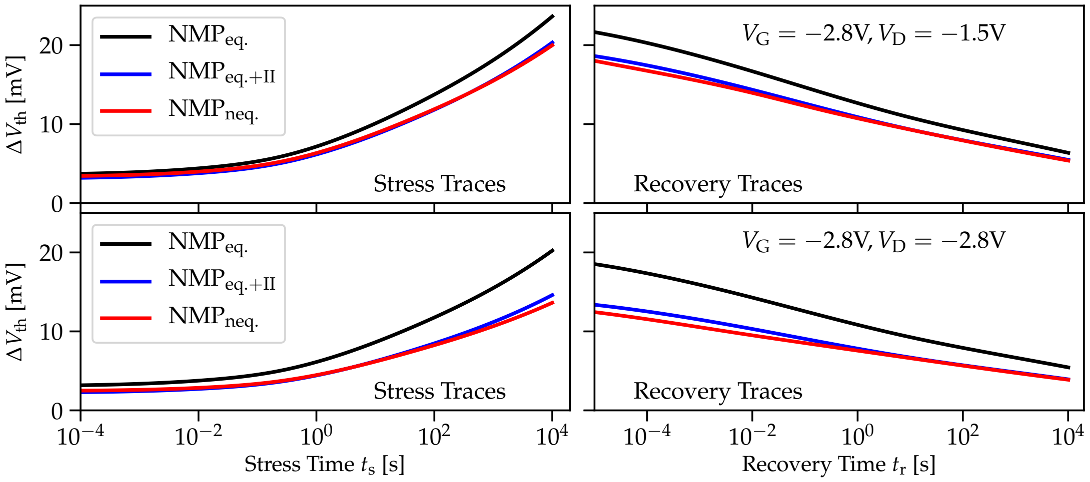

FIGURE 5.21: Benchmark of the three different model variants for two different stress conditions within the mixed–mode stress regime. The NMP$_{\text{eq.+II}}$ and the NMP$_{\text{neq.}}$ model yield similar results for large statistics of defect distributions across the gate oxide of the device.

To gain a detailed understanding of how exactly heated carriers and the non–equilibrium EDFs influence the degradation and recovery dynamics of large area MOSFETs, the defect distribution needs to be looked at in more depth. Fig. 5.22 shows simulation snapshots for $V_\text{G} = V_\text{D} = -2.8\,\text{V}$ after 10 ks of stress calculated with the NMP$_{\text{eq.}}$ and the NMP$_{\text{neq.}}$ model variant compared to results for *pure* BTI conditions at $V_\text{D} = 0.0\,\text{V}$. Clearly visible is the uniform distribution of the charge density along the Si/SiO$_2$ interface (upper panel) for defects above the Fermi level of the device (lower panel). Increasing the drain bias illustrates the well known effect of a non–uniform oxide field F_ox which shifts the trap levels below E_F, particularly at the drain side, where they remain neutral. Taking the non–equilibrium EDFs into account reveals that fewer defects in the channel (and partly at the source side) are able to capture a charge, thereby reducing the total amount of degradation and recovery. On the other hand, defects located in the vicinity of the drain end potentially interact with the heated carrier ensemble and become charged, even though their effective trap level is well below E_F. Within the simulations, however, only around $\sim 2\%$ of the active defects exhibit an increased occupancy proportional to the drain voltage V_D. The measurement data presented in [295] further support this finding.

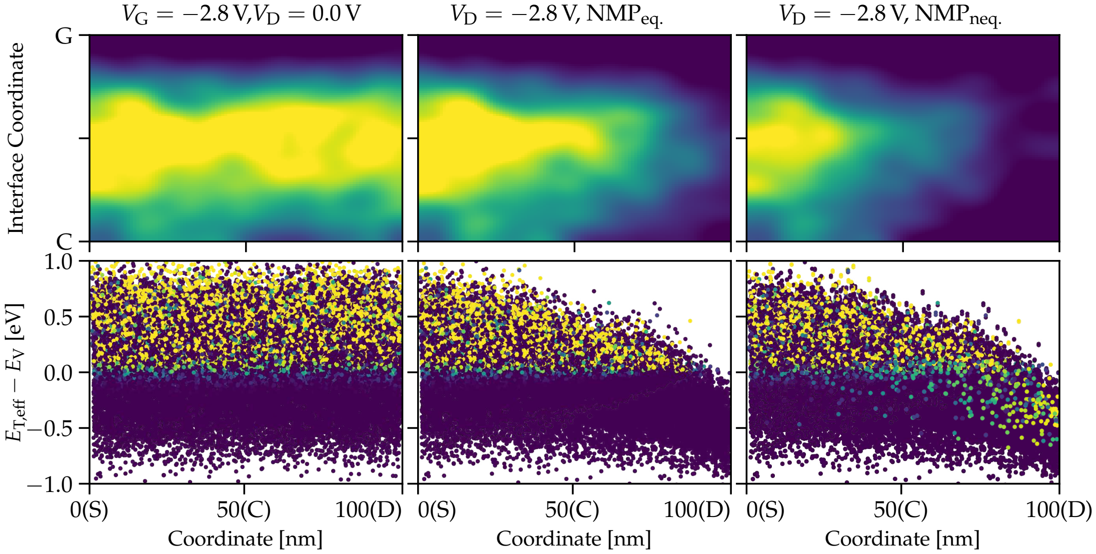

FIGURE 5.22: Detailed comparison of the NMP$_\mathrm{eq.}$ versus the NMP$_\mathrm{neq.}$ approach applied to model the behaviour of a large area pMOSFET stressed at severe mixed–mode conditions, $V_\mathrm{G} = V_\mathrm{D} = -2.8\,\mathrm{V}$. The simulation snapshots compare the distribution of charged defects across the oxide simulated with both model variants. Using the NMP$_\mathrm{eq.}$ model, traps in the vicinity of the source region are unaffected by a drain bias V_D, while defects in the middle of channel and, particularly, located at the drain side stay uncharged due to the reduced oxide field F_ox and the shifted effective trap level. On the other hand, the NMP$_\mathrm{neq.}$ model predicts an even more reduced charge density which is extended towards the source side of the device. Furthermore, one can see that defects in the drain region *remain* charged due to the interaction with energetic carriers.

To conclude, the presented simulation benchmark supports the validity of the extended model NMP$_\mathrm{eq.+II}$ and indicates that the impact of an increased drain bias onto oxide defects is mainly due to the interaction with secondary generated carriers by II.

5.4 Alternating Stress Modes

To finally stress the conceptual limits of independent degradation mode descriptions, the following experiments and simulations have been performed using alternating stress conditions followed by a final relaxation phase, see [MJJ2]. In total 14 devices, divided into two groups, have been stressed and measured at a temperature of $T = 443\,\mathrm{K}$ and bias conditions of $V_\mathrm{G} = -2.8\,\mathrm{V}$, $V_\mathrm{D} = 0.0\,\mathrm{V}$ (BTI)

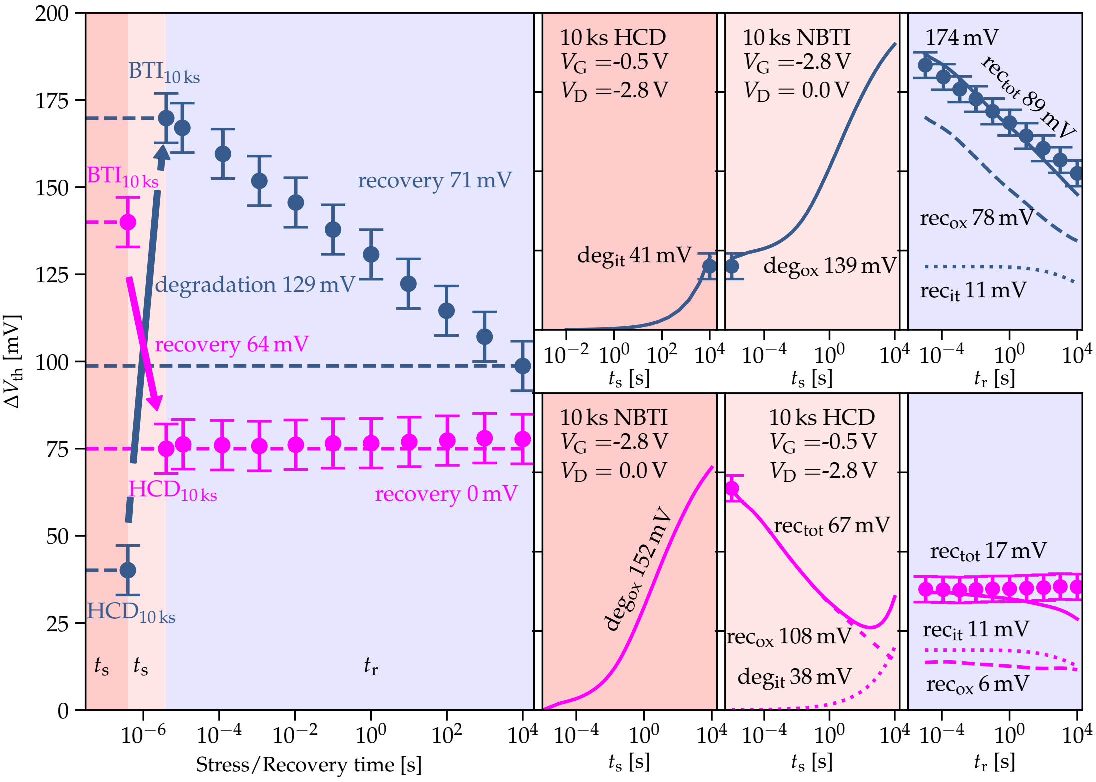

FIGURE 5.23: Experimental and simulation results for the alternating stress conditions experiment. **Left:** Measurement data for 7 devices subjected to each sequence. While HCD⇒BTI (blue) is intuitive to understand, BTI⇒HCD (magenta) exhibits an *abnormal* recovery trend starting from the HCD stress phase. **Top Right**: Simulation results for the first group. In this case HCD only adds a (permanent) damage whereas BTI follows the well known behaviour. **Bottom Right:** Results obtained for the second group. The first BTI cycle proceeds as expected, however, the subsequent HCD stress actually accelerated the discharging dynamics of oxide defects due to the effect of II and simultaneously creates additional damage due to interface states.

and $V_\mathrm{G} = -0.5\,\mathrm{V}$, $V_\mathrm{D} = -2.8\,\mathrm{V}$ (HCD). The first group was subjected to 10 ks of HCD stress followed by a 10 ks BTI stress phase and a final relaxation of 10 ks at recovery conditions ($V_\mathrm{G} = -0.5\,\mathrm{V}$, $V_\mathrm{D} = 0.0V$). The stress sequences have been switched for the second group of devices, i.e. BTI with a subsequent HCD cycle and a final relaxation phase. The acquired experimental data set is summarized in Fig. 5.23. After the HCD stress cycle the first group experiences a threshold voltage shift of $\Delta V_\mathrm{th} = 40\,\mathrm{mV}$, which increases to a drift of $\Delta V_\mathrm{th} = 170\,\mathrm{mV}$ due to the subsequent BTI cycle. Within the relaxation phase the degradation recovers to $\Delta V_\mathrm{th} = 98\,\mathrm{mV}$. Interestingly, if BTI is applied prior to HCD, the first stress phase creates $\Delta V_\mathrm{th} = 140\,\mathrm{mV}$ of total degradation. Even more intriguingly, it seems that the following 10 ks HCD stress does not trigger additional damage, but rather decreases the ΔV_th shift by 65 mV. Moreover, the final 10 ks relaxation period does not show any additional recovery effect. By means of the simulation framework introduced above, see Sec. 5.3, a combination of the hot–carrier degradation model and the $\mathrm{NMP}_{\mathrm{eq.+II}}$ model developed in Chapter 4, it is possible to shed light on the mechanisms behind this puzzling phenomenon. The results for the first group of devices (HCD⇒BTI⇒Relaxation) is illustrated in the top panels of Fig. 5.23. The initial *pure* hot–carrier stress induces $\sim 45\,\mathrm{mV}$ of degradation, mainly due to the presence of energetic electrons at this specific (off–state–stress) bias combination, see Fig. 5.19 (left panels). The subsequent BTI stress and relaxation cycle follows the well known characteristics of NBTI, matching the experimental results very well. One can, therefore, conclude that HCD only adds a *pre–existing* damage to the device, which slightly perturbs the device electrostatics, but without further implications for oxide defects.

The situation for the second group of devices, exposed to the sequence BTI⇒HCD⇒Relaxation, is quite different, as is show in the bottom panels of Fig. 5.23. Starting with BTI, the device experiences $\sim 140\,\mathrm{mV}$ of drift. Due to the device being *fresh*, i.e. without any damage at the interface, this value is slightly higher than for the BTI sequence within the first group. The following 10 ks HCD stress reveals an interesting behaviour. Contrary to the assumption that another portion of damage will be added to the device, the chosen HCD condition strongly influences the discharging dynamics of oxide defects. The high concentration of secondary generated electrons along the channel, see Fig. 5.19, effectively accelerates the discharging dynamics of charged oxide traps which leads to an increased recovery of BTI damage. The competing effect of newly created damage due to HCD, however, masks this mechanism within the experiments and is only accessible by simulations. Note that the impact of HCD is slightly reduced due to charged oxide defects perturbing the device electrostatics. Within the final relaxation phase the simulations predict a total recovery of 17 mV, whereas the experimental data show a flat line for 10 ks. For the sake of completeness the effect of interface state recovery according to the mechanism proposed by STESMANS [221] has also been included within the final relaxation sequence. However, as apparently visible in the measurements for the second device group, this mechanism is absent within the recorded traces. Neglecting this effect would lead to an even better agreement between simulations and experiments for the last recovery phase.

CHAPTER 6

Conclusions & Outlook

6.1 Conclusions

The present work addressed open questions associated with non–equilibrium reliability issues such as the creation of defects at the Si/SiO_2 interface and the charging kinetics of pre–existing oxide traps. A profound understanding of the involved processes is not only a vital component for the description of the individual degradation regimes, hot–carrier degradation (HCD) and non–equilibrium bias temperature instability (BTI), but also an essential step towards full $\{V_G, V_D\}$ bias space characterizations.

A major part of this thesis focuses on the **interaction of energetic carriers with Si–H bonds** at the Si/SiO_2 interface region. New concepts and methodologies have been introduced to capture the intricate behaviour of hot–carrier induced degradation. A *resonance scattering excitation mechanism* has been identified as the main driving force of Si–H bond rupture and the subsequent creation of an interface defect. While this idea was already proposed in one of the pioneering papers published by the group of Hess, it was not rigorously pursued in any implementation. Ultimately, the derived framework considers all relevant external influences such as energetic carriers and an applied electric field as well as dissipation processes due to the surrounding environment. In conjunction with *ab initio* methods which allowed to extract essential parameters for all individual contributions, the presented modeling approach provides detailed insight into the phenomenon of HCD. Additionally, density functional theory calculations have been used to finally reveal the microscopic Si–H bond breaking mechanism at the semiconductor–oxide interface. Subsequent H migration trajectories and passivation reactions based on H_2 cracking have been further investigated to establish a complete picture of hydrogen at the Si/SiO_2 interface. The established model has been applied to capture the trends of HCD in two devices, an nMOSFET and a pMOSFET with different channel lengths. Together with a detailed analysis the simulation results give new insight into the degradation characteristics and provide an accurate description on a microscopic level using a consistent parameter set.

The physically meaningful concept of a resonance based mechanism, furthermore, highlights some intriguing findings. First, the approach is *virtually* free of any fitting parameters due to its combination with *ab initio* based methods. Second, the previously used phenomenological *multiple carrier* and *single carrier* processes are actually a manifestation of the same fundamental interaction, a *resonance scattering* excitation. Moreover, besides the physical interpretation, the presented formulation allows for another intuitive understanding of another peculiarity of HCD: Occasional reports suggest that the degradation in nMOS devices is larger than in their pMOS counterpart. Considering that the available resonance state for holes is higher in energy than for electrons, as suggested by the DFT study, would facilitate the first physically reasonable explanations. Finally, note, that the methodology is free of empirical parameters and widely applied in the field of quantum chemistry describing surface phenomena. Thus, the formulations is generally applicable to new and emerging material combinations, such as SiGe or graphene based devices.

The second topic discussed in this thesis the **dynamics of oxide defects interacting with energetic carriers**. Usually, charge trapping at pre–existing defect sites in SiO_2 is investigated around the respective worst case conditions for BTI, namely at equilibrium conditions. Unfortunately, only a very limited number of studies is available reporting data regarding the behaviour of oxide defects with increasing drain bias stress. However, the vast majority of these observations concludes that a simple electrostatic consideration is not sufficient to explain the measurements. Therefore, the current 4–state NMP framework has been extended towards non–equilibrium energy distribution functions (EDFs), which includes the interaction with a *heated* carrier ensemble in the valence and conduction band[1] Since the NMP model already takes a whole band of states into account using the concept of the lineshape function (LSF), the natural extension only requires the implementation of the respective EDFs. Two model variants with increasing complexity have been introduced: a full non–equilibrium variant $\mathrm{NMP_{neq.}}$ which considers a self–consistent solution of the coupled Boltzmann transport equation for electrons and holes, as well as an extended approach $\mathrm{NMP_{eq.+II}}$ where the effect of impact ionization (II) has been approximated using semi–empirical models.

The different model variants have been compared against experimentally recorded characteristics for two individual oxide defects for a broad range of stress conditions. The rather puzzling measurements trends can be fully understood by taking the interactions with energetic minority and secondary carriers into account. As was shown in a detailed analysis such an interplay can lead to a substantially different trap behaviour. Interestingly, the presented study reveals that even defects located at the source side of the device can be heavily affected by an applied drain bias.

Finally, both individual modeling frameworks have been used in conjunction culminating in a rigorous simulation study of a pMOSFETs full $\{V_\mathrm{G}, V_\mathrm{D}\}$ bias map. The comprehensive study reveals the degradation and recovery dynamics over a wide range of bias conditions by explicitly modeling the charge transition kinetics of oxide defects as well as the creation of interface states. The simulation results properly capture the experimental trends and are further supported by a detailed analysis of the involved mechanisms. Additionally a dedicated experiment performing alternating BTI and HCD stress cycles revealed a peculiar feature of *accelerated* recovery conditions.

The established results provide an in–depth description and understanding of degradation and recovery dynamics in full bias space and ultimately stress the conceptual limits of independent degradation regimes.

6.2 Outlook

A fundamental understanding of reliability issues on a microscopic scale provides the basis for new developments and emerging technologies alike in the field of microelectronics. The concepts derived within this thesis enable new insight into

---

[1] This, however, depends on the applied bias conditions.

the main degradation modes and should serve as a basis for subsequent research activities. In the following some ideas are listed which hopefully inspire subsequent studies.

Atomistic Models need to be thoroughly analyzed. The utilized Si/SiO$_2$ interface structures exhibit a cell size of $16 \times 16 \times 32\,\text{Å}$ with around 475 atoms. Although their geometrical and electronic properties compare well to experimental perceptions, see Section 3.1 and Appendix A, a rather large residual strain at the interface seems to be present. Test calculations with increasing xy and z dimensions, see Appendix A, indeed show pronounced relaxation effects for both variants. Therefore, further insights into the actual oxidation process are required for a better microscopic picture of the Si/SiO$_2$ transitions regions. Currently, these next steps are part of the EU project "Modeling Unconventional Nanoscaled Device FABrication" (MUNDFAB) which should help to identify the optimal atomistic model dimensions in terms of accuracy and computational effort.

Defect Configurations and their properties have been investigated in Sec. 3.1 as well as in Appendix B. Selected P_b center configurations within this thesis reflect the prevailing opinion of an sp^3 hybridized dangling bond orbital together with an amphoteric trap level character [84, 88, 91, 93]. However, their detailed microscopical structure can not be fully validated using this information. An ultimate benchmark offers the selectivity of electrically detected magnetic resonance (EDMR), a method frequently used in the literature. Thus, the theoretical values for the defect electronic structure and the (super–) hyperfine interactions can directly be compared to experimental data [314, 315]. The utilized DFT setup, see Chapter 3, however, is not suitable for such calculations, as they require an *explicit* description of the *core electrons*, and hence, an *all electron basis set*[2].

Resonance scattering mechanisms as introduced in Chapter 2 and theoretically described in Chapter 4, are commonly used to explain electron stimulated and current driven desorption phenomena on surfaces [102, 103, 316]. Despite the use of *ab initio* methods to characterize this process, see Chapter 3, a more rigorous approach utilizing time dependent density functional theory (TDDFT) could complement the findings. TDDFT explicitly takes the wavefunction of the incident charge carriers into account and allows one to study the interaction between a single electron and a molecular resonance [317, 318]. Thereby, the *hot* electron directly probes the resonance state and its properties. Furthermore, once the electron scattered at the resonance and the Si–H bond has been excited, the actual bond breaking dynamics can be simulated in real time using TDDFT.

The resonance potential energy curves $V^{-/+}(q)$ presented in Chap. 3 have been calculated assuming the *same* bond breaking trajectory as for the *neu-*

---

[2] Note that such a *complete* basis set dramatically increases the computational efforts.

tral configuration $V(q)$. However, the excited state motion of the Si–H bond, or more generally, adsorbates, possibly follows substantially different dynamics[3]. Hence, a more rigorous description of the negatively and positively charged potential energy surfaces is highly desired. Constrained DFT [238, 319] and Δ self–consistent field [320–322] are two methods particularly suited for such calculations, although computationally challenging for the Si/SiO$_2$ system.

Recovery Dynamics of interface defects need to be further investigated. Despite the predominant and experimentally validated opinion that H_2 is responsible for the passivation of active P_b centers [221, 222, 248, 249], several important question remain open. First, the preferred H_2 cracking site and the reaction pathway of the remaining H atom. Expanding on the results presented in Section 3.6, a much larger statistics of possible reactions within the SiO$_2$ network is required to identify the dominant dynamics. Second, while the various experimental studies extracted consistent energies of P_b center passivation between 1.4 and 1.6 eV, the reaction rate constant within the formula proposed by STESMANS is largely treated as an empirical *fitting* parameter. Values between 10^{-4} and $10^{-9}\,\text{cm}^3/\text{mol}\,\text{s}$ have been reported which seems inconsistent with a unique reaction [248, 249]. A possible explanation could be given in terms of the different technologies used for the studies. While the H_2 content as well as the associated reactions in devices having thicker oxides ($> 10\,\text{nm}$) are mainly determined by SiO$_2$ bulk properties, their characteristics in thinner oxides ($< 4\,\text{nm}$) can be distorted due to the influence of the interfacial regions, see Section 3.1 and Appendix A. Assuming an interfacial transition region of 0.5 nm, a substantial part of the oxide is governed by the SiO$_2$ properties of the transition region, e.g. distorted bond lengths and angles. However, this idea needs to be thoroughly tested using *ab initio* methods.

Modeling of Hot Carrier Degradation can be further extended towards novel material system based on Germanium. Similar to Si–H bonds at the Si/SiO$_2$ interface being responsible for HCD in Si based devices, Ge–H bonds can be expected as defect precursors in Ge transistors. However, recent DFT studies suggest a more intricate picture in which O vacancy related defects play a major role for degradation [MJC8, 323–325]. Likewise, HCD, and in general reliability issues, in transistors employing 2D channel materials is largely unexplored and an emerging research field [MJC11].

Additionally, the *harmonic approximation* of the full framework introduced in Chapter 4 and Section 4.1, can be further simplified by assuming that both potential energy curves, $V(q)$ and $V^{-/+}$, have the same frequency. Thus, for displaced harmonic oscillators the formula for the *effective cross section* can be reduced to an analytic expression [280]. However, only transition rates between neighbouring levels $\Delta n = \pm 1$ are allowed within this approximation,

---

[3] see, Sec. 3.4, the discussion on the positively charged complex $V^+(q)$.

whereas *overtone* excitations are explicitly neglected. Therefore, its applicability needs to be thoroughly tested and significant deviations of certain parameters compared to *ab initio* results are to be expected.

Full bias space degradation characteristics have recently gained attention. The presented approach, the $\mathrm{NMP_{eq.+II}}$ model in conjunction with the framework describing HCD, properly captures the trends across $\{V_\mathrm{G}, V_\mathrm{D}\}$ bias space. Nevertheless, small yet important differences can be noted, such as strong distortion of $I_\mathrm{D,lin}$ and the position of the drift minimum, see the discussion in Sec. 5. Such peculiar features *could* possibly be understood using a *microscopical* description of defect creation and transformation, as provided by the recently developed *Hydrogen release model* [16, 18, 19, 326]. The redistribution of *neutral* hydrogen within the oxide is assumed to be responsible for transformation of active precursor sites into positive defects as well as the creation of P_b centers at the interface due to the formation of $\mathrm{H_2}$. An extension towards interfacial H release together with its subsequent migration pathways, see Section 3.6, could reveal an interplay between HCD and BTI on an atomistic level, not accessible in current modeling approaches.

Appendices

Appendices overview

APPENDIX A

Structural Properties of Si/SiO$_2$ Models

A.1 Geometrical Characterization

In order to properly assess the quality of the utilized Si/a–SiO$_2$/Si interface models, an analysis provides information of the geometrical and structural properties of the three atomistic models. The four panels in Fig. A.1 show the Si–O–Si and O–Si–O angle distribution within the structures as well as a function of their position across the structures. Particularly at the interfaces to c–Si, the O–Si–O angles show a compressed distribution compared to bulk SiO$_2$ which can be attributed to the lattice mismatch and the resulting compressive stress.

The Si–O and Si–Si bond length distributions are shown in the four panels of Fig. A.2. One can again clearly see that within the direct vicinity of the interfacial regions Si–O and also Si–Si bonds tend to be more stretched and compressed, respectively. Note that the Si–Si nearest neighbour distance actually shows a bimodal distribution; one for the bond lengths in the Si substrate and the other one for the nearest Si neighbours in the amorphous SiO$_2$ layers.

A.2 Effects of Cell Size

Although the presented structural and electronic properties of the Si/SiO$_2$ interface models agree well with the experimental perceptions[1], yet, it was mentioned in Chapter 3 that the limited cell size potentially introduces an artificial strain at the interface region. Such larger distortions would explain a broadened distribution of calculated barriers, see Chap. 3.

The utilized interface models in this work have a cell size of $16 \times 16 \times 32\,\text{Å}$ and contain 473–475 atoms, depending on the number of defects which had to be

---

[1] Note that, a detailed microscopic picture of the direct interface region has not been established yet.

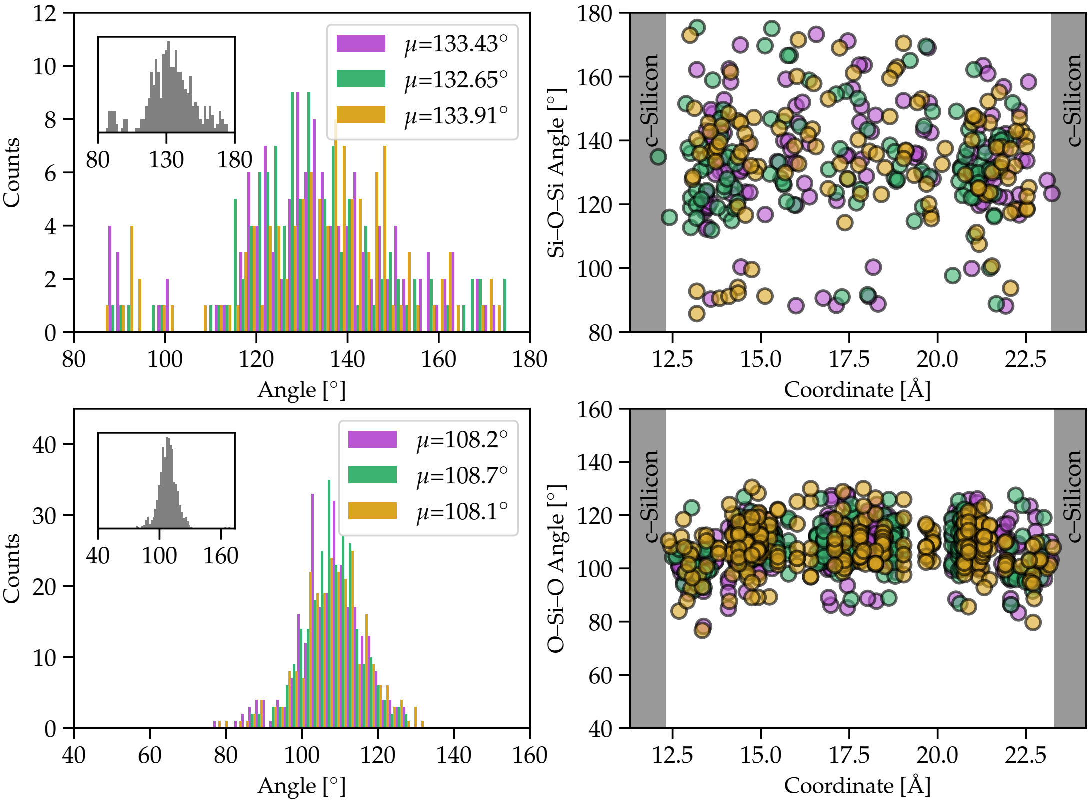

FIGURE A.1: O–Si–O (**Upper**) and Si–O–Si (**Lower**) angle distribution within the utilized interface models. The data are shown as a histogram (**Left**) and as a function of their position across the structure (**Right**).

passivated in the SiO$_2$ and transition region. Furthermore, the oxide thickness is around 1.1 nm. Assuming the ideal scenario of *one* interface defect and *one* oxide defect, the resulting *theoretical* defect densities are around 1–2 orders of magnitude higher than the commonly assumed value of $N_{\mathrm{it}} = 1 \times 10^{12} - 1 \times 10^{13}\,/\mathrm{cm}^2$ and $N_{\mathrm{ot}} = 1 \times 10^{19} - 1 \times 10^{20}\,/\mathrm{cm}^3$. Moreover, taking into account that a H anneal during processing additionally leads to the relief of strain at the interface, an artificially large defect density can indeed introduce a higher strain in the structure.

Three different Si/SiO$_2$ interface model variants have been investigated to explore the effects of cell size, and hence defect density, onto the residual strain at the interfacial transition region, see Fig. A.3. First, the structure chosen for this thesis with a cell size of $16 \times 16 \times 32$ Å including a ~ 11 Å thick SiO$_2$ oxide (1) and ~ 475 atoms in total. Second, a model with an increased oxide thickness of ~ 28 Å but the same xy dimensions, with a total cell size of $16 \times 16 \times 52$ Å and ~ 792 atoms (2). The increased number of oxide layers should facilitate the formation of bulk SiO$_2$ properties and hence a strain reduction in the z direction effectively allowing the interface to properly relax. Finally, the largest atomistic model used has a total size of $48 \times 32 \times 32$ Å which contains ~ 2832 atoms. The x and y dimensions were tripled and doubled, respectively, compared to the initial structure, allowing to reduce the density of interface states (assumed *one* P_{b} center) by almost one order of magnitude.

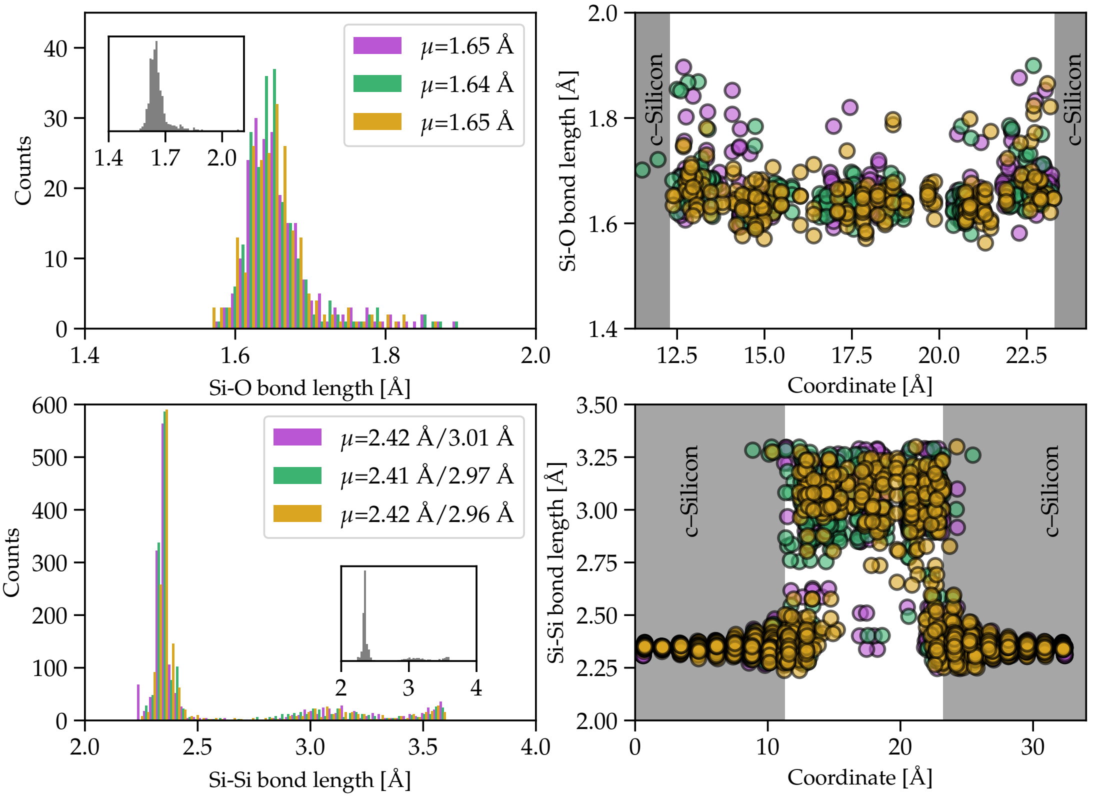

FIGURE A.2: Si–O (**Upper**) and Si–Si (**Lower**) bond length distribution within the utilized interface models. The data are shown as a histogram (**Left**) and as a function of their position across the structure (**Right**).

Again, to quantify the quality of the interface, the deviated of the highlighted silicon layers with respect to their positions in *c*–Si has been used as a measure of strain and distortion, see Fig. A.3. To provide a fair comparison, the results in Fig. A.3 show the *mean* lattice distortion of various different structures (6(1), 20(2), 12(3)). Furthermore, all models have been created in the exact same way (see Sec. 3.1) with a final cell optimization using DFT in conjunction with a PBE functional. As already shown in Sec. 3.1, the smallest models exhibit some severely distorted atoms in the Si transition region with a mean distortion in the first three layers of $\langle \Delta \mathbf{r} \rangle = 0.31$ Å and maximum values above 0.5 Å. Quite surprisingly, the structures 2) (extended z) and 3) (extended xy) yield very similar results in terms of average and maximum distortions, see Fig. A.3. The increase in xy reduces the self–interaction of defect configurations at the Si/SiO$_2$ interface which intuitively should reduce the remanent stress. On the other hand, a thicker oxide region, structure 3), exhibits a similar effect. Due to the flexibility of the (bulk) SiO$_2$ network, residual strain associated with a defect configuration at the interface, can be effectively absorbed resulting in a smoother interface region. In order to be fully confident about the validity of the results, further, systematic investigations need to be performed. Nevertheless, the results suggest that for subsequent studies structures like 2), with an increased oxide thickness, should be used which provide the best tradeoff between credibility and computational efforts.

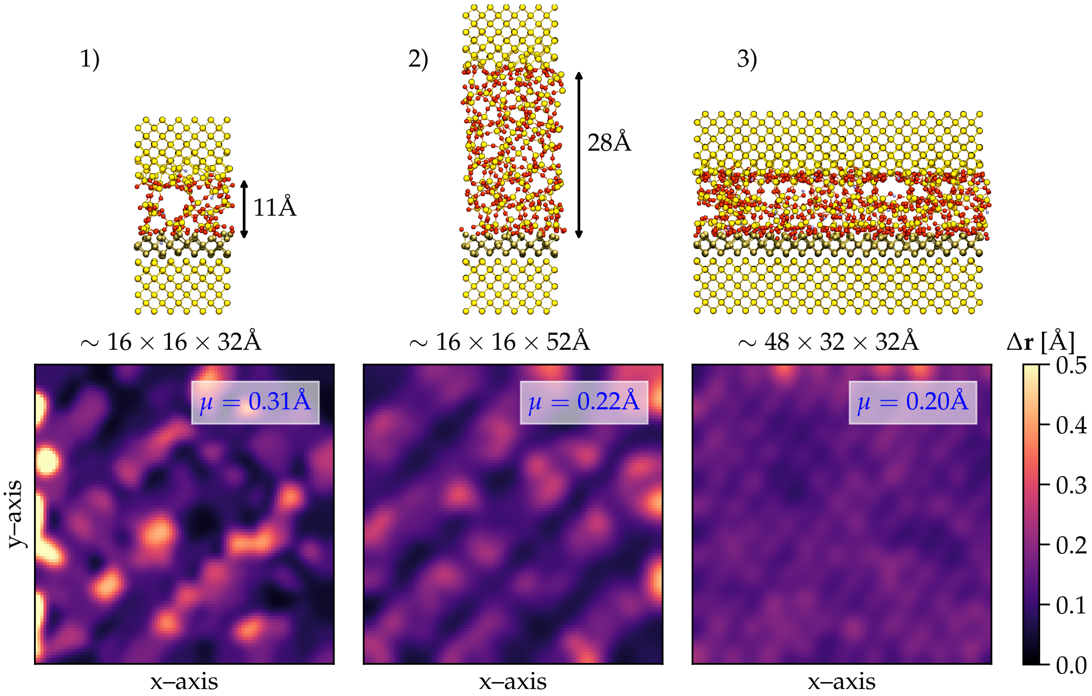

FIGURE A.3: Si/SiO$_2$ interface models with different cell sizes (**Upper**) together with the calculated deviations of the highlighted interfacial Si atoms compared to their respective position in c–Si (**Lower**). Interestingly, extending the initial structure (**Left**) along the z direction (**Middle**) or the xy plane (**Right**) yields similar results.

APPENDIX B

Defect Properties

To gain further insight into the resulting Si dangling bond defects their properties upon charge capture have been investigated. Three different types of defects have been selected and the formation energies for neutral and negatively/positively charged states have been calculated. The selected defects including the corresponding spin density can be see in Fig. B.1: a) a sub–interfacial (one layer away from the interface) Si trivalently back–bonded to three other Si atoms with no other O atoms in the direct vicinity, b) a Si–DB directly at the interface with an oxygen atom 1.9 Å away and c) a Si–DB back–bonded to two Si's and one O atom (rendering in compatible to a P_{b1}–type structure). All defects possess an unpaired electron, as indicated by the spin density, with no other defect present in the model. Subsequently, the different charge states, neutral, negative and positive, of each defect have been calculated. The results are shown in in Fig. B.1, which shows the difference in the electron density with respect to the neutral configuration. Blue refers to an increase of electron density, whereas the red translucent profiles indicate a decrease of electron density. Clearly visible is that the added electron (or hole) is indeed localized within the direct vicinity of the Si–DBs. However, particularly the positive charge state for configurations b) and c) suggests that the hole is shared between the Si and the O (Fig. B.1 middle and right). This, however, is to be expected, since oxygen is slightly negatively charged in the SiO_2 network, see Chap. 3.

In order to reliably extract the formation energies for the different charge states of the interface defects, the electrostatic correction methodology presented in [200] and implemented in the SXDEFECTALIGN2D program has been applied. All results together with the corresponding Mulliken charges with respect to the neutral configuration are shown in Figs. B.2 and B.3. The model potential is in very good agreement with the electrostatic potential from DFT for both charge states, Q=±1, of the Si–DB, as can be seen in the lower panels of the respective figures. A reasonable dielectric profile was used throughout the calculation and the spatial placement of the Gaussian model charge is further supported by the Mulliken charges shown in Figs. B.2 and B.3. The correction constant was found by aligning

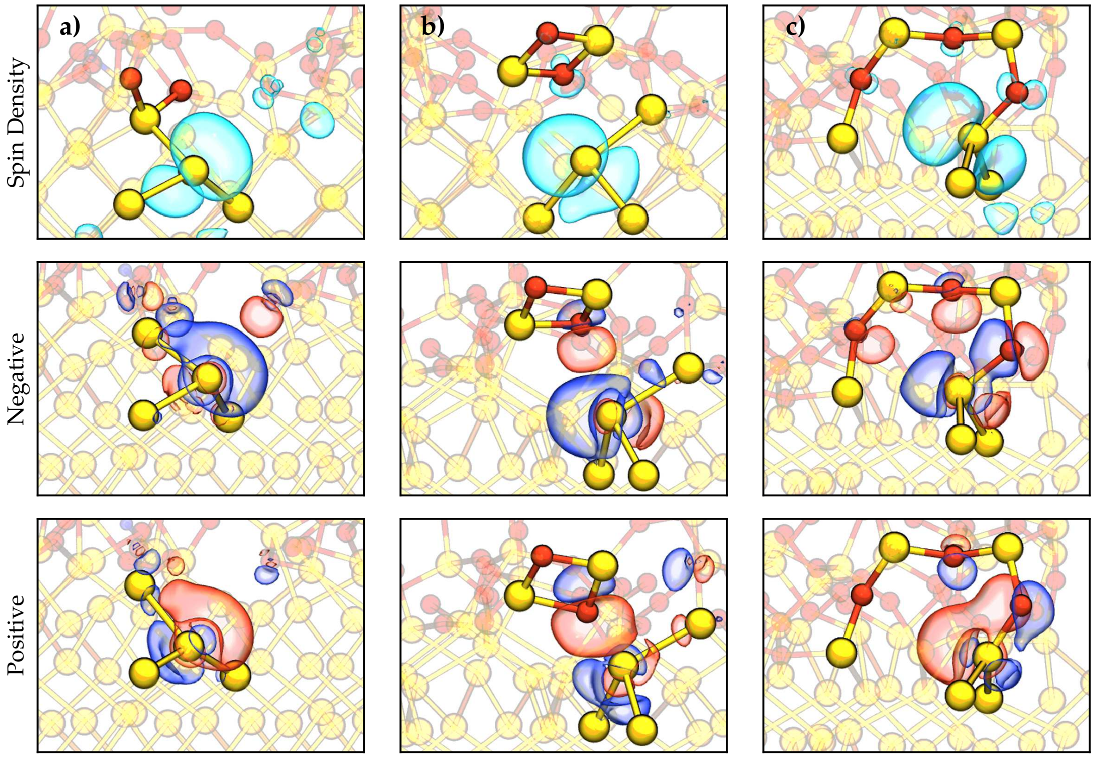

FIGURE B.1: Three different interface defect configurations including the corresponding spin density shown as translucent profiles (**Upper**). The isosurfaces are drawn at a value of 0.01. Difference of the electron density for the negatively (**Upper**) and positively (**Lower**) charged Si–DB configurations with respect to the neutral charge state. Blue profiles indicate an increase of electron density and red profiles a decrease of electron density. The isosurfaces are drawn at a value of $-0.01\,\mathrm{e}$ (blue) and $0.01\,\mathrm{e}$ (red).

the model and the DFT potential far away from the defect, by considering the average over the oscillations within the DFT potential which result from microscopic screening. Finally, with the extracted corrections, the formation energies for the different charge states could be reliably calculated, see Sec. 3.1

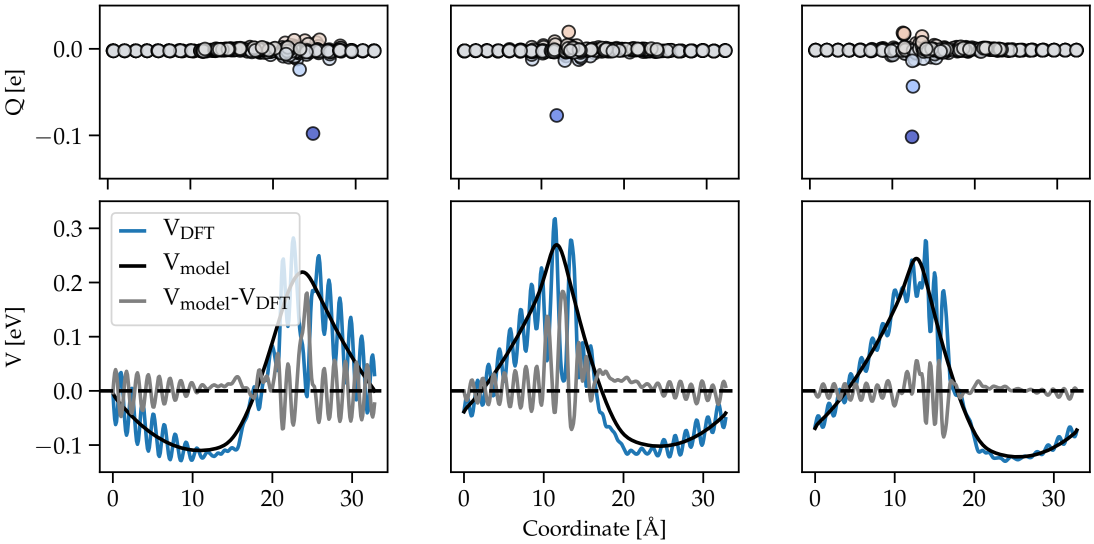

FIGURE B.2: **Upper:** Change of the Mulliken charges with respect to the neutral configuration for the negatively charged defects. **Lower:** A comparison of the model potential ($\mathrm{V_{model}}$) for $Q = -1$ calculated within [200] and the electrostatic potential directly extracted from DFT calculations.

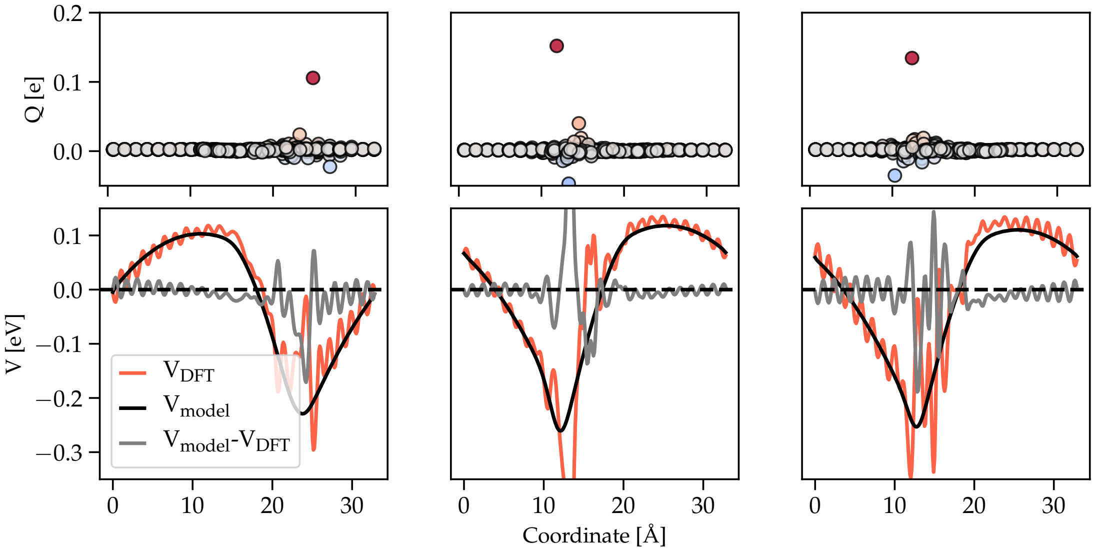

FIGURE B.3: **Upper:** Change of the Mulliken charges with respect to the neutral configuration for the positively charged defects. **Lower:** A comparison of the model potential ($\mathrm{V_{model}}$) for $Q = +1$ calculated within [200] and the electrostatic potential directly extracted from DFT calculations.

APPENDIX C

Electric Field & Material Properties

In order to validate the approach used within Sec. 3.3 to include the effect of an electric field, the *Berry–phase* method as implemented in Cp2k will be thoroughly tested in the following. Fundamental material properties, such as the polarization and the permittivity for bulk amorphous silicon dioxide (a–SiO$_2$), bulk c–Si as well as an Si/a–SiO$_2$/Si interface structure will be calculated. For all calculations 3D periodic boundary conditions are applied. Two types of calculations were run with field strengths of up to 10 MV/cm: one with fixed atomic positions, which gives the high–frequency permittivity ϵ_∞, and another where the effects of lattice relaxations are included, yielding the static permittivity ϵ.

The Figs. C.1 and C.2 summarize the results for bulk a–SiO$_2$ as well as for crystalline silicon. To ensure that the created a–SiO$_2$ model possesses an isotropic polarization, the field has been applied along the x, y and z–axis, whereas for the Si model, the field was only considered along the z direction within the calculations. Quite reassuringly, the calculated values for the static and high–frequency permittivities for both materials are in excellent agreement with the experimental values. While for silicon the permittivity is virtually independent of the frequency [327], the dielectric constant for SiO$_2$ decreases from 3.81 at static electric fields to 1.96 for ϵ_∞ [328, 329]. Furthermore, as is shown in the insets, the approach using Wannier functions and (3.2) gives the same results as the Berry phase method.

Unfortunately, for a heterostructure, i.e. a Si/a–SiO$_2$/Si interface, the above mentioned approaches are not applicable. However, one possibility to evaluate the spatially dependent dielectric constants is given by the *induced charge density* (ICD) method [330–333]. Within this approach the local microscopic polarization $p(\boldsymbol{r})$ can be evaluated as

$$\overline{p}(z) = \overline{p}_{-\infty} - \int_{-\infty}^{z} \overline{\rho}_{\mathrm{ind}}(z')\mathrm{d}z', \tag{C.1}$$

with $\overline{p}(z)$ and $\overline{\rho}(z)$ being the planar averaged polarization and the induced charge density, respectively and $\overline{p}_{-\infty}$ is a boundary condition constant, as will be dis-

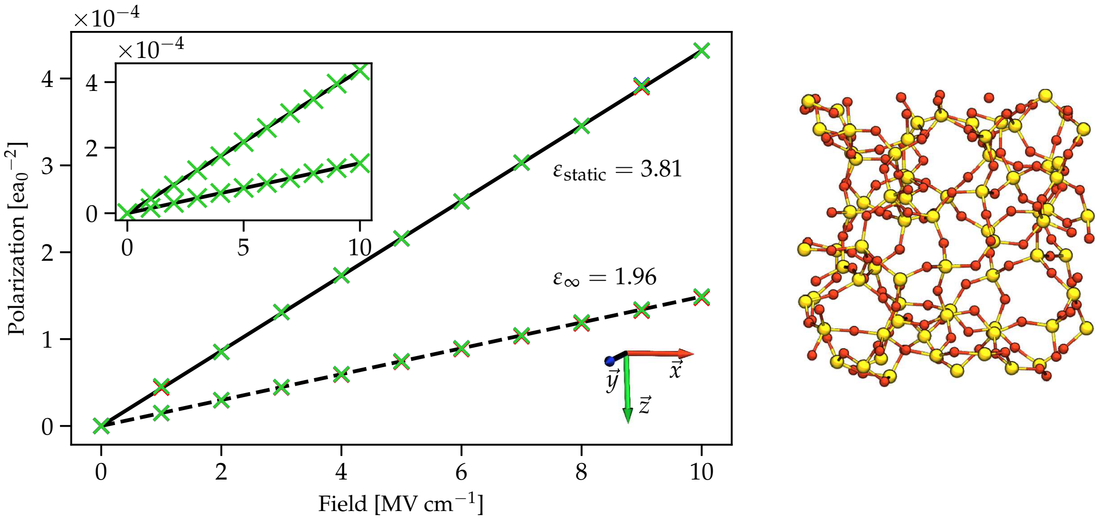

FIGURE C.1: The extracted polarization using the Berry phase method of *a*–SiO_2 as a function of increasing field strengths. Additionally, the inset shows the calculated polarization by means of the Wannier center approach. Both methods agree extremely well with each other.

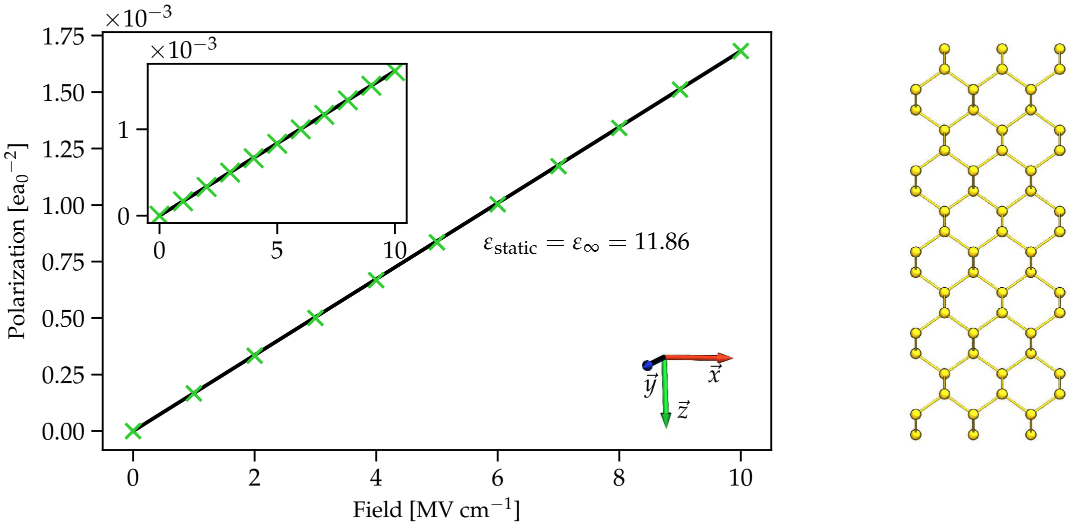

FIGURE C.2: The extracted polarization using the Berry phase method of *c*–Si as a function of increasing field strengths. Additionally the inset shows the calculated polarization by means of the Wannier center approach. Both methods agree extremely well with each other.

cussed below. Thereby, $\overline{p}(z)$ is defined as the difference in charge density upon the application of different electric field strength ($E = \pm 1\,\mathrm{MV/cm}$ is used here). The resulting polarization profile can be further used to determine the spatially dependent relative permittivity of linear dielectrics by using the following relation

$$\varepsilon(z) = \frac{\varepsilon_0 E_{\text{ext}}}{\varepsilon_0 E_{\text{ext}} - \overline{p}(z)}, \tag{C.2}$$

where ε_0 is the vacuum permittivity and E_{ext} is the externally applied field.

Two different realizations of the atomistic interface structure were utilized: the Si/a–SiO$_2$/Si unit cell, as well as a slab model, where a 5 Å vacuum gap was introduced on either side. The Si atoms facing the vacuum were passivated by H, which creates two surfaces. Thus, in the latter case $\overline{p}_{-\infty}$ can be set to zero due to the vanishing induced charge, while for the interface cell the constant is set to the polarization of Si, assuming bulk Si at $-\infty$. Again, single point calculations as well as geometry relaxations have been conducted for both models.

The resulting polarization together with the permittivity profiles across the structures is shown in Fig. C.3. Overall, a very good agreement with experimental values as well as with the results presented above is achieved. However, by taking a closer look, some particular features and differences between the two atomistic models can be highlighted.

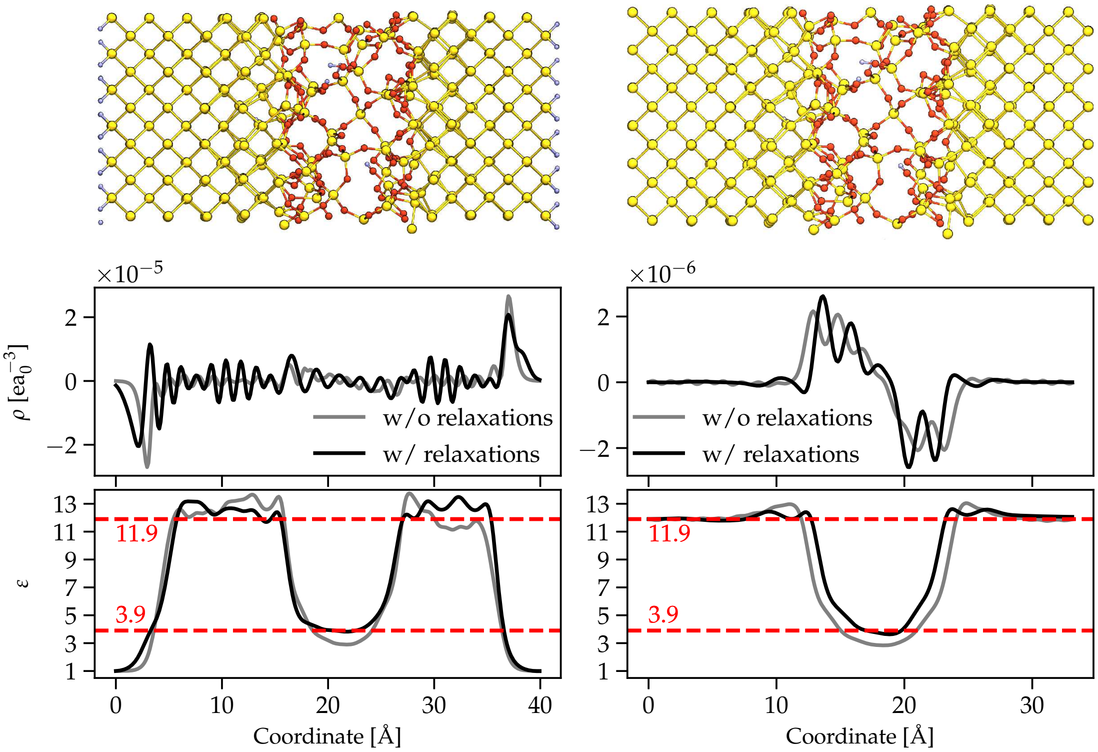

FIGURE C.3: Optical and static dielectric constant profiles across the interface slab using the ICD method with a H passivated Si/a–SiO$_2$/Si model.

First, lattice relaxations have a strong impact on the results of the slab model. Whereas the unrelaxed structure shows an increasing permittivity trend towards the Si/a–SiO$_2$ interface regions, the optimized variant actually shows the opposite trend. This result can be explained by an expansion of 0.1 Å for the whole structure during the relaxation procedure. Thus, particularly in the direct interfacial regions, atoms relax into new equilibrium positions, thereby balancing the shift of the electronic density. In contrast, the unit cell model shows a consistently enhanced permittivity directly at the interface, albeit for the relaxed structure this effect is reduced. Since the atomistic structure within the cell is not able to expand in the z direction, structural reconfigurations affect the position and the width of the interfacial region, as can be seen in Fig. C.3.

Second, both models clearly show an interfacial *transition* region with a width of $4 - 6$ Å to resemble the bulk properties of the respective material. Such a region, with altered electronic properties, was confirmed by experiments [192, 193], constraining the minimum thickness for a SiO_2 gate dielectric to a theoretical value of 7 Å, which is in good agreement with the results presented here.

APPENDIX D

Si-H Bending Dynamics

In order to validate the methodology used to calculate the vibrational relaxation time as well the applicability of the REAXFF force–field, the following section presents the results for a Si–H bending mode. The Si–H bending motion is a well studied system in the literature and offers comparability to recent theoretical studies [270, 273, 274]. The investigated atomistic model here is a H passivated reconstructed Si(100)–2×1 surface with 500 atoms. A normal–mode analysis has been carried out and *one* of the 10 normal modes which could be classified as a Si–H bending mode was selected for the study, see Fig. D.1 (left panel).

The theoretical concepts and calculation details are described in detail in Sec. 4.1. The results are summarized in Table. D.1. Again, the total lifetime τ_1^{total} is governed by a two–phonon process due to the energy forbidden one–phonon dissipations[1].

Mode	T [K]	τ_1^{total}	$\Gamma_{1,0}^{(1)}$	$\tau_1^{(1)}$	$\Gamma_{1,0}^{(2a)}$	$\Gamma_{1,0}^{(2b)}$	$\tau_1^{(2)}$
Si–$\mathrm{H}_{\mathrm{bend}}^{1\to 0}$	0	0.407	0.149	6.675	2.304	0.0015	0.433
	300 (↓)	0.202	0.229	5.405	4.751	0.003	0.210
	300 (↑)		0.0451		0.0019	0.0001	

TABLE D.1: Calculated vibrational lifetimes (τ_1^{total}, $\tau_1^{(1)}$ and $\tau_1^{(2)}$) together with the corresponding rates ($\Gamma_{1,0}^{(1)}$, $\Gamma_{1,0}^{(2a)}$ and $\Gamma_{1,0}^{(2b)}$) for the first excited system–mode and two different temperatures. The units for the lifetimes and rates are ps and ps^{-1}, respectively.

Analogous to the Si–H bond breaking mode in Sec. 4.1, $\Gamma_{1,0}^{(1)}$ shows a strong γ dependence ($\tau_1^{(1)} = 34.4\,\mathrm{ps} - 3.24\,\mathrm{ps}$), whereas $\Gamma_{1,0}^{(2)}$ seems to be rather insensitive ($\tau_1^{(2)} = 0.435\,\mathrm{ps} - 0.428\,\mathrm{ps}$) due to changes between 1 and 10 cm^{-1}.

---

[1] Note that the collective Si–H bending modes on the surface have not been considered in the calculations. Only normal–modes associated with the Si lattice contribute to the dissipation to avoid an artificially large coupling.

Two–phonon processes have been examined as well in detail. Fig. D.1 (right panel) shows the contributions of phonon pairs $\{\omega_k, \omega_l\}$ to the total rate. For the Si–surface system the energy is transferred along the diagonal $\hbar\omega_k + \hbar\omega_l = \Delta E_{1,0}$, as to be expected, with the biggest contribution comprising one low– and one high–energy phonon in the range of $21 - 26\,\mathrm{meV}$ and $52 - 57\,\mathrm{meV}$. Furthermore, also ratios of $\omega_k/\omega_l \sim 1/6, 1/1.5$ yield non–negligible contributions to the total rate $\Gamma^{(2)}_{1,0}$, whereas $\omega_k/\omega_l \sim 1/1$ $(\Gamma^{(2b)}_{1,0})$ only plays a minor role.

In summary, the results are compatible with previously published results [270, 273, 274] and support the concept as well as the results presented in Sec. 4.1.

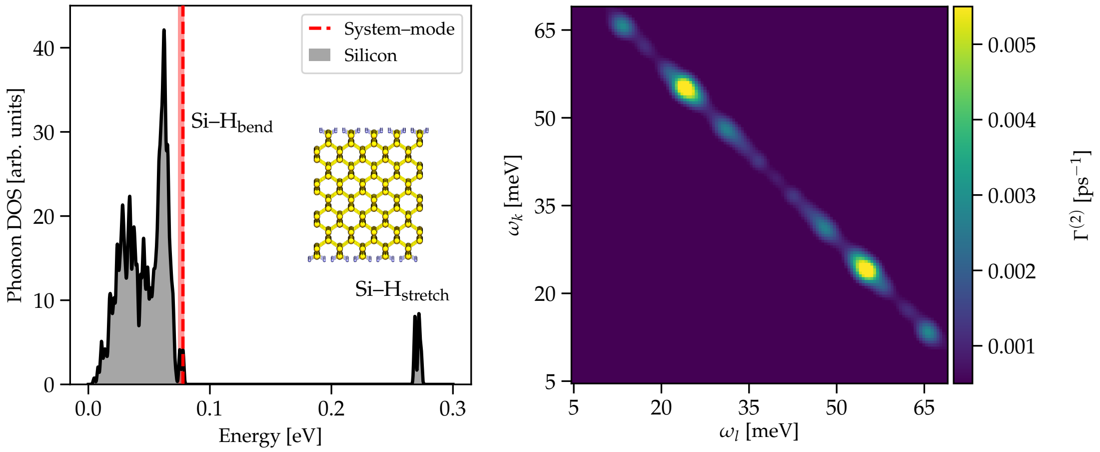

FIGURE D.1: **Left:** The phonon mode spectrum of a fully reconstructed Si(100) 2×1 surface passivated with H atoms. The normal–modes associated with the Si–H bending modes are highlighted. **Right:** The contributions of phonon pairs $\{\omega_k, \omega_l\}$ to the transition rate $\Gamma^{(2)\downarrow}_{1,0}$ using a 2D histogram with a bin size of $5\,\mathrm{cm}^{-1} \times 5\,\mathrm{cm}^{-1}$.

APPENDIX E

Calculation of Bond Breaking Rates

The Si–H bond breaking rate ultimately determines the created damage at the Si/SiO$_2$ interface and, hence, affects the simulated reliability characteristics of device, rendering the calculation of Γ^{break} of particular importance. Below, different concepts to calculate Γ^{break} are introduced and compared against each other, eventually motivating the choice of using the WKB

First, a purely **classical** rate approach is given by

$$\Gamma^{\text{break}}_{\text{cla}} = \sum_i P_i \Gamma^{\text{tot}}_{i,\text{cont}}, \tag{E.1}$$

with P_i being the quasi–equilibrium population of state i and $\Gamma_{i,\text{cont}}$ is the excitation rate from state i to the first level above the transition barrier between the left and right well, referred to as *continuum* state. The classical rate only takes into account the left well of the ground state potential.

Second, a **semi-classical** calculation of the breakage rates is given by the **WKB approximation**

$$\begin{aligned}\Gamma^{\text{break}}_{\text{WKB}} &= \sum_{i=1}^{f} \Gamma_{i,\text{WKB}}\, P_i = \\ &= \sum_{i=1}^{f} \exp\Big(-\frac{2}{\hbar}\int\limits_{x_{1,i}}^{x_{2,i}} \sqrt{2(V-E_i)}\mathrm{d}x\Big) P_i,\end{aligned} \tag{E.2}$$

where P_i is again the state population and $\Gamma_{i,\text{WKB}}$ is given by the tunneling probability through the barrier between the classical turning points x_1 and x_2. Only eigenstates in the left well which have a partner of similar energy in the right well are included in the calculation[1].

---

[1] The WKB method, at a first glance, seems physically incorrect due to the orthogonality of the wavefunctions in the left and right well, respectively. However, the resonance mediated process via an intermediate potential effectively enables the coupling of ϕ_{L} and ϕ_{R}.

Finally, **propagating the density matrix** in time is the most rigorous approach and allows one to directly access the population dynamics of the system. Starting with a 100% localization in the left well of the ground state, e.g. $P_0 = 1$, $P_{i\neq 0} = 0$, the transition rate can be defined as

$$\Gamma^{\mathrm{break}}_{\mathrm{DM}} = -\frac{\mathrm{d}P_{\mathrm{L}}(t)}{\mathrm{d}t} = \frac{\mathrm{d}P_{\mathrm{R}}(t)}{\mathrm{d}t}, \tag{E.3}$$

assuming a negligible back flow of population. $P_{\mathrm{L,R}}(t)$ are the total populations of the left and right well, respectively, at time t. The calculations presented here use a Runge–Kutta integrator of fourth order with a timestep of 100 a.u. and a total propagation time of 10 ns.

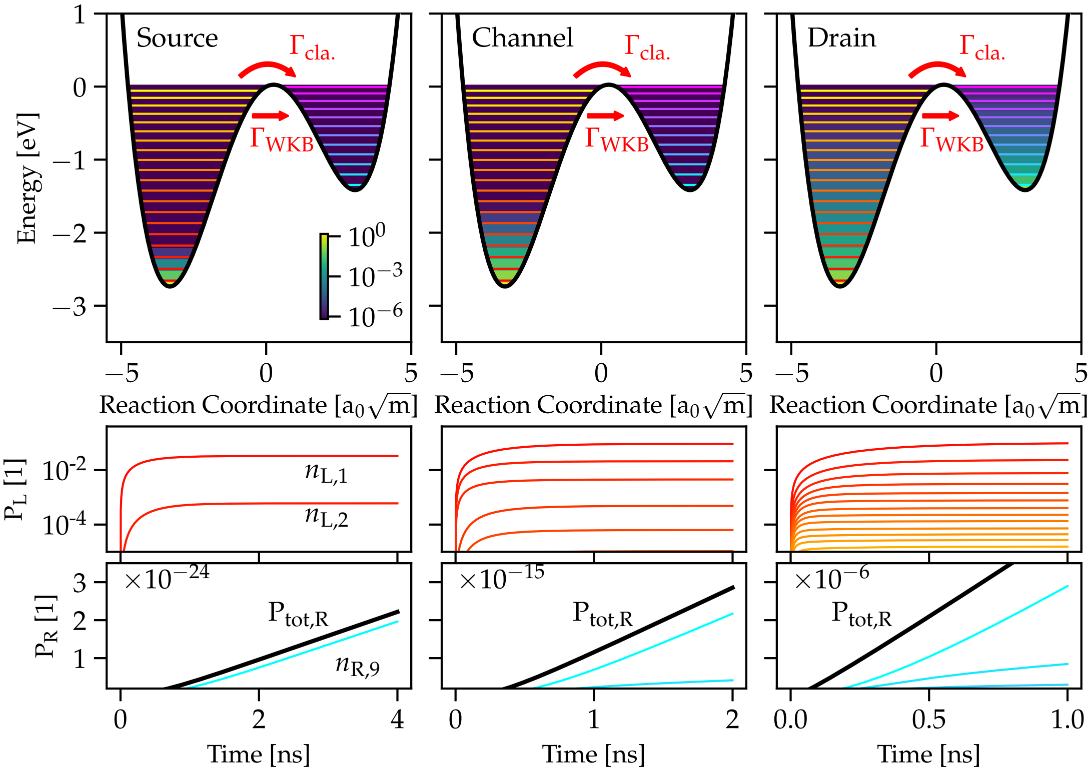

FIGURE E.1: A simulation benchmark of the methods to calculate the bond breaking rate Γ^{break} considering three different regimes along the interface. The classical approach generally underestimates Γ^{break} compared to the WKB approach and the rigorous density matrix propagation.

The results for all three different rates at selected points along the Si/SiO$_2$ interface are summarized in Fig. E.1 and Table E.1. One can see that the classical approach $\Gamma^{\mathrm{break}}_{\mathrm{cla}}$ underestimates the rate by at least one order of magnitude, whereas the WKB method and the density matrix propagation give similar values. Although $\Gamma^{\mathrm{break}}_{\mathrm{DM}}$ employs the most accurate method, its computational effort is unfeasible for the work presented here. Taking into account that the numerical simulation of a MOSFET and the energy distribution function includes several hundred mesh points at the interface as well as the inherent distribution of parameters, which requires to randomly sample the parameter space, would have made the calculations prohibitively expensive.

	$\Gamma^{\text{break}}_{\text{Source}}$ $[\text{s}^{-1}]$	$\Gamma^{\text{break}}_{\text{Channel}}$ $[\text{s}^{-1}]$	$\Gamma^{\text{break}}_{\text{Drain}}$ $[\text{s}^{-1}]$
classical	1.6×10^{-18}	3.6×10^{-7}	3.8×10^{2}
semi–classical WKB	2.4×10^{-16}	1.0×10^{-6}	2.1×10^{3}
ρ propagation $(\frac{\mathrm{d}P_{\text{tot,R}}}{\mathrm{d}t})$	6.2×10^{-16}	1.1×10^{-6}	4.8×10^{3}

TABLE E.1: The calculated bond breaking rates Γ^{break} using the three different approaches, classical, WKB and propagation the density matrix. While the latter to variants yield very similar rates, the classical calculation method tends to consistently underestimate Γ^{break}.

APPENDIX F

Details of Metadynamics Calculations

In total 30 well–tempered metadynamics (WTMD) simulations have been carried out. The bias factors have been varied between 80 and 180 as well as bias heights ranging from 9 to 20 meV. The accessible phase space region was limited during these calculations using a restraining potential which acts on the collective variables, see Fig. F.1 (right panel).

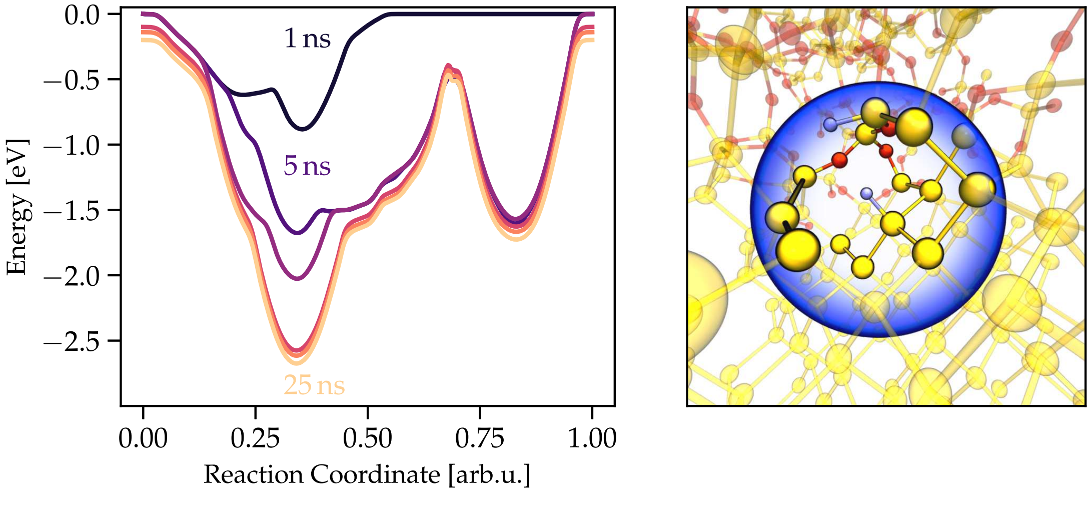

FIGURE F.1: **Left:** The accessible spatial region within the simulations is shown as the blue translucent sphere including the direct vicinity of the Si–H bond of interest. A restraining potential has been used to limit the phase space region and prevent the H from potentially moving away. **Right:** Assessment of the convergence of the simulations. One can see that for 1 ns of simulation time only the region around the equilibrium position has been explored. For longer times a greater phase space region has been sampled, ultimately converging to a MEP at around 20 ns. The negligible changes between 20 and 25 ns indicate the convergence of the simulation.

Note that simulations with large bias factors and/or bias heights did not properly converge and have been discarded. Nevertheless, simulations utilizing smaller parameters – bias factors of 80/90 and heights between $9-10\,\mathrm{meV}$ – indeed converged to a rather unique FES, see Sec. 3.2. The final results presented in Sec. 3.2 have been obtained by performing 50×10^6 time steps with a step size of 0.5 fs. In total, 1×10^5 Gaussian functions have been *added* to the drive the system, each with a width of 0.5 Å and a height of 9 meV. The summed up Gaussian potentials were used to calculate the free energy landscape (FES) and the respective minimum energy path (MEP).

The left panel of Fig. F.1 assesses the convergence of the WTMD run by plotting the evolution of the MEP with simulation time. Clearly visible is the increasing sampling of the spatial regions with time. The reconstructed paths for 20 and 25 ns simulation time are almost identical, thereby indicating the convergence of the simulation.

Bibliography

[1] J. H. Stathis, S. Mahapatra, and T. Grasser. “Controversial Issues in Negative Bias Temperature Instability”. In: *Microelectronics Reliability* 81 (2018), pp. 244–251. ISSN: 0026-2714. DOI: `10.1016/j.microrel.2017.12.035`.

[2] K. O. Jeppson and C. M. Svensson. “Negative Bias Stress of MOS Devices at High Eelectric Fields and Degradation of MNOS Devices”. In: *Journal of Applied Physics* 48.5 (1977), pp. 2004–2014. DOI: `10.1063/1.323909`.

[3] T. Grasser, H. Reisinger, P.-J. Wagner, and B. Kaczer. “Time-Dependent Defect Spectroscopy for Characterization of Border Traps in Metal-Oxide-Semiconductor Transistors”. In: *Phys. Rev. B* 82 (24 Dec. 2010), p. 245318. DOI: `10.1103/PhysRevB.82.245318`.

[4] T. Grasser, K. Rott, H. Reisinger, M. Waltl, F. Schanovsky, and B. Kaczer. “NBTI in Nanoscale MOSFETs-The Ultimate Modeling Benchmark”. In: *IEEE Transactions on Electron Devices* 61.11 (Nov. 2014), pp. 3586–3593. DOI: `10.1109/TED.2014.2353578`.

[5] M. Kirton and M. Uren. “Noise in Solid-State Microstructures: A New Perspective on Individual Defects, Interface States and Low-Frequency (1/f) Noise”. In: *Advances in Physics* 38.4 (1989), pp. 367–468. DOI: `10.1080/00018738900101122`.

[6] T. Grasser, B. Kaczer, W. Goes, H. Reisinger, T. Aichinger, P. Hehenberger, P. Wagner, F. Schanovsky, J. Franco, M. T. Toledano Luque, and M. Nelhiebel. “The Paradigm Shift in Understanding the Bias Temperature Instability: From Reaction–Diffusion to Switching Oxide Traps”. In: *IEEE Transactions on Electron Devices* 58.11 (Nov. 2011), pp. 3652–3666. DOI: `10.1109/TED.2011.2164543`.

[7] T. Grasser. “Stochastic Charge Trapping in Oxides: From Random Telegraph Noise to Bias Temperature Instabilities”. In: *Microelectronics Reliability* 52.1 (2012). invited, pp. 39–70. DOI: `10.1016/j.microrel.2011.09.002`.

[8] T. Grasser. *Bias Temperature Instability for Ddevices and Circuits*. New York: Springer, 2014. ISBN: 978-1-4614-7908-6. DOI: `10.1007/978-1-4614-7909-3`.

[9] T. Grasser, W. Goes, Y. Wimmer, F. Schanovsky, G. Rzepa, M. Waltl, K. Rott, H. Reisinger, V. V. Afanas'ev, A. Stesmans, A. .-M. El-Sayed, and A. L. Shluger. “On the Microscopic Structure of Hole Traps in pMOSFETs”. In: *2014 IEEE International Electron Devices Meeting*. Dec. 2014, pp. 21.1.1–21.1.4. DOI: 10.1109/IEDM.2014.7047093.

[10] F. Schanovsky, W. Gös, and T. Grasser. “Multiphonon Hole Trapping from First Principles”. In: *Journal of Vacuum Science & Technology B* 29.1 (2011), 01A201. DOI: 10.1116/1.3533269.

[11] F. Schanovsky, O. Baumgartner, V. Sverdlov, and T. Grasser. “A Multi Scale Modeling Approach to Non-Radiative Multi Phonon Transitions at Oxide Defects in MOS Structures”. In: *Journal of Computational Electronics* 11.3 (2012), pp. 218–224. DOI: 10.1007/s10825-012-0403-1.

[12] G. Rzepa, M. Waltl, W. Gös, B. Kaczer, and T. Grasser. “Microscopic Oxide Defects Causing BTI, RTN, and SILC on High-K FinFETs”. In: *Proceedings of the International Conference on Simulation of Semiconductor Processes and Devices (SISPAD)*. 2015, pp. 144–147. DOI: 10.1109/SISPAD.2015.7292279.

[13] G. Rzepa, M. Waltl, W. Gös, B. Kaczer, J. Franco, T. Chiarella, N. Horiguchi, and T. Grasser. “Complete Extraction of Defect Bands Responsible for Instabilities in n and pFinFETs”. In: *2016 Symposium on VLSI Technology Digest of Technical Papers*. 2016, pp. 208–209. DOI: 10.1109/VLSIT.2016.7573437.

[14] Y. Y. Illarionov, G. Rzepa, M. Waltl, T. Knobloch, A. Grill, M. M. Furchi, T. Mueller, and T. Grasser. “The Role of Charge Trapping in MoS_2/SiO_2 and MoS_2/hBN Field-Effect Transistors”. In: *2D Materials* 3.3 (2016), p. 035004. DOI: 10.1088/2053-1583/3/3/035004.

[15] M. Waltl, G. Rzepa, A. Grill, W. Gös, J. Franco, B. Kaczer, L. Witters, J. Mitard, N. Horiguchi, and T. Grasser. “Superior NBTI in High-k SiGe Transistors - Part II: Theory”. In: *IEEE Transactions on Electron Devices* 64.5 (2017), pp. 2099–2105. DOI: 10.1109/TED.2017.2686454.

[16] T. Grasser, M. Waltl, G. Rzepa, W. Goes, Y. Wimmer, A. .-M. El-Sayed, A. L. Shluger, H. Reisinger, and B. Kaczer. “The “Permanent” Component of NBTI Revisited: Saturation, Degradation-reversal, and Annealing”. In: *2016 IEEE International Reliability Physics Symposium (IRPS)*. Apr. 2016, 5A-2-1-5A-2–8. DOI: 10.1109/IRPS.2016.7574504.

[17] T. Grasser, M. Waltl, Y. Wimmer, W. Goes, R. Kosik, G. Rzepa, H. Reisinger, G. Pobegen, A. .-M. El-Sayed, A. Shluger, and B. Kaczer. “Gate-Sided Hydrogen Release as the Origin of ”Permanent” NBTI Degradation: From Single Defects to Lifetimes”. In: *2015 IEEE International Electron Devices Meeting (IEDM)*. Dec. 2015, pp. 20.1.1–20.1.4. DOI: 10.1109/IEDM.2015.7409739.

[18] T. Grasser, M. Waltl, K. Puschkarsky, B. Stampfer, G. Rzepa, G. Pobegen, H. Reisinger, H. Arimura, and B. Kaczer. "Implications of Gate-Sided Hydrogen Release for Post-Stress Degradation Build-Up After BTI Stress". In: *2017 IEEE International Reliability Physics Symposium (IRPS)*. Apr. 2017, 6A-2.1-6A–2.6. DOI: 10.1109/IRPS.2017.7936334.

[19] T. Grasser, B. Stampfer, M. Waltl, G. Rzepa, K. Rupp, F. Schanovsky, G. Pobegen, K. Puschkarsky, H. Reisinger, B. O'Sullivan, and B. Kaczer. "Characterization and Physical Modeling of the Temporal Evolution of Near–Interfacial States resulting from NBTI/PBTI Stress in nMOS/pMOS Transistors". In: *2018 IEEE International Reliability Physics Symposium (IRPS)*. Mar. 2018, 2A.2-1-2A.2–10. DOI: 10.1109/IRPS.2018.8353540.

[20] S. Novak, C. Parker, D. Becher, M. Liu, M. Agostinelli, M. Chahal, P. Packan, P. Nayak, S. Ramey, and S. Natarajan. "Transistor Aging and Reliability in 14nm Tri-Gate Technology". In: *2015 IEEE International Reliability Physics Symposium*. Apr. 2015, 2F.2.1–2F.2.5. DOI: 10.1109/IRPS.2015.7112692.

[21] A. Rahman, J. Dacuna, P. Nayak, G. Leatherman, and S. Ramey. "Reliability Studies of a 10nm High-Performance and Low-Power CMOS Technology Featuring 3rd Generation FinFET and 5th Generation HK/MG". In: *IRPS*. Mar. 2018, 6F.4-1-6F.4–6. DOI: 10.1109/IRPS.2018.8353648.

[22] S. R. Stiffler, R. Ramachandran, W. K. Henson, N. D. Zamdmer, K. McStay, G. La Rosa, K. M. Boyd, S. Lee, C. Ortolland, and P. C. Parries. "Process Technology for IBM 14-nm Processor Designs Featuring Silicon-On-Insulator FinFETs". In: *IBM Journal of Research and Development* 62.2/3 (Mar. 2018), 11:1–11:7. DOI: 10.1147/JRD.2018.2800518.

[23] J. H. Lee, Y. M. Shcu, C. C. Wu, Y. M. Liu, Y. C. Chou, and S. C. Chin. "An Electrical Failure Analysis (EFA) Flow to Quantitatively Identify Invisible Defect on Individual Transistor: Using the Characterization of Random Dopant Fluctuation (RDF) as an Example". In: *2018 IEEE International Symposium on the Physical and Failure Analysis of Integrated Circuits (IPFA)*. July 2018, pp. 1–5. DOI: 10.1109/IPFA.2018.8452513.

[24] B. Kaczer, J. Franco, M. Cho, T. Grasser, P. J. Roussel, S. Tyaginov, M. Bina, Y. Wimmer, L. M. Procel, L. Trojman, F. Crupi, G. Pitner, V. Putcha, P. Weckx, E. Bury, Z. Ji, A. De Keersgieter, T. Chiarella, N. Horiguchi, G. Groeseneken, and A. Thean. "Origins and Implications of Increased Channel Hot Carrier Variability in nFinFETs". In: *2015 IEEE International Reliability Physics Symposium*. Apr. 2015, 3B.5.1–3B.5.6. DOI: 10.1109/IRPS.2015.7112706.

[25] P. Magnone, F. Crupi, N. Wils, H. P. Tuinhout, and C. Fiegna. “Characterization and Modeling of Hot Carrier-Induced Variability in Subthreshold Region”. In: *IEEE Transactions on Electron Devices* 59.8 (Aug. 2012), pp. 2093–2099. DOI: `10.1109/TED.2012.2200683`.

[26] A. Makarov, B. Kaczer, P. Roussel, A. Chasin, A. Grill, M. Vandemaele, G. Hellings, A.-M. El-Sayed, T. Grasser, D. Linten, and S. E. Tyaginov. “Stochastic Modeling of the Impact of Random Dopants on Hot-Carrier Degradation in n-FinFETs”. In: *IEEE Electron Device Letters* 40.6 (2019), pp. 870–873. DOI: `10.1109/LED.2019.2913625`.

[27] P. Paliwoda, Z. Chbili, A. Kerber, T. Nigam, K. Nagahiro, S. Cimino, M. Toledano-Luque, L. Pantisano, B. W. Min, and D. Misra. “Self-Heating Effects on Hot Carrier Degradation and Its Impact on Logic Circuit Reliability”. In: *IEEE Transactions on Device and Materials Reliability* 19.2 (June 2019), pp. 249–254. DOI: `10.1109/TDMR.2019.2916230`.

[28] M. A. Alam, B. K. Mahajan, Y. Chen, W. Ahn, H. Jiang, and S. H. Shin. “A Device-to-System Perspective Regarding Self-Heating Enhanced Hot Carrier Degradation in Modern Field-Effect Transistors: A Topical Review”. In: *IEEE Transactions on Electron Devices* 66.11 (Nov. 2019), pp. 4556–4565. DOI: `10.1109/TED.2019.2941445`.

[29] S. E. Liu, J. S. Wang, Y. R. Lu, D. S. Huang, C. F. Huang, W. H. Hsieh, J. H. Lee, Y. S. Tsai, J. R. Shih, Y. Lee, and K. Wu. “Self-Heating Effect in FinFETs and its Impact on Devices Reliability Characterization”. In: *2014 IEEE International Reliability Physics Symposium*. June 2014, 4A.4.1–4A.4.4. DOI: `10.1109/IRPS.2014.6860642`.

[30] S. Mittl and F. Guarin. “Self-Heating and its Implications on Hot Carrier Reliability Evaluations”. In: *2015 IEEE International Reliability Physics Symposium*. Apr. 2015, 4A.4.1–4A.4.6. DOI: `10.1109/IRPS.2015.7112726`.

[31] C. Hu, S. C. Tam, F.-C. Hsu, P.-K. Ko, T.-Y. Chan, and K. W. Terrill. “Hot-Electron-Induced MOSFET Degradation-Model, Monitor, and Improvement”. In: *IEEE Transactions on Electron Devices* 32.2 (Feb. 1985), pp. 375–385. DOI: `10.1109/T-ED.1985.21952`.

[32] B. S. Doyle, M. Bourcerie, C. Bergonzoni, R. Benecchi, A. Bravis, K. R. Mistry, and A. Boudou. “The Generation and Characterization of Electron and Hole Traps Created by Hole Injection During Low Gate Voltage Hot-Carrier Stressing of n-MOS Transistors”. In: *IEEE Transactions on Electron Devices* 37.8 (Aug. 1990), pp. 1869–1876. DOI: `10.1109/16.57138`.

[33] S. E. Rauch and G. La Rosa. “The Energy-Driven Paradigm of nMOSFET Hot-Carrier Effects”. In: *IEEE Transactions on Device and Materials Reliability* 5.4 (Dec. 2005), pp. 701–705. DOI: `10.1109/TDMR.2005.860560`.

[34] C. Guerin, V. Huard, and A. Bravaix. “General Framework About Defect Creation at the Si/SiO_2 Interface”. In: *Journal of Applied Physics* 105.11 (2009), p. 114513. DOI: 10.1063/1.3133096.

[35] M. Bina, S. Tyaginov, J. Franco, K. Rupp, Y. Wimmer, D. Osintsev, B. Kaczer, and T. Grasser. “Predictive Hot-Carrier Modeling of n-Channel MOSFETs”. In: *IEEE Transactions on Electron Devices* 61.9 (Sept. 2014), pp. 3103–3110. DOI: 10.1109/TED.2014.2340575.

[36] E. H. Nicollian, C. N. Berglund, P. F. Schmidt, and J. M. Andrews. “Electrochemical Charging of Thermal SiO_2 Films by Injected Electron Currents”. In: *Journal of Applied Physics* 42.13 (1971), pp. 5654–5664. DOI: 10.1063/1.1659996.

[37] Chenming Hu. “Lucky-Electron Model of Channel Hot Electron Emission”. In: *1979 International Electron Devices Meeting*. 1979, pp. 22–25. DOI: 10.1109/IEDM.1979.189529.

[38] W. Shockley. “Problems Related to p-n Junctions in Silicon”. In: *Solid-State Electronics* 2.1 (1961), pp. 35–67. DOI: 10.1016/0038-1101(61)90054-5.

[39] Woltjer and Paulzen. “Universal Description of Hot-Carrier-Induced Interface States in nMOSFETs”. In: *1992 International Technical Digest on Electron Devices Meeting*. 1992, pp. 535–538. DOI: 10.1109/IEDM.1992.307418.

[40] R. Woltjer, G. M. Paulzen, H. G. Pomp, H. Lifka, and P. H. Woerlee. “Three Hot-Carrier Degradation Mechanisms in Deep-Submicron pMOSFETs”. In: *IEEE Transactions on Electron Devices* 42.1 (1995), pp. 109–115. DOI: 10.1109/16.370028.

[41] K. Mistry and B. Doyle. “A Model for AC Hot-Carrier Degradation in n-Channel MOSFETs”. In: *IEEE Electron Device Letters* 12.9 (1991), pp. 492–494. DOI: 10.1109/55.116928.

[42] K. R. Mistry and B. Doyle. “AC Versus DC Hot-Carrier Degradation in n-Channel MOSFETs”. In: *IEEE Transactions on Electron Devices* 40.1 (1993), pp. 96–104. DOI: 10.1109/16.249430.

[43] D. J. DiMaria and J. W. Stasiak. “Trap Creation in Silicon Dioxide Produced by Hot Electrons”. In: *Journal of Applied Physics* 65.6 (1989), pp. 2342–2356. DOI: 10.1063/1.342824.

[44] D. J. DiMaria. “Defect Generation Under Substrate-Hot-Electron Injection into Ultrathin Silicon Dioxide Layers”. In: *Journal of Applied Physics* 86.4 (1999), pp. 2100–2109. DOI: 10.1063/1.371016.

[45] D. J. DiMaria and J. H. Stathis. “Anode Hole Injection, Defect Generation, and Breakdown in Ultrathin Silicon Dioxide Films”. In: *Journal of Applied Physics* 89.9 (2001), pp. 5015–5024. DOI: 10.1063/1.1363680.

[46] S. E. Rauch and G. La Rosa. “The Energy Driven Paradigm of nMOSFET Hot Carrier Effects”. In: *2005 IEEE International Reliability Physics Symposium, 2005. Proceedings. 43rd Annual.* 2005, pp. 708–709. DOI: 10.1109/RELPHY.2005.1493216.

[47] K. Hess, L. Register, B. Tuttle, J. Lyding, and I. Kizilyalli. “Impact of Nanostructure Research on Conventional Solid-State Electronics: The Giant Isotope Effect in Hydrogen Desorption and CMOS Lifetime”. In: *Physica E: Low-dimensional Systems and Nanostructures* 3.1–3 (1998), pp. 1–7. DOI: 10.1016/S1386-9477(98)00211-2.

[48] K. Hess. “Theory of Channel Hot-Carrier Degradation in MOSFETs”. In: *Physica B: Condensed Matter* 272.1-4 (Dec. 1999), pp. 527–531. DOI: 10.1016/S0921-4526(99)00363-4.

[49] K. Hess, A. Haggag, W. McMahon, B. Fischer, K. Cheng, J. Lee, and J. Lyding. “Simulation of Si-SiO$_2$ Defect Generation in CMOS Chips: From Atomistic Structure to Chip Failure Rates”. In: *2000 IEEE International Electron Devices Meeting (IEDM).* Dec. 2000, pp. 93–96. DOI: 10.1109/IEDM.2000.904266.

[50] W. McMahon and K. Hess. “A Multi-Carrier Model for Interface Trap Generation”. In: *Journal of Computational Electronics* 1.3 (2002), pp. 395–398. DOI: 10.1023/A:1020716111756.

[51] W. McMahon, K. Matsuda, J. Lee, K. Hess, and J. Lyding. “The Effects of a Multiple Carrier Model of Interface Trap Ggeneration on Lifetime Extraction for MOSFETs”. In: *2002 International Conference on Modeling and Simulation of Microsystems - MSM 2002.* Ed. by M. Laudon and B. Romanowicz. 0970827571. 2002, pp. 576–579.

[52] W. McMahon, A. Haggag, and K. Hess. “Reliability Scaling Issues for Nanoscale Devices”. In: *IEEE Transactions on Nanotechnology* 2.1 (Mar. 2003), pp. 33–38. DOI: 10.1109/TNANO.2003.808515.

[53] C. Guerin, V. Huard, and A. Bravaix. “The Energy-Driven Hot-Carrier Degradation Modes of nMOSFETs”. In: *IEEE Transactions on Device and Materials Reliability* 7.2 (2007), pp. 225–235. DOI: 10.1109/TDMR.2007.901180.

[54] A. Bravaix, C. Guerin, V. Huard, D. Roy, J. M. Roux, and E. Vincent. “Hot-Carrier Acceleration Factors for Low Power Management in DC-AC Stressed 40nm NMOS Node at High Temperature”. In: *2009 IEEE International Reliability Physics Symposium.* Apr. 2009, pp. 531–548. DOI: 10.1109/IRPS.2009.5173308.

[55] A. Bravaix, V. Huard, D. Goguenheim, and E. Vincent. “Hot-Carrier to Cold-Carrier Device Lifetime Modeling with Temperature for Low Power 40nm Si-bulk NMOS and PMOS FETs”. In: *2011 International Electron Devices Meeting.* Dec. 2011, pp. 27.5.1–27.5.4. DOI: 10.1109/IEDM.2011.6131625.

[56] A. Bravaix, Y. M. Randriamihaja, V. Huard, D. Angot, X. Federspiel, W. Arfaoui, P. Mora, F. Cacho, M. Saliva, C. Besset, S. Renard, D. Roy, and E. Vincent. "Impact of the Gate-Stack Change from 40nm Node SiON to 28nm High-K Metal Gate on the Hot-Carrier and Bias Temperature Damage". In: *2013 IEEE International Reliability Physics Symposium (IRPS)*. Apr. 2013, pp. 2D.6.1–2D.6.9. DOI: 10.1109/IRPS.2013.6531961.

[57] S. Tyaginov, I. Starkov, O. Triebl, H. Ceric, T. Grasser, H. Enichlmair, J. M. Park, and C. Jungemann. "Secondary Generated Holes as a Crucial Component for Modeling of HC Degradation in High-Voltage n-MOSFET". In: *2011 International Conference on Simulation of Semiconductor Processes and Devices*. Sept. 2011, pp. 123–126. DOI: 10.1109/SISPAD.2011.6035065.

[58] M. Born and R. Oppenheimer. "Zur Quantentheorie der Molekeln". In: *Annalen der Physik* 389.20 (1927), pp. 457–484. DOI: 10.1002/andp.19273892002.

[59] M. Born and K. Huang. *Dynamical Theory of Crystal Lattices*. Oxford New York: Oxford University Press, 1988.

[60] Y. Wimmer, W. Gös, A.-M. El-Sayed, A. L. Shluger, and T. Grasser. "On the Validity of the Harmonic Potential Energy Surface Approximation for Nonradiative Multiphonon Charge Transitions in Oxide Defects". In: *Book of Abstracts of the International Workshop on Computational Electronics (IWCE)*. 2015, pp. 97–98.

[61] Y. Wimmer. "Hydrogen Related Defects in Amorphous SiO_2 and the Negative Bias Temperature Instability". PhD thesis. E360, 2017.

[62] Y. Wimmer, A.-M. El-Sayed, W. Gös, T. Grasser, and A. L. Shluger. "Role of Hydrogen in Volatile Behaviour of Defects in SiO_2-Based Electronic Devices". In: *Proceedings of the Royal Society A: Mathematical, Physical and Engineering Science* 472.2190 (June 2016), p. 20160009. DOI: 10.1098/rspa.2016.0009.

[63] C. H. Henry and D. V. Lang. "Nonradiative Capture and Recombination by Multiphonon Emission in GaAs and GaP". In: *Phys. Rev. B* 15 (2 Jan. 1977), pp. 989–1016. DOI: 10.1103/PhysRevB.15.989.

[64] A. Nitzan. *Chemical Dynamics in Condensed Phases : Relaxation, Transfer and Reactions in Condensed Molecular Systems*. Oxford New York: Oxford University Press, 2006. ISBN: 9780198529798. DOI: 10.1002/cphc.200700074.

[65] T. Chachiyo and J. H. Rodriguez. "A Direct Method for Locating Minimum-Energy Crossing Points (MECPs) in Spin-Forbidden Transitions and Nonadiabatic Reactions". In: *The Journal of Chemical Physics* 123.9 (2005), p. 094711. DOI: 10.1063/1.2007708.

[66] Y. Jia, S. Poncé, A. Miglio, M. Mikami, and X. Gonze. “Beyond the One-Dimensional Configuration Coordinate Model of Photoluminescence”. In: *Phys. Rev. B* 100 (15 Oct. 2019), p. 155109. DOI: 10.1103/PhysRevB.100.155109.

[67] *http://viennashe.sourceforge.net/*. 2014.

[68] P. Sharma, S. E. Tyaginov, S. E. Rauch, J. Franco, A. Makarov, M. I. Vexler, B. Kaczer, and T. Grasser. “Hot-Carrier Degradation Modeling of Decananometer nMOSFETs Using the Drift-Diffusion Approach”. In: *IEEE Electron Device Letters* 38.2 (2017), pp. 160–163. DOI: 10.1109/LED.2016.2645901.

[69] J. W. Lyding, K. Hess, and I. C. Kizilyalli. “Reduction of Hot Electron Degradation in Metal Oxide Semiconductor Transistors by Deuterium Processing”. In: *Applied Physics Letters* 68.18 (1996), pp. 2526–2528. DOI: 10.1063/1.116172.

[70] E. Li, E. Rosenbaum, J. Tao, and P. Fang. “CMOS Hot Carrier Lifetime Improvement from Deuterium Anneal”. In: *56th Annual Device Research Conference Digest*. June 1998, pp. 22–23. DOI: 10.1109/DRC.1998.731105.

[71] W. F. Clark, E. Cartier, and E. Y. Wu. “Hot Carrier Lifetime and Dielectric Breakdown in MOSFETs Processed with Deuterium”. In: *2001 6th International Symposium on Plasma and Process Induced Damage*. May 2001, pp. 80–85. DOI: 10.1109/PPID.2001.929984.

[72] Z. Chen, P. Ong, A. K. Mylin, V. Singh, and S. Chetlur. “Direct Evidence of Multiple Vibrational Excitation for the Si-H/D Bond Breaking in Metal-Oxide-Semiconductor Transistors”. In: *Applied Physics Letters* 81.17 (2002), pp. 3278–3280. DOI: 10.1063/1.1516863.

[73] K. L. Brower. “Dissociation Kinetics of Hydrogen-Passivated (111) Si-SiO_2 Interface Defects”. In: *Phys. Rev. B* 42 (6 Aug. 1990), pp. 3444–3453. DOI: 10.1103/PhysRevB.42.3444.

[74] G. Boendgen and P. Saalfrank. “STM-Induced Desorption of Hydrogen from a Silicon Surface: An Open-System Density Matrix Study”. In: *The Journal of Physical Chemistry B* 102.41 (1998), pp. 8029–8035. DOI: 10.1021/jp9823695.

[75] P. Guyot-Sionnest, P. H. Lin, and E. M. Hiller. “Vibrational Dynamics of the Si-H Stretching Modes of the Si(100)/H:2×1 Surface”. In: *The Journal of Chemical Physics* 102.10 (1995), p. 4269. DOI: 10.1063/1.469474.

[76] S. Sakong, P. Kratzer, X. Han, T. Balgar, and E. Hasselbrink. “Isotope Effects in the Vibrational Lifetime of Hydrogen on Germanium(100): Theory and Experiment”. In: *The Journal of Chemical Physics* 131.12 (2009), p. 124502. DOI: 10.1063/1.3224121.

[77] M. M. Albert and N. H. Tolk. “Absolute Total Cross Sections for Electron-Stimulated Desorption of Hydrogen and Deuterium from Silicon (111) Measured by Second Harmonic Generation”. In: *Phys. Rev. B* 63 (3 Dec. 2000), p. 035308. DOI: 10.1103/PhysRevB.63.035308.

[78] P. Avouris, R. Walkup, A. Rossi, H. Akpati, P. Nordlander, T.-C. Shen, G. Abeln, and J. Lyding. “Breaking Individual Chemical Bonds via STM-Induced Excitations”. In: *Surface Science* 363.1 (1996). Dynamical Quantum Processes on Solid Surfaces, pp. 368–377. DOI: 10.1016/0039-6028(96)00163-X.

[79] R. Biswas, Y.-P. Li, and B. C. Pan. “Enhanced Stability of Deuterium in Silicon”. In: *Applied Physics Letters* 72.26 (1998), pp. 3500–3502. DOI: 10.1063/1.121640.

[80] K. Cheng, J. Lee, Z. Chen, S. A. Shah, K. Hess, J.-P. Leburton, and J. W. Lyding. “Fundamental Connection Between Hydrogen/Deuterium Desorption at Silicon Surfaces in Ultrahigh Vacuum and at Oxide/Silicon Interfaces in Metal-Oxide-Semiconductor Devices”. In: *Journal of Vacuum Science* 19.4 (2001), p. 1119. DOI: 10.1116/1.1385687.

[81] E. Foley, a. Kam, J. Lyding, and P. Avouris. “Cryogenic UHV-STM Study of Hydrogen and Deuterium Desorption from Si (100)”. In: *Physical Review Letters* 80.100 (1998), pp. 1336–1339. DOI: 10.1103/PhysRevLett.80.1336.

[82] J. W. Lyding, K. Hess, G. C. Abeln, D. S. Thompson, J. S. Moore, M. C. Hersam, E. T. Foley, J. Lee, S. T. Hwang, H. Choi, and Avouris. “Ultrahigh Vacuum-Scanning Tunneling Microscopy Nanofabrication and Hydrogen”. In: *Appl. Surf. Sci.* 130-132 (1998), pp. 221–230. DOI: 10.1016/S0169-4332(98)00054-3.

[83] P. M. Lenahan. “What can Electron Paramagnetic Resonance Tell us About the Si/SiO_2 System?” In: *Journal of Vacuum Science* 16.4 (1998), p. 2134. DOI: 10.1116/1.590301.

[84] R. M. Lenahan, J. P. Campbell, A. Y. Kang, S. T. Liu, and R. A. Weimer. “Radiation-Induced Leakage Currents: Atomic Scale Mechanisms”. In: *IEEE Transactions on Nuclear Science* 48.6 (2001), pp. 2101–2106. DOI: 10.1109/23.983179.

[85] P. M. Lenahan, T. D. Mishima, J. Jumper, T. N. Fogarty, and R. T. Wilkins. “Direct Experimental Evidence for Atomic Scale Structural Changes Involved in the Interface-Trap Transformation Process”. In: *IEEE Transactions on Nuclear Science* 48.6 (2001), pp. 2131–2135. DOI: 10.1109/23.983184.

[86] P. M. Lenahan, T. D. Mishima, T. N. Fogarty, and R. Wilkins. “Atomic-Scale Processes Involved in Long-Term Changes in the Density of States Distribution at the Si/SiO$_2$ Interface”. In: *Applied Physics Letters* 79.20 (2001), pp. 3266–3268. DOI: 10.1063/1.1418261.

[87] P. M. Lenahan and S. E. Curry. “First Observation of the 29Si Hyperfine Spectra of Silicon Dangling Bond Centers in Silicon Nitride”. In: *Applied Physics Letters* 56.2 (1990), pp. 157–159. DOI: 10.1063/1.103278.

[88] P. Lenahan. “Atomic Scale Defects Involved in MOS Reliability Problems”. In: *Microelectronic Engineering* 69.2-4 (Sept. 2003), pp. 173–181. DOI: 10.1016/S0167-9317(03)00294-6.

[89] J. P. Campbell and P. M. Lenahan. “Density of States of P$_{b1}$ Si/SiO$_2$ Interface Trap Centers”. In: *Applied Physics Letters* 80.11 (2002), pp. 1945–1947. DOI: 10.1063/1.1461053.

[90] J. P. Campbell, P. M. Lenahan, A. T. Krishnan, and S. Krishnan. “Direct Observation of the Structure of Defect Centers Involved in the Negative Bias Temperature Instability”. In: *Applied Physics Letters* 87.20 (2005), p. 204106. DOI: 10.1063/1.2131197.

[91] A. Stesmans and V. V. Afanas’ev. “Electrical Activity of Interfacial Paramagnetic Defects in Thermal (100)Si/SiO$_2$”. In: *Physical Review B* 57.16 (Apr. 1998), pp. 10030–10034. DOI: 10.1103/PhysRevB.57.10030.

[92] A. Stesmans, B. Nouwen, and V. V. Afanas’ev. “P$_{b1}$ Interface Defect in Thermal (100)Si/SiO$_2$: ^{29}Si Hyperfine Interaction”. In: *Physical Review B* 58.23 (1998), pp. 15801–15809. DOI: 10.1103/PhysRevB.58.15801.

[93] A. Stesmans, B. Nouwen, and V. Afanas’ev. “Interface Defect in Thermal Hyperfine Interaction”. In: *Physical Review B - Condensed Matter and Materials Physics* 58.23 (Dec. 1998), pp. 15801–15809. DOI: 10.1103/PhysRevB.58.15801.

[94] A. Stesmans and V. V. Afanas’ev. “Electron Spin Resonance Features of Interface Defects in Thermal (100)Si/SiO$_2$”. In: *Journal of Applied Physics* 83.5 (1998), pp. 2449–2457. DOI: 10.1063/1.367005.

[95] V. V. Afanas’ev and A. Stesmans. “Thermally Induced Si(100)/SiO$_2$ Interface Degradation in Poly-Si/SiO$_2$/Si Structures: Evidence for a Hydrogen-Stimulated Process”. In: *Journal of The Electrochemical Society* 148.5 (2001), G279–G282. DOI: 10.1149/1.1362553.

[96] H. Raza. “Theoretical Study of Isolated Dangling Bonds, Dangling Bond Wires, and Dangling Bond Clusters on H:Si(001)-(2×1) Surface”. In: *Phys. Rev. B* 76 (4 July 2007), p. 045308. DOI: 10.1103/PhysRevB.76.045308.

[97] A. Stesmans and V. V. Afanas'ev. "Undetectability of the Point Defect as an Interface State in Thermal". In: *Journal of Physics: Condensed Matter* 10.1 (Jan. 1998), pp. L19–L25. DOI: 10.1088/0953-8984/10/1/003.

[98] E. H. Poindexter, P. J. Caplan, B. E. Deal, and R. R. Razouk. "Interface States and Electron Spin Resonance Centers in Thermally Oxidized (111) and (100) Silicon Wafers". In: *Journal of Applied Physics* 52.2 (1981), pp. 879–884. DOI: 10.1063/1.328771.

[99] P. Lenahan. "Deep Level Defects Involved in MOS Device Instabilities". In: *Microelectronics Reliability* 47.6 (2007), pp. 890–898. DOI: 10.1016/j.microrel.2006.10.016.

[100] J. W. Lyding, T.-C. Shen, J. S. Hubacek, J. R. Tucker, and G. C. Abeln. "Nanoscale Patterning and Oxidation of H-Passivated Si(100)-2×1 Surfaces With an Ultrahigh Vauum Scanning Tunneling Microscope". In: *Applied Physics Letters* 64.15 (1994), pp. 2010–2012. DOI: 10.1063/1.111722.

[101] P. Saalfrank. "Quantum Dynamical Approach to Ultrafast Molecular Desorption from Surfaces". In: *Chemical Reviews* 106.10 (2006), pp. 4116–4159. DOI: 10.1021/cr0501691.

[102] L. Gao, P. P. Pal, T. Seideman, N. P. Guisinger, and J. R. Guest. "Current-Driven Hydrogen Desorption from Graphene: Experiment and Theory". In: *Journal of Physical Chemistry Letters* 7.3 (2016), pp. 486–494. DOI: 10.1021/acs.jpclett.5b02471.

[103] S. Mukherjee, F. Libisch, N. Large, O. Neumann, L. V. Brown, J. Cheng, J. B. Lassiter, E. A. Carter, P. Nordlander, and N. J. Halas. "Hot Electrons Do the Impossible: Plasmo-Induced Dissociation of H_2 on Au". In: *Nano Letters* 13.1 (2013), pp. 240–247. DOI: 10.1021/nl303940z.

[104] P. Avouris, R. Walkup, A. Rossi, T.-C. Shen, G. Abeln, J. Tucker, and J. Lyding. "STM-Induced H Atom Desorption from Si(100): Isotope Effects and Site Selectivity". In: *Chemical Physics Letters* 257.1 (1996), pp. 148–154. DOI: 10.1016/0009-2614(96)00518-0.

[105] B. Persson and P. Avouris. "Local Bond Breaking via STM-Induced Excitations: The Role of Temperature". In: *Surface Science* 390.1 (1997), pp. 45–54. DOI: 10.1016/S0039-6028(97)00507-4.

[106] T. C. Shen. "Atomic-Scale Desorption Through Electronic and Vibrational Excitation Mechanisms". In: *Science* 268 (1995), pp. 1590–1592. DOI: 10.1126/science.268.5217.1590.

[107] T. C. Shen and P. Avouris. "Electron Stimulated Desorption Induced by the Scanning Tunneling Microscope". In: *Surface Science* 390 (1997), pp. 35–44. DOI: 10.1016/S0039-6028(97)00506-2.

[108] T. C. Shen, J. A. Steckel, and K. D. Jordan. “Electron-Stimulated Bond Rearrangements on the H/Si(100)-3×1 Surface”. In: *Surface Science* 446.3 (2000), pp. 211–218. DOI: 10.1016/S0039-6028(99)01147-4.

[109] J. Kanasaki, K. Ichihashi, and K. Tanimura. “Scanning Tunnelling Microscopy Study on Hydrogen Removal from Si(001)-(2×1): H Surface Excited with Low-Energy Electron Beams”. In: *Surface Science* 602.7 (2008), pp. 1322–1327. DOI: 10.1016/j.susc.2007.12.046.

[110] C. Thirstrup, M. Sakurai, T. Nakayama, and M. Aono. “Atomic Scale Modifications of Hydrogen-Terminated Silicon 2×1 and 3×1 (001) Surfaces by Scanning Tunneling Microscope”. In: *Surface Science* 411.1-2 (1998), pp. 203–214. DOI: 10.1016/S0039-6028(98)00364-1.

[111] X. Tong and R. A. Wolkow. “Electron-Induced H Atom Desorption Patterns Created with a Scanning Tunneling Microscope: Implications for Controlled Atomic-Scale Patterning on H-Si(100)”. In: *Surface Science* 600.16 (2006), pp. L199–L203. DOI: 10.1016/j.susc.2006.06.038.

[112] A. J. Mayne and D. Riedel. “Electronic Control of Single-Molecule Dynamics”. In: *Chemical reviews* 106 (2006), pp. 4355–4378. DOI: 10.1021/cr050177h.

[113] M. Sakurai, C. Thirstrup, T. Nakayama, and M. Aono. “Atomic Scale Extraction of Hydrogen Atoms Adsorbed on Si(001) with the Scanning Tunneling Microscope”. In: *Applied Surface Science* 121 (1997), pp. 107–110. DOI: 10.1016/S0169-4332(97)00266-3.

[114] K. Stokbro, C. Thirstrup, M. Sakurai, U. Quaade, B. Hu, F. Perez-Murano, and F. Grey. “STM-Induced Hydrogen Desorption via a Hole Resonance”. In: *Physical Review Letters* 80.12 (1998), pp. 2618–2621. DOI: 10.1103/PhysRevLett.80.2618.

[115] K. Stokbro, B. Y.-K. Hu, C. Thirstrup, and X. C. Xie. “First-Principles Theory of Inelastic Currents in a Scanning Tunneling Microscope”. In: *Phys. Rev. B* 58 (12 Sept. 1998), pp. 8038–8041. DOI: 10.1103/PhysRevB.58.8038.

[116] N. Itoh and A. M. Stoneham. “Treatment of Semiconductor Surfaces by Laser-Induced Electronic Excitation”. In: *J. Phys. Condens. Matter* 13.26 (2001), R489. DOI: 10.1088/0953-8984/13/26/201.

[117] T. Vondrak and X.-Y. Zhu. “Dissociation of a Surface Bond by Direct Optical Excitation: H-Si(100)”. In: *Physical Review Letters* 82.9 (1999), pp. 1967–1970. DOI: 10.1103/PhysRevLett.82.1967.

[118] T. Vondrak and X.-Y. Zhu. “Direct Photodesorption of Atomic Hydrogen from Si(100) at 157 nm: Experiment and Simulation”. In: *The Journal of Physical Chemistry B* 103.23 (1999), pp. 4892–4899. DOI: 10.1021/jp990636g.

[119] L. Soukiassian, A. J. Mayne, M. Carbone, and G. Dujardin. “Atomic-Scale Desorption of H Atoms from the Si(100)-2×1:H Surface: Inelastic Electron Interactions”. In: *Phys. Rev. B* 68 (3 July 2003), p. 035303. DOI: `10.1103/PhysRevB.68.035303`.

[120] A. J. Mayne, D. Riedel, G. Comtet, and G. Dujardin. “Atomic-Scale Studies of Hydrogenated Semiconductor Surfaces”. In: *Progress in Surface Science* 81.1 (2006), pp. 1–51. DOI: `10.1016/j.progsurf.2006.01.001`.

[121] K. Morgenstern, N. Lorente, and K.-H. Rieder. “Controlled Manipulation of Single Atoms and Small Molecules using the Scanning Tunnelling Microscope”. In: *physica status solidi (b)* 250.9 (2013), pp. 1671–1751. DOI: `10.1002/pssb.201248392`.

[122] R. E. Palmer and P. J. Rous. “Resonances in Electron Scattering by Molecules on Surfaces”. In: *Rev. Mod. Phys.* 64 (2 Apr. 1992), pp. 383–440. DOI: `10.1103/RevModPhys.64.383`.

[123] J. Gadzuk, L. Richter, S. Buntin, D. King, and R. Cavanagh. “Laser-Excited Hot-Electron Induced Desorption: A Theoretical Model Applied to NO/Pt(111)”. In: *Surface Science* 235.2 (1990), pp. 317–333. DOI: `10.1016/0039-6028(90)90807-K`.

[124] F. Weik, A. de Meijere, and E. Hasselbrink. “Wavelength Dependence of the Photochemistry of O_2 on Pd(111) and the Role of Hot Electron Cascades”. In: *The Journal of Chemical Physics* 99.1 (1993), pp. 682–694. DOI: `10.1063/1.465741`.

[125] G. Dujardin, F. Rose, J. Tribollet, and A. J. Mayne. “Inelastic Transport of Tunnel and Field-Emitted Electrons through a Single Atom”. In: *Phys. Rev. B* 63 (8 Feb. 2001), p. 081305. DOI: `10.1103/PhysRevB.63.081305`.

[126] T. Tewksbury and H.-S. Lee. “Characterization, Modeling, and Minimization of Transient Threshold Voltage Shifts in MOSFETs”. In: *IEEE Journal of Solid-State Circuits* 29.3 (1994), pp. 239–252. DOI: `10.1109/4.278345`.

[127] A. Lelis, H. Boesch, T. Oldham, and F. McLean. “Reversibility of Trapped Hole Annealing”. In: *IEEE Transactions on Nuclear Science* 35.6 (1988), pp. 1186–1191. DOI: `10.1109/23.25437`.

[128] A. Lelis and T. Oldham. “Time Dependence of Switching Oxide Traps”. In: *IEEE Transactions on Nuclear Science* 41.6 (Dec. 1994), pp. 1835–1843. DOI: `10.1109/23.340515`.

[129] H. Eyring. “The Activated Complex in Chemical Reactions”. In: *The Journal of Chemical Physics* 3.2 (1935), pp. 107–115. DOI: `10.1063/1.1749604`.

[130] M. G. Evans and M. Polanyi. “Some Applications of the Transition State Method to the Calculation of Reaction Velocities, especially in Solution”. In: *Trans. Faraday Soc.* 31 (0 1935), pp. 875–894. DOI: `10.1039/TF9353100875`.

[131] J. L. Bao and D. G. Truhlar. “Variational Transition State Theory: Theoretical Framework and Recent Developments”. In: *Chem. Soc. Rev.* 46 (24 2017), pp. 7548–7596. DOI: `10.1039/C7CS00602K`.

[132] H. Mökkönen, T. Ikonen, T. Ala-Nissila, and H. Jónsson. “Transition State Theory Approach to Polymer Escape from a One Dimensional Potential Well”. In: *The Journal of Chemical Physics* 142.22 (2015), p. 224906. DOI: `10.1063/1.4921959`.

[133] H. Feng, K. Zhang, and J. Wang. “Non-Equilibrium Transition State Rate Theory”. In: *Chem. Sci.* 5 (10 2014), pp. 3761–3769. DOI: `10.1039/C4SC00831F`.

[134] K. Huang and A. Rhys. “Theory of Light Absorption and Non-Radiative Transitions in F-Centres”. In: *Proceedings of the Royal Society of London A: Mathematical, Physical and Engineering Sciences* 204.1078 (1950), pp. 406–423. ISSN: 0080-4630. DOI: `10.1098/rspa.1950.0184`.

[135] R. Kubo. “Thermal Ionization of Trapped Electrons”. In: *Phys. Rev.* 86 (6 June 1952), pp. 929–937. DOI: `10.1103/PhysRev.86.929`.

[136] R. Kubo and Y. Toyozawa. “Application of the Method of Generating Function to Radiative and Non-Radiative Transitions of a Trapped Electron in a Crystal”. In: *Progress of Theoretical Physics* 13.2 (Feb. 1955), pp. 160–182. DOI: `10.1143/PTP.13.160`.

[137] H. Gummel and M. Lax. “Thermal Capture of Electrons in Silicon”. In: *Annals of Physics* 2.1 (1957), pp. 28–56. ISSN: 0003-4916. DOI: `10.1016/0003-4916(57)90034-9`.

[138] J. Collins. “Non-Radiative Processes in Crystals and in Nanocrystals”. In: *ECS Journal of Solid State Science and Technology* 5.1 (Oct. 2015), R3170–R3184. DOI: `10.1149/2.0221601jss`.

[139] P. A. M. Dirac. “Note on Exchange Phenomena in the Thomas Atom”. In: *Mathematical Proceedings of the Cambridge Philosophical Society* 26.3 (1930), pp. 376–385. DOI: `10.1017/S0305004100016108`.

[140] J. Franck and E. G. Dymond. “Elementary Processes of Photochemical Reactions”. In: *Trans. Faraday Soc.* 21 (2 1926), pp. 536–542. DOI: `10.1039/TF9262100536`.

[141] E. Condon. “A Theory of Intensity Distribution in Band Systems”. In: *Phys. Rev.* 28 (6 Dec. 1926), pp. 1182–1201. DOI: `10.1103/PhysRev.28.1182`.

[142] M. Lax. “The Franck-Condon Principle and Its Application to Crystals”. In: *The Journal of Chemical Physics* 20.11 (1952), pp. 1752–1760. DOI: 10.1063/1.1700283.

[143] J. H. Zheng, H. S. Tan, and S. C. Ng. “Theory of Non-Radiative Capture of Carriers by Multiphonon Processes for Deep Centres in Semiconductors”. In: *Journal of Physics: Condensed Matter* 6.9 (1994), p. 1695. DOI: 10.1088/0953-8984/6/9/012.

[144] F. Schanovsky. “Atomistic Modeling in the Context of the Bias Temperature Instability”. PhD thesis. E360, 2013.

[145] P. Schmidt. “Computationally Efficient Recurrence Relations for One-Dimensional Franck–Condon Overlap Integrals”. In: *Molecular Physics* 108.11 (2010), pp. 1513–1529. DOI: 10.1080/00268971003762142.

[146] G. Rzepa. “Efficient Phyical Modeling of Bias Temperature Instability”. PhD thesis. E360, 2018.

[147] R. A. Marcus. “Electron Transfer Reactions in Chemistry. Theory and Experiment”. In: *Rev. Mod. Phys.* 65 (3 July 1993), pp. 599–610. DOI: 10.1103/RevModPhys.65.599.

[148] G. D. Barmparis, Y. S. Puzyrev, X.-G. Zhang, and S. T. Pantelides. “Theory of Inelastic Multiphonon Scattering and Carrier Capture by Defects in Semiconductors: Application to Capture Cross Sections”. In: *Phys. Rev. B* 92 (21 Dec. 2015), p. 214111. DOI: 10.1103/PhysRevB.92.214111.

[149] L. Shi, K. Xu, and L.-W. Wang. “Comparative Study of Ab Initio Nonradiative Recombination Rate Calculations under Different Formalisms”. In: *Phys. Rev. B* 91 (20 May 2015), p. 205315. DOI: 10.1103/PhysRevB.91.205315.

[150] G. Nan, X. Yang, L. Wang, Z. Shuai, and Y. Zhao. “Nuclear Tunneling Effects of Charge Transport in Rubrene, Tetracene, and Pentacene”. In: *Phys. Rev. B* 79 (11 Mar. 2009), p. 115203. DOI: 10.1103/PhysRevB.79.115203.

[151] A. Alkauskas, Q. Yan, and C. G. Van de Walle. “First-Principles Theory of Nonradiative Carrier Capture via Multiphonon Emission”. In: *Phys. Rev. B* 90 (7 Aug. 2014), p. 075202. DOI: 10.1103/PhysRevB.90.075202.

[152] L. Shi and L.-W. Wang. “Ab Initio Calculations of Deep-Level Carrier Nonradiative Recombination Rates in Bulk Semiconductors”. In: *Phys. Rev. Lett.* 109 (24 Dec. 2012), p. 245501. DOI: 10.1103/PhysRevLett.109.245501.

[153] Y.-Y. Liu, F. Liu, R. Wang, J.-W. Luo, X. Jiang, R. Huang, S.-S. Li, and L.-W. Wang. “Characterizing the Charge Trapping across Crystalline and Amorphous Si/SiO$_2$/HfO$_2$ Stacks from First-Principle Calculations”. In: *Phys. Rev. Applied* 12 (6 Dec. 2019), p. 064012. DOI: `10.1103/PhysRevApplied.12.064012`.

[154] Y.-Y. Liu, F. Zheng, X. Jiang, J.-W. Luo, S.-S. Li, and L.-W. Wang. “Ab Initio Investigation of Charge Trapping Across the Crystalline-Si-Amorphous-SiO$_2$ Interface”. In: *Phys. Rev. Applied* 11 (4 Apr. 2019), p. 044058. DOI: `10.1103/PhysRevApplied.11.044058`.

[155] J. Strand, M. Kaviani, D. Gao, A.-M. El-Sayed, V. V. Afanas’ev, and A. L. Shluger. “Intrinsic Charge Trapping in Amorphous Oxide Films: Status and Challenges”. In: *Journal of Physics: Condensed Matter* 30.23 (May 2018), p. 233001. DOI: `10.1088/1361-648x/aac005`.

[156] K. P. McKenna and J. Blumberger. “Crossover From Incoherent to Coherent Electron Tunneling Between Defects in MgO”. In: *Phys. Rev. B* 86 (24 Dec. 2012), p. 245110. DOI: `10.1103/PhysRevB.86.245110`.

[157] K. McKenna and J. Blumberger. “First Principles Modeling of Electron Tunneling Between Defects in m-HfO$_2$”. In: *Microelectronic Engineering* 147 (2015). Insulating Films on Semiconductors 2015, pp. 235–238. ISSN: 0167-9317. DOI: `10.1016/j.mee.2015.04.009`.

[158] J. Blumberger and K. P. McKenna. “Constrained Density Functional Theory Applied to Electron Tunnelling Between Defects in MgO”. In: *Phys. Chem. Chem. Phys.* 15 (6 2013), pp. 2184–2196. DOI: `10.1039/C2CP42537H`.

[159] M. Zelený, J. Hegedüs, A. S. Foster, D. A. Drabold, S. R. Elliott, and R. M. Nieminen. “Ab Initio Study of Cu Diffusion in α-Cristobalite”. In: *New Journal of Physics* 14.11 (Nov. 2012), p. 113029. DOI: `10.1088/1367-2630/14/11/113029`.

[160] A.-M. El-Sayed, M. B. Watkins, T. Grasser, and A. L. Shluger. “Effect of Electric Field on Migration of Defects in Oxides: Vacancies and Interstitials in Bulk MgO”. In: *Physical Review B* 98.6 (Aug. 2018), p. 064102. DOI: `10.1103/PhysRevB.98.064102`.

[161] T. E. Markland and M. Ceriotti. “Nuclear Quantum Effects Enter the Mainstream”. In: *Nature Reviews Chemistry* 2.3 (2018), p. 0109. DOI: `10.1038/s41570-017-0109`.

[162] J. O. Richardson and S. C. Althorpe. “Ring-Polymer Molecular Dynamics Rate-Theory in the Deep-Tunneling Regime: Connection with Semiclassical Instanton Theory”. In: *The Journal of Chemical Physics* 131.21 (2009), p. 214106. DOI: `10.1063/1.3267318`.

[163] J. O. Richardson and M. Thoss. “Communication: Nonadiabatic Ring-Polymer Molecular Dynamics”. In: *The Journal of Chemical Physics* 139.3 (2013), p. 031102. DOI: `10.1063/1.4816124`.

[164] J. O. Richardson, C. Pérez, S. Lobsiger, A. A. Reid, B. Temelso, G. C. Shields, Z. Kisiel, D. J. Wales, B. H. Pate, and S. C. Althorpe. "Concerted Hydrogen-Bond Breaking by Quantum Tunneling in the Water Hexamer Prism". In: *Science* 351.6279 (2016), pp. 1310–1313. DOI: `10.1126/science.aae0012`.

[165] I. R. Craig and D. E. Manolopoulos. "Quantum Statistics and Classical Mechanics: Real Time Correlation Functions from Ring Polymer Molecular Dynamics". In: *The Journal of Chemical Physics* 121.8 (2004), pp. 3368–3373. DOI: `10.1063/1.1777575`.

[166] F. Schanovsky, W. Gös, and T. Grasser. "An Advanced Description of Oxide Traps in MOS Transistors and its Relation to DFT". In: *Journal of Computational Electronics* 9.3-4 (2010), pp. 135–140. DOI: `10.1007/s10825-010-0323-x`.

[167] K. L. Yip and W. B. Fowler. "Electronic Structure of $E_1{}'$ Centers in SiO_2". In: *Phys. Rev. B* 11 (6 Mar. 1975), pp. 2327–2338. DOI: `10.1103/PhysRevB.11.2327`.

[168] E. P. O'Reilly and J. Robertson. "Theory of Defects in Vitreous Silicon Dioxide". In: *Phys. Rev. B* 27 (6 Mar. 1983), pp. 3780–3795. DOI: `10.1103/PhysRevB.27.3780`.

[169] J. K. Rudra, W. B. Fowler, and F. J. Feigl. "Model for the E_2' Center in Alpha Quartz". In: *Phys. Rev. Lett.* 55 (23 Dec. 1985), pp. 2614–2617. DOI: `10.1103/PhysRevLett.55.2614`.

[170] P. M. Lenahan, J. P. Campbell, A. T. Krishnan, and S. Krishnan. "A Model for NBTI in Nitrided Oxide MOSFETs Which Does Not Involve Hydrogen or Diffusion". In: *IEEE Transactions on Device and Materials Reliability* 11.2 (June 2011), pp. 219–226. DOI: `10.1109/TDMR.2010.2063031`.

[171] T. Aichinger, S. Puchner, M. Nelhiebel, T. Grasser, and H. Hutter. "Impact of Hydrogen on Recoverable and Permanent Damage Following Negative Bias Temperature Stress". In: *2010 IEEE International Reliability Physics Symposium.* May 2010, pp. 1063–1068. DOI: `10.1109/IRPS.2010.5488672`.

[172] A. T. Krishnan, S. Chakravarthi, P. Nicollian, V. Reddy, and S. Krishnan. "Negative Bias Temperature Instability Mechanism: The Role of Molecular Hydrogen". In: *Applied Physics Letters* 88.15 (2006), p. 153518. DOI: `10.1063/1.2191828`.

[173] A.-M. El-Sayed, M. B. Watkins, T. Grasser, V. V. Afanas'Ev, and A. L. Shluger. "Hydrogen-Induced Rupture of Strained Si-O Bonds in Amorphous Silicon Dioxide". In: *Physical Review Letters* 114.11 (2015), pp. 115503-1–115503-5. DOI: `10.1103/PhysRevLett.114.115503`.

[174] A.-M. El-Sayed, Y. Wimmer, W. Goes, T. Grasser, V. V. Afanas'ev, and A. L. Shluger. "Theoretical Models of Hydrogen-Induced Defects in Amorphous Silicon Dioxide". In: *Physical Review B* 92.1 (July 2015), p. 014107. DOI: 10.1103/PhysRevB.92.014107.

[175] A.-M. El-Sayed, M. B. Watkins, T. Grasser, V. V. Afanas'Ev, and A. L. Shluger. "Hole Trapping at Hydrogenic Defects in Amorphous Silicon Dioxide". In: *Microelectronic Engineering* 147 (2015), pp. 141–144. DOI: 10.1016/j.mee.2015.04.073.

[176] S. Ling, A.-M. El-Sayed, F. Lopez-Gejo, M. B. Watkins, V. V. AfanasÉv, and A. L. Shluger. "A Computational Study of Si-H Bonds as Precursors for Neutral E′ Centres in Amorphous Silica and at the Si/SiO$_2$ Interface". In: *Microelectronic Engineering* 109 (Sept. 2013), pp. 310–313. DOI: 10.1016/j.mee.2013.03.028.

[177] L. Gerrer, S. Ling, S. M. Amoroso, P. Asenov, A. L. Shluger, and A. Asenov. "From Atoms to Product Reliability: Toward a Generalized Multiscale Simulation Approach". In: *Journal of Computational Electronics* 12.4 (Dec. 2013), pp. 638–650. DOI: 10.1007/s10825-013-0513-4.

[178] U. Khalilov, E. C. Neyts, G. Pourtois, and A. C. T. van Duin. "Can We Control the Thickness of Ultrathin Silica Layers by Hyperthermal Silicon Oxidation at Room Temperature?" In: *The Journal of Physical Chemistry C* 115.50 (Dec. 2011), pp. 24839–24848. DOI: 10.1021/jp2082566.

[179] U. Khalilov, G. Pourtois, S. Huygh, A. C. T. van Duin, E. C. Neyts, and A. Bogaerts. "New Mechanism for Oxidation of Native Silicon Oxide". In: *The Journal of Physical Chemistry C* 117.19 (May 2013), pp. 9819–9825. DOI: 10.1021/jp400433u.

[180] M. H. Evans, M. Caussanel, R. D. Schrimpf, and S. T. Pantelides. "First-Principles Calculations of Mobilities in Ultrathin Double-Gate MOSFETs". In: *Journal of Computational Electronics* 6.1-3 (Apr. 2007), pp. 85–88. DOI: 10.1007/s10825-006-0070-1.

[181] R. Buczko, S. J. Pennycook, and S. T. Pantelides. "Bonding Arrangements at the Si-SiO$_2$ and SiC-SiO$_2$ Interfaces and a Possible Origin of their Contrasting Properties". In: *Physical Review Letters* 84.5 (Jan. 2000), pp. 943–946. DOI: 10.1103/PhysRevLett.84.943.

[182] E. Kobeda and E. A. Irene. "Intrinsic SiO$_2$ Film Stress Measurements on Thermally Oxidized Si". In: *Journal of Vacuum Science & Technology B: Microelectronics Processing and Phenomena* 5.1 (1987), pp. 15–19. DOI: 10.1116/1.583853.

[183] E. P. EerNisse. "Stress in Thermal SiO$_2$ During Growth". In: *Applied Physics Letters* 35.1 (1979), pp. 8–10. DOI: 10.1063/1.90905.

[184] H. W. Conru. "Measuring Small-Area Si/SiO_2 Interface Stress with SEM". In: *Journal of Applied Physics* 47.5 (1976), pp. 2079–2081. DOI: 10.1063/1.322850.

[185] R. J. Jaccodine and W. A. Schlegel. "Measurement of Strains at Si-SiO_2 Interface". In: *Journal of Applied Physics* 37.6 (1966), pp. 2429–2434. DOI: 10.1063/1.1708831.

[186] S. C. H. Lin and I. Pugacz-Muraszkiewicz. "Local Stress Measurement in Thin Thermal SiO_2 Films on Si Substrates". In: *Journal of Applied Physics* 43.1 (1972), pp. 119–125. DOI: 10.1063/1.1660794.

[187] Y. Sugita, S. Watanabe, N. Awaji, and S. Komiya. "Structural Fluctuation of SiO_2 Network at the Interface with Si". In: *Applied Surface Science* 100-101 (1996), pp. 268–271. ISSN: 0169-4332. DOI: 10.1016/0169-4332(96)00302-9.

[188] S. Miyazaki, H. Nishimura, M. Fukuda, L. Ley, and J. Ristein. "Structure and Electronic States of Ultrathin SiO_2 Thermally Grown on Si(100) and Si(111) Surfaces". In: *Applied Surface Science* 113-114 (1997). Proceedings of the Eighth International Conference on Solid Films and Surfaces, pp. 585–589. DOI: 10.1016/S0169-4332(96)00805-7.

[189] K. Hirose, H. Nohira, T. Koike, K. Sakano, and T. Hattori. "Structural Transition Layer at SiO_2/Si Interfaces". In: *Phys. Rev. B* 59 (8 Feb. 1999), pp. 5617–5621. DOI: 10.1103/PhysRevB.59.5617.

[190] A. C. Diebold, D. Venables, Y. Chabal, D. Muller, M. Weldon, and E. Garfunkel. "Characterization and Production Metrology of Thin Transistor Gate Oxide Films". In: *Materials Science in Semiconductor Processing* 2.2 (1999), pp. 103–147. ISSN: 1369-8001. DOI: 10.1016/S1369-8001(99)00009-8.

[191] N. Miyata, H. Watanabe, and M. Ichikawa. "Atomic-Scale Structure of SiO_2/Si Interface Formed by Furnace Oxidation". In: *Phys. Rev. B* 58 (20 Nov. 1998), pp. 13670–13676. DOI: 10.1103/PhysRevB.58.13670.

[192] D. A. Muller, T. Sorsch, S. Moccio, F. H. Baumann, K. Evans-Lutterodt, and G. Timp. "The Electronic Structure at the Atomic Scale of Ultrathin Gate Oxides". In: *Nature* 399.6738 (June 1999), pp. 758–761. DOI: 10.1038/21602.

[193] D. A. Muller and G. D. Wilk. "Atomic Scale Measurements of the Interfacial Electronic Structure and Chemistry of Zirconium Silicate Gate Dielectrics". In: *Applied Physics Letters* 79.25 (Dec. 2001), pp. 4195–4197. DOI: 10.1063/1.1426268.

[194] Y. Yamashita, S. Yamamoto, K. Mukai, J. Yoshinobu, Y. Harada, T. Tokushima, T. Takeuchi, Y. Takata, S. Shin, K. Akagi, and S. Tsuneyuki. “Direct Observation of Site-Specific Valence Electronic Structure at the SiO_2/Si Interface”. In: *Phys. Rev. B* 73 (4 Jan. 2006), p. 045336. DOI: 10.1103/PhysRevB.73.045336.

[195] C. Kaneta, T. Yamasaki, T. Uchiyama, T. Uda, and K. Terakura. “Structure and Electronic Property of Si(100)/SiO_2 Interface”. In: *Microelectronic Engineering* 48.1 (1999). Insulating Films on Semiconductors, pp. 117–120. DOI: 10.1016/S0167-9317(99)00351-2.

[196] J. H. Oh, H. W. Yeom, Y. Hagimoto, K. Ono, M. Oshima, N. Hirashita, M. Nywa, A. Toriumi, and A. Kakizaki. “Chemical Structure of the Ultrathin SiO_2/Si (100) Interface: An Angle-Resolved Si 2*p* Photoemission Study”. In: *Phys. Rev. B* 63 (20 Apr. 2001), p. 205310. DOI: 10.1103/PhysRevB.63.205310.

[197] J. C. Fogarty, H. M. Aktulga, A. Y. Grama, A. C. T. van Duin, and S. A. Pandit. “A Reactive Molecular Dynamics Simulation of the Silica-Water Interface”. In: *The Journal of Chemical Physics* 132.17 (May 2010), p. 174704. DOI: 10.1063/1.3407433.

[198] H. Aktulga, J. Fogarty, S. Pandit, and A. Grama. “Parallel Reactive Molecular Dynamics: Numerical Methods and Algorithmic Techniques”. In: *Parallel Computing* 38.4-5 (Apr. 2012), pp. 245–259. DOI: 10.1016/j.parco.2011.08.005.

[199] Y. Yu, B. Wang, M. Wang, G. Sant, and M. Bauchy. “Revisiting Silica with ReaxFF: Towards Improved Predictions of Glass Structure and Properties via Reactive Molecular Dynamics”. In: *Journal of Non-Crystalline Solids* 443 (2016), pp. 148–154. DOI: 10.1016/j.jnoncrysol.2016.03.026.

[200] C. Freysoldt and J. Neugebauer. “First-Principles Calculations for Charged Defects at Surfaces, Interfaces, and Two-Dimensional Materials in the Presence of Electric Fields”. In: *Phys. Rev. B* 97 (20 May 2018), p. 205425. DOI: 10.1103/PhysRevB.97.205425.

[201] A. Stesmans. “Dissociation Kinetics of Hydrogen-Passivated P_b Defects at the (111)Si/SiO_2 Interface”. In: *Phys. Rev. B* 61 (12 Mar. 2000), pp. 8393–8403. DOI: 10.1103/PhysRevB.61.8393.

[202] B. Tuttle and J. B. Adams. “Structure, Dissociation, and the Vibrational Signatures of Hydrogen Clusters in Amorphous Silicon”. In: *Physical Review B* 56.8 (Aug. 1997), pp. 4565–4572. DOI: 10.1103/PhysRevB.56.4565.

[203] B. Tuttle and C. G. Van de Walle. “Structure, Energetics, and Vibrational Properties of Si-H Bond Dissociation in Silicon”. In: *Physical Review B* 59.20 (May 1999), pp. 12884–12889. DOI: 10.1103/PhysRevB.59.12884.

[204] B. Tuttle. “Hydrogen and P_b Defects at the Si-SiO$_2$ Interface: An Ab Initio Cluster Study”. In: *Phys. Rev. B* 60 (4 July 1999), pp. 2631–2637. DOI: `10.1103/PhysRevB.60.2631`.

[205] B. Tuttle. “Energetics and Diffusion of Hydrogen in SiO$_2$”. In: *Phys. Rev. B* 61 (7 Feb. 2000), pp. 4417–4420. DOI: `10.1103/PhysRevB.61.4417`.

[206] B. R. Tuttle, D. R. Hughart, R. D. Schrimpf, D. M. Fleetwood, and S. T. Pantelides. “Defect Interactions of H$_2$ in SiO$_2$: Implications for ELDRS and Latent Interface Trap Buildup”. In: *IEEE Transactions on Nuclear Science* 57.6 (Dec. 2010), pp. 3046–3053. DOI: `10.1109/TNS.2010.2086076`.

[207] C. G. Van De Walle. “Energies of Various Configurations of Hydrogen in Silicon”. In: *Physical Review B* 49.7 (Feb. 1994), pp. 4579–4585. DOI: `10.1103/PhysRevB.49.4579`.

[208] “Structure, Energetics, and Dissociation of Si-H Bonds at Dangling Bonds in Silicon”. In: *Physical Review B* 49.20 (May 1994), pp. 14766–14769. DOI: `10.1103/PhysRevB.49.14766`.

[209] C. Van de Walle and B. Tuttle. “Microscopic Theory of Hydrogen in Silicon Devices”. In: *IEEE Transactions on Electron Devices* 47.10 (2000), pp. 1779–1786. DOI: `10.1109/16.870547`.

[210] B. Tuttle, K. Hess, and L. Register. “Hydrogen-Related Defect Creation at the Si(100)-SiO$_2$ Interface of Metal-Oxide-Semiconductor Field Effect Transistors During Hot Electron Stress”. In: *Superlattices and Microstructures* 27.5 (2000), pp. 441–445. DOI: `10.1006/spmi.2000.0859`.

[211] B. R. Tuttle, W. McMahon, and K. Hess. “Hydrogen and Hot Electron Defect Creation at the Si(100)/SiO$_2$ Interface of Metal-Oxide-Semiconductor Field Effect Transistors”. In: *Superlattices and Microstructures* 27.2 (2000), pp. 229–233. DOI: `10.1006/spmi.1999.0804`.

[212] A. A. Bonapasta. “Theory of H Sites in Undoped Crystalline Semiconductors”. In: *Physica B: Condensed Matter* 170.1-4 (Apr. 1991), pp. 168–180. DOI: `10.1016/0921-4526(91)90120-4`.

[213] N. M. Johnson, C. Herring, and C. G. Van de Walle. “Inverted Order of Acceptor and Donor Levels of Monatomic Hydrogen in Silicon”. In: *Physical Review Letters* 73.1 (July 1994), pp. 130–133. DOI: `10.1103/PhysRevLett.73.130`.

[214] N. H. Nickel, G. B. Anderson, N. M. Johnson, and J. Walker. “Nucleation of Hydrogen-Induced Platelets in Silicon”. In: *Physical Review B* 62.12 (Sept. 2000), pp. 8012–8015. DOI: `10.1103/PhysRevB.62.8012`.

[215] R. Elber and M. Karplus. “A Method for Determining Reaction Paths in Large Molecules: Application to Myoglobin”. In: *Chemical Physics Letters* 139.5 (1987), pp. 375–380. DOI: `10.1016/0009-2614(87)80576-6`.

[216] G. Henkelman, B. P. Uberuaga, and H. Jónsson. “A Climbing Image Nudged Elastic Band Method for Finding Saddle Points and Minimum Energy Paths”. In: *The Journal of Chemical Physics* 113.22 (Dec. 2000), pp. 9901–9904. DOI: `10.1063/1.1329672`.

[217] G. Henkelman and H. Jónsson. “A Dimer Method for Finding Saddle Points on High Dimensional Potential Surfaces Using only First Derivatives”. In: *The Journal of Chemical Physics* 111.15 (1999), pp. 7010–7022. DOI: `10.1063/1.480097`.

[218] A. Barducci, G. Bussi, and M. Parrinello. “Well-Tempered Metadynamics: A Smoothly Converging and Tunable Free-Energy Method”. In: *Phys. Rev. Lett.* 100 (2 Jan. 2008), p. 020603. DOI: `10.1103/PhysRevLett.100.020603`.

[219] J. F. Dama, M. Parrinello, and G. A. Voth. “Well-Tempered Metadynamics Converges Asymptotically”. In: *Phys. Rev. Lett.* 112 (24 June 2014), p. 240602. DOI: `10.1103/PhysRevLett.112.240602`.

[220] G. A. Tribello, M. Bonomi, D. Branduardi, C. Camilloni, and G. Bussi. “PLUMED 2: New Feathers for an Old Bird”. In: *Computer Physics Communications* 185.2 (Feb. 2014), pp. 604–613. DOI: `10.1016/j.cpc.2013.09.018`.

[221] A. Stesmans. “Revision of H_2 Passivation of P_b Interface Defects in Standard (111)Si/SiO_2”. In: *Applied Physics Letters* 68.19 (May 1996), pp. 2723–2725. DOI: `10.1063/1.115577`.

[222] K. L. Brower. “Kinetics of H_2 Passivation of P_b Centers at the (111) Si-SiO_2 Interface”. In: *Physical Review B* 38.14 (Nov. 1988), pp. 9657–9666. DOI: `10.1103/PhysRevB.38.9657`.

[223] G. Henkelman, A. Arnaldsson, and H. Jónsson. “A Fast and Robust Algorithm for Bader Decomposition of Charge Density”. In: *Computational Materials Science* 36.3 (June 2006), pp. 354–360. DOI: `10.1016/j.commatsci.2005.04.010`.

[224] W. Tang, E. Sanville, and G. Henkelman. “A Grid-Based Bader Analysis Algorithm Without Lattice Bias”. In: *Journal of Physics: Condensed Matter* 21.8 (Feb. 2009), p. 084204. DOI: `10.1088/0953-8984/21/8/084204`.

[225] M. Yu and D. R. Trinkle. “Accurate and Efficient Algorithm for Bader Charge Integration”. In: *The Journal of Chemical Physics* 134.6 (Feb. 2011), p. 064111. DOI: `10.1063/1.3553716`.

[226] M. Houssa, J. L. Autran, A. Stesmans, and M. M. Heyns. “Model for Interface Defect and Positive Charge Generation in Ultrathin SiO_2/ZrO_2 Gate Dielectric stacks”. In: *Applied Physics Letters* 81.4 (July 2002), pp. 709–711. DOI: `10.1063/1.1496146`.

[227] M. Houssa, J. Autran, M. Heyns, and A. Stesmans. “Model for Defect Generation at the (100)Si/SiO$_2$ Interface During Electron Injection in MOS Structures”. In: *Applied Surface Science* 212-213.SPEC. (May 2003), pp. 749–752. DOI: 10.1016/S0169-4332(03)00042-4.

[228] R. Biswas and Y.-P. Li. “Hydrogen Flip Model for Light-Induced Changes of Amorphous Silicon”. In: *Physical Review Letters* 82.12 (Mar. 1999), pp. 2512–2515. DOI: 10.1103/PhysRevLett.82.2512.

[229] R. D. King-Smith and D. Vanderbilt. “Theory of Polarization of Crystalline Solids”. In: *Physical Review B* 47.3 (Jan. 1993), pp. 1651–1654. DOI: 10.1103/PhysRevB.47.1651.

[230] “Macroscopic Polarization in Crystalline Dielectrics: The Geometric Phase Approach”. In: *Reviews of Modern Physics* 66.3 (July 1994), pp. 899–915. DOI: 10.1103/RevModPhys.66.899.

[231] I. Souza, J. Íñiguez, and D. Vanderbilt. “First-Principles Approach to Insulators in Finite Electric Fields”. In: *Physical Review Letters* 89.11 (Aug. 2002), p. 117602. DOI: 10.1103/PhysRevLett.89.117602.

[232] N. A. Spaldin. “A Beginner’s Guide to the Modern Theory of Polarization”. In: *Journal of Solid State Chemistry* 195 (Nov. 2012), pp. 2–10. DOI: 10.1016/j.jssc.2012.05.010.

[233] “Ab Initio Molecular Dynamics in a Finite Homogeneous Electric Field”. In: *Physical Review Letters* 89.15 (Sept. 2002), p. 157602. DOI: 10.1103/PhysRevLett.89.157602.

[234] D. Vanderbilt and R. D. King-Smith. “Electric Polarization as a Bulk Quantity and its Relation to Surface Charge”. In: *Physical Review B* 48.7 (Aug. 1993), pp. 4442–4455. DOI: 10.1103/PhysRevB.48.4442.

[235] C. Zhang, J. Hutter, and M. Sprik. “Computing the Kirkwood g-Factor by Combining Constant Maxwell Electric Field and Electric Displacement Simulations: Application to the Dielectric Constant of Liquid Water”. In: *The Journal of Physical Chemistry Letters* 7.14 (July 2016), pp. 2696–2701. DOI: 10.1021/acs.jpclett.6b01127.

[236] K. Stokbro, U. J. Quaade, R. Lin, C. Thirstrup, and F. Grey. “Electronic Mechanism of STM-Induced Diffusion of Hydrogen on Si(100)”. In: *Faraday Discuss.* 117 (0 2000), pp. 231–240. DOI: 10.1039/B003179H.

[237] A. Abe, K. Yamashita, and P. Saalfrank. “STM and Laser-Driven Atom Switch: An Open-System Density-Matrix Study of H/Si(100)”. In: *Phys. Rev. B* 67 (23 June 2003), p. 235411. DOI: 10.1103/PhysRevB.67.235411.

[238] Q. Wu and T. Van Voorhis. “Extracting Electron Transfer Coupling Elements from Constrained Density Functional Theory”. In: *The Journal of Chemical Physics* 125.16 (2006), p. 164105. DOI: 10.1063/1.2360263.

[239] B. Kaduk, T. Kowalczyk, and T. Van Voorhis. “Constrained Density Functional Theory”. In: *Chemical Reviews* 112.1 (2012), pp. 321–370. DOI: 10.1021/cr200148b.

[240] N. Holmberg and K. Laasonen. “Efficient Constrained Density Functional Theory Implementation for Simulation of Condensed Phase Electron Transfer Reactions”. In: *Journal of Chemical Theory and Computation* 13.2 (2017), pp. 587–601. DOI: 10.1021/acs.jctc.6b01085.

[241] N. Holmberg and K. Laasonen. “Diabatic Model for Electrochemical Hydrogen Evolution Based on Constrained DFT Configuration Interaction”. In: *The Journal of Chemical Physics* 149.10 (2018), p. 104702. DOI: 10.1063/1.5038959.

[242] A.-M. El-Sayed, M. B. Watkins, V. V. Afanas’ev, and A. L. Shluger. “Nature of Intrinsic and Extrinsic Electron Trapping in SiO_2”. In: *Phys. Rev. B* 89 (12 Mar. 2014), p. 125201. DOI: 10.1103/PhysRevB.89.125201.

[243] A. Stesmans. “Passivation of Pb_0 and Pb_1 Interface Defects in Thermal (100) Si/SiO_2 with Molecular Hydrogen”. In: *Applied Physics Letters* 68.15 (1996), pp. 2076–2078. DOI: 10.1063/1.116308.

[244] A. Stesmans. “Interaction of P_b Defects at the (111)Si/SiO_2 Interface with Molecular Hydrogen: Simultaneous Action of Passivation and Dissociation”. In: *Journal of Applied Physics* 88.1 (July 2000), pp. 489–497. DOI: 10.1063/1.373684.

[245] A. Stesmans. “Influence of Interface Relaxation on Passivation Kinetics in $_2$2 of Coordination P_b Defects at the (111)Si/SiO_2 Interface Revealed by Electron Spin Resonance”. In: *Journal of Applied Physics* 92.3 (2002), pp. 1317–1328. DOI: 10.1063/1.1482427.

[246] E. Cartier, J. H. Stathis, and D. A. Buchanan. “Passivation and Depassivation of Silicon Dangling Bonds at the Si/SiO_2 Interface by Atomic Hydrogen”. In: *Applied Physics Letters* 63.11 (1993), pp. 1510–1512. DOI: 10.1063/1.110758.

[247] E. Cartier, D. A. Buchanan, and G. J. Dunn. “Atomic Hydrogen-Induced Interface Degradation of Reoxidized-Nitrided Silicon Dioxide on Silicon”. In: *Applied Physics Letters* 64.7 (1994), pp. 901–903. DOI: 10.1063/1.110990.

[248] G. Pobegen, S. Tyaginov, M. Nelhiebel, and T. Grasser. “Observation of Normally Distributed Energies for Interface Trap Recovery After Hot-Carrier Degradation”. In: *IEEE Electron Device Letters* 34.8 (Aug. 2013), pp. 939–941. DOI: 10.1109/LED.2013.2262521.

[249] M. Vandemaele, K. Chuang, E. Bury, S. Tyaginov, G. Groeseneken, and B. Kaczer. “The Influence of Gate Bias on the Anneal of Hot-Carrier Degradation”. In: *2020 IEEE International Reliability Physics Symposium (IRPS)*. 2020, pp. 1–7. DOI: `10.1109/IRPS45951.2020.9128218`.

[250] L.-A. Ragnarsson and P. Lundgren. “Electrical Characterization of P_b Centers in (100)Si–SiO_2 Structures: The Influence of Surface Potential on Passivation During Post Metallization Anneal”. In: *Journal of Applied Physics* 88.2 (2000), pp. 938–942. DOI: `10.1063/1.373759`.

[251] S. T. Pantelides, S. Wang, A. Franceschetti, R. Buczko, M. Di Ventra, S. N. Rashkeev, L. Tsetseris, M. Evans, I. Batyrev, L. C. Feldman, S. Dhar, K. McDonald, R. A. Weller, R. Schrimpf, D. Fleetwood, X. Zhou, J. R. Williams, C. C. Tin, G. Chung, T. Isaacs-Smith, S. Wang, S. Pennycook, G. Duscher, K. Van Benthem, and L. Porter. “Si/SiO_2 and SiC/SiO_2 Interfaces for MOSFETs - Challenges and Advances”. In: *Silicon Carbide and Related Materials 2005*. Vol. 527. Materials Science Forum. Trans Tech Publications Ltd, Oct. 2006, pp. 935–948. DOI: `10.4028/www.scientific.net/MSF.527-529.935`.

[252] “Hydrogen in MOSFETs - A Primary Agent of Reliability Issues”. In: *Microelectronics Reliability* 47.6 (June 2007), pp. 903–911. DOI: `10.1016/j.microrel.2006.10.011`.

[253] L. Tsetseris and S. T. Pantelides. “Migration, Incorporation, and Passivation Reactions of Molecular Hydrogen at the Si(100)/SiO_2 Interface”. In: *Phys. Rev. B* 70 (24 Dec. 2004), p. 245320. DOI: `10.1103/PhysRevB.70.245320`.

[254] L. Tsetseris and S. T. Pantelides. “Hydrogenation/Deuteration of the Si-SiO_2 Interface: Atomic-Scale Mechanisms and Limitations”. In: *Applied Physics Letters* 86.11 (2005), pp. 1–3. DOI: `10.1063/1.1883710`.

[255] L. Tsetseris and S. T. Pantelides. “Reactions of Excess Hydrogen at a Si(111) Surface with H Termination: First-Principles Calculations”. In: *Physical Review B - Condensed Matter and Materials Physics* 74.11 (2006), pp. 1–4. DOI: `10.1103/PhysRevB.74.113301`.

[256] L. Tsetseris, X. J. Zhou, D. M. Fleetwood, R. D. Schrimpf, and S. T. Pantelides. “Hydrogen-Related Instabilities in MOS Devices Under Bias Temperature Stress”. In: *IEEE Transactions on Device and Materials Reliability* 7.4 (Dec. 2007), pp. 502–508. DOI: `10.1109/TDMR.2007.910438`.

[257] A. Van Wieringen and N. Warmoltz. “On the Permeation of Hydrogen and Helium in Single Crystal Silicon and Germanium at Elevated Temperatures”. In: *Physica* 22.6-12 (Jan. 1956), pp. 849–865. DOI: `10.1016/S0031-8914(56)90039-8`.

[258] C. G. Van de Walle. “Universal Alignment of Hydrogen Levels in Semiconductors and Insulators”. In: *Physica B: Condensed Matter* 376-377.1 (Apr. 2006), pp. 1–6. DOI: 10.1016/j.physb.2005.12.004.

[259] C. Herring, N. M. Johnson, and C. G. Van de Walle. “Energy Levels of Isolated Interstitial Hydrogen in Silicon”. In: *Phys. Rev. B* 64 (12 Sept. 2001), p. 125209. DOI: 10.1103/PhysRevB.64.125209.

[260] M. Vitiello, N. Lopez, F. Illas, and G. Pacchioni. “H_2 Cracking at SiO_2 Defect Centers”. In: *The Journal of Physical Chemistry A* 104.20 (2000), pp. 4674–4684. DOI: 10.1021/jp993214f.

[261] A. Yokozawa and Y. Miyamoto. “First-Principles Calculations for Charged States of Hydrogen Atoms in SiO_2”. In: *Phys. Rev. B* 55 (20 May 1997), pp. 13783–13788. DOI: 10.1103/PhysRevB.55.13783.

[262] J. Godet, F. Giustino, and A. Pasquarello. “Proton-Induced Fixed Positive Charge at the Si(100)-SiO_2 Interface”. In: *Phys. Rev. Lett.* 99 (12 Sept. 2007), p. 126102. DOI: 10.1103/PhysRevLett.99.126102.

[263] J. Godet and A. Pasquarello. “Proton Diffusion Mechanism in Amorphous SiO_2”. In: *Phys. Rev. Lett.* 97 (15 Oct. 2006), p. 155901. DOI: 10.1103/PhysRevLett.97.155901.

[264] S. A. Sheikholeslam, H. Manzano, C. Grecu, and A. Ivanov. “Reduced Hydrogen Diffusion in Strained Amorphous SiO_2: Understanding Ageing in MOSFET Devices”. In: *J. Mater. Chem. C* 4 (34 2016), pp. 8104–8110. DOI: 10.1039/C6TC02647H.

[265] Q. Zhang, S. Tang, and R. M. Wallace. “Proton Trapping and Diffusion in SiO_2 Thin Films: a First-Principles Study”. In: *Applied Surface Science* 172.1 (2001), pp. 41–46. DOI: 10.1016/S0169-4332(00)00839-4.

[266] T. E. Tsai, D. L. Griscom, and E. J. Friebele. “Medium-Range Structural Order and Fractal Annealing Kinetics of Radiolytic Atomic Hydrogen in High-Purity Silica”. In: *Phys. Rev. B* 40 (9 Sept. 1989), pp. 6374–6380. DOI: 10.1103/PhysRevB.40.6374.

[267] I. A. Shkrob and A. D. Trifunac. “Time-Resolved EPR of Spin-Polarized Mobile H Atoms in Amorphous Silica: The Involvement of Small Polarons”. In: *Phys. Rev. B* 54 (21 Dec. 1996), pp. 15073–15078. DOI: 10.1103/PhysRevB.54.15073.

[268] K. Blum. *Density Matrix Theory and Applications*. Ed. by K. Blum. Springer Verlag, 2012. DOI: 10.1007/978-3-642-20561-3.

[269] G. Lindblad. “On the Generators of Quantum Dynamical Semigroups”. In: *Communications in Mathematical Physics* 48 (June 1976), pp. 119–130. DOI: 10.1007/BF01608499.

[270] I. Andrianov and P. Saalfrank. “Free Vibrational Relaxation of H Adsorbed on a Si(100) Surface Investigated with the Multi-Configurational Time-Dependent Hartree Method”. In: *Chemical Physics Letters* 433.1-3 (2006), pp. 91–96. DOI: `10.1016/j.cplett.2006.11.067`.

[271] I. Andrianov and P. Saalfrank. “Theoretical Study of Vibration-Phonon Coupling of H Adsorbed on a Si(100) Surface.” In: *The Journal of chemical physics* 124.3 (2006), p. 34710. DOI: `10.1063/1.2161191`.

[272] F. Bouakline, F. Lüder, R. Martinazzo, and P. Saalfrank. “Reduced and Exact Quantum Dynamics of the Vibrational Relaxation of a Molecular System Interacting with a Finite-Dimensional Bath”. In: *Journal of Physical Chemistry A* 116 (2012), pp. 11118–11127. DOI: `10.1021/jp304466u`.

[273] F. Bouakline, U. Lorenz, G. Melani, G. K. Paramonov, and P. Saalfrank. “Isotopic Effects in Vibrational Relaxation Dynamics of H on a Si(100) Surface”. In: *The Journal of Chemical Physics* 147.14 (2017), p. 144703. DOI: `10.1063/1.4994635`.

[274] U. Lorenz and P. Saalfrank. “A Novel System-Bath Hamiltonian for Vibration-Phonon Coupling: Formulation, and Application to the Relaxation of Si-H and Si-D Bending Modes of H/D:Si(100)-(2×1)”. In: *Chemical Physics* 482 (2017), pp. 69–80. DOI: `10.1016/j.chemphys.2016.06.004`.

[275] I. Andrianov and P. Saalfrank. “Vibrational Relaxation rates for H on a Si (10):(2×1) Surface : A Two-Dimensional Model”. In: *Chem. Phys. Lett.* 350.12 (2001), pp. 191–197. DOI: `10.1016/S0009-2614(01)01304-5`.

[276] K. Zenichowski, T. Klamroth, and P. Saalfrank. “Open-System Density Matrix Description of an STM-Driven Atomic Switch: H on Si(100)”. In: *Applied Physics A* 93.2 (Nov. 2008), pp. 319–333. DOI: `10.1007/s00339-008-4833-3`.

[277] B. Persson and J. Demuth. “Inelastic Electron Tunnelling from a Metal Tip”. In: *Solid State Communications* 57.9 (1986), pp. 769–772. DOI: `10.1016/0038-1098(86)90856-2`.

[278] R. E. Walkup, D. M. Newns, and P. Avouris. “Role of Multiple Enelastic Transitions in Atom Transfer with the Scanning Tunneling Microscope”. In: *Phys. Rev. B* 48 (3 July 1993), pp. 1858–1861. DOI: `10.1103/PhysRevB.48.1858`.

[279] R. Walkup, D. Newns, and P. Avouris. “Vibrational Heating and Atom Transfer with the STM”. In: *Journal of Electron Spectroscopy and Related Phenomena* 64 (1993), pp. 523–532. DOI: `10.1016/0368-2048(93)80118-6`.

[280] S. Gao, M. Persson, and B. I. Lundqvist. “Theory of Atom Transfer with a Scanning Tunneling Microscope”. In: *Phys. Rev. B* 55 (7 Feb. 1997), pp. 4825–4836. DOI: 10.1103/PhysRevB.55.4825.

[281] G. P. Salam, M. Persson, and R. E. Palmer. “Possibility of Coherent Multiple Excitation in Atom Transfer with a Scanning Tunneling Microscope”. In: *Physical Review B* 49.15 (1994), pp. 10655–10662. DOI: 10.1103/PhysRevB.49.10655.

[282] J. W. Gadzuk. “Inelastic Resonance Scattering, Tunneling, and Desorption”. In: *Physical Review B* 44.24 (1991), pp. 13466–13477. DOI: 10.1103/PhysRevB.44.13466.

[283] J. W. Gadzuk. “Resonance-Assisted, Hot-Electron-Induced Desorption”. In: *Surface Science* 342.1-3 (1995), pp. 345–358. DOI: 10.1016/0039-6028(95)00607-9.

[284] B. Persson and H. Ueba. “Theory of Inelastic Tunneling Induced Motion of Adsorbates on Metal Surfaces”. In: *Surface Science* 502 (2002), pp. 18–25. ISSN: 0039-6028. DOI: 10.1016/S0039-6028(01)01893-3.

[285] S. Gao. “Quantum Kinetic Theory of Vibrational Heating and Bond Breaking by Hot Electrons”. In: *Physical Review B* 55.3 (1997), pp. 1876–1886. DOI: 10.1103/PhysRevB.55.1876.

[286] J. E. Shelby. “Molecular Diffusion and Solubility of Hydrogen Isotopes in Vitreous Silica”. In: *Journal of Applied Physics* 48.8 (1977), pp. 3387–3394. DOI: 10.1063/1.324180.

[287] M. C. Wang, Z. Y. Hsieh, C. S. Liao, C. H. Tu, S. Y. Chen, and H. S. Huang. “Effective Edge Width for 65 nm pMOSFETs and Their Variations Under CHC Stress”. In: *IEEE Electron Device Letters* 32.5 (May 2011), pp. 584–586. DOI: 10.1109/LED.2011.2109696.

[288] I. Polishchuk, Y.-C. Yeo, Q. Lu, T.-J. King, and C. Hu. “Hot-Carrier Reliability Comparison for pMOSFETs with Ultrathin Silicon-Nitride and Silicon-Oxide Gate Dielectrics”. In: *IEEE Transactions on Device and Materials Reliability* 1.3 (Sept. 2001), pp. 158–162. ISSN: 1530-4388. DOI: 10.1109/7298.974831.

[289] C. Jungemann and B. Meinerzhagen. *Hierarchical Device Simulation*. Ed. by S. Selberherr. Springer, Wien, 2003. DOI: 10.1007/978-3-7091-6086-2.

[290] F. Hsu and K. Chiu. “Temperature Dependence of Hot-Electron-Induced Degradation in MOSFETs”. In: *IEEE Electron Device Letters* 5.5 (1984), pp. 148–150. DOI: 10.1109/EDL.1984.25865.

[291] M. Song, K. P. MacWilliams, and J. C. S. Woo. “Comparison of NMOS and PMOS Hot Carrier Effects from 300 to 77 K”. In: *IEEE Transactions on Electron Devices* 44.2 (1997), pp. 268–276. DOI: 10.1109/16.557714.

[292] Z. Song, Z. Chen, A. Z. Yong, Y. Song, J. Wu, and K. Chien. "The Failure Mechanism Worst Stress Condition for Hot Carrier Injection of NMOS". In: *ECS Transactions* 52.1 (Mar. 2013), pp. 947–952. DOI: `10.1149/05201.0947ecst`.

[293] E. Amat, T. Kauerauf, R. Degraeve, R. Rodríguez, M. Nafría, X. Aymerich, and G. Groeseneken. "Channel Hot-Carrier Degradation in pMOS and nMOS Short Channel Transistors with high-κ Dielectric Stack". In: *Microelectronic Engineering* 87.1 (2010), pp. 47–50. ISSN: 0167-9317. DOI: `10.1016/j.mee.2009.05.013`.

[294] K. T. Lee, C. Y. Kang, O. S. Yoo, R. Choi, B. H. Lee, J. C. Lee, H. Lee, and Y. Jeong. "PBTI-Associated High-Temperature Hot Carrier Degradation of nMOSFETs With Metal-Gate/High-κ Dielectrics". In: *IEEE Electron Device Letters* 29.4 (2008), pp. 389–391. DOI: `10.1109/LED.2008.918257`.

[295] X. Ju and D. S. Ang. "Response of Switching Hole Traps in the Small–Area pMOSFET Under Channel Hot-Hole Effect". In: *2019 IEEE International Reliability Physics Symposium (IRPS)*. Mar. 2019, pp. 1–4. DOI: `10.1109/IRPS.2019.8720476`.

[296] X. Ju and D. S. Ang. "Alteration of Gate-Oxide Trap Capture/Emission Time Constants by Channel Hot-Carrier Effect in the Metal-Oxide-Semiconductor Field-Effect Transistor". In: *IEEE Access* 8 (2020), pp. 14048–14053. DOI: `10.1109/ACCESS.2020.2966577`.

[297] D. Jabs, K. H. Bach, and C. Jungemann. "Avalanche Breakdown Evolution Under Hot-Carrier Stress: A New Microscopic Simulation Approach Applied to a Vertical Power MOSFET". In: *Journal of Computational Electronics* 17.3 (Sept. 2018), pp. 1249–1256. DOI: `10.1007/s10825-018-1196-7`.

[298] S.-M. Hong, C. Jungemann, and M. Bollhofer. "A Deterministic Boltzmann Equation Solver for Two-Dimensional Semiconductor Devices". In: *2008 International Conference on Simulation of Semiconductor Processes and Devices*. Sept. 2008, pp. 293–296. DOI: `10.1109/SISPAD.2008.4648295`.

[299] S.-M. Hong and C. Jungemann. "A Fully Coupled Scheme for a Boltzmann-Poisson Equation Solver Based on a Spherical Harmonics Expansion". In: *Journal of Computational Electronics* 8.3 (Oct. 2009), p. 225. DOI: `10.1007/s10825-009-0294-y`.

[300] G. A. Rott, K. Rott, H. Reisinger, W. Gustin, and T. Grasser. "Mixture of Negative Bias Temperature Instability and Hot–Carrier Driven Threshold Voltage Degradation of 130 nm Technology p-Channel Transistors". In: *Microelectronics Reliability* 54.9-10 (2014), pp. 2310–2314. DOI: `10.1016/j.microrel.2014.07.040`.

[301] C. Schlünder, R. Brederlow, B. Ankele, W. Gustin, K. Goser, and R. Thewes. "Effects of Inhomogeneous Negative Bias Temperature Stress on p-Channel MOSFETs of Aanalog and RF Circuits". In: *Microelectronics Reliability* 45.1 (2005), pp. 39–46. ISSN: 0026-2714. DOI: `10.1016/j.microrel.2004.03.017`.

[302] P. Chaparala and D. Brisbin. "Impact of NBTI and HCI on pMOSFET Threshold Voltage Drift". In: *Microelectronics Reliability* 45.1 (2005), pp. 13–18. DOI: `10.1016/j.microrel.2004.03.016`.

[303] X. Federspiel, M. Rafik, D. Angot, F. Cacho, and D. Roy. "Interaction between BTI and HCI Degradation in High-κ Devices". In: *2013 IEEE International Reliability Physics Symposium (IRPS)*. Apr. 2013, XT.9.1–XT.9.4. DOI: `10.1109/IRPS.2013.6532124`.

[304] B. S. Doyle, B. J. Fishbein, and K. R. Mistry. "NBTI-enhanced Hot Carrier Damage in p-Channel MOSFETs". In: *International Electron Devices Meeting 1991 [Technical Digest]*. Dec. 1991, 529–532A. DOI: `10.1109/IEDM.1991.235340`.

[305] H. Aono, E. Murakami, K. Okuyama, K. Makabe, K. Kuroda, K. Watanabe, H. Ozaki, K. Yanagisawa, K. Kubota, and Y. Ohji. "NBT-induced Hot Carrier (HC) Effect: Positive Feedback Mechanism in p-MOSFET's Degradation". In: *2002 IEEE International Reliability Physics Symposium (IRPS)*. Apr. 2002, pp. 79–85. DOI: `10.1109/RELPHY.2002.996613`.

[306] G. La Rosa, F. Guarin, S. Rauch, A. Acovic, J. Lukaitis, and E. Crabbe. "NBTI-Channel Hot Carrier Effects in pMOSFETs in Advanced CMOS Technologies". In: *1997 IEEE International Reliability Physics Symposium Proceedings. 35th Annual*. Apr. 1997, pp. 282–286. DOI: `10.1109/RELPHY.1997.584274`.

[307] Yandong He and Ganggang Zhang. "Experimental Insights on the Degradation and Recovery of pMOSFET under Non–Uniform NBTI Stresses". In: *18th IEEE International Symposium on the Physical and Failure Analysis of Integrated Circuits (IPFA)*. July 2011, pp. 1–6. DOI: `10.1109/IPFA.2011.5992767`.

[308] A. Chasin, E. Bury, B. Kaczer, J. Franco, P. Roussel, R. Ritzenthaler, H. Mertens, N. Horiguchi, D. Linten, and A. Mocuta. "Complete Degradation Mapping of Stacked Gate-All-Around Si Nanowire Transistors considering both Intrinsic and Extrinsic Effects". In: *2017 IEEE International Electron Devices Meeting (IEDM)*. Dec. 2017, pp. 7.1.1–7.1.4. DOI: `10.1109/IEDM.2017.8268343`.

[309] M. Duan, J. F. Zhang, J. C. Zhang, W. Zhang, Z. Ji, B. Benbakhti, X. F. Zheng, Y. Hao, D. Vigar, F. Adamu-Lema, V. Chandra, R. Aitken, B. Kaczer, G. Groeseneken, and A. Asenov. "Interaction between Hot Carrier Aging and PBTI Degradation in nMOSFETs: Characterization,

Modelling and Lifetime Prediction". In: *2017 IEEE International Reliability Physics Symposium (IRPS)*. Apr. 2017, XT-5.1-XT–5.7. DOI: 10.1109/IRPS.2017.7936419.

[310] E. Bury, A. Chasin, M. Vandemaele, S. Van Beek, J. Franco, B. Kaczer, and D. Linten. "Array-Based Statistical Characterization of CMOS Degradation Modes and Modeling of the Time-Dependent Variability Induced by Different Stress Patterns in the $\{V_G,V_D\}$ Bias Space". In: *2019 IEEE International Reliability Physics Symposium (IRPS)*. Mar. 2019, pp. 1–6. DOI: 10.1109/IRPS.2019.8720592.

[311] M. Vandemaele, B. Kaczer, Z. Stanojevic, S. E. Tyaginov, A. Makarov, A. Chasin, H. Mertens, D. Linten, and G. Groeseneken. "Distribution Function Based Simulations of Hot-Carrier Degradation in Nanowire FETs". In: *Proceedings of the IEEE International Integrated Reliability Workshop (IIRW)*. 2018. ISBN: 978-1-5386-6039-3. DOI: 10.1109/IIRW.2018.8727081.

[312] B. Kaczer, T. Grasser, P. J. Roussel, J. Martin-Martinez, R. O'Connor, B. J. O'Sullivan, and G. Groeseneken. "Ubiquitous Relaxation in BTI Stressing-New Evaluation and Insights". In: *Proceedings of the International Reliability Physics Symposium (IRPS)*. 2008, pp. 20–27. DOI: 10.1109/RELPHY.2008.4558858.

[313] S. Selberherr. *Analysis and Simulation of Semiconductor Devices*. Springer-Verlag, Wien - New York, 1984. DOI: 10.1007/978-3-7091-8752-4.

[314] F. Hoehne, J. Lu, A. R. Stegner, M. Stutzmann, M. S. Brandt, M. Rohrmüller, W. G. Schmidt, and U. Gerstmann. "Electrically Detected Electron-Spin-Echo Envelope Modulation: A Highly Sensitive Technique for Resolving Complex Interface Structures". In: *Phys. Rev. Lett.* 106 (19 May 2011), p. 196101. DOI: 10.1103/PhysRevLett.106.196101.

[315] J. Cottom, G. Gruber, G. Pobegen, T. Aichinger, and A. L. Shluger. "Recombination Defects at the 4H-SiC/SiO_2 Interface Investigated with Electrically Detected Magnetic Resonance and Ab Initio Calculations". In: *Journal of Applied Physics* 124.4 (2018), p. 045302. DOI: 10.1063/1.5024608.

[316] T. Olsen, J. Gavnholt, and J. Schiøtz. "Hot-Electron-Mediated Desorption Rates Calculated from Excited-State Potential Energy Surfaces". In: *Phys. Rev. B* 79 (3 Jan. 2009), p. 035403. DOI: 10.1103/PhysRevB.79.035403.

[317] J. Gavnholt, A. Rubio, T. Olsen, K. S. Thygesen, and J. Schiøtz. "Hot-Electron-Assisted Femtochemistry at Surfaces: A Time-Dependent Density Functional Theory Approach". In: *Phys. Rev. B* 79 (19 May 2009), p. 195405. DOI: 10.1103/PhysRevB.79.195405.

[318] T. Kreibich and E. K. U. Gross. “Multicomponent Density-Functional Theory for Electrons and Nuclei”. In: *Phys. Rev. Lett.* 86 (14 Apr. 2001), pp. 2984–2987. DOI: 10.1103/PhysRevLett.86.2984.

[319] Q. Wu and T. Van Voorhis. “Direct Pptimization Method to Study Constrained Systems within Density-Functional Theory”. In: *Phys. Rev. A* 72 (2 Aug. 2005), p. 024502. DOI: 10.1103/PhysRevA.72.024502.

[320] J. Gavnholt, T. Olsen, M. Engelund, and J. Schiøtz. “Δ Self-Consistent Field Method to Obtain Potential Energy Surfaces of Excited Molecules on Surfaces”. In: *Phys. Rev. B* 78 (7 Aug. 2008), p. 075441. DOI: 10.1103/PhysRevB.78.075441.

[321] T. Baruah, M. Olguin, and R. R. Zope. “Charge Transfer Excited State Energies by Perturbative Delta Self Consistent Field Method”. In: *The Journal of Chemical Physics* 137.8 (2012), p. 084316. DOI: 10.1063/1.4739269.

[322] A. Hellman, B. Razaznejad, and B. I. Lundqvist. “Potential-Energy Surfaces for Excited States in Extended Systems”. In: *The Journal of Chemical Physics* 120.10 (2004), pp. 4593–4602. DOI: 10.1063/1.1645787.

[323] M. Houssa, G. Pourtois, V. V. Afanas’ev, and A. Stesmans. “First-Principles Study of Ge Dangling Bonds in GeO_2 and Correlation with Electron Spin Resonance at Ge/GeO_2 Interfaces”. In: *Applied Physics Letters* 99.21 (2011), p. 212103. DOI: 10.1063/1.3662860.

[324] L. Tsetseris and S. T. Pantelides. “Morphology and Defect Properties of the Ge-GeO_2 Interface”. In: *Applied Physics Letters* 95.26 (2009), p. 262107. DOI: 10.1063/1.3280385.

[325] P. Broqvist, J. F. Binder, and A. Pasquarello. “First Principles Study of Electronic and Structural Properties of the Ge/GeO_2 Interface”. In: *Physica B: Condensed Matter* 407.15 (2012), pp. 2926–2931. DOI: 10.1016/j.physb.2011.08.037.

[326] T. Grasser, M. Waltl, W. Goes, Y. Wimmer, A. .-M. El-Sayed, A. L. Shluger, and B. Kaczer. “On the Volatility of Oxide Defects: Activation, Deactivation, and Transformation”. In: *2015 IEEE International Reliability Physics Symposium.* Apr. 2015, 5A.3.1–5A.3.8. DOI: 10.1109/IRPS.2015.7112739.

[327] “Silicon (Si) High-Frequency Dielectric Constant”. In: *Group IV Elements, IV-IV and III-V Compounds. Part a - Lattice Properties.* Ed. by O. Madelung, U. Rössler, and M. Schulz. Berlin, Heidelberg: Springer Berlin Heidelberg, 2001, pp. 1–7. DOI: 10.1007/10551045_218.

[328] J. Matsuoka, N. Kitamura, S. Fujinaga, T. Kitaoka, and H. Yamashita. “Temperature Dependence of Refractive Index of SiO_2 Glass”. In: *Journal of Non-Crystalline Solids* 135.1 (1991), pp. 86–89. DOI: 10.1016/0022-3093(91)90447-E.

[329] W. A. Pliskin and R. P. Esch. “Refractive Index of SiO_2 Films Grown on Silicon”. In: *Journal of Applied Physics* 36.6 (1965), pp. 2011–2013. DOI: 10.1063/1.1714393.

[330] Y. Park, K.-j. Kong, H. Chang, and M. Shin. “First-Principles Studies of the Electronic and Dielectric Properties of $Si/SiO_2/HfO_2$ Interfaces”. In: *Japanese Journal of Applied Physics* 52.4R (Apr. 2013), p. 041803. DOI: 10.7567/JJAP.52.041803.

[331] N. Shi and R. Ramprasad. “Atomic-Scale Dielectric Permittivity Profiles in Slabs and Multilayers”. In: *Physical Review B* 74.4 (July 2006), p. 045318. DOI: 10.1103/PhysRevB.74.045318.

[332] S. Wakui, J. Nakamura, and A. Natori. “Atomic Scale Dielectric Constant Near the SiO_2/Si(001) Interface”. In: *Journal of Vacuum Science & Technology B: Microelectronics and Nanometer Structures* 26.4 (2008), p. 1579. DOI: 10.1116/1.2937734.

[333] F. Giustino and A. Pasquarello. “Theory of Atomic-Scale Dielectric Permittivity at Insulator Interfaces”. In: *Phys. Rev. B* 71 (14 Apr. 2005), p. 144104. DOI: 10.1103/PhysRevB.71.144104.

List of Publications

Scientific Journals

[MJJ1] Y. Illarionov, T. Knobloch, **M. Jech**, M. Lanza, D. Akinwande, M. I. Vexler, T. Müller, M. Lemme, G. Fiori, F. Schwierz, and T. Grasser. "Insulators for 2D Nanoelectronics: The Gap to Bridge". In: *Nature Communications* 11 (2020), p. 3385. DOI: 10.1038/s41467-020-16640-8.

[MJJ2] **M. Jech**, G. Rott, H. Reisinger, S. Tyaginov, G. Rzepa, A. Grill, D. Jabs, C. Jungemann, M. Waltl, and T. Grasser. "Mixed Hot-Carrier/Bias Temperature Instability Degradation Regimes in Full V_G, V_D Bias Space: Implications and Peculiarities". In: *IEEE Transactions on Electron Devices* 67.8 (2020), pp. 3315–3322. DOI: 10.1109/TED.2020.3000749.

[MJJ3] **M. Jech**, A.-M. El-Sayed, S. Tyaginov, A. L. Shluger, and T. Grasser. "*Ab Initio* Treatment of Silicon-Hydrogen Bond Rupture at Si/SiO$_2$ Interfaces". In: *Phys. Rev. B* 100 (19 2019), p. 195302. DOI: 10.1103/PhysRevB.100.195302.

[MJJ4] **M. Jech**, B. Ullmann, G. Rzepa, S. E. Tyaginov, A. Grill, M. Waltl, D. Jabs, C. Jungemann, and T. Grasser. "Impact of Mixed Negative Bias Temperature Instability and Hot Carrier Stress on MOSFET Characteristics-Part II: Theory". In: *IEEE Transactions on Electron Devices* 66.1 (2019), pp. 241–248. DOI: 10.1109/TED.2018.2873421.

[MJJ5] A. Makarov, B. Kaczer, A. Chasin, M. Vandemaele, E. Bury, **M. Jech**, A. Grill, G. Hellings, A.-M. El-Sayed, T. Grasser, D. Linten, and S. E. Tyaginov. "Bi-Modal Variability of nFinFET Characteristics During Hot-Carrier Stress: A Modeling Approach". In: *IEEE Electron Device Letters* 40.10 (2019), pp. 1579–1582. DOI: 10.1109/LED.2019.2933729.

[MJJ6] B. Ullmann, **M. Jech**, K. Puschkarsky, G. A. Rott, M. Waltl, Y. Illarionov, H. Reisinger, and T. Grasser. "Impact of Mixed Negative Bias Temperature Instability and Hot Carrier Stress on MOSFET Characteristics-Part I: Experimental". In: *IEEE Transactions on Electron Devices* 66.1 (2019), pp. 232–240. DOI: 10.1109/TED.2018.2873419.

[MJJ7] W. Gös, Y. Wimmer, A.-M. El-Sayed, G. Rzepa, **M. Jech**, A. L. Shluger, and T. Grasser. “Identification of Oxide Defects in Semiconductor Devices: A Systematic Approach Linking DFT to Rate Equations and Experimental Evidence”. In: *Microelectronics Reliability* 87 (2018), pp. 286–320. DOI: 10.1016/j.microrel.2017.12.021.

[MJJ8] G. Rzepa, J. Franco, B. J. O’Sullivan, A. Subirats, M. Simicic, G. Hellings, P. Weckx, **M. Jech**, T. Knobloch, M. Waltl, P. J. Roussel, D. Linten, B. Kaczer, and T. Grasser. “Comphy – A Compact-Physics Framework for Unified Modeling of BTI”. In: *Microelectronics Reliability* 85.1 (2018), pp. 49–65. DOI: 10.1016/j.microrel.2018.04.002.

[MJJ9] B. Kaczer, J. Franco, S. E. Tyaginov, **M. Jech**, G. Rzepa, T. Grasser, B. J. O’Sullivan, R. Ritzenhaler, T. Schram, A. Spessot, D. Linten, and N. Horiguchi. “Mapping of CMOS FET Degradation in Bias Space–Application to Dram Peripheral Devices”. In: *Journal of Vacuum Science & Technology B* 35.1 (2017), 01A109-1–01A109-6. DOI: 10.1116/1.4972872.

[MJJ10] **M. Jech**, P. Sharma, S. E. Tyaginov, F. Rudolf, and T. Grasser. “On the Limits of Applicability of Drift-Diffusion Based Hot Carrier Degradation Modeling”. In: *Japanese Journal of Applied Physics* 55.4S (2016), pp. 1–6. DOI: 10.7567/JJAP.55.04ED14.

[MJJ11] P. Sharma, S. E. Tyaginov, **M. Jech**, Y. Wimmer, F. Rudolf, H. Enichlmair, J. Park, H. Ceric, and T. Grasser. “The Role of Cold Carriers and the Multiple-Carrier Process of Si-H Bond Dissociation for Hot-Carrier Degradation in n- and p-channel LDMOS Devices”. In: *Solid-State Electronics* 115.Part B (2016), pp. 185–191. DOI: 10.1016/j.sse.2015.08.014.

[MJJ12] S. Tyaginov, **M. Jech**, J. Franco, P. Sharma, B. Kaczer, and T. Grasser. “Understanding and Modeling the Temperature Behavior of Hot-Carrier Degradation in SiON nMOSFETs”. In: *IEEE Electron Device Letters* 37.1 (2016), pp. 84–87. DOI: 10.1109/LED.2015.2503920.

Conference Proceedings

[MJC1] J. Franco, J.-F. de Marneffe, A. Vandooren, Y. Kimura, L. Nyns, Z. Wu, A.-M. El-Sayed, **M. Jech**, D. Waldhoer, D. Claes, H. Arimura, L.-A. Ragnarsson, V. Afanas’ev, A. Stesmans, N. Horiguchi, D. Linten, T. Grasser, and B. Kaczer. “Atomic Hydrogen Exposureto Enable High–Quality Low–Temperature SiO_2 with Excellent pMOS NBTI Reliability Compatible with 3D Sequential Tier Stacking”. In: *2020 IEEE International Electron Devices Meeting (IEDM)*. Dec. 2020, accepted.

[MJC2] D. Milardovich, **M. Jech**, D. Waldhör, M. Waltl, and T. Grasser. "Machine Learning Prediction of Formation Energies in a-SiO$_2$". In: *Proceedings of the International Conference on Simulation of Semiconductor Processes and Devices (SISPAD)*. 2020, pp. 339–342.

[MJC3] B. Ruch, **M. Jech**, G. Pobegen, and T. Grasser. "Applicability of Shockley–Read–Hall Theory for Interface States". In: *2020 IEEE International Electron Devices Meeting (IEDM)*. Dec. 2020, accepted.

[MJC4] S. Tyaginov, A. Grill, M. Vandemaele, T. Grasser, G. Hellings, A. Makarov, **M. Jech**, D. Linten, and B. Kaczer. "A Compact Physics Analytical Model for Hot-Carrier Degradation". In: *2020 IEEE International Reliability Physics Symposium (IRPS)*. 2020, pp. 1–7. DOI: 10.1109/IRPS45951.2020.9128327.

[MJC5] **M. Jech**, S. Tyaginov, B. Kaczer, J. Franco, D. Jabs, C. Jungemann, M. Waltl, and T. Grasser. "First–Principles Parameter–Free Modeling of n- and p-ET Hot-Carrier Degradation". In: *2019 IEEE International Electron Devices Meeting (IEDM)*. 2019, 24.1.1–24.1.4, Best Student Paper Award. DOI: 10.1109/IEDM19573.2019.8993630.

[MJC6] A. Makarov, B. Kaczer, P. Roussel, A. Chasin, M. Vandemaele, G. Hellings, A.-M. El-Sayed, **M. Jech**, T. Grasser, D. Linten, and S. Tyaginov. "Stochastic Modeling of Hot-Carrier Degradation in nFinFETs Considering the Impact of Random Traps and Random Dopants". In: *ESSDERC 2019 - 49th European Solid-State Device Research Conference (ESSDERC)*. 2019, pp. 262–265. DOI: 10.1109/ESSDERC.2019.8901721.

[MJC7] A. Makarov, B. Kaczer, P. Roussel, A. Chasin, M. Vandemaele, G. Hellings, A.-M. El-Sayed, **M. Jech**, T. Grasser, D. Linten, and S. E. Tyaginov. "Simulation Study: The Effect of Random Dopants and Random Traps on Hot-Carrier Degradation in nFinFETs". In: *Extended Abstracts of the International Conference on Solid State Devices and Materials (SSDM)*. 2019, pp. 609–610.

[MJC8] S. Tyaginov, A.-M. El-Sayed, A. Makarov, A. Chasin, H. Arimura, M. Vandemaele, **M. Jech**, E. Capogreco, L. Witters, A. Grill, A. De Keersgieter, G. Eneman, D. Linten, and B. Kaczer. "Understanding and Physical Modeling Superior Hot-Carrier Reliability of Ge pNWFETs". In: *2019 IEEE International Electron Devices Meeting (IEDM)*. 2019, pp. 21.3.1–21.3.4. DOI: 10.1109/IEDM19573.2019.8993644.

[MJC9] S. E. Tyaginov, A. Chasin, A. Makarov, A.-M. El-Sayed, **M. Jech**, A. De Keersgieter, G. Eneman, M. Vandemaele, J. Franco, D. Linten, and B. Kaczer. "Physics-based Modeling of Hot-Carrier Degradation in Ge NWFETs". In: *Extended Abstracts of the International Conference on Solid State Devices and Materials (SSDM)*. 2019, pp. 565–566.

[MJC10] S. E. Tyaginov, **M. Jech**, G. Rzepa, A. Grill, A.-M. El-Sayed, G. Pobegen, A. Makarov, and T. Grasser. “Border Trap Based Modeling of SiC Transistor Transfer Characteristics”. In: *Proceedings of the IEEE International Integrated Reliability Workshop (IIRW)*. 2018. DOI: 10.1109/IIRW.2018.8727083.

[MJC11] Y. Illarionov, M. Waltl, **M. Jech**, J.-S. Kim, D. Akinwande, and T. Grasser. “Reliability of Black Phosphorus Field-Effect Transistors with Respect to Bias-Temperature and Hot-Carrier Stress”. In: *2017 IEEE International Reliability Physics Symposium (IRPS)*. 2017, 6A-6.1–6A-6.6. DOI: 10.1109/IRPS.2017.7936338.

[MJC12] T. Knobloch, G. Rzepa, Y. Illarionov, M. Waltl, F. Schanovsky, **M. Jech**, B. Stampfer, M. M. Furchi, T. Müller, and T. Grasser. “Physical Modeling of the Hysteresis in MoS_2 Transistors”. In: *Proceedings of the European Solid-State Device Research Conference (ESSDERC)*. 2017, pp. 284–287. DOI: 10.1109/ESSDERC.2017.8066647.

[MJC13] A. Makarov, S. E. Tyaginov, B. Kaczer, **M. Jech**, A. Chasin, A. Grill, G. Hellings, M. I. Vexler, D. Linten, and T. Grasser. “Hot-Carrier Degradation in FinFETs: Modeling, Peculiarities, and Impact of Device Topology”. In: *2017 IEEE International Electron Devices Meeting (IEDM)*. Dec. 2017, pp. 13.1.1–13.1.4. DOI: 10.1109/IEDM.2017.8268381.

[MJC14] G. Rzepa, J. Franco, A. Subirats, **M. Jech**, A. Chasin, A. Grill, M. Waltl, T. Knobloch, B. Stampfer, T. Chiarella, N. Horiguchi, L. Å. Ragnarsson, D. Linten, B. Kaczer, and T. Grasser. “Efficient physical defect model applied to PBTI in high-κ stacks”. In: *2017 IEEE International Reliability Physics Symposium (IRPS)*. 2017, XT-11.1-XT–11.6.

[MJC15] B. Ullmann, **M. Jech**, S. Tyaginov, M. Waltl, Y. Illarionov, A. Grill, K. Puschkarsky, H. Reisinger, and T. Grasser. “The Impact of Mixed Negative Bias Temperature Instability and Hot Carrier stress on Single Oxide Defects”. In: *2017 IEEE International Reliability Physics Symposium (IRPS)*. Apr. 2017, XT-10.1-XT–10.6. DOI: 10.1109/IRPS.2017.7936424.

[MJC16] S. E. Tyaginov, A. Makarov, **M. Jech**, J. Franco, P. Sharma, B. Kaczer, and T. Grasser. “On the Effect of Interface Traps on the Carrier Distribution Function During Hot-Carrier Degradation”. In: *Proceedings of the IEEE International Integrated Reliability Workshop (IIRW*. 2016, pp. 95–98. DOI: 10.1109/IIRW.2016.7904911.

[MJC17] **M. Jech**, P. Sharma, S. Tyaginov, F. Rudolf, and T. Grasser. “The Limits of Applicability of the Analytic Model for Hot Carrier Degradation”. In: *Extended Abstracts of the International Conference on Solid State Devices and Materials (SSDM)*. 2015, PS.3–13.

[MJC18] P. Sharma, **M. Jech**, S. Tyaginov, F. Rudolf, K. Rupp, H. Enichlmair, J. Park, and T. Grasser. “Modeling of Hot-Carrier Degradation in LDMOS Devices Using a Drift-Diffusion Based Approach”. In: *2015 International Conference on Simulation of Semiconductor Processes and Devices (SISPAD)*. 2015, pp. 60–63. DOI: 10.1109/SISPAD.2015.7292258.

[MJC19] S. Tyaginov, **M. Jech**, P. Sharma, J. Franco, B. Kaczer, and T. Grasser. “On The Temperature Behavior of Hot-Carrier Degradation”. In: *2015 IEEE International Integrated Reliability Workshop (IIRW)*. 2015, pp. 143–146. DOI: 10.1109/IIRW.2015.7437088.